Imperial College London

Doctoral Thesis

Modelling non-isothermal transport phenomena in mixtures, colloids and polar fluids

---

Oliver Richard Gittus

A thesis submitted in fulfilment of the requirements
for the degree of Doctor of Philosophy

in the

Department of Chemistry

To my mum and dad, for their love and support.

Abstract

This thesis works towards understanding, from a fundamental perspective, the non-isothermal transport properties of a diverse range of fluids. Namely, the thermal diffusion and thermal conductivity of molecular mixtures, colloids and polar fluids. To this end, we employ molecular simulations as a primary tool for investigation. We also derive analytical theoretical models. In Chapter 3 we show that simple liquid mixtures can feature a minimum in the Soret coefficient as a function of composition. We link the minimum to the non-ideality of the mixtures, and explain its microscopic origin in terms of their atomic coordination structure. Chapter 4 uncovers the mass dipole contribution to the (pseudo-)isotopic Soret effect in molecular mixtures. In the mixtures of rod-like molecules studied, it arises mainly through the thermal diffusion coefficient via the modification of a librational mode. We demonstrate that it can lead to new phenomenology in the Soret coefficient, including a reversal in sign. Chapter 5 connects the thermal orientation and thermophoresis of rod-like colloids with mass anisotropy. Using both theory and simulation, we show how the Soret coefficients of these colloids depend on their internal mass distribution and average orientation. Chapter 6 investigates the thermal polarization of acetonitrile. We rationalize trends in the thermopolarization coefficient in terms of physical properties, such as rotational diffusion and the dielectric constant of the fluid. Using acetonitrile as an exemplar, we quantify, for the first time, how thermal polarization impacts the thermal conductivity of polar fluids. Chapter 7 presents comprehensive benchmarks of the thermophysical properties of water for two state-of-the-art ReaxFF force fields. Based on our results, we recommend potential avenues of improvement for these models. Chapter 8 examines the anomalous thermal conductivity of water. We establish correlations with other thermophysical properties: the speed of sound, compressibility, sound attenuation coefficient and kinematic longitudinal viscosity. A possible explanation for the thermal conductivity maximum at constant pressure is provided.

Declaration of Authorship

I hereby confirm that this thesis represents my own work. All results or material that are not part of my own work are explicitly cited or referenced. No part of this thesis has been submitted to satisfy the requirements of any other degree.

Oliver R. Gittus

Copyright Declaration

The copyright of this thesis rests with the author. Unless otherwise indicated, its contents are licensed under a Creative Commons Attribution – Non Commercial – No Derivatives 4.0 International Licence (CC BY-NC-ND). Under this licence, you may copy and redistribute the material in any medium or format on the condition that; you credit the author, do not use it for commercial purposes and do not distribute modified versions of the work. When reusing or sharing this work, ensure you make the licence terms clear to others by naming the licence and linking to the licence text. Please seek permission from the copyright holder for uses of this work that are not included in this licence or permitted under UK Copyright Law.

Acknowledgements

This PhD has been a journey. These years have been some of the most stimulating and exciting of my life, and in some respects, also some of the most challenging. I am grateful for the friends, family and colleagues who have been there for the ups and downs.

First of all, I would like to thank Fernando for his guidance and support. My impression is that life as a professor is a busy one, but you always managed to make time. I cannot fully express my gratitude for the many hours we have spent discussing science and life in general. I very much looked forward to our weekly virtual meetings during the pandemic, and when not resident in London.

It's been a joy to be part of the Bresme group. Thank you everyone for the lab life! Thank you Juan for the mentorship during the early days of my PhD. Thank you Silvia, for the coffees in the park during lock-down, and for the emotional support.

My particular gratitude goes to the close friends from my undergrad. days. Thank you Emrys, Hugo, Matt, Miguel and Arthur. There is too much to write here. Thanks for everything guys!

Thank you to my mum and dad for their love and support. This thesis is dedicated to them.

List of Publications

Work presented in this thesis has been published in the following.

Part of Chapter 3 has been published in:

- O. R. Gittus and F. Bresme, "On the microscopic origin of Soret coefficient minima in liquid mixtures", *Physical Chemistry Chemical Physics*, **25**(3), 1606, 2023. DOI:10.1039/D2CP04256H.
  - Published as a *Communication*.

Part of Chapter 4 has been published in:

- O. R. Gittus and F. Bresme, "Mass dipole contribution to the isotopic Soret effect in molecular mixtures", *The Journal of Chemical Physics*, accepted.

Part of Chapter 5 has been published in

- O. R. Gittus, J. D. Olarte-Plata and F. Bresme, "Thermal orientation and thermophoresis of anisotropic colloids: The role of the internal composition", *European Physical Journal E*, **42**(7), 90, 2019. DOI: 10.1140/epje/i2019-11852-5.
  - Part of the *Topical Issue on Thermal Non-Equilibrium Phenomena in Soft Matter*.

Part of Chapter 6 has been published in

- O. R. Gittus, P. Albella and F. Bresme, "Polarization of acetonitrile under thermal fields via non-equilibrium molecular dynamics simulations", *The Journal of Chemical Physics*, **153**(20), 204503, 2020. DOI: 10.1063/5.0025148.

Part of Chapter 7 has been published in

- O. R. Gittus and F. Bresme, "Thermophysical properties of water using reactive force fields", *The Journal of Chemical Physics*, **155**(11), 114501, 2021. DOI: 10.1063/5.0057868.
  - Selected as *Featured*.
  - Selected as an AIP *Scilight* (DOI: 10.1063/10.0006233).
  - Selected for the cover of *J. Chem. Phys.* **155**(11).

Contents

1 Introduction **1**

1.1 Thermal fields in technology and Nature . . . 1

1.2 Non-isothermal transport phenomena in fluids . . . 2

1.2.1 Thermal conductivity . . . 2

1.2.2 Thermal diffusion . . . 2

1.2.3 Thermal orientation and polarization . . . 5

1.3 Scope of the thesis . . . 5

2 Theoretical description of non-isothermal transport phenomena **13**

2.1 Linear non-equilibrium thermodynamics . . . 13

2.1.1 Scope and limitations of LNET . . . 13

2.1.2 Local equilibrium hypothesis . . . 14

2.1.3 Affinities, fluxes and entropy production . . . 15

2.1.4 Entropy production in a continuous medium . . . 16

2.1.5 Linear response . . . 17

2.1.6 Curie's principle . . . 18

2.1.7 Onsager-Casimir relations . . . 18

2.1.8 Stationary states and minimum entropy production . . . 19

2.2 Non-isothermal transport and coupling phenomena . . . 20

2.2.1 Thermal conductivity . . . 20

2.2.2 Thermal diffusion . . . 20

2.2.3 Thermal orientation . . . 23

2.2.4 Thermal polarization . . . 24

3 On the microscopic origin of Soret coefficient minima in liquid mixtures **27**

3.1 Introduction . . . 27

3.2 Methods . . . 28

3.3 Results and discussion . . . 30

3.3.1 Equation of state and phase diagram . . . 30

3.3.2 Soret coefficient minimum and its physical origin . . . 31
3.3.3 Theoretical models . . . 35
3.3.4 Thermal conductivity . . . 37
3.4 Closing remarks and summary . . . 38

4 Mass dipole contribution to the isotopic Soret effect in molecular mixtures 43
4.1 Introduction . . . 43
4.2 Methods . . . 45
4.2.1 Particle model . . . 45
4.2.2 Simulation details . . . 46
4.2.3 Transport properties from simulations . . . 48
4.3 Results and Discussion . . . 49
4.3.1 Equation of state and phase diagram . . . 49
4.3.2 Mass dipole contribution and its microscopic origin . . . 51
4.3.3 Coupling with the moment of inertia contribution . . . 57
4.3.4 An empirical equation for the isotopic Soret effect . . . 60
4.3.5 Thermal orientation . . . 62
4.4 Conclusions . . . 64

5 Thermophoresis and thermal orientation of anisotropic colloids 67
5.1 Introduction . . . 67
5.2 Theoretical model . . . 68
5.3 Methods . . . 70
5.4 Results and discussion . . . 72
5.4.1 Thermal orientation . . . 74
5.4.2 Thermophoresis . . . 76
5.4.3 Linking the Soret coefficient and average orientation . . . 78
5.5 Conclusions . . . 79

6 Thermal polarization and thermal conductivity of acetonitrile 83
6.1 Introduction . . . 83
6.2 Methods . . . 84
6.2.1 Non-equilibrium molecular dynamics simulations . . . 85
6.2.2 Equilibrium simulations . . . 86
6.3 Results and discussion . . . 86
6.3.1 Equation of state and phase diagram . . . 86
6.3.2 Thermal polarization . . . 87

6.3.3 Thermal conductivity . . . 92
6.4 Conclusions . . . 95

7 Thermophysical properties of water using reactive force fields 99
7.1 Introduction . . . 99
7.1.1 Motivation . . . 99
7.1.2 ReaxFF in the context of state-of-the-art water models . . . 100
7.2 Methods . . . 101
7.2.1 ReaxFF models . . . 101
7.2.2 Simulation details . . . 102
7.3 Results and discussion . . . 107
7.3.1 Radial distribution functions . . . 107
7.3.2 Atomic charges and electrostatic moments . . . 109
7.3.3 Vibrational power spectrum . . . 113
7.3.4 Potential energy curves of the water monomer and dimer . . . 116
7.3.5 Density and thermal expansion . . . 118
7.3.6 Enthalpy of vaporization . . . 120
7.3.7 Surface tension . . . 121
7.3.8 Isothermal compressibility . . . 123
7.3.9 Isobaric and isochoric heat capacity . . . 124
7.3.10 Speed of sound . . . 128
7.3.11 Self-diffusion coefficient . . . 129
7.3.12 Shear viscosity . . . 132
7.3.13 Thermal conductivity . . . 133
7.4 Conclusions . . . 137

8 On the anomalous thermal conductivity of water 149
8.1 Introduction . . . 149
8.2 Methods . . . 149
8.2.1 Non-equilibrium molecular dynamics simulations . . . 150
8.2.2 Equilibrium simulations . . . 152
8.3 Results and discussion . . . 152
8.3.1 Thermodynamic conditions and the equation of state . . . 152
8.3.2 Thermal conductivity . . . 154
8.3.3 Correlations with the speed of sound and compressibility . . . 161
8.3.4 Correlations with sound attenuation and longitudinal viscosity . . . 166
8.4 Conclusions . . . 167

9 Conclusions and future work **173**

A Theoretical background **179**

A.1 Global and local balance equations 179

A.2 Curie's principle for an isotropic medium 180

A.3 Minimum entropy production theorem 181

B Methods and supporting information for Chapter 3 **185**

B.1 Soret coefficient and thermal conductivity from NEMD 185

B.1.1 Simulation details 185

B.1.2 Linear response 187

B.1.3 Finite-size effects 187

B.2 Equilibrium molecular dynamics simulations 188

B.3 Radial distribution functions 189

B.4 Partial molar properties 190

B.5 The phenomenological coefficients 190

B.6 Chemical potentials 193

B.7 Self-diffusion coefficients and shear viscosity 194

B.8 Activation energies for diffusion and viscous flow 196

B.9 Kirkwood-Buff integrals from grand canonical Monte Carlo simulations 198

B.10 Kirkwood-Buff integrals from molecular dynamics (NVT) simulations 199

B.11 Melting points of the pure components 201

C Supporting information for Chapter 4 **207**

C.1 Soret coefficient: verification of the linear regime 207

C.2 Soret coefficient: finite-size effects 208

C.3 Convergence of Green-Kubo integral formulas 209

C.4 Diffusion coefficients: finite-size effects 211

C.5 Isotropic-nematic coexistence 213

C.6 Thermal diffusion coefficient: fitting empirical equations 214

D Additional numerical data for Chapter 6 **217**

E Supporting information for Chapter 8 **219**

E.1 Response functions: SHAKE vs. RATTLE 219

E.2 Structure and dynamics benchmarks 222

E.3 Order parameters for water 227

E.4 Shear, bulk and longitudinal viscosity 230

List of Figures

1.1 To the hot or to the cold? A roadmap to identify the direction of the thermophoretic motion. Only general trends are identified, which do not hold for all mixtures. The list of factors are illustrative, not exhaustive. 3

3.1 Equation of state and phase diagram of the LJ mixture. (a) The number density ρ_N for ($P = 0.46\ \epsilon\sigma^{-3}$, $T = 0.62\ \epsilon k_B^{-1}$) as a function of mole fraction x_1, as predicted by MD(NPT), GCMC and NEMD simulations. All simulated systems correspond to a liquid, which is metastable for $x_1 \leq x_l$, where x_l is the mole fraction of the liquidus shown in (b). (b) The estimated solid solution phase diagram of the mixture at $P = 0.46\ \epsilon\sigma^{-3}$. The symbols are: S = solid solution; L = liquid mixture; S+L = solid and liquid coexistence. 31

3.2 The Soret coefficient and related properties of the LJ mixture as a function mole fraction x_1. (a) The Soret coefficient S_T; the solid lines show cubic functions fit to the $S_T(x_1)$ data. (b) The mutual diffusion coefficient D_{12} (left axis) and thermal diffusion coefficient D_T (right axis). (c) The thermodynamic factor Γ; the solid lines show polynomial functions fit to $\Gamma(x_1)$ with the infinite-dilution constraint $\Gamma(1) = 1$. (d) The ratio of phenomenological coefficients L'_{1q}/L_{11}; the solid line shows the weighted arithmetic mean. 32

3.3 The thermodynamic factor Γ, and its ideal Γ^{id} and excess Γ^{ex} contributions, as a function of mole fraction x_1. All results correspond to the FEP data. 33

3.4 Analysis of the thermodynamic factor Γ as a function of mole fraction x_1 using Kirkwood-Buff theory. (a) Excess coordination numbers $n_{ij}^{\mathrm{ex},\infty}$ and (b) related functions f and f_{ij}. (c) Γ and its first-order approximation $\Gamma^{(1)}$ (see main text for additional details). Symbols: sideways triangles and dotted lines ($\cdots\triangleleft\cdots$) denote the KBI(RDF) data; downwards triangles (--$\triangledown$--) and dashed lines denote the KBI(GCMC) data. In (c), dotted and dashed lines show polynomial functions fit to the KBI(RDF) and KBI(GCMC) data respectively. Fits to $\Gamma(x_1)$ were performed with the infinite-dilution constraint $\Gamma(0) = 1$. 34

3.5 Soret coefficient S_T as a function of x_1 as predicted by various models, as defined in the main text. The NEMD values S_T^{NEMD} are shown for reference. The solid lines show cubic functions fit to the $S_T(x_1)$ data. 36

3.6 Thermal conductivity λ as a function of (a) mole fraction x_1 and (b) number density ρ_N as well as $\rho_N^{2/3}$. (c) The decrease in λ due to heat-mass coupling, $|\delta\lambda|$ and $\delta\lambda'$. In (c), circles with dashed lines (--○--) show the absolute values (left axis) and downward triangles with dotted lines ($\cdot\cdot\triangledown\cdot\cdot$) show the values as a percentage of λ (right axis). Where error bars have not been shown, uncertainties are smaller than the size of the symbols. 38

4.1 The shish-kebab model of length $N = 7$. 45

4.2 Representative (a) temperature T and monomer number density $\rho_{N,\mathrm{mon}}$ profiles, and (b) mole fraction, x_1 and x_2, profiles for the NEMD simulations. The blue (cold) and red (hot) indicate the location of the thermostatting regions in the simulation cell. The profiles correspond to the $(I_1 = I_2, d_1, d_2) = (80m\sigma^2, 2.7\sigma, 0)$ mixture. . . 47

4.3 Phase diagram and equation of state (EOS). T, $\rho_{N,\mathrm{mon}}$ and ϕ are the temperature, monomer number density and volume fraction, respectively. The data is colour coded according to the uniaxial (orientational) order parameter S_2. The dashed isotropic-nematic coexistence line is to guide the eye. The inset shows the EOS at pressure $P = 1.121\epsilon\sigma^{-3}$, as predicted by equilibrium-NPT and NEMD simulations. Symbols: I=isotropic; N=nematic. 50

4.4 Transport coefficients for the isotopic mixtures with: (a) $I = I_1 = I_2$ and $d_2 = 0$; and (b) $I = I_1 = I_2 = 80m\sigma^2$ and $d_1 \neq d_2$. The (i) Soret coefficient, (ii) thermal diffusion coefficient D_T and (iii) mutual diffusion coefficient D_{12}, as a function of $d_1 - d_2$. d_i and I_i are the mass dipole and moment of inertia of species $i = 1, 2$, respectively. The solid lines show equations that model the data: see the main text for details. 52

4.5 (a) The mutual diffusion coefficient D_{12} *vs.* the Darken approximation D_{12}^{Darken}. (b) D_{12}^{Darken}, (c) ΔD_1 and (d) ΔD_2 as a function of the mass dipole, d_1, of species 1. $\Delta D_i = D_i - D_i(d_1 = 0.5\sigma)$ is the change in self-diffusion coefficient D_i of species $i = 1, 2$ relative to the corresponding mixture with $d_1 = 0.5\sigma$. 53

4.6 Rotational and translational diffusion coefficients, and their correlation with the thermal diffusion coefficient D_T. (a) $D_{r,1}$ as a function of the mass dipole d_1 of species 1. (b) The ratio $D_1/D_{r,1}$ as a function of d_1. (c) D_T *vs.* $-(D_{r,1} - D_{r,2})$. (d) D_T *vs.* $-(D_1 - D_2)$. $D_{r,i}$ and D_i are the rotational and translational diffusion coefficients, respectively, of species $i = 1, 2$. 54

4.7 Power spectra of species 1 of the $(I_1 = I_2, d_1, d_2) = (80m\sigma^2, d_1, 0)$ mixtures. The intensity I_X *vs.* frequency ν for the (a) "all-atom" (I_{atom}) (b) rotational (I_{rot}) and (c) translational centre-of-mass (I_{trans}) power spectra. In (a) and (b), the vertical solid lines show the librational mode frequencies ν_{lib}. In (b), the dash-dot (-.) lines denote the fitted spectra I_{fit} and the inset shows the individual fitted functions for the $(I_1 = I_2, d_1, d_2) = (80m\sigma^2, 2.7\sigma, 0)$ mixture. 56

4.8 Thermal diffusion coefficient D_T as a function of $\nu_{\text{lib},1} - \nu_{\text{lib},2}$, where $\nu_{\text{lib},i}$ is the librational frequency of species i. The solid line shows the fit to $D_T = b(\nu_{\text{lib},1} - \nu_{\text{lib},2})$. Error bars correspond to maximum/minimum values based on the sensitivity of the fitting procedure for Eqs. 4.19,4.20&4.21. 57

4.9 The Soret coefficient S_T as a function of: (a) the relative $(I_1 - I_2)/(I_1 + I_2)$ and (b) absolute $(I_1 - I_2)$ differences in moment of inertia I_i of species $i = 1, 2$ for mixtures with mass dipoles $d_1 = d_2 = 0$; (c) $(I_1 - I_2)$ for mixtures with $d_1 = d_2$; and (d) $(d_1 - d_2)$ for mixtures with (I_1, d_1, I_2, d_2). In (d), the solid lines show fits to Eq. 4.25, and the label units for I_i and d_i are $m\sigma^2$ and σ, respectively. 59

4.10 Empirical models (a) A (Eq. 4.28) and (b) B (Eq. 4.29) for the isotopic Soret effect. (i) S_T *vs.* S_T^{X} for model $\text{X} = \text{A}, \text{B}$, where S_T^{X} and S_T are the predicted and reference (simulated) Soret coefficients, respectively. (ii) The error $S_T^{\text{X}} - S_T$ as a function of the mass dipole contribution $S_T^{d,\text{X}}$ and moment of inertia contribution $S_T^{I,\text{X}}$ of model $\text{X} = \text{A}, \text{B}$. Data are colour coded according to the error $S_T^{\text{X}} - S_T$. 61

4.11 Thermal orientation of the rod-like molecules. (a) The average orientation $\langle \cos\theta_{z,i} \rangle$ of species $i = 1, 2$ as a function of position z in the NEMD simulations. The blue (cold) and red (hot) indicate the location of the thermostatting regions in the simulation cell. The profiles correspond to the same system shown in Fig. 4.2. (b) Average orientation $\langle \cos\theta_1 \rangle$ of species 1 for different mixtures: (i) $\langle \cos\theta_1 \rangle / |\nabla T|$ *vs.* the mass dipole d_1; (ii) the Soret coefficient S_T *vs.* $\langle \cos\theta_1 \rangle$ for different temperature gradients ∇T. 63

5.1 Free body diagram of the anisotropic colloid in a thermal field. 69

5.2 The shish-kebab model. (a) Range of mass dipoles d as a function of the mass m_a of the single asymmetric bead at position a. (b) Graphical representations of colloids with $a = 3$ and $a = 5$. The bead of mass m_a is shown in yellow. 71

5.3 Simulation methodology. (a) Snapshot of the simulation setup for a colloid with with $a = 5$. (b) Representative solvent temperature T_s (top) and number density $\rho_{N,s}$ (bottom) profiles for different temperature gradients ∇T. Thermostatting regions are shaded red (hot) and blue (cold). 71

5.4 Soret coefficient S_T (a-c) and average orientation $\langle\cos\theta\rangle$ (d-f) of the colloids as a function of the mass m_a of the asymmetric bead at position a. Predictions from phenomenological equations (Eq. 5.4 and Eq. 5.22, with Eq. 5.18) are shown by solid lines, with the shaded area representing the associated uncertainty. 73

5.5 Average orientation (a) $\langle\cos\theta\rangle$ and (b) $\langle\cos\theta\rangle/\nabla T$ as a function of mass dipole d for different temperature gradients ∇T. Predictions made using the phenomenological equation (Eq. 5.4 with Eq. 5.18) are shown by solid lines, with the shaded area representing the associated uncertainty. 75

5.6 The "reduced" von Mises parameter $\kappa\cdot(T/N\nabla T)$ as a function of the mass dipole d. The solid line represents the prediction made using the phenomenological Eq. 5.18. The shaded area represents the associated uncertainty. 75

5.7 Ratio of the Soret coefficient of mass-asymmetric S_T^{asym} and mass-symmetric S_T^{sym} colloids as a function of the average orientation (a) $|\langle\cos\theta\rangle|$ and (b) $|\langle\cos\theta\rangle|^3$. Theoretical predictions from Eq. 5.23 and Eq. 5.26 are shown by solid and dashed lines respectively. 79

6.1 Simulation methods. (a) Graphical representation of the TraPPE force field of acetonitrile. The charge q and Lennard-Jones parameters ϵ and σ are shown under their corresponding species, while rigid bond distances are shown above the molecule. (b) NEMD simulations: (i) snapshot of the simulation cell, thermostat regions are represented by enlarged red (hot) and cold (blue) molecules; (ii) representative temperature T and density ρ profiles for pressures P_{zz}. 84

6.2 Thermodynamic states investigated in this work with reference to the coexistence curve of acetonitrile: coexistence densities from this work ($\triangledown$) and previous simulations[9] (--$\times$); NEMD (dots $\cdot$, which may appear as thick lines) and equilibrium-NPT ($\circ$) data. Our data is colour coded according to the pressure P of the system. . . 87

6.3 Thermal polarization of acetonitrile. (a) Electrostatic potential ϕ across the simulation cell. (b-d) Total S_{TP}, dipolar S_{TP}^{P} and higher-order $S_{\text{TP}}^{\text{HO}}$ thermal polarization coefficients along the high density and critical isochores. (e) S_{TP} and (f) $S_{\text{TP}}^{P}/S_{\text{TP}}^{\text{HO}}$ with reference to the phase diagram. 89

6.4 Dielectric properties of acetonitrile. (a) Convergence of the static relative permittivity ε_r with time t for the thermodynamics states $(\rho, T) = (0.770\ \text{g cm}^{-3}, 303\ \text{K})$ and $(0.249\ \text{g cm}^{-3}, 638\ \text{K})$. (b) Total dipole correlation functions, $\langle\mathbf{P}(t)\cdot\mathbf{P}(0)\rangle\ /\ \langle\mathbf{P}(0)\cdot\mathbf{P}(0)\rangle$, for the same thermodynamic states. Dashed lines show the fit to the exponential function $f(t) = A\exp\{(-t/\tau_P\}$. 91

6.5 Thermal conductivity λ of acetonitrile: (a) along the high density and critical isochores, with experimental values measured at ambient pressure (see text for discussion); and (b) with reference to the phase diagram. 93
6.6 The decrease $|\delta\lambda|$ in thermal conductivity of acetonitrile due to thermal polarization. 94

7.1 Radial distribution functions (RDFs) of liquid water at 300 K and 0.997 g cm^{-3} as predicted by selected force fields. (a) Oxygen-oxygen RDFs g_{OO} and coordination numbers n_{OO}. (b) Oxygen-hydrogen RDFs g_{OH} and coordination numbers n_{OH}. (c) Hydrogen-hydrogen RDFs g_{HH} and coordination numbers n_{HH}. $r_{\alpha\beta}$ is the radial distance between species α and β. Experimental RDFs are from Refs. 53,69. 108
7.2 Atomic charge and molecular multipole moment probability density functions f_X (where X is the variable) for liquid water at 300 K and 0.997 g cm^{-3}, as predicted by selected force fields: (a) Oxygen (left) and hydrogen (right) atomic charges q_{O} and q_{H}, respectively; (b) total molecular charge q_{mol}; (c) molecular dipole moment μ as measured relative to the centre of mass, μ_{COM}, and centre of geometry, μ_{GC}; and (d) the instantaneous difference $\Delta\mu = \mu_{\mathrm{COM}} - \mu_{\mathrm{GC}}$. 110
7.3 (a) Molecular dipole moments μ, (b) oxygen atomic charges q_{O}, and (c) hydrogen atomic charges q_{H} of liquid water at temperatures T along the 1 bar isobar, as predicted by selected force fields. In all cases the error bars represent the standard deviation σ. In (a), both $\sigma(\mu_{\mathrm{COM}})$ and $\sigma(\mu_{\mathrm{GC}})$ are shown with $\sigma(\mu_{\mathrm{COM}}) > \sigma(\mu_{\mathrm{GC}})$, while $\langle\mu_{\mathrm{GC}}\rangle$ and $\langle\mu_{\mathrm{GC}}\rangle$ cannot be distinguished on the scale of the plot. 110
7.4 Vibrational power spectrum of liquid water at 300 K and 0.997 g cm^{-3}, as predicted by selected force fields. I is the intensity at wavenumber $\tilde{\nu}$. Power spectra share the same normalization condition $\int_0^\infty I(\tilde{\nu})d\tilde{\nu} = C$, where C is a constant. Experimental lines are from Refs. 58–61. 114
7.5 Oxygen atom power spectra of liquid water at 300 K and 0.997 g cm^{-3} as predicted by selected force fields. I_{O} is the intensity at wavenumber $\tilde{\nu}$. Power spectra share the same normalization condition $\int_0^\infty I_{\mathrm{O}}(\tilde{\nu})d\tilde{\nu} = C$, where C is a constant. Experimental lines are from Refs. 60,61. 115

7.6 Potential energy curves (PECs) of the water monomer and dimer as predicted by selected force fields. (a) The water monomer bond dissociation PEC: the potential energy E_P as a function of $r_{\mathrm{OH}} - r_0$, where r_{OH} is the oxygen-hydrogen distance and r_0 is the distance at the minimum-energy geometry; E_P is shifted relative to its value at infinite separation $E_P(r_{\mathrm{OH}} \to \infty)$. The inset shows E_P relative to that of the minimum-energy geometry E_P^{min}, close to r_0. (b) The angle-strain PEC: $E_P - E_P^{\mathrm{min}}$ as a function of $\theta_{\mathrm{HOH}}^{\mathrm{angle}} - \theta_0$, where $\theta_{\mathrm{HOH}}^{\mathrm{angle}}$ is the H-O-H angle, and θ_0 is $\theta_{\mathrm{HOH}}^{\mathrm{angle}}$ at the minimum-energy geometry. (c) The interaction energy $E_P^{\mathrm{int}} = E_P^{\mathrm{min}}((\mathrm{H_2O})_2) - 2E_P^{\mathrm{min}}(\mathrm{H_2O})$ of the C_s water dimer as a function of oxygen-oxygen distance r_{OO}. 117

7.7 Density ρ (a) and thermal expansion coefficient α_P (b) of liquid water at temperatures T along the 1 bar isobar, as predicted by selected force fields. In (a), uncertainties associated with ρ are smaller than the size of the symbols. Experimental values are from Ref. 52. 119

7.8 Enthalpy of vaporization ΔH_{vap} at temperatures T predicted by selected force fields. Uncertainties are smaller than the size of the symbols. Experimental values are from Ref. 52. 121

7.9 (a) Density ρ profiles of the liquid-vapour interface systems along the z-axis perpendicular to the interface. For clarity, the density profiles of water-2017 and CHON-2017_weak have been shifted vertically by 0.2 g cm^{-3} and 0.4 g cm^{-3}, respectively. (b) Convergence of the the surface tension Π with simulation time t. 122

7.10 Isothermal compressibility β_T of liquid water at temperatures T along the 1 bar isobar, as predicted by selected force fields. Experimental values are calculated from Ref. 52. 124

7.11 Heat capacities and related quantities of liquid water at temperature T along the 1 bar isobar, as predicted by selected force fields: (a) isobaric heat capacity C_P, the solid line is a cubic function fit to the water-2017 data; (b) quantum-corrected isobaric heat capacity C_P^{qc}; (c) isochoric heat capacity C_V; (d) quantum-corrected isochoric heat capacity C_V^{qc}; (e) heat capacity ratio $\gamma = C_P/C_V$; (f) quantum-corrected ratio $\gamma^{\mathrm{qc}} = C_P^{\mathrm{qc}}/C_V^{\mathrm{qc}}$; (g) quantum correction C_V^{Δ}; and (h) intramolecular contribution $C_V^{\Delta,\mathrm{intra}}$ to the quantum-correction. Experimental values are from or calculated from Ref. 52. 127

7.12 Isentropic speed of sound of liquid water at temperatures T along the 1 bar isobar, as predicted by selected force fields. c_S and c_S^{qc} are the classical and quantum-corrected speed of sound, respectively. For CHON-2017_weak, the solid and dotted lines show cubic functions fit to the c_S and c_S^{qc} data, respectively. Experimental values are from Ref. 52. 129

7.13 Finite-size analysis for the self-diffusion coefficients of liquid water at 300 K and 0.997 g cm^{-3}, as predicted by selected force fields. Extrapolation of size-dependent diffusion coefficients D_{PBC} to $L^{-1} = 0$, where L is the length of the cubic simulation box. 130

7.14 Shear viscosity of mSPCFw water from the Green-Kubo integral formula. (a) The normalised autocorrelation function $C_{P_{\alpha\beta}}(t)/C_{P_{\alpha\beta}}(0)$, where t is the elapsed time. (b) The convergence of the integral $I_{P_{\alpha\beta}}(t') = \int_0^{t'} C_{P_{\alpha\beta}}(t)dt$ where t' is the correlation time used as the upper limit of the integral; $(I_{P_{\alpha\beta}}(t') - I^{\mathrm{f}}_{P_{\alpha\beta}})/I^{\mathrm{f}}_{P_{\alpha\beta}}$ is the relative deviation of $I_{P_{\alpha\beta}}(t')$ from the final value $I^{\mathrm{f}}_{P_{\alpha\beta}} = I_{P_{\alpha\beta}}(t'/\mathrm{ps} = 10)$ used to calculate the viscosity. 133

7.15 Representative temperature T profiles for the NEMD simulations. Data corresponds to CHON-2017_weak and $L_z = 75$ Å. The blue (cold) and red (hot) shaded areas indicate the location of the thermostatting regions, set to temperatures T_c and T_h, respectively. 134

7.16 Thermal conductivity λ at 300 K and 1.00 g cm^{-3} as predicted by selected force fields. (a) The linear response of heat flux J_q with local temperature gradient ∇T. Results correspond to $L_z = 75$ Å. Statistical uncertainties are smaller than the symbols. (b) Finite-size analysis: L_z is the length of the simulation cell parallel to the direction of heat flux. For $L_z = 75$ Å, the results corresponding to the linear response fitted in (a) have been plotted. 135

7.17 Deviation from experimental reference values of 15 properties of water predicted by the CHON-2017_weak and water-2017 ReaxFF force fields as well as the classical empirical mSPCFw and TIP4P/2005 force fields. All values correspond to 300 K (where appropriate) and either 1 bar, the vapour pressure for coexistence properties (ΔH_{vap} and Π), or 1.00 g cm^{-3} (see the main text for details). Symbol meanings are given in the main text. Experimental values are from Refs. 52,53,55,58,59,62–64,66 and values for TIP4P/2005 are from Refs. 19,20,73,104,108,128,136,141,153. . . . 138

8.1 Representative temperature T and density ρ profiles for the NEMD simulations. The blue (cold) and red (hot) indicate the location of the thermostatting regions in the simulation cell. The profiles correspond to TIP4P/2005 and $P = (10 \pm 1)$ bar. 151

8.2 Equation of state of water, as predicted by selected force fields. (a) Density ρ as a function of temperature T from NEMD and equilibrium-NPT simulations. (b) Pressure P along the 0.997 g cm^{-3} isochore from NEMD and equilibrium-NVT simulations. Statistical uncertainties associated with the simulation data cannot be discerned on the scales of the plots. In (a), the experimental $\rho(T)$ lines for $P/\text{bar} = 10, 12$ cannot be discerned from the $P = 22$ bar data on the scale of the plot, except for their lower boiling points. Experimental data is from Ref. 3. . . . 153

8.3 Thermal conductivity λ of water at close to 300 K and 1.00 g cm^{-3}, as predicted by selected computational models. Bars are colour coded and labelled according to the type of model; classical force fields are labelled NS-X, where N is the number of sites, and X=R,F denotes either rigid (R) or flexible (F). The classical force field values are from this work and correspond to a LJ cutoff of 19 Å, except for TIP4P/2005f from Ref. 45, which used a cutoff of 12 Å. The (machine-learned) DFT data is from, or estimated from, Ref. 46. The experimental value is from Ref. 47. See Table 8.2 for details and numerical data. 155

8.4 The effect of the Lennard-Jones cutoff r_c on the thermal conductivity λ of selected classical force fields for water. All values correspont to 300 K and (0.997 ± 0.001) g cm^{-3}. σ_{OO} is the σ ("size") parameter of the oxygen-oxygen Lennard-Jones potential of the force field. 157

8.5 Thermal conductivity λ of water as a function of temperature T along the 0.997 g cm^{-3} isochore, as predicted by selected force fields. For the simulation data, solid lines show fits to cubic functions. Experimental values are from Ref. 47. 158

8.6 (a) Thermal conductivity λ of water as a function of temperature T along different isobars, as predicted by selected force fields. (b) The temperature of the thermal conductivity maximum, $T_{\max(\lambda)}$, as a function of pressure P. In (a), the experimental $\lambda(T)$ lines for $P/\text{bar} = 10, 12$ cannot be discerned from the $P = 22$ bar data on the scale of the plot, except for their lower boiling points. Experimental values are from Ref. 47. 159

8.7 Thermal conductivity λ of the water-2017 force field as a function of temperature T. The data is colour coded according to the pressures P. The dashed line shows the interpolated $\lambda(T)$ data corresponding to 10 bar. 160

8.8 Bridgman thermal conductivity and related quantities along the 0.997 g cm^{-3} isochore, from experiment and as predicted by selected force fields. (a) Thermal conductivity predicted by the Bridgman equation, λ_{B}, as a function of temperature T. For the simulation data, solid lines show fits to cubic functions. (b) λ_{B} *vs.* the thermal conductivity λ; the inset shows $d\lambda_{\mathrm{B}}/dT$ *vs.* $d\lambda/dT$. (c) Isothermal compressibility β_T *vs.* T. (d) γ^{-1} *vs.* T, where γ is the adiabatic index. Experimental data are from, or calculated from, Refs. 47 & 3. 162

8.9 Thermodynamic properties of water as a function of temperature T along different isobars, as predicted by selected force fields and from experiment. The (a) Bridgman thermal conductivity λ_{B}, (b) isentropic seed of sound c_S, (c) isentropic compressibility β_S, and (d) isothermal compressibility β_T. For the simulation data, solid lines show fits to cubic functions to guide the eye. Experimental data for $P/\mathrm{bar} = 10, 12$ cannot be discerned from the $P = 22$ bar data on the scale of the plots, except for their lower boiling points. Experimental data are from, or calculated from, Ref. 3. 164

8.10 The temperature T_{ex} at which extrema (maxima or minima) in thermophysical properties occur as a function of temperature at constant pressure P, as predicted by selected force fields. (a) T_{ex} as a function of P. (b) Correlation plots of T_{ex} *vs.* $T_{\mathrm{max}(\lambda)}$, where $T_{\mathrm{max}(\lambda)}$ is the temperature of the thermal conductivity maximum. The: (i) Bridgman thermal conductivity λ_{B}; (ii) isentropic speed of sound c_S; (iii) isentropic compressibility β_S; and (iv) isothermal compressibility β_T. In (b), the black line shows $T_{\mathrm{ex}} = T_{\mathrm{max}(\lambda)}$ for reference. Experimental data are from, or calculated from, Refs. 47 & 3. 165

8.11 The (a) sound attenuation coefficient Γ, (b) kinematic longitudinal viscosity b, (c) $2\Gamma - b$, and (d) isobaric heat capacity C_P as a function of temperature T along the 0.997 g cm^{-3} isochore, as predicted by selected force fields. In (b), the experimental value[74] corresponds to 298.15 K and ambient pressure. Experimental data are from, or calculated from, Refs. 47, 3 & 74. 166

B.1 Representative (a) temperature T and number density ρ_N profiles, and (b) mole fraction, x_1 and x_2, profiles for the NEMD simulations. The blue (cold) and red (hot) indicate the location of the thermostatting regions in the simulation cell. . . 186

B.2 Linear response of the Soret coefficient S_T and thermal conductivity λ: (a) mole fraction gradient ∇x_1, (b) S_T, (c) heat flux J_q and (d) λ as a function of temperature gradient ∇T. The solid lines show fits to $\nabla x_1 = -x_1 x_2 S_T \nabla T$ in (a) and (b), and to Fourier's law $-J_q = \lambda \nabla T$ in (c) and (d). In (a) and (c), statistical uncertainties are smaller than the size of the symbols. In (b) and (d) the shaded areas show the uncertainty associated with the fits. 187

B.3 Finite-size effects on the Soret coefficient S_T calculated from NEMD simulations. $L_\perp = L_x = L_y$ is the length of the simulation cell in the direction perpendicular to the heat flux. Solid lines show cubic functions fit to $S_T(x_1)$ where x_1 is the mole fraction of species 1. 188

B.4 Radial distribution functions g_{ij} and coordination number n_{ij} of the Lennard-Jones mixtures: (a) g_{11} and n_{11}; (b) g_{22} and n_{22}; (c) g_{12} and n_{12}. r_{ij} is the radial distance between species i and j. Solid lines show g_{ij} (left axis) and the dashed lines show n_{ij} (right axis). 189

B.5 Partial molar properties z_i of component $i = 1, 2$ as a function of mole fraction x_1: (a) partial molar enthalpy h_i; (b) partial molar internal energy u_i; and (c) partial molar volume v_i. Statistical uncertainties are smaller or comparable to the size of the symbols. 190

B.6 (a) Correlation functions $\langle \boldsymbol{J}_\alpha(t) \cdot \boldsymbol{J}_\beta(0) \rangle$ as a function of time lag t. (b) Convergence of the phenomenological coefficients $L_{\alpha\beta}(t')$ with the correlation time t' used as the upper limit of the integral in Eq. B.3. In (a)(ii) and (b)(ii): solid lines show $\langle \boldsymbol{J}_1(t) \cdot \boldsymbol{J}_q(0) \rangle$ and L_{1q}; dotted lines show $\langle \boldsymbol{J}_q(t) \cdot \boldsymbol{J}_1(0) \rangle$ and L_{q1} 191

B.7 The phenomenological coefficients as a function of the mole fraction x_1: (a) L_{qq} and L'_{qq}; (b) $L_{1q} = L_{q1}$; (c) L_{11}; and (d) $L'_{1q} = L'_{q1}$. (e) The difference in specific partial enthalpies $h_{s,1} - h_{s,2}$, where $h_{s,i}$ is the specific partial enthalpy of component i. Where error bars are not shown, the statistical uncertainty is smaller than the size of the symbol. 192

B.8 The chemical potential and its derivative as a function of mole fraction x_i. (a) Total μ_i, ideal μ_i^{id} and excess μ_i^{ex} chemical potentials μ_i of species $i = 1, 2$. (b) $(\partial \mu_1 / \partial x_1)_{P,T}$ and its ideal and excess contributions. In (a), statistical uncertainties are smaller than the size of the symbols. 194

B.9 Self-diffusion coefficients and shear viscosities of the Lennard-Jones mixtures. (a) Mean-square displacement (MSD) *vs.* time t for the $x_1 = 0.5$ and $N = 1000$ system. (b) Finite-size analysis for the $x_1 = 0.5$ mixture: $D_{i,\mathrm{PBC}}$ is the finite-size diffusion coefficient of species i and L is the length of the cubic simulation cell. Symbols: circles ($\circ$) and diamonds ($\diamond$) show the data from NVT and NVE MD simulations, respectively. Solid lines show a linear fit to the NVT data; dashed lines show a straight line through the single NVE data point with the gradient determined from η_{GK}. (c) The viscosities η as a function of mole fraction x_1, as determined from the different methods (see main text). (d) "Infinite-size" diffusion coefficients $D_{i,0}$ of species i as a function of x_1. $D_{i,0}$ from the two methods, NVT simulations with direct extrapolation (η_{YH}) and NVE simulations with η_{GK}, cannot be distinguished on the scale of the plot. Where error bars are not explicitly shown, the statistical uncertainty is smaller than the size of the symbol. 195

B.10 (a) Autocorrelation functions $\langle P_{\alpha\beta}(t) P_{\alpha\beta}(0)\rangle$ as a function of time lag t. (b) Convergence of shear viscosity $\eta(t')$ with the correlation time t' used as the upper limit of the integral in Eq. B.15. 196

B.11 The Soret coefficient predicted by the Artola-Rousseau-Galliéro and Prigogine models, $S_T^{\mathrm{ARG/P}}$, and related quantities. The self-diffusion coefficients D_i as a function of temperature T for species (a) $i = 1$ and (b) $i = 2$. $\ln D_i$ *vs.* T^{-1} for species (c) $i = 1$ and (d) $i = 2$; the solid lines show linear fits to $\ln D_i = \ln D_i^0 - \Delta G_i^{\ddagger}/(k_B T)$. (e) The activation energies $\Delta G_i^{\ddagger}$ and (e) $S_T^{\mathrm{ARG/P}}$ as a function of mole fraction x_1. Where error bars have not been shown, uncertainties are smaller than the size of the symbols. 197

B.12 $\ln(\eta_i)$ *vs.* $\Delta U_c/(k_B T)$, where η_i and ΔU_c are the shear viscosity and cohesive energy of a pure liquid of species $i = 1, 2$. (a) Species 1 and (b) species 2. The solid lines show linear fits to $\ln \eta_i = \ln A + U_c/(\tau_i k_B T)$. The data points correspond to $P = 0.46\epsilon\sigma^{-3}$ and $T/(\epsilon k_B^{-1}) = 0.605$, 0.61, 0.615, 0.62, 0.625 and 0.63. 198

B.13 Extrapolation of the finite-volume Kirkwood-Buff integrals G_{ij}^V to $R^{-1} = 0$, where R is the radius of the subvolume: (a) G_{11}^V, (b) G_{22}^V and (c) G_{12}^V. The data shown corresponds to mole fraction $x_1 = 0.5$ and a system size of $N = 5 \times 10^6$ particles. Symbols: circles ($\cdot\cdot\circ\cdot\cdot$) and downward triangles ($\cdot\cdot\triangledown\cdot\cdot$) denote the use of pair correlation function g_{ij} (uncorrected) and the corrected g_{ij}^{GV}, respectively, although these cannot be easily distinguished on the scale of the plots. 200

B.14 Finite-size analysis of the infinite-size Kirkwood-Buff integrals G_{ij} as a function of simulation cell length L, for different mole fractions x_1. (a) G_{11}, (b) G_{22}, (c) G_{12}, and (d) thermodynamic factor Γ. 200

B.15 Melting points of the pure components determined using the direct coexistence method. (a) Snapshot of the simulation cell in the process of melting/freezing. (b) Lennard-Jones liquids and FCC solids at temperatures T characterized by their average Q_6 order parameter. Species 1 (species 2) is shown in red (blue) and on the left (right) axis. (c) Probability of freezing P_f as a function of temperature T for species 1 (left) and 2 (right). Solid lines show the fitted sigmoid-like functions (Eq. B.23). 202

C.1 Verification of the linear regime for thermal diffusion: the (a) mole fraction gradient ∇x_1 and (b) S_T as a function of temperature gradient ∇T. The solid lines show fits to $\nabla x_1 = -x_1 x_2 S_T \nabla T$. 207

C.2 Finite-size effects on the Soret coefficient S_T of the $(I_1 = I_2, d_1, d_2) = (80m\sigma^2, 2.7\sigma, 0)$ mixture calculated from NEMD simulations. $L_\perp = L_x = L_y$ is the length of the simulation cell in the direction parallel to the heat flux. Black and blue error bars show the 95% confidence interval and the standard error of the mean, respectively. 208

C.3 (a) Normalized autocorrelation functions $\langle \boldsymbol{J}_1(t) \cdot \boldsymbol{J}_1(0) \rangle / \langle \boldsymbol{J}_1(0) \cdot \boldsymbol{J}_1(0) \rangle$ as a function of time lag t. (b) Convergence of the integral $I_{L_{11}} = \int_0^{t'} \langle \boldsymbol{J}_1(t) \cdot \boldsymbol{J}_1(0) \rangle dt$ with the correlation time t' used as the upper limit of the integral; $(I_{L_{11}}(t') - I^f_{L_{11}})/I^f_{L_{11}}$ is the relative deviation of $I_{L_{11}}(t')$ from the final value $I^f_{L_{11}} = I_{L_{11}}(t' = 500\tau)$ used to calculate the phenomenological coefficient L_{11}. Data is shown for all the mixtures that L_{11} was calculated for. 209

C.4 (a) Normalized autocorrelation functions $\langle P_{\alpha\beta}(t) P_{\alpha\beta}(0) \rangle / \langle P_{\alpha\beta}(0) P_{\alpha\beta}(0) \rangle$ as a function of time lag t. (b) Convergence of the integral $I_\eta = \int_0^{t'} \langle P_{\alpha\beta}(t) P_{\alpha\beta}(0) \rangle dt$ with the correlation time t' used as the upper limit of the integral; $(I_\eta(t') - I^f_\eta)/I^f_\eta$ is the relative deviation of $I_\eta(t')$ from the final value $I^f_\eta = I_\eta(t' = 500\tau)$ used to calculate the viscosity. Data is shown for all the mixtures that the shear viscosity was calculated for. 210

C.5 (a) Normalized autocorrelation functions $\langle \boldsymbol{\omega}_j(t) \cdot \boldsymbol{\omega}_j(0) \rangle / \langle \boldsymbol{\omega}_j(0) \cdot \boldsymbol{\omega}_j(0) \rangle$ as a function of time lag t. (b) Convergence of the integral $I_{D_r} = \int_0^{t'} \langle \boldsymbol{\omega}_j(t) \cdot \boldsymbol{\omega}_j(0) \rangle dt$ with the correlation time t' used as the upper limit of the integral; $(I_{D_r}(t') - I^f_{D_r})/I^f_{D_r}$ is the relative deviation of $I_{D_r}(t')$ from the final value $I^f_\eta = I_{D_r}(t' = 200\tau)$ used to calculate the rotational diffusion coefficient D_r. Data is shown for all the components and mixtures that D_r was calculated for. 210

C.6 The impact of finite-size effects on diffusion coefficients. The (a) corrected and uncorrected diffusion coefficients D_X and (b) finite-size correction $\Delta_{\mathrm{YH}}(D_X)$ as a percentage of the uncorrected D_X for: (i) the Fickian mutual diffusion coefficient D_{12}; the Darken approximation D_{12}^{Darken}; and the self-diffusion coefficients (iii) D_1 and (iv) D_2. (c) The corrected and uncorrected change in self-diffusion coefficient, $\Delta D_i = D_i - D_i(d_1 = 0.5\sigma)$: (i) $i = 1$ and (ii) $i = 2$. All data are shown as a function of mass dipole, d_1, of species 1. In (a) and (c), the corrected and uncorrected D_X are denoted by dotted (...) and dashed (---) lines, respectively. 212

C.7 Isotropic-nematic coexistence. (a) Uniaxial orientational order parameter S_2 as a function of T/T_{IN}, close to the coexistence temperature T_{IN}, where T is the temperature. (b) Phase diagrams: (i) T_{IN} *vs.* coexistence volume fractions ϕ_X and monomer number densities $\rho_{N,\mathrm{mon},X}$, where $X = I$ (isotropic) and N (nematic); (ii) T_{IN} *vs.* coexistence pressure P_{IN}. Uncertainties are smaller or comparable to the size of the symbols, except for T/T_{IN} in (a) where the error bars have been omitted for clarity. 213

C.8 Fitting the empirical equations for the thermal diffusion coefficient: $\ln D_T$ *vs.* $\ln(d_1 - d_2)$ for (a) the $(I = I_1 = I_2, d_1, d_2 = 0)$ and (b) $(I = I_1 = I_2, d_1, d_2 \neq 0)$ mixtures. In (b), the constraint $k = k_{d_2=0}$, as determined from (a), was applied. 214

E.1 Probability density functions of the density ρ of SPC/E using SHAKE and RATTLE. 220

E.2 Thermodynamic properties and response functions of SPC/E predicted using SHAKE and RATTLE. The (a) enthalpy H, (b) isobaric heat capacity C_P, (c)&(e) density ρ, (d) thermal expansion coefficient α_P and (e) isothermal compressibility β_T. T is the temperature and P is the pressure. (a)-(d) correspond to $P = 1$ bar; (e)&(f) correspond to $T = 300$ K. In (b),(d)&(f), the SHAKE and RATTLE labels correspond to the fluctuation relations Eqs. E.2; the equation of state (EOS) results correspond to Eqs. E.1. 221

E.3 Vibrational power spectrum of liquid water at temperatures T and 0.997 g cm^{-3}, as predicted by the mSPCFw, CHON-2017_weak and water-2017 force fields. I is the intensity at wavenumber $\tilde{\nu}$. Power spectra share the same normalization condition $\int_0^\infty I(\tilde{\nu})d\tilde{\nu} = C$, where C is a constant. For clarity the intensity for CHON-2017_weak and water-2017 have been shifted by 1 and 2, respectively. . . . 222

E.4 The average number of hydrogen bonds $\langle n_{\mathrm{HB}} \rangle$ as a function of temperature T for selected force fields. The data corresponds to 0.997 g cm^{-3}. Hydrogen bonds were defined by the standard geometric criteria: an O-O distance of $r_{\mathrm{HB}} \leq 3.5$ Å and an H-O$\cdots$O angle of $\theta_{\mathrm{HB}} \leq 30°$. 223

E.5 The rotational diffusion coefficient D_r as a function of temperature T for selected force fields. The data corresponds to 0.997 g cm^{-3}. 223

E.6 Radial distribution functions (RDFs) of liquid water at temperature T and 0.997 g cm^{-3} as predicted by selected force fields. (top) Oxygen-oxygen RDFs g_{OO}. (middle) Oxygen-hydrogen RDFs g_{OH} (bottom) Hydrogen-hydrogen RDFs g_{HH}. $r_{\alpha\beta}$ is the radial distance between species α and β. 224

E.7 Radial distribution functions (RDFs) of water at 300 K and 0.997 g cm^{-3} as predicted by selected flexible and rigid force fields. (a) Oxygen-oxygen RDFs g_{OO} and coordination numbers n_{OO}. (b) Oxygen-hydrogen RDFs g_{OH} and coordination numbers n_{OH}. (c) Hydrogen-hydrogen RDFs g_{HH} and coordination numbers n_{HH}. $r_{\alpha\beta}$ is the radial distance between species α and β. Data corresponds to a Lennard-Jones cutoff of 19 Å. 225

E.8 Radial distribution functions (RDFs) of water at temperatures T and $P = 10$ bar, as predicted by the TIP4P/2005 and water-2017 force fields. (a) Oxygen-oxygen RDFs g_{OO}. (b) Oxygen-hydrogen RDFs g_{OH}. (c) Hydrogen-hydrogen RDFs g_{HH}. $r_{\alpha\beta}$ is the radial distance between species α and β. The data is colour coded according to the temperature T. 226

E.9 Average order parameters of water as a function of temperature T along the 10 bar isobar, as predicted by the TIP4P/2005 and water-2017 force fields: (a) Orientational tetrahedral order parameter, q; (b) translational tetrahedral order parameter, S_k; (c) asphericity of the Voronoi cell, η_{AVC}; the Steinhardt order parameters, (d) Q_4, (e) Q_5 and (f) Q_6. Statistical uncertainties are smaller than the size of the symbols. 228

E.10 Order parameter probability density functions f_X (where X is the variable) of water at temperatures T and pressure $P = 10$ bar, as predicted by the TIP4P/2005 and water-2017 force fields: (a) Orientational tetrahedral order parameter, q; (b) translational tetrahedral order parameter, S_k; (c) asphericity of the Voronoi cell, η_{AVC}; the Steinhardt order parameters, (d) Q_4, (e) Q_5 and (f) Q_6. The data is colour coded according to the temperature T. 229

E.11 Viscosity of water as a function of temperature T along the 0.997 g cm^{-3} isochore, as predicted by selected force fields. The (a) shear viscosity η, (b) bulk viscosity ζ, (c) longitudinal viscosity ξ and (d) the ratio ζ/η. The experimental data of Holmes *et. al.*[12] corresponds to 298.15 K and ambient pressure. In (a), the experimental data of Huber *et. al.*[13] corresponds to 0.997 g cm^{-3}. 230

List of Tables

6.1 Properties related to the thermal polarization of acetonitrile at selected thermodynamic conditions (density ρ and temperature T): thermal polarization coefficient S_{TP}; static relative permittivity ε_r; dipolar relaxation times τ_P (total) and τ_p (averaged molecular); L_{pp} and L_{pq} are the phenomenological coefficients; $\delta\lambda$ is the difference between the total thermal conductivity λ and that in the absence of the thermal polarization coupling effect $\lambda_{L_{pq}=0}$. Statistical uncertainties in the least significant figure are given in parenthesis. 91

7.1 Thermophysical properties of water at 300 K and 0.997 g cm^{-3}, as predicted by ReaxFF and mSPCFw force fields. Symbol meanings are given in the main text. Parentheses contain the statistical uncertainties or estimated errors in the least significant figure. 105

7.2 Thermodynamic properties of water at standard pressure, as predicted by ReaxFF water and mSPCFw force fields. All properties correspond to 300 K and/or 1 bar, except for coexistence properties (ΔH_{vap} and Π) which correspond to the vapour pressure at 300 K. Symbol meanings are given in the main text. Parentheses contain the statistical uncertainties or estimated errors in the least significant figure. . . . 106

7.3 Molecular geometry and multipole moments of a water molecule in vacuum for selected force fields. $r_{\mathrm{OH}}^{\mathrm{bond}}$ and $\theta_{\mathrm{HOH}}^{\mathrm{angle}}$ are the O-H bond length and H-O-H bond angle, respectively; q_{H} is the atomic partial charge for hydrogen; μ and Q_T are the dipole and quadrupole moment, respectively. Statistical uncertainties in the least significant figure are given in parentheses. 112

7.4 Normal mode frequencies of a water molecule in vacuum for selected force fields. $\tilde{\nu}_1$, $\tilde{\nu}_2$ and $\tilde{\nu}_3$ denote the wavenumbers of the symmetric stretch, bend and asymmetric stretch, respectively. 115

7.5 The effect of thermostat and timestep δt on the dynamics of mSPCFw water. Results correspond to a 521-molecule water-box with a density of 0.997 g cm^{-3} and average simulation temperature T. $D_{N=521}$, η_{GK} and C_V^{Δ} are the self-diffusion coefficient, Green-Kubo shear viscosity (Eq. 7.18) and quantum-correction to the isochoric heat capacity (Eq. 7.3.9), respectively. Statistical uncertainties in the least significant figure are given in parentheses. 132

7.6 Non-equilibrium molecular dynamics simulation parameters and results for the calculation of thermal conductivity λ. L_z is the length of the simulation box parallel to the direction of heat flux. ρ_{box}, T_{box} and P_{zz} are the average density, temperature and pressure parallel to the direction of heat flux, respectively. T_h and T_c are the temperatures of the hot and cold thermostats; ∇T is the resulting temperature gradient. All local properties (columns 8-11) were computed at thermodynamic conditions specified by density ρ and temperature T. Statistical uncertainties in the least significant figure are given in parentheses. 136

8.1 NEMD simulation parameters. Symbol meanings are defined in the main text. . . 151

8.2 Thermal conductivity λ at near-standard thermodynamic conditions as predicted by computational models. T, P and ρ are the temperature, pressure and density, respectively. Statistical uncertainties in the least significant figure are given in parentheses. 156

8.3 The temperature T_{ex} at which extrema in thermophysical properties occur as a function of temperature at constant pressure P, as predicted by selected force fields. The temperatures of the density maximum T_{MD}, isothermal compressibility minimum $T_{\mathrm{min}(\beta_T)}$, isentropic compressibility minimum $T_{\mathrm{min}(\beta_S)}$, isentropic speed of sound maximum $T_{\mathrm{max}(c_S)}$, Bridgman thermal conductivity maximum $T_{\mathrm{max}(\lambda_{\mathrm{B}})}$, and thermal conductivity maximum $T_{\mathrm{max}(\lambda)}$. 161

B.1 Solid-liquid coexistence properties of the pure LJ components at $P = 0.46\ \epsilon\sigma^{-3}$: the melting temperature T_m; coexistence number densities of the FCC solid and liquid phases, $\rho_{N,s}$ and $\rho_{N,l}$, respectively; and the enthalpy of fusion ΔH_{fus} 203

C.1 Isotropic-nematic coexistence properties: coexistence pressure P_{IN} and temperature T_{IN}; coexistence volume fraction (monomer number density) of the isotropic and nematic phases, ϕ_I and ϕ_N ($\rho_{N,\mathrm{mon},I}$ and $\rho_{N,\mathrm{mon},N}$), respectively. 213

D.1 Thermodynamic states simulated using non-equilibrium molecular dynamics. ρ_{box}, T_{box}, P_{zz}, represent the average density, temperature and pressure parallel to the direction of the heat flux, respectively. T_h and T_c are the temperatures of the hot and cold thermostats, λ is the thermal conductivity, S_{TP} is the thermal polarization coefficient, and E and E_P are the total electrostatic field and the dipolar contribution to the total field, respectively. All local properties (columns 8-12) were computed at the thermodynamics conditions specified by density ρ and temperature T. Statistical uncertainties (standard error of the mean) in the least significant figure are given in parenthesis. 218

Chapter 1

Introduction

1.1 Thermal fields in technology and Nature

Thermal fields present new ways to manipulate soft matter, mixtures and fluids in general. It is now possible to generate large temperature gradients ($\sim 10^6$ to 10^8 K m^{-1}) with nanoscale precision,[1–4] bringing thermally controlled mass and energy transport to the realms of micro and nanotechnology. For example: the spatial manipulation of nanoparticles and biomolecules using laser heating and cooling;[4–7] internal temperature gradients propel thermophoretic microswimmers[8–12] and thermal fields drive and control directed motion in other[13–16] nanomachines;[4,17] plasmonic nanoparticles can be used as heat sources remotely controlled by light;[3] microscale thermophoresis is used to analyse the interactions of proteins and small molecules in biological liquids;[18,19] temperature gradients can even control the growth of, and transport within, biological structures[20–24]. These examples alone have applications and far-reaching potential in a diverse range of fields, including nanomedicine,[24–28] cell biology,[22–24] analytical chemistry,[19,29] photothermal and hot electron chemistry,[30–32] solar light harvesting,[3] and micro/nanofluidics[29,33–35].[3,4] There is also ongoing interest in thermal fields for waste heat recovery; such efforts have focused on thermoelectricity,[36–38] although the recently discovered thermal polarization[39] and orientation[40] effects offer new avenues for the rectification of rotational Brownian motion. Indeed, to "characterize and control matter away–especially far away–from equilibrium" was named one of the five grand challenges in basic energy science by the U.S.A Department of Energy (Basic Energy Sciences Advisory Committee, Office of Science),[41] and thermal non-equilibrium is vital part of this remit.

Non-isothermal conditions are ubiquitous in Nature, and give rise to natural phenomena on scales ranging from microscopic to geological. Thermal diffusion plays an important role in the differentiation of igneous rock in the Earth's mantle and crust,[42,43] the seasonal fractionation of nitrogen and argon isotopes in the air trapped in polar ice,[44,45] the spatial variation of composition in crude oil reservoirs,[46,47] among other[48] geophysical processes. It is thought to have played a role in the evolution of lunar magma oceans,[49] while thermal creep assists dust lifting, in illuminated

dust beds and within dust devils, on the surface of Mars[50]. Back on Earth, thermal diffusion has garnered much attention for its possible role in the origin of life.[51–56]

1.2 Non-isothermal transport phenomena in fluids

1.2.1 Thermal conductivity

What determines the thermal conductivity of a dense fluid? Predicting the thermal conductivity of fluids from first-principles is a challenging problem. The exceptions to this are dilute monatomic fluids (gases as well as supercritical fluids), for which elementary kinetic theory and Chapman-Enskog theory give expressions explicitly in terms of molecular parameters. Many models for dense fluids start by modifying the kinetic transport picture of the Boltzmann equation for dilute fluid particles,[57,58] as represented by Enskog's approach. The Enskog equation extends kinetic theory to finite density, and works well for hard sphere fluids.[59,60] Bridgman imagined liquid molecules arranged in a cubic lattice, with the internal energy difference due to the temperature gradient being "handed down a row of molecules with the velocity of sound".[61] Given its assumptions, the resultant Bridgman equation is remarkably accurate for many liquids at $\sim$ 300 K and 1 bar,[61,62] and inspired a family of similar models that give comparable or moderately improved results for some liquids.[57,58,62] The application of other models to thermal conductivity, such as the significant structure theory[63] and Kirkwood theory[64], also predict reasonable values for select molecular liquids and thermodynamic conditions.[57,58] All these models demonstrate trends with thermophysical properties such as density, heat capacity, enthalpy of vaporization and the speed of sound. However, to date, no accurate analytical model exists for dense fluids. Hydrodynamics provides a more rigorous connection but without microscopic insight, and crucially relates thermal conductivity to the sound attenuation coefficient and viscosity, and directly to the fluid's equilibrium density fluctuations.[65] Molecular simulations are now the de facto standard for rationalizing the thermal conductivities of dense fluids in terms of their microscopic properties.

1.2.2 Thermal diffusion

Thermal diffusion (thermally driven mass transport) is quantified by the Soret coefficient S_T, which measures the mass separation of mixtures and suspensions in a thermal field. By convention a component is thermophobic (moves to lower temperatures) if $S_T > 0$, and thermophilic (moves to higher temperatures) if $S_T < 0$. A universal physical picture for why particles move in temperature gradients remains elusive. General phenomenological equation for thermal diffusion can be derived using the framework of linear non-equilibrium thermodynamics (LNET). More specific phenomenological or empirical equations are used for different categories of mixtures (e.g., aqueous

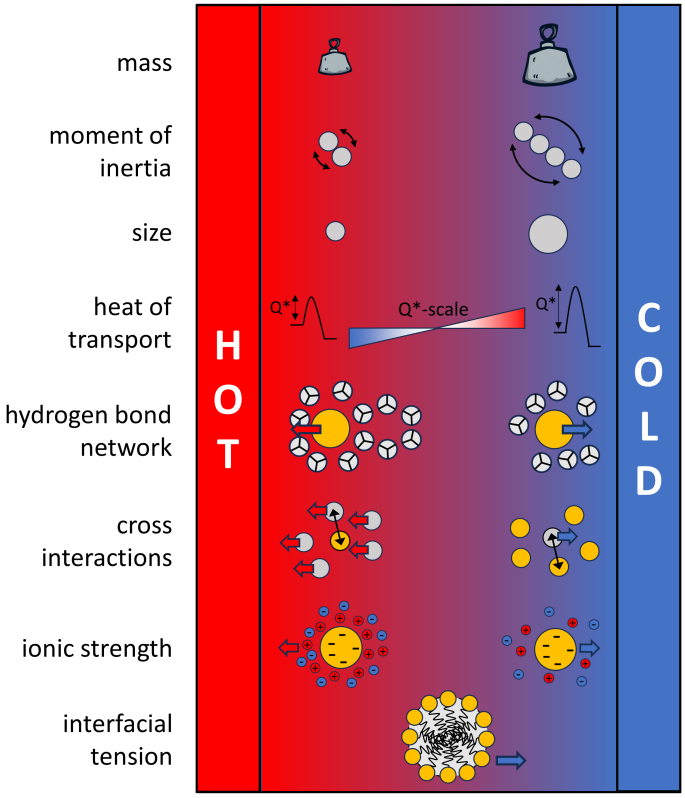


FIGURE 1.1: To the hot or to the cold? A roadmap to identify the direction of the thermophoretic motion. Only general trends are identified, which do not hold for all mixtures. The list of factors are illustrative, not exhaustive.

salt solutions, non-polar organic solvent mixtures, charged colloidal suspensions, etc.), and are usually fit to experimental or simulation data.[29,48,66] Theoretical models that attempt to predict S_T *a priori* from the physical properties and thermodynamic conditions of the mixture are only accurate in a very limited number of cases.[67,68] As illustrated in Fig. 1.1, many factors can influence the Soret coefficient of a mixture. Indeed, rationalizing the phenomenology observed in experiments in terms of microscopic behaviour is at the frontier of thermal diffusion research.[29,48,66,69]

Molecular mixtures

Using binary mixtures of isotopologues of benzene and cyclohexane, Debuschewitz and Köhler[70] demonstrated that the Soret coefficient could be split into two additive contributions:

$$S_T = S_T^{\text{chem}} + S_T^{\text{iso}} \tag{1.1}$$

The chemical contribution S_T^{chem} depends on the intermolecular and intramolecular interactions (i.e., the potential energy surface), while the isotopic contribution S_T^{iso} depends only on the mass and mass distribution of the molecules or atoms. Simulations have verified that Eq. 1.1 holds reasonably well for binary Lennard-Jones mixtures, in both the liquid and dense supercritical states, even if slight couplings have been observed.[68,71–74] The application of Eq. 1.1 to the interpretation

of S_T data for molecular mixtures is now standard procedure.[29,48,66,69] Extensive experimental studies on both polar and non-polar organic solvent mixtures have observed that $S_T^{\rm iso}$ is approximately independent of concentration such that $S_T(x_1) = S_T^{\rm chem}(x_1) + S_T^{\rm iso}$, where x_1 is the mole fraction of species 1.[70,75,76] However, simulations of isotopic binary Lennard-Jones mixtures found a significant composition dependence over a wide range of thermodynamic conditions for large mass differences $M_1/M_2 = 5, 10$ (M_i is the mass of species $i = 1, 2$).[77] Many theoretical models also imply concentration-dependent $S_T^{\rm iso}$ contributions,[68] although the application of the kinetic model of Artola, Rousseau and Galliéro to Lennard-Jones mixtures with $M_1/M_2 = 2$ concluded that the composition dependence of $S_T^{\rm iso}$ is much smaller than for $S_T^{\rm chem}$.[72] For dense supercritical Lennard-Jones mixtures, the concentration dependence of $S_T^{\rm chem}$ was shown to primarily depend on the cross-interactions between unlike particles.[78]

$S_T^{\rm iso}$ is often referred to the pseudo-isotopic Soret effect because it applies to both isotopic and non-isotopic mixtures. It can be relatively large, and even the dominant contribution in molecular mixtures.[70,75,76] Trivially, it is the dominant contribution in mixtures that feature a reversal in sign of S_T as a function of composition, when $S_T^{\rm chem}(x_1) \approx 0$.[70,75] The pseudo-isotopic Soret effect is both kinetic and thermodynamic in origin. The kinetic contribution arises from mechanical collisions between unlike particles, while the thermodynamic contribution is a quantum effect. Indeed, it is only due to quantum effects that isotopic substitution changes the thermodynamic state. For binary liquid mixtures at room temperature, it has been argued that the thermodynamic contribution originates from atomic/molecular vibrations and librations; the characteristic quantum oscillator energies for these motions are mass-dependent, such that is energetically favourable for the heavy particle to migrate to the cold region.[79] Assuming a classical partition function, equilibrium thermodynamic averages are independent of particle masses, and from a local equilibrium perspective $S_T^{\rm iso}$ is purely kinetic in origin. For this reason, classical thermodynamic models of thermal diffusion either neglect $S_T^{\rm iso}$, or incorporate it in an *ad hoc* manner, e.g. via kinetic theory as in Ref. 80. Similarly, classical molecular simulations do not capture the thermodynamic contribution to $S_T^{\rm iso}$.

Colloidal suspensions

Thermal diffusion in colloidal suspensions is often referred to as thermophoresis. It is one instance of a wider class of transport phenomena collectively dubbed "phoretic motion", whose motion is mainly driven by local hydrodynamic stresses occurring at the colloid-solvent interface (as opposed to volume forces acting throughout the fluid).[48,81,82] Over the past two decades, a host of experimental studies have revealed dependencies of S_T on: experimental conditions such as temperature; colloid-solvent interactions and suspension properties such as ionic strength and solute concentration; and colloid properties such as size, mass, moment of inertia or charge.[29,69,81,82] In

many cases, predicting the sign of S_T is highly non-trivial. The effect of particle shape has also attracted attention. Theoretical work considering non-spherical particles in the free-molecular[83] (i.e. aerosols) and slip[84] regimes of flow, predicted thermophoretic velocities that depend on the alignment of the particles with respect to the thermal field.[83,84] Similarly, hydrodynamic simulations of colloidal nanorods reported an anosotropic thermophoretic response, with non-zero Soret coefficients perpendicular to the temperature gradient.[85] Experimental studies of rigid rod-like colloids (the mutant Y21M *fd*-virus) could not detect a change in S_T due to shape anisotropy for the chosen experimental conditions.[86] However, hydrodynamic and atomistic simulations have shown that S_T increases with both the length and aspect ratio of rod-like colloids in the dilute regime.[85,87] Very recently, Olarte-Plata *et. al.* showed that mass anisotropy can impact the Soret coefficient of rod-like colloids, presenting a new way to manipulate the thermophoretic response of colloidal suspensions.[87]

1.2.3 Thermal orientation and polarization

Particles can preferentially orient with respect to an applied thermal field in a phenomenon termed thermal orientation (TO). For polar fluids, TO generates an electrostatic field, causing the thermal polarization (TP) of the medium. TO has been observed in simulations of non-polar molecular fluids[40] and colloids[87]. TP has been studied using models of simple polar fluids,[88–90] and extensively in water[39,91,92]. TO and TP are theoretically described using LNET. Phenomenological equations have also been derived using mean-field theory approaches[89,90,93] and Fokker-Planck-Smoluchowski type equations[94]. The TP of water has been shown to influence the thermoelectric response of alkali halide salt solutions,[95] and TO to affect the Soret coefficients of dilute colloid suspensions[87]. On the whole however, how TO and TP impact transport properties remains relatively unexplored. Very recently, thermal orientation has been experimentally observed in gold-capped Janus particles.[96] TO and TP have not yet been experimentally observed in molecular fluids, doing so is a challenging but important next step for understanding (and validating) these coupling effects.

1.3 Scope of the thesis

This thesis works towards understanding, from a fundamental perspective, the non-isothermal transport properties of a diverse range of fluids. To this end, we employ both computer simulations and analytical theoretical models with a focus on questions (objectives) O1 and O2. Simulations in particular are a powerful tool for isolating the effects of specific material properties, and exploring thermodynamic conditions that are difficult to achieve in experiments. We take advantage of this in our third objective (O3). We also assess computational models, for potential use, and for the significant physical insight that can be gleaned from why models succeed or fail (O4).

- (O1) How do the microscopic properties of fluids determine their macroscopic response to a thermal field?
- (O2) How do coupling effects alter non-isothermal transport properties?
- (O3) The discovery of new phenomenology.
- (O4) The assessment of computational models.

The structure of this thesis is as follows.

Chapter 2 introduces the framework of linear non-equilibrium thermodynamics, followed by its application to the non-isothermal phenomena encountered in this thesis.

In **Chapter 3** we show that simple liquid mixtures can feature a minimum in the Soret coefficient as a function of composition. We link the minimum to the non-ideality of the mixtures, and explain its microscopic origin in terms of their atomic coordination structure. [O1,O2,O3]

Chapter 4 uncovers the mass dipole contribution to the (pseudo-)isotopic Soret effect in molecular mixtures. In the mixtures of rod-like molecules studied, it arises mainly through the thermal diffusion coefficient via the modification of a librational mode. We demonstrate that it can lead to new phenomenology in the Soret coefficient, including a reversal in sign. [O1,O2,O3]

Chapter 5 connects the thermal orientation and thermophoresis of rod-like colloids with mass anisotropy. Using both theory and simulation, we show how the Soret coefficients of these colloids depend on their internal mass distribution and average orientation. [O1,O2]

Chapter 6 investigates the thermal polarization of acetonitrile. We rationalize trends in the thermopolarization coefficient in terms of physical properties, such as rotational diffusion and the dielectric constant of the fluid. Using acetonitrile as an exemplar, we quantify, for the first time, how thermal polarization impacts the thermal conductivity of polar fluids. [O2,O3]

Chapter 7 presents comprehensive benchmarks of the thermophysical properties of water for two state-of-the-art ReaxFF force fields. These include structural, electrostatic, vibrational, thermodynamic, coexistence, and transport properties at ambient conditions (300 K and 0.997 g cm^{-3}) and along the standard pressure (1 bar) isobar. Based on our results, we recommend potential avenues of improvement for these models. [O4]

Chapter 8 examines the anomalous thermal conductivity of water at near-standard conditions, along the "standard liquid" 0.997 g cm^{-3} isochore and different isobars for pressures $P < 1500$ bar. Correlations with thermophysical properties are established, namely the speed of sound, compressibility, sound attenuation coefficient and kinematic longitudinal viscosity. A possible explanation for the thermal conductivity maximum at constant pressure is provided. [O1,O4]

Chapter 9 closes the thesis with a summary of the main conclusions and directions for future work.

Bibliography

[1] C. R. Crick, P. Albella, B. Ng, A. P. Ivanov, T. Roschuk, M. P. Cecchini, F. Bresme, S. A. Maier and J. B. Edel, *Nano Lett.*, 2015, **15**, 553–559.

[2] A. O. Govorov, W. Zhang, T. Skeini, H. Richardson, J. Lee and N. A. Kotov, *Nanoscale Res. Lett.*, 2006, **1**, 84.

[3] G. Baffou, F. Cichos and R. Quidant, *Nat. Mater.*, 2020, **19**, 946–958.

[4] Z. Chen, J. Li and Y. Zheng, *Chem. Rev.*, 2022, **122**, 3122–3179.

[5] H.-R. Jiang, H. Wada, N. Yoshinaga and M. Sano, *Phys. Rev. Lett.*, 2009, **102**, 208301.

[6] Y. He, M. Tsutsui, R. H. Scheicher, F. Bai, M. Taniguchi and T. Kawai, *ACS Nano*, 2013, **7**, 538–546.

[7] J. Li, Z. Chen, Y. Liu, P. S. Kollipara, Y. Feng, Z. Zhang and Y. Zheng, *Sci. Adv.*, 2021, **7**, eabh1101.

[8] H.-R. Jiang, N. Yoshinaga and M. Sano, *Phys. Rev. Lett.*, 2010, **105**, 268302.

[9] S. J. Ebbens and J. R. Howse, *Soft Matter*, 2010, **6**, 726–738.

[10] A. P. Bregulla, H. Yang and F. Cichos, *ACS Nano*, 2014, **8**, 6542–6550.

[11] Z. Wu, T. Si, W. Gao, X. Lin, J. Wang and Q. He, *Small*, 2016, **12**, 577–582.

[12] C. Lozano, B. ten Hagen, H. Löwen and C. Bechinger, *Nat. Commun.*, 2016, **7**, 12828.

[13] S. Balasubramanian, D. Kagan, K. M. Manesh, P. Calvo-Marzal, G.-U. Flechsig and J. Wang, *Small*, 2009, **5**, 1569–1574.

[14] V. Magdanz, G. Stoychev, L. Ionov, S. Sanchez and O. G. Schmidt, *Angew. Chem. Int. Ed.*, 2014, **53**, 2673–2677.

[15] Y. Tu, F. Peng, X. Sui, Y. Men, P. B. White, J. C. M. van Hest and D. A. Wilson, *Nat. Chem.*, 2017, **9**, 480–486.

[16] A. Barreiro, R. Rurali, E. R. Hernández, J. Moser, T. Pichler, L. Forró and A. Bachtold, *Science*, 2008, **320**, 775–778.

[17] Y. Tu, F. Peng and D. A. Wilson, *Adv. Mater.*, 2017, **29**, 1701970.

[18] C. J. Wienken, P. Baaske, U. Rothbauer, D. Braun and S. Duhr, *Nat. Commun.*, 2010, **1**, 100.

[19] M. Asmari, R. Ratih, H. A. Alhazmi and S. El Deeb, *Methods*, 2018, **146**, 107–119.

[20] E. L. Talbot, L. Parolini, J. Kotar, L. D. Michele and P. Cicuta, *Proc. Natl. Acad. Sci. U.S.A.*, 2017, **114**, 846–851.

[21] E. L. Talbot, J. Kotar, L. Di Michele and P. Cicuta, *Soft Matter*, 2019, **15**, 1676–1683.

[22] M. Zhu, G. Baffou, N. Meyerbröker and J. Polleux, *ACS Nano*, 2012, **6**, 7227–7233.

[23] A. Bahadori, L. B. Oddershede and P. M. Bendix, *Nano Res.*, 2017, **10**, 2034–2045.

[24] B. V. Parakhonskiy, W. J. Parak, D. Volodkin and A. G. Skirtach, *Langmuir*, 2019, **35**, 8574–8583.

[25] D. Li, C. Liu, Y. Yang, L. Wang and Y. Shen, *Light Sci. Appl.*, 2020, **9**, 84.

[26] T. Cui, S. Wu, Y. Sun, J. Ren and X. Qu, *Nano Letters*, 2020, **20**, 7350–7358.

[27] W. He, J. Frueh, N. Hu, L. Liu, M. Gai and Q. He, *Adv. Sci*, 2016, **3**, 1600206.

[28] E. Boulais, R. Lachaine, A. Hatef and M. Meunier, *J. Photochem. Photobiol. C*, 2013, **17**, 26–49.

[29] D. Niether and S. Wiegand, *J. Phys.: Condens. Matter*, 2019, **31**, 503003.

[30] G. Baffou and R. Quidant, *Chem. Soc. Rev.*, 2014, **43**, 3898–3907.

[31] H.-H. Shin, J.-J. Koo, K. S. Lee and Z. H. Kim, *Appl. Mater. Today*, 2019, **16**, 112–119.

[32] J. Qiu and W. D. Wei, *J. Phys. Chem. C*, 2014, **118**, 20735–20749.

[33] A. P. Bregulla, A. Würger, K. Günther, M. Mertig and F. Cichos, *Phys. Rev. Lett.*, 2016, **116**, 188303.

[34] J. S. Donner, G. Baffou, D. McCloskey and R. Quidant, *ACS Nano*, 2011, **5**, 5457–5462.

[35] D. Vigolo, R. Rusconi, H. A. Stone and R. Piazza, *Soft Matter*, 2010, **6**, 3489–3493.

[36] G. J. Snyder and E. S. Toberer, *Nat. Mater.*, 2008, **7**, 105–114.

[37] M. F. Dupont, D. R. MacFarlane and J. M. Pringle, *Chem. Commun.*, 2017, **53**, 6288–6302.

[38] M. Rahimi, A. P. Straub, F. Zhang, X. Zhu, M. Elimelech, C. A. Gorski and B. E. Logan, *Energy Environ. Sci.*, 2018, **11**, 276–285.

[39] F. Bresme, A. Lervik, D. Bedeaux and S. Kjelstrup, *Phys. Rev. Lett.*, 2008, **101**, 020602.

[40] F. Römer, F. Bresme, J. Muscatello, D. Bedeaux and J. M. Rubí, *Phys. Rev. Lett.*, 2012, **108**, 105901.

[41] G. R. Fleming and M. A. Ratner, *Phys. Today*, 2008, **61**, 28–33.

[42] D. Walker and S. E. DeLong, *Contrib. Mineral. Petrol.*, 1982, **79**, 231–240.

[43] C. Lundstrom, *Geochim. Cosmochim. Acta*, 2009, **73**, 5709–5729.

[44] J. P. Severinghaus, A. Grachev and M. Battle, *Geochem. Geophys. Geosyst.*, 2001, **2**, 1048.

[45] J. P. Severinghaus, T. Sowers, E. J. Brook, R. B. Alley and M. L. Bender, *Nature*, 1998, **391**, 141–146.

[46] F. Montel, J. Bickert, A. Lagisquet and G. Gallíero, *J. Pet. Sci. Eng.*, 2007, **58**, 391–402.

[47] M. Touzet, G. Galliero, V. Lazzeri, M. Z. Saghir, F. Montel and J.-C. Legros, *C. R. Mec.*, 2011, **339**, 318–323.

[48] W. Köhler and K. I. Morozov, *J. Non-Equilib. Thermodyn.*, 2016, **41**, 151–197.

[49] D. Walker, C. E. Lesher and J. F. Hays, *Proc. Lunar Planet. Sci.*, 1981, **12B**, 991–999.

[50] M. Küpper and G. Wurm, *J. Geophys. Res. Planets*, 2015, **120**, 1346–1356.

[51] D. Braun and A. Libchaber, *Phys. Rev. Lett.*, 2002, **89**, 188103.

[52] P. Baaske, F. M. Weinert, S. Duhr, K. H. Lemke, M. J. Russell and D. Braun, *Proc. Natl. Acad. Sci. U.S.A.*, 2007, **104**, 9346–9351.

[53] I. Budin, R. J. Bruckner and J. W. Szostak, *J. Am. Chem. Soc.*, 2009, **131**, 9628–9629.

[54] M. Kreysing, L. Keil, S. Lanzmich and D. Braun, *Nat. Chem.*, 2015, **7**, 203–208.

[55] M. Morasch, J. Liu, C. F. Dirscherl, A. Ianeselli, A. Kühnlein, K. Le Vay, P. Schwintek, S. Islam, M. K. Corpinot, B. Scheu, D. B. Dingwell, P. Schwille, H. Mutschler, M. W. Powner, C. B. Mast and D. Braun, *Nat. Chem.*, 2019, **11**, 779–788.

[56] R. Rubio-Sánchez, D. K. O'Flaherty, A. Wang, F. Coscia, G. Petris, L. Di Michele, P. Cicuta and C. Bonfio, *J. Am. Chem. Soc.*, 2021, **143**, 16589–16598.

[57] E. McLaughlin, *Chem. Rev.*, 1964, **64**, 389–428.

[58] G. Chen, *J. Heat Transfer*, 2021, **144**, year.

[59] S. Pieprzyk, A. C. Brańka, D. M. Heyes and M. N. Bannerman, *Phys. Chem. Chem. Phys.*, 2020, **22**, 8834–8845.

[60] Y. Ishii, K. Sato, M. Salanne, P. A. Madden and N. Ohtori, *J. Chem. Phys.*, 2014, **140**, 114502.

[61] P. W. Bridgman, *Proc. Natl. Acad. Sci. U.S.A.*, 1923, **9**, 341–345.

[62] Q. Xi, J. Zhong, J. He, X. Xu, T. Nakayama, Y. Wang, J. Liu, J. Zhou and B. Li, *Chinese Phys. Lett.*, 2020, **37**, 104401.

[63] S. H. Lin, H. Eyring and W. J. Davis, *J. Phys. Chem.*, 1964, **68**, 3017–3020.

[64] S. A. Rice and A. R. Allnatt, *J. Chem. Phys.*, 1961, **34**, 2144–2155.

[65] J.-P. Hansen and I. R. McDonald, *Theory of Simple Liquids with Applications to Soft Matter*, Academic Press, 4th edn., 2013.

[66] P.-A. Artola and B. Rousseau, *Mol. Phys.*, 2013, **111**, 3394–3403.

[67] M. Eslamian and M. Z. Saghir, *J. Non-Equilib. Thermodyn.*, 2009, **34**, 97–131.

[68] H. Hoang and G. Galliero, *Eur. Phys. J. E*, 2022, **45**, 42.

[69] S. Wiegand, *J. Phys.: Condens. Matter*, 2004, **16**, R357–R379.

[70] C. Debuschewitz and W. Köhler, *Phys. Rev. Lett.*, 2001, **87**, 055901.

[71] G. Galliero, B. Duguay and J. Caltagirone, *Fluid Phase Equilib.*, 2003, **208**, 171–188.

[72] P.-A. Artola, B. Rousseau and G. Galliero, *J. Am. Chem. Soc.*, 2008, **130**, 10963–10969.

[73] D. Reith and F. Müller-Plathe, *J. Chem. Phys.*, 2000, **112**, 2436–2443.

[74] G. Galliéro, *Fluid Phase Equilib.*, 2004, **224**, 13–22.

[75] G. Wittko and W. Köhler, *J. Chem. Phys*, 2005, **123**, 014506.

[76] B. Pur, W. Köhler and K. I. Morozov, *J. Chem. Phys.*, 2020, **152**, 054501.

[77] G. Galliero, M. Bugel, B. Duguay and F. Montel, *J. Non-Equilib. Thermodyn.*, 2007, **32**, 251–258.

[78] P.-A. Artola and B. Rousseau, *Phys. Rev. Lett.*, 2007, **98**, 125901.

[79] S. Hartmann, W. Köhler and K. I. Morozov, *Soft Matter*, 2012, **8**, 1355–1360.

[80] L. J. T. M. Kempers, *J. Chem. Phys.*, 2001, **115**, 6330–6341.

[81] R. Piazza and A. Parola, *J. Phys.: Condens. Matter*, 2008, **20**, 153102.

[82] A. Würger, *Rep. Prog. Phys.*, 2010, **73**, 126601.

[83] P. Garcia-Ybarra and D. E. Rosner, *AIChE J.*, 1989, **35**, 139–147.

[84] K. Leong, *J. Aerosol Sci.*, 1984, **15**, 511–517.

[85] Z. Tan, M. Yang and M. Ripoll, *Soft Matter*, 2017, **13**, 7283–7291.

[86] P. Blanco, H. Kriegs, M. P. Lettinga, P. Holmqvist and S. Wiegand, *Biomacromolecules*, 2011, **12**, 1602–1609.

[87] J. Olarte-Plata, J. M. Rubi and F. Bresme, *Phys. Rev. E*, 2018, **97**, 052607.

[88] C. D. Daub, P.-O. Åstrand and F. Bresme, *Phys. Chem. Chem. Phys.*, 2014, **16**, 22097–22106.

[89] A. A. Lee, *Soft Matter*, 2016, **12**, 8661–8665.

[90] P. Wirnsberger, C. Dellago, D. Frenkel and A. Reinhardt, *Phys. Rev. Lett.*, 2018, **120**, 226001.

[91] I. Iriarte-Carretero, M. A. Gonzalez, J. Armstrong, F. Fernandez-Alonso and F. Bresme, *Phys. Chem. Chem. Phys.*, 2016, **18**, 19894–19901.

[92] A. Chapman and F. Bresme, *Phys. Chem. Chem. Phys.*, 2022, **24**, 14924–14936.

[93] A. Gardin and A. Ferrarini, *Phys. Chem. Chem. Phys.*, 2019, **21**, 104–113.

[94] J. D. Olarte-Plata and F. Bresme, *Phys. Chem. Chem. Phys.*, 2019, **21**, 1131–1140.

[95] S. Di Lecce and F. Bresme, *J. Phys. Chem. B*, 2018, **122**, 1662–1668.

[96] S. Auschra, A. Bregulla, K. Kroy and F. Cichos, *Eur. Phys. J. E*, 2021, **44**, 90.

Chapter 2

Theoretical description of non-isothermal transport phenomena

2.1 Linear non-equilibrium thermodynamics

2.1.1 Scope and limitations of LNET

Close to equilibrium, transport phenomena are governed by linear phenomenological laws. Linear non-equilibrium thermodynamics (LNET) provides a framework for the derivation of such laws. Two key assumptions of LNET are (1) local equilibrium and (2) linear response. General validity criteria for (1) are discussed in Sec. 2.1.2, but we note that for non-isothermal conditions, computer simulations of dense fluids typically satisfy local equilibrium with large temperature gradients $\nabla T \sim$ 10-30 K nm^{-1}, and find linear response with these same gradients (see, e.g., Sec. 7.3.13 and Chapter 8 for water).[1–3] Local equilibrium implies that the phenomenological coefficients appearing in LNET correspond to the long-wavelength limit of a perturbing field (e.g., a shear or electric field) and are therefore independent of frequency, which is in contrast to generalized hydrodynamics where the coefficients are frequency and wavelength dependent.[4] The Onsager-Casimir reciprocal relations (Sec. 2.1.7) were derived for the microscopic scale close to equilibrium, and their extrapolation to macroscopic thermodynamics has been questioned.[4,5] For example, in a strictly thermodynamic framework it is impossible to demonstrate the fluctuation regression hypothesis.[5] Nevertheless, the reciprocal relations hold for a wide range of phenomena and experimental conditions.[6–8] One major shortcoming of LNET is that it predicts that some signals propagate at infinite velocity.[a] However, in most practical situations the characteristic time scale of a thermodynamic variable is much greater than its signal transit time, lessening the impact of this deficiency.[4] Other

[a] For example, in the case of an isotropic rigid body with constant thermal conductivity and heat capacity, a parabolic partial differential equation is obtained for the temperature distribution. This implies that a temperature disturbance will propagate at infinite velocity across the body, such that it will be felt instantaneously across the entire body. Another notable example is the Navier-Stokes' equation.[4]

thermodynamic theories, such as extended irreversible thermodynamics (which solves the paradox of infinite-velocity signal propagation), go beyond the assumption of local equilibrium.[4,5]

2.1.2 Local equilibrium hypothesis

Undoubtedly, the most important assumption underlying LNET is that of local equilibrium. The local equilibrium hypothesis (LEH) can be stated as: *The macroscopic system out of thermodynamic equilibrium is comprised of small volume elements for which the local and instantaneous relations between thermodynamic quantities are the same as for a uniform system in equilibrium.*

Two important consequences of the LEH are: (1) all thermodynamic variables such as entropy, temperature and chemical potential, are well defined outside equilibrium, but are allowed to vary with space and time; and (2) local state variables are related by equilibrium equations of state, in particular the Gibbs' relation remains locally valid. The Gibbs' relation expresses the differential of the entropy S of a macroscopic system in terms of conjugate pairs of intensive variables F_i and extensive state variables (conserved quantities) X_i as

$$dS = \sum_i \frac{\partial S}{\partial X_i} dX_i = \sum_i F_i dX_i \tag{2.1}$$

Invoking the LEH, this is valid for each small volume element j, such that

$$dS(t) = \sum_j dS_j(t) = \sum_j \sum_i F_{i,j}(t) dX_{i,j}(t) \tag{2.2}$$

Eq. 2.2 can be generalised to a continuous medium by writing the thermodynamic quantities as functions of position $\boldsymbol{r}$:

$$ds(\boldsymbol{r},t) = \sum_i F_i(\boldsymbol{r},t)\ dx_i(\boldsymbol{r},t) \tag{2.3}$$

$$d\zeta(\boldsymbol{r},t) = \sum_i F_i(\boldsymbol{r},t)\ d\xi_i(\boldsymbol{r},t) \tag{2.4}$$

$$dS(t) = \int d\boldsymbol{r} \sum_i F_i(\boldsymbol{r},t)\ d\xi_i(\boldsymbol{r},t) \tag{2.5}$$

where s and x_i are S and X_i per unit mass, respectively. Analogously, ζ and ξ_i are S and X_i per unit volume. These reduced quantities are related through the mass density $\rho(\boldsymbol{r},t)$ by $\zeta = \rho s$ and $\xi = \rho x$. It follows that the local intensive variables $F_i(\boldsymbol{r},t)$ are defined as

$$F_i(\boldsymbol{r},t) = \frac{\partial \zeta(\boldsymbol{r},t)}{\partial \xi_i(\boldsymbol{r},t)} \tag{2.6}$$

A further consequence of the LEH is that (3) the system is locally stable, and the analogous

equilibrium stability criteria are obeyed. For example, the isochoric heat capacity (thermal stability) and isothermal compressibility (mechanical stability) are positive definite.[4]

The LEH can be justified in terms of characteristic length and time scales. Consider a local thermodynamic variable Π that undergoes equilibrium fluctuations $\delta\Pi_{\text{eq}}$. If an external gradient $\nabla\Pi$ produces a change of $|\nabla\Pi|\lambda$ over length λ, then the LEH is valid for $|\nabla\Pi|\lambda/\Pi < \delta\Pi_{\text{eq}}/\Pi \ll 1$.[5] (E.g., the characteristic length scale λ of a gas can be taken from the mean free path between successive collisions.) The magnitude of $|\nabla\Pi|\lambda/\Pi$ depends on Π and the material, and has been the subject of some discussion[9]. The LEH must also be justified by the separation of two time scales, the equilibration time τ_m of a volume element, and the macroscopic time scale characteristic of the experiment τ_M. The LEH is valid for Deborah numbers $De = \tau_m/\tau_M \ll 1$, corresponding to volume elements that have sufficient time to relax into a state of local equilibrium after exchanging mass and/or energy with neighbouring elements. The LEH is not valid for $De \gg 1$, typical of systems with long relaxation times (e.g., polymers for which τ_m can be ~100 s) or of high-frequency or very fast phenomena (e.g., ultrasound propagation and shock waves, for which $\tau_M \sim 10^{-5}$-10^{-10} s).[4] From the perspective of kinetic theory, the LEH is only justified when the Maxwell-Boltzmann distribution is approximately maintained. Indeed, the velocity part of the Boltzman H-function can be used to quantify the degree of departure from local equilibrium.[9]

2.1.3 Affinities, fluxes and entropy production

In this section we illustrate the physical meaning of fluxes and affinities through a simple example, that of a discrete system composed of two subsystems.[5]

Consider an isolated system $Y = A \cup B$ composed of two weakly coupled subsystems A and B, with the set of globally conserved extensive thermodynamic quantities $\{X_i\}$. In this case, $X_i^Y = X_i^A + X_i^B = C$, where C is a constant, and the total entropy is therefore defined as $S^Y(X_1^Y, X_2^Y, ...) = S^A(X_1^A, X_2^A, ...) + S^B(X_1^B, X_2^B, ...)$. At equilibrium, the total entropy S^Y is maximized, such that

$$\left.\frac{\partial S^Y}{\partial X_i^A}\right|_{X_i^Y} = \left.\frac{\partial (S^A + S^B)}{\partial X_i^A}\right|_{X_i^Y} = \frac{\partial S^A}{\partial X_i^A} - \frac{\partial S^B}{\partial X_i^B} = F_i^A - F_i^B = 0 \tag{2.7}$$

The quantities $\mathcal{F}_i^A = -\mathcal{F}_i^B = F_i^A - F_i^B$ are termed *affinities* and act as generalized forces that drive the system to equilibrium: $\mathcal{F}_i^A = 0$ at equilibrium, otherwise an irreversible process occurs that drives the system towards equilibrium by exchanging X_i between A and B. The rate of this exchange $J_i^A = -J_i^B = dX_i^A/dt$ is termed the *flux*, and characterizes the response of the system

under non-equilibrium conditions. The rate of global entropy change, the *entropy production*

$$\frac{dS^Y}{dt} = \sum_i \frac{\partial S^Y}{\partial X_i^A}\frac{dX_i^A}{dt} = \sum_i \mathcal{F}_i^A J_i^A = \sum_i \mathcal{F}_i^B J_i^B \tag{2.8}$$

has a bilinear structure: it is the sum of the products of each conjugate affinity-flux pair.

2.1.4 Entropy production in a continuous medium

The phenomenological description of non-equilibrium processes within the framework of LNET starts with the explicit expression for entropy production σ_S. Entropy is a non-conserved extensive quantity, and has a *global balance*, Eq. 2.9, and *local balance*, Eq. 2.10, equations of the form (see Appendix A.1)

$$\frac{dS(t)}{dt} = \frac{d^e S(t)}{dt} + \frac{d^i S(t)}{dt} = -\int_\Sigma \boldsymbol{J}_S \cdot \boldsymbol{n}\, d\Sigma + \int_V \sigma_S\, d\boldsymbol{r} \tag{2.9}$$

$$\frac{\partial(\rho s)}{\partial t} = -\nabla \cdot \boldsymbol{J}_S + \sigma_S \tag{2.10}$$

where $(d^e S/dt)$ and $(d^i S/dt)$ are the rates of exchange with the environment and the rate of internal production, respectively, and $\boldsymbol{J}_S$ is the entropy flux density. For non-isolated systems, the second law states that $d^i S/dt \geq 0$. In LNET, applying the LEH results in the stronger restriction that $\sigma_S(\boldsymbol{r}, t) \geq 0$. In both cases, the equality corresponds to reversible changes or equilibrium, and positive entropy production corresponds to irreversible processes. The quantities $T(d^i S/dt)$ and $T\sigma_S$ are rates of energy dissipation (historically the "uncompensated heat") due to irreversible processes.[4]

The goal is to find an expression for σ_S in terms of affinities and fluxes. Invoking the LEH in its differential form (Eqs. 2.3 & 2.4) suggests that

$$\boldsymbol{J}_S = \sum_i F_i \boldsymbol{J}_i \tag{2.11}$$

where $\boldsymbol{J}_i$ is the flux density of X_i. According to Eq. 2.4 (recalling that $\zeta = \rho s$ and $\xi = \rho x$), the LHS of Eq. 2.10 is given by

$$\frac{\partial(\rho s)}{\partial t} = \sum_i F_i \frac{\partial(\rho x_i)}{\partial t} \tag{2.12}$$

The first term on the RHS may be calculated as:

$$\nabla \cdot \boldsymbol{J}_S = \nabla \cdot \big(\sum_i F_i \boldsymbol{J}_i\big) = \sum_i \big(\nabla F_i \cdot \boldsymbol{J}_i + F_i \nabla \cdot \boldsymbol{J}_i\big) \tag{2.13}$$

Substituting these two terms into Eq. 2.10 gives:

$$\sigma_S = \sum_i \left(F_i \frac{\partial(\rho x_i)}{\partial t} + \nabla F_i \cdot \boldsymbol{J}_i + F_i \nabla \cdot \boldsymbol{J}_i \right) \tag{2.14}$$

where, owing to the the continuity equations for extensive conserved quantities (see Appendix A.1), the first and third terms in the sum cancel each other. Therefore, the final equation for σ_S reads

$$\sigma_S = \sum_i \nabla F_i \cdot \boldsymbol{J}_i = \sum_i \mathcal{F}_i \cdot \boldsymbol{J}_i \tag{2.15}$$

where the conjugate affinity $\mathcal{F}_i$ of $\boldsymbol{J}_i$ is defined as $\mathcal{F}_i = \nabla F_i$. The entropy production has a bilinear structure: it is the sum of the products of each flux density and its conjugate affinity (analogous to the discrete system considered in Sec. 2.1.3). [5]

2.1.5 Linear response

In a continuous medium in local equilibrium, the local fluxes are determined by local values of the affinities:[b 5]

$$J_i(\boldsymbol{r}, t) = J_i[\mathcal{F}_1(\boldsymbol{r}, t), \mathcal{F}_2(\boldsymbol{r}, t), ..., \mathcal{F}_n(\boldsymbol{r}, t)] \tag{2.16}$$

where J_i depends on not just its conjugate affinity $\mathcal{F}_i$ (direct effects), but also on other affinities $\mathcal{F}_{j \neq i}$ (indirect effects). In the *linear regime*, when deviations from equilibrium are small, the Taylor expansion of Eq. 2.16 can be limited to the first-order term (noting that there is no zeroth-order term since the fluxes vanish with the affinities):

$$J_i(\boldsymbol{r}, t) = \sum_k L_{ik} \mathcal{F}_k(\boldsymbol{r}, t) \,, \quad L_{ik} = \frac{\partial J_i}{\partial \mathcal{F}_k} \tag{2.17}$$

where the *phenomenological coefficients* $L_{ik}(F_1, F_2, ..., F_n)$ are functions of equilibrium values of intensive variables F_i but not $\mathcal{F}_i = \nabla F_i$. Eqs. 2.17 are known as *linear flux-force (flux-affinity) relations*. The domain of validity of linear response (Eq. 2.17) is not necessarily the same as that of local equilibrium.

In the linear regime, the entropy production can be written as

$$\sigma_S = \sum_{i,k} L_{ik} \mathcal{F}_i \mathcal{F}_k \tag{2.18}$$

[b] For simplicity, tensor notation has been dropped in this section. J_i and $\mathcal{F}_i$ can represent both scalars and components of vectors and tensors. The index i denotes the nature of the variable, and for vectors and tensors, its component as well.

where $\sigma_S \geq 0$ implies

$$L_{ii} \geq 0\,, \qquad L_{ii}L_{kk} - \frac{1}{4}(L_{ik} + L_{ki})^2 \geq 0 \tag{2.19}$$

and only the symmetric part $\boldsymbol{L}^{(s)}$ of the matrix $\boldsymbol{L}$ of elements L_{ik} contributes to the entropy production:

$$\sigma_S = \sum_{i,k} L_{ik}^{(s)} \mathcal{F}_i \mathcal{F}_k. \tag{2.20}$$

2.1.6 Curie's principle

Formulated in 1894, Curie's principle can be stated as the maxim "the symmetries of the causes are to be found in the effects".[10] Curie's principle has several consequences in LNET. In anisotropic media, such as a crystal invariant under some transformations of a symmetry group, it reduces the number of independent phenomenological coefficients. In isotropic media, fluxes and affinities with tensorial orders that differ by one unit cannot be coupled. For example, a chemical affinity (a scalar) cannot give rise to a heat flux (a vector), similarly a temperature gradient (a vector) cannot induce mechanical stress (a second-order tensor).[4–6]

In this thesis we consider only isotropic media and no higher than second-order fluxes and affinities. Consider therefore an isotropic medium subject to fluxes j (scalar), $\boldsymbol{J}$ (vector) and $\boldsymbol{T}$ (second-order symmetric tensor) with affinities $\boldsymbol{f}$ (vector) and $\boldsymbol{\mathcal{F}}$ (second-order tensor):

$$j = j(\boldsymbol{f}, \boldsymbol{\mathcal{F}}), \quad \boldsymbol{J} = \boldsymbol{J}(\boldsymbol{f}, \boldsymbol{\mathcal{F}}), \quad \boldsymbol{T} = \boldsymbol{T}(\boldsymbol{\mathcal{F}}) \tag{2.21}$$

It can be shown (see Appendix A.2) that within the linear regime

$$j = l \operatorname{Tr} \boldsymbol{\mathcal{F}}\,, \quad \boldsymbol{J} = A_1 \boldsymbol{f}\,, \quad \boldsymbol{T} = B_1 (\operatorname{Tr} \boldsymbol{\mathcal{F}}) \boldsymbol{I} + B_2 \boldsymbol{\mathcal{F}} \tag{2.22}$$

where l, A_1, B_1 and B_2 are scalars independent of the affinities $\boldsymbol{f}$ and $\boldsymbol{\mathcal{F}}$. Eq. 2.22 shows that, in this case, spatial symmetry only allows the coupling between fluxes and affinities of the same tensorial order.

2.1.7 Onsager-Casimir relations

Onsager's reciprocal relations[11,12] $L_{ik} = L_{ki}$ were established based on "microscopic reversibility", which is the invariance of the microscopic equations of motion w.r.t. time reversal $t \to -t$. They hold for fluctuations $\delta A_i(t) = A_i(t) - A_i^{\mathrm{eq}}$ of extensive state variable A_i w.r.t. its equilibrium value A_i^{eq}, which are even functions of time $\delta A_i(t) = \delta A_i(-t)$. Casimir[13] extended Onsager's relations to the case of odd parity in one of the variables, $-\delta A_i(t) = \delta A_i(-t)$. For conserved extensive variables

of densities x_i and x_k, and signatures ϵ_i and ϵ_k, the Onsager-Casimir reciprocity relations are

$$L_{ik} = \epsilon_i \epsilon_k L_{ki} \tag{2.23}$$

where $\epsilon_a = 1, -1$ with $a = i, k$. For example energy density and particle (number) density are even functions of time ($\epsilon_i = 1$); the fluxes of these quantities are odd. Conversely, momentum density is an odd function of time ($\epsilon_i = -1$), and its flux (tensorial) is even. A further generalization of the Onsager-Casimir relations is required in the presence of a magnetic field and/or a rotating frame of reference (not considered here).[4,5]

2.1.8 Stationary states and minimum entropy production

A stationary state is one that does not change with time; they are characterized by a set of time-independent state variables X_i. Invoking the LEH, entropy is one of these time-independent variables, and

$$\frac{dS}{dt} = \frac{d^e S(t)}{dt} + \frac{d^i S(t)}{dt} = 0 \tag{2.24}$$

As noted in Sec. 2.1.4, $d^i S(t)/dt \geq 0$, which together with Eq. 2.24 implies

$$\frac{d^e S(t)}{dt} \leq 0 \tag{2.25}$$

Thus, to maintain a non-equilibrium stationary state, entropy must be continually transferred from the system to the external environment.

Minimum entropy production theorem

In equilibrium thermodynamics, the maximization of entropy for isolated systems, and the minimization of other thermodynamic potentials under different thermodynamic constraints are important examples of variational principles. Out of equilibrium, variational principles are much more limited in scope. It can be shown (see Appendix A.3) that the total entropy production P_S of a non-equilibrium process occurring in volume V at rest with time-independent boundary conditions obeys

$$\underbrace{\frac{\mathrm{d}P_S}{\mathrm{d}t} \leq 0}_{\text{transient regime}} \quad , \quad \underbrace{\frac{\mathrm{d}P_S}{\mathrm{d}t} = 0}_{\text{stationary state}} \tag{2.26}$$

under the additional assumptions of (1) linear response, (2) constant L_{ik} and (3) $L_{ik} = L_{ki}$. Eqs. 2.26 shows that P_S decreases with time in the transient regime, until it reaches a minimum at the stationary state.[4,5]

For the stationary state, $\mathrm{d}P_S/\,\mathrm{d}t = 0$ can be cast in the form of a variational principle:

$$\delta P_S = \delta \int \sigma_S(F_i, \nabla F_i, ...)\,\mathrm{d}V = 0 \tag{2.27}$$

where δ is the variational symbol. The Euler-Lagrange equations can be shown to be the stationary balance relations, such that the stationary state is characterized by an extremum of entropy production. Since the second variation is positive definite, $\delta^2 P_S > 0$, this extremum is a minimum.[4]

2.2 Non-isothermal transport and coupling phenomena

2.2.1 Thermal conductivity

The thermal conductivity λ of any medium is defined macroscopically by Fourier's law, $\boldsymbol{J}_q = -\lambda\nabla T$ (valid by definition in the linear regime), where $\boldsymbol{J}_q$ is the heat flux. Consider an isotropic medium in which only heat conduction occurs, and no coupling effects present. From LNET:[6]

$$\sigma_S = -\frac{1}{T^2}\boldsymbol{J}_q \cdot \nabla T\,, \qquad \boldsymbol{J}_q = -\frac{L_{qq}}{T^2}\nabla T \tag{2.28}$$

which gives $\lambda = L_{qq}/T^2$ by comparison to Fourier's law.

2.2.2 Thermal diffusion

Thermal diffusion, also called the Soret effect, is when a temperature gradient induces a concentration gradient in a mixture. The coupled heat and mass transport in a binary mixture under a thermal field can be described by the constitutive relations[6]

$$\boldsymbol{J}'_q = -\lambda'_0\nabla T - \rho w_1 \mu^w_{11} T D^D_T \nabla w_1 \tag{2.29}$$

$$\boldsymbol{J}_1 = -\rho w_1 w_2 D_T \nabla T - \rho D_{12}\nabla w_1 \tag{2.30}$$

where $\boldsymbol{J}'_q$ is the reduced heat flux; $\boldsymbol{J}_1$ is the mass flux of species 1 measured in the centre-of-mass frame of reference ($\boldsymbol{J}_1 = -\boldsymbol{J}_2$); ρ is the mass density of the mixture; w_i is the mass fraction of species $i = 1, 2$; and $\mu^w_{11} = (\partial\mu_{s,1}/\partial w_1)_{P,T}$ is the derivative of the specific chemical potential of species 1, $\mu_{s,1}$, with respect to w_1 at constant temperature T and pressure P. Eqs. 2.29 and 2.30 are governed by four transport coefficients: the thermal conductivity in the absence of coupling effects λ'_0, the Dufour coefficient D^D_T, the thermal diffusion coefficient D_T and the mutual diffusion coefficient D_{12}. An additional transport coefficient, the Soret coefficient S_T, is introduced in order

to quantify the strength of the thermal diffusion phenomenon:

$$S_T \equiv \frac{D_T}{D_{12}} \tag{2.31}$$

By definition (Eq. 2.31) S_T is a measure of the relative strength between thermally induced diffusion (characterised by D_T) and concentration-driven Fickian diffusion (characterised by D_{12}). At the stationary state characterised by zero net mass flux ($\boldsymbol{J}_1 = 0$), Eq. 2.30 leads to

$$S_T = -\left(\frac{1}{w_1 w_2}\frac{\nabla w_1}{\nabla T}\right)_{\boldsymbol{J}_1=0} = -\left(\frac{1}{x_1 x_2}\frac{\nabla x_1}{\nabla T}\right)_{\boldsymbol{J}_1=0} \tag{2.32}$$

where the mole fraction x_i (related to w_i by $w_i = x_i m_i/(x_1 m_1 + x_2 m_2)$ where m_i is the mass of species $i = 1, 2$) can also be used as the "concentration variable" required to specify composition.

Thermal diffusion can also be formally described within the framework of LNET. [6] The starting point to derive phemenological equations in LNET is the entropy production σ_S. For an isotropic binary mixture with no chemical reactions present, and not subject to viscous flow or external fields, this is given by

$$\begin{aligned}\sigma_S &= -\frac{1}{T^2}\boldsymbol{J}_q \nabla T - \sum_{i=1}^{2} \boldsymbol{J}_i \nabla\left(\frac{\mu_{s,i}}{T}\right) \\ &= -\frac{1}{T^2}\boldsymbol{J}_q \nabla T - \frac{1}{T}\boldsymbol{J}_1\left[T\nabla\left(\frac{\mu_{s,1}-\mu_{s,2}}{T}\right)\right]\end{aligned} \tag{2.33}$$

where $\boldsymbol{J}_q$ is the (un-reduced) heat flux, which is the internal energy flux. Under these conditions, the pressure is uniform over the system assuming mechanical equilibrium is rapidly established. The resultant linear flux-affinity relations are:

$$\boldsymbol{J}_q = -L_{qq}\frac{\nabla T}{T^2} - L_{q1}\nabla\left(\frac{\mu_{s,1}-\mu_{s,2}}{T}\right) \tag{2.34}$$

$$\boldsymbol{J}_1 = -L_{1q}\frac{\nabla T}{T^2} - L_{11}\nabla\left(\frac{\mu_{s,1}-\mu_{s,2}}{T}\right) \tag{2.35}$$

Taking advantage of the thermodynamic relation

$$T\nabla\left(\frac{\mu_{s,i}}{T}\right) = \nabla_T \mu_i - \frac{h_{s,i}}{T}\nabla T \tag{2.36}$$

where $h_{s,i}$ is the partial specific enthalpy of species i, one obtains an alternative equation for entropy production:

$$\sigma_S = -\frac{1}{T^2}\boldsymbol{J}'_q \nabla T - \frac{1}{T}\boldsymbol{J}_1 \nabla_T(\mu_{s,1}-\mu_{s,2}) \tag{2.37}$$

where $\boldsymbol{J}'_q = \boldsymbol{J}_q - (h_1 - h_2)\boldsymbol{J}_1$. The difference between $\boldsymbol{J}'_q$ and $\boldsymbol{J}_q$ corresponds to the heat transported due to diffusion. Finally, using the Gibbs-Duhem relation $\sum_{i=1}^{2} w_i \nabla_{T,P} \mu_{s,i} = 0$ gives

$$\sigma_S = -\frac{1}{T^2}\boldsymbol{J}'_q \nabla T - \frac{\mu_{11}^w}{T(1-w_1)}\boldsymbol{J}_1 \nabla w_1 \tag{2.38}$$

This expression for entropy production (Eq. 2.38) leads to the following phenomenological relations between fluxes and affinities:

$$\boldsymbol{J}'_q = -L'_{qq}\frac{\nabla T}{T^2} - L'_{q1}\frac{\mu_{11}^w}{T(1-w_1)}\nabla w_1 \tag{2.39}$$

$$\boldsymbol{J}_1 = -L'_{1q}\frac{\nabla T}{T^2} - L'_{11}\frac{\mu_{11}^w}{T(1-w_1)}\nabla w_1 \tag{2.40}$$

where $L'_{\alpha\beta}$ are the phenomenological coefficients, with the prime denoting the inclusion of the enthalpic terms, noting that $L_{11} = L'_{11}$. Comparing Eqs. 2.39 and 2.40 to Eqs. 2.29 and 2.30 gives expressions for the transport properties in terms of the phenomenological coefficients:

$$\lambda_0 = \frac{L'_{qq}}{T^2} \tag{2.41}$$

$$D_{12} = \frac{L_{11}\mu_{11}^w}{\rho(1-w_1)T} \tag{2.42}$$

$$D_T = \frac{L'_{1q}}{\rho w_1(1-w_1)T^2} \tag{2.43}$$

$$D_T^F = \frac{L'_{q1}}{\rho w_1(1-w_1)T^2} \tag{2.44}$$

$$S_T = \frac{L'_{1q}}{L_{11}\mu_{11}^w T w_1} = \frac{L'_{1q}}{L_{11} T w_1}\left(\frac{\partial \mu_{s,1}}{\partial w_1}\right)^{-1}_{P,T} \tag{2.45}$$

Onsager's reciprocal relation $L'_{1q} = L'_{q1}$ implies $D_T = D_T^F$, and the requirement of positive-definite entropy production results in the inequalities

$$L'_{qq} \geq 0\,, \quad L_{11} \geq 0\,, \quad L'_{qq}L_{11} - L'^{,2}_{1q} \geq 0 \tag{2.46}$$

which imply non-negative transport coefficients $\lambda'_0 \geq 0$ and $D_{12} \geq 0$.

At the $\boldsymbol{J}_1 = 0$ stationary state, the heat fluxes are given by $\boldsymbol{J}_q = -(L_{qq} - L_{1q}L_{q1}/L_{11})/(\nabla T/T^2)$ and $\boldsymbol{J}'_q = -(L'_{qq} - L'_{1q}L'_{q1}/L_{11})/(\nabla T/T^2)$, which comparing to Fourier's law gives the following expression for the thermal conductivity of the mixture

$$\lambda = \frac{1}{T^2}\left(L_{qq} - \frac{L_{1q}L_{q1}}{L_{11}}\right)_{\boldsymbol{J}_1=0} = \frac{1}{T^2}\left(L'_{qq} - \frac{L'_{1q}L'_{q1}}{L_{11}}\right)_{\boldsymbol{J}_1=0} \tag{2.47}$$

where $L_{1q}L_{q1}/L_{11} = L_{1q}^2/L_{11} \geq 0$ and $L'_{1q}L'_{q1}/L_{11} = L'^2_{1q}/L_{11} \geq 0$ imply that the Soret effect always decreases λ.

2.2.3 Thermal orientation

Thermal orientation is when a thermal field induces the net orientation of particles (e.g., molecules or colloids) in a material.[14,15] Consider an isotropic, non-polar and single-component medium in which the particles adopt an average orientation $\langle \boldsymbol{n} \rangle$, where $\boldsymbol{n} = (\cos\theta, \sin\theta)$ is the vector defining the particle's direction (for example often chosen to be in the direction of a molecular axis). To derive an expression for entropy production using LNET, the energy required to obtain this alignment is required. Assuming a harmonic potential $E = (k_E/2)\langle \boldsymbol{n} \rangle^2$, the entropy production is given by[14]

$$\sigma_S = -\frac{k_E}{T}\langle \boldsymbol{n} \rangle \cdot \left(\frac{\partial \langle \boldsymbol{n} \rangle}{\partial t} \right) - \frac{1}{T^2}\boldsymbol{J}_q \cdot \nabla T \tag{2.48}$$

and the corresponding linear affinity-flux relations are

$$\frac{\partial \langle \boldsymbol{n} \rangle}{\partial t} = -\frac{L_{nn}}{T} k_E \langle \boldsymbol{n} \rangle - \frac{L_{nq}}{T^2}\nabla T \tag{2.49}$$

$$\boldsymbol{J}_q = -\frac{L_{qn}}{T} k_E \langle \boldsymbol{n} \rangle - \frac{L_{qq}}{T^2}\nabla T \tag{2.50}$$

where Onsager's reciprocal relations imply $L_{nq} = L_{qn}$, and the requirement of positive definite entropy production leads to

$$L_{qq} \geq 0\,, \quad L_{nn} \geq 0\,, \quad L_{qq}L_{nn} - L_{nq}^2 \geq 0 \tag{2.51}$$

In the $(\partial \langle \boldsymbol{n} \rangle / \partial t) = 0$ stationary state, the average orientation is given by

$$\langle \boldsymbol{n} \rangle = -\frac{L_{nq}}{k_E L_{nn}} \frac{\nabla T}{T} \tag{2.52}$$

and if the z-axis is defined so that it is parallel to $\boldsymbol{J}_q$, then:

$$\langle \cos\theta_z \rangle = -\frac{L_{nq}}{k_E L_{nn}} \frac{\nabla_x T}{T} \tag{2.53}$$

The stationary state heat flux is $\boldsymbol{J}_q = -(L_{qq} - L_{nq}L_{qn}/L_{nn})(\nabla T/T^2)$ and by comparison to Fourier's law ($\boldsymbol{J}_q = -\lambda \nabla T$), the thermal conductivity is given by

$$\lambda = \frac{1}{T^2}\left(L_{qq} - \frac{L_{nq}L_{qn}}{L_{nn}} \right)_{(\partial \langle \boldsymbol{n} \rangle / \partial t) = 0} \tag{2.54}$$

where $L_{nq}^2/L_{nn} \geq 0$ implies that the thermal orientation effect always decreases λ.

2.2.4 Thermal polarization

Thermal polarization is when a thermal field induces an electrostatic field in a polarizable medium, such as a polar fluid (e.g., water).[16] Consider an isotropic polarizable medium subjected to a thermal flux. According to LNET the entropy production is given by[6,16,17]

$$\sigma_S = -\frac{1}{T}\frac{\partial \boldsymbol{P}}{\partial t}\cdot(\boldsymbol{E}_{\mathrm{eq}} - \mathbf{E}) - \frac{1}{T^2}\boldsymbol{J}_q \nabla T \tag{2.55}$$

where: $\boldsymbol{P}$ is the polarization, and $\partial\boldsymbol{P}/\partial t$ the displacement current; $\boldsymbol{E}$ is the electric field; $\boldsymbol{E}_{\mathrm{eq}} = \boldsymbol{P}/(\chi_e \varepsilon_0)$ is the field under equilibrium conditions that corresponds to $\boldsymbol{P}$, where $\chi_e = \varepsilon_r - 1$ is the electric susceptibility, ε_r the static relative permittivity, and ε_0 the permittivity of free space. The resultant linear flux-affinity relations are

$$\frac{\partial \boldsymbol{P}}{\partial t} = -\frac{L_{pp}}{T}(\boldsymbol{E}_{\mathrm{eq}} - \mathbf{E}) - \frac{L_{pq}}{T^2}\nabla T \tag{2.56}$$

$$\boldsymbol{J}_q = -\frac{L_{qp}}{T}(\boldsymbol{E}_{\mathrm{eq}} - \mathbf{E}) - \frac{L_{qq}}{T^2}\nabla T \tag{2.57}$$

where Onsager's reciprocal relations imply $L_{pq} = L_{qp}$, and positive definite entropy production leads to

$$L_{qq} \geq 0\,, \quad L_{pp} \geq 0\,, \quad L_{qq}L_{pp} - L_{pq}^2 \geq 0 \tag{2.58}$$

From Eqs. 2.55, 2.56 and 2.57, the entropy production can be written in terms of the phenomenological coefficients as

$$\sigma_S = \left(L_{qq} - \frac{L_{pq}L_{qp}}{L_{pp}}\right)\left|\frac{\nabla T}{T^2}\right|^2 + \frac{1}{L_{pp}}\left|\frac{\partial \boldsymbol{P}}{\partial t}\right|^2 \tag{2.59}$$

The entropy production at the $\partial\boldsymbol{P}/\partial t = 0$ stationary state decreases w.r.t. the isotropic state ($L_{pq} = 0$) if the medium becomes polarized ($L_{pq} \neq 0$) because $L_{pq}L_{qp}/L_{pp} = L_{pq}^2/L_{pp} \geq 0$. This is the driving force for the thermal polarization effect.

Considering that the system is absent of free charges such that $\boldsymbol{P} = -\varepsilon_0 \boldsymbol{E}$, the stationary state electric field is given by

$$\boldsymbol{E} = \left[\left(1 - \frac{1}{\varepsilon_r}\right)\frac{L_{pq}}{L_{pp}}\frac{\nabla T}{T}\right]_{(\partial \boldsymbol{P}/\partial t)=0} \tag{2.60}$$

which implies the linear response $\boldsymbol{E} \propto \nabla T$. The thermal polarization coefficient $S_{\mathrm{TP}} = E/\nabla T$ can therefore be introduced to quantify the response of the medium.

The heat flux at the stationary state is given by $\boldsymbol{J}_q = -(L_{qq} - L_{pq}L_{qp}/L_{pp})(\nabla T/T^2)$, which

comparing to Fourier's law ($\boldsymbol{J}_q = -\lambda \nabla T$) gives the following expression for the thermal conductivity

$$\lambda = \frac{1}{T^2}\left(L_{qq} - \frac{L_{pq}L_{qp}}{L_{pp}}\right)_{(\partial \boldsymbol{P}/\partial t)=0} \tag{2.61}$$

where $L_{pq}^2/L_{pp} \geq 0$ implies that the thermal polarization effect always decreases λ.

Bibliography

[1] *Experimental Thermodynamics Volume X*, ed. D. Bedeaux, S. Kjelstrup and J. Sengers, The Royal Society of Chemistry, 2016, pp. P001–405.

[2] F. Römer, A. Lervik and F. Bresme, *J. Chem. Phys.*, 2012, **137**, 074503.

[3] F. Bresme and J. Armstrong, *J. Chem. Phys.*, 2014, **140**, 016102.

[4] G. Lebon, D. Jou and J. Casas-Vázquez, *Understanding Non-equilibrium Thermodynamics: Foundations, Applications, Frontiers*, Springer, Berlin, Heidelberg, 2008.

[5] N. Pottier, *Nonequilibrium Statistical Physics: Linear Irreversible Processes*, Oxford University Press, 2010.

[6] S. R. de Groot and P. Mazur, *Non-Equilibrium Thermodynamics*, Dover, 1984.

[7] D. G. Miller, *J. Phys. Chem.*, 1959, **63**, 570–578.

[8] D. G. Miller, *Chem. Rev.*, 1960, **60**, 15–37.

[9] B. Hafskjold and S. K. Ratkje, *J. Stat. Phys.*, 1995, **78**, 463–494.

[10] E. Castellani and J. Ismael, *Philos. Sci.*, 2016, **83**, 1002–1013.

[11] L. Onsager, *Phys. Rev.*, 1931, **37**, 405–426.

[12] L. Onsager, *Phys. Rev.*, 1931, **38**, 2265–2279.

[13] H. B. G. Casimir, *Rev. Mod. Phys.*, 1945, **17**, 343–350.

[14] F. Römer, F. Bresme, J. Muscatello, D. Bedeaux and J. M. Rubí, *Phys. Rev. Lett.*, 2012, **108**, 105901.

[15] J. Olarte-Plata, J. M. Rubi and F. Bresme, *Phys. Rev. E*, 2018, **97**, 052607.

[16] F. Bresme, A. Lervik, D. Bedeaux and S. Kjelstrup, *Phys. Rev. Lett.*, 2008, **101**, 020602.

[17] M. Marvan, *Czech. J. Phys. B*, 1969, **19**, 1240–1245.

Chapter 3

On the microscopic origin of Soret coefficient minima in liquid mixtures

3.1 Introduction

Thermal diffusion was discovered in the 19^{th} century: first observed by Ludwig[1], and later systematically investigated by Soret[2]. With the advancement of experimental and computational techniques, thermal diffusion research has gone through a renaissance in the last 20 years.[3–9] However, a universal physical picture for thermal diffusion in dense fluids remains elusive, and several outstanding questions persist. One such question is the microscopic origin of the forces driving the phenomenology observed in thermal diffusion measurements.

Aqueous solutions feature a particularly rich phenomenology. For example, experiments and simulations report changes in the thermophilicity of alkali halide salt solutions with temperature. The solutions are thermophobic ($S_T > 0$) at high temperatures and thermophilic ($S_T < 0$) at low temperatures.[10–12] Interestingly, Gaeta et al. reported minima in the Soret coefficients of $NaCl_{(aq)}$ and $KCl_{(aq)}$ as a function of concentration.[11] These experiments were performed with thermogravitational columns, and the minima could not be reproduced using state-of-the-art thermal diffusion forced Rayleigh scattering techniques, which circumvent convection effects.[12] Hence the S_T minimum remained controversial for many years. However, this situation changed with recent experiments[13] and computer simulations[14] of $LiCl_{(aq)}$ that support the existence of a minimum in the Soret coefficient. Very recently, minima at high concentrations (~ 2 M) were observed for thiocyanate ($NaSCN_{(aq)}$ and $KSCN_{(aq)}$) and acetate ($CH_3COOK_{(aq)}$) salt solutions,[15,16] giving further impetus to the investigation of the physical origin of the Soret coefficient minima. Understanding the physical variables that control the S_T minimum is also potentially relevant for explaining the thermoelectric response of aqueous solutions.[14]

In addition to aqueous electrolyte solutions, minima in the Soret coefficient with composition were observed in mixtures of polar fluids: ethanol/water [7,17,18], dimethyl-sulfoxide/water [19], and acetone/water [19,20]. In all these systems (electrolyte solutions and polar fluid mixtures), one of the components is water. This observation might suggest that the Soret coefficient minima are interlinked with water as a solvent and, therefore, its specific thermal transport properties. Indeed, existing molecular simulations of atomistic (non-polar) Lennard-Jones (LJ) binary mixtures at supercritical conditions do not offer evidence for the existence of minima in the Soret coefficient with composition. [21] However, some experiments of non-polar or weakly polar liquid mixtures reported maxima/minima in the Soret coefficient (e.g., cyclohexane/cis-decaline) and in some cases, accounting for an extrapolation to infinite dilution, a weak extrema can be inferred (e.g., toluene/1,3-dichlorobenzene). [22] That work made no attempt to explain the microscopic origin of the extrema in S_T, but crucially highlights the importance of the thermodynamic factor, Γ, a key quantity determining the heat of transport [14,23].

To investigate the existence of Soret coefficient minima in non-polar mixtures, and to probe the microscopic origin of such minima, we have performed computer simulations of the simplest liquid binary mixture, modelled with the Lennard-Jones model, which accounts for dispersion interactions. Advancing the discussion below, we show for the first time that a minimum in the Soret coefficient at a specific composition, and constant temperature and pressure, can be observed in simple non-polar liquid mixtures, hence showing that the minimum in the Soret coefficient is a general physical phenomenon. We demonstrate that the S_T minimum arises due to a coincident minimum in the thermodynamic factor, and provide a microscopic explanation for both minima in terms of the atomic coordination structures of the mixtures.

3.2 Methods

We investigate the non-equilibrium behaviour of liquid binary Lennard-Jones mixtures at constant temperature T, pressure P, and different mole fractions $x_1 = N_1/(N_1 + N_2)$, where N_i is the number of particles of type i. Inter-particle interactions were modelled using the LJTS potential, which is the LJ potential $\mathcal{V}_{ij}^{\mathrm{LJ}}(r) = 4\epsilon_{ij}[(\sigma_{ij}/r)^{12} - (\sigma_{ij}/r)^{6}]$ truncated and shifted at a cutoff radius of $r_c = 2.5\sigma$, $\mathcal{V}_{ij}^{\mathrm{LJTS}}(r) = (\mathcal{V}_{ij}^{\mathrm{LJ}}(r) - \mathcal{V}_{ij}^{\mathrm{LJ}}(r_c))\theta(r_c - r)$ with θ being the Heaviside step function. All the particles have the same diameter and mass, but the interactions between particles of type "1" or "2" are different. The parameters $\epsilon = \epsilon_{22}$ and $\sigma = \sigma_{11} = \sigma_{22}$ together with the mass of each particle $m_1 = m_2 = m$ define the usual LJ units. The energy scale was defined in terms of the high-boiling component, with $\epsilon_{11}/\epsilon_{22} = 0.6$. The Lorentz-Berthelot combining rules were used for the inter-species interaction parameters: $\epsilon_{12} = \sqrt{\epsilon_{11}\epsilon_{22}} = \sqrt{0.6}\epsilon$ and $\sigma_{12} = (\sigma_{11} + \sigma_{22})/2 = \sigma$. Experiments of liquid mixtures have reported extrema in S_T, therefore we target subcritical conditions for the LJ

mixtures. The mixtures were modelled at temperature $T = 0.62\ \epsilon k_{\mathrm{B}}^{-1}$ and pressure $P = 0.46\ \epsilon\sigma^{-3}$, below the critical point[24] for both species. The entire $0 \leq x_1 \leq 1$ composition domain is therefore expected to be subcritical. We note that along this isobar-isotherm, we estimate the liquidus to be at $x_1 \approx 0.2$ (see Sec. 3.3.1). Simulations below this mole fraction correspond to a metastable liquid mixture. Nevertheless, as we will show below, the observed S_T minimum is safely within the liquid mixture portion of the phase diagram.

We performed a variety of equilibrium molecular simulations (EMS), molecular dynamics (MD) and Monte Carlo methods, as well as non-equilibrium molecular dynamics (NEMD) simulations to calculate S_T and related quantities. From NEMD, S_T was evaluated at the stationary state characterised by zero net mass flux ($\boldsymbol{J}_1 = 0$) as

$$S_T = -\left(\frac{1}{w_1 w_2}\frac{\nabla w_1}{\nabla T}\right)_{\boldsymbol{J}_1=0} = -\left(\frac{1}{x_1 x_2}\frac{\nabla x_1}{\nabla T}\right)_{\boldsymbol{J}_1=0} \tag{3.1}$$

where x_i and w_i are the mole and mass fractions of species i (related by $w_i = x_i m_i/(x_1 m_1 + x_2 m_2)$ where m_i is the mass of species $i = 1, 2$). EMS methods calculate,

$$S_T \equiv \frac{D_T}{D_{12}} \tag{3.2}$$

from[25] (see Sec. 2.2.2)

$$D_{12} = \frac{L_{11}}{\rho(1-w_1)T}\left(\frac{\partial \mu_{s,1}}{\partial w_1}\right)_{P,T} \tag{3.3}$$

$$D_T = \frac{L'_{1q}}{\rho w_1 (1-w_1) T^2} \tag{3.4}$$

where D_{12} is the mutual diffusion coefficient and D_T is the thermal diffusion coefficient. Onsager's phenomenological coefficients $L_{\alpha\beta}$ were calculated from MD simulations in the *NVE* ensemble, using the Green-Kubo (GK) integral formulas and taking into account the enthalpy terms for the primed coefficients $L'_{\alpha\beta}$. The chemical potential μ_1, and subsequently the specific chemical potential $\mu_{s,1} = \mu_1/m_1$, was calculated from MD simulations using a free energy perturbation (FEP) method at constant T and P. $(\partial\mu_1/\partial x_1)_{P,T}$ was then calculated from the numerical derivative of μ_1. $(\partial\mu_1/\partial x_1)_{P,T}$ was also obtained from Kirkwood–Buff solution theory via two different methods of evaluating the Kirkwood-Buff integrals (KBIs): (1) from particle number fluctuations in grand canonical Monte Carlo (GCMC) simulations and (2) from the extrapolation to infinite system size of finite-volume KBIs[26], which were in turn calculated using radial distribution functions (RDFs) from MD simulations in the *NVT* ensemble. Thus, three EMS methods were used to calculate $(\partial\mu_1/\partial x_1)_{P,T}$ and subsequently the thermodynamic factor: FEP, KBI(RDF) and KBI(GCMC).

Combining these with the GK calculations for the phenomenological coefficients give three corresponding "equilibrium" routes to S_T, GK+FEP, GK+KBI(RDF) and GK+KBI(GCMC), in addition to NEMD simulations. In addition, other thermophysical properties such as the equation of state, diffusion coefficients, viscosities and activation energies were calculated from equilibrium-MD simulations in the *NVE*, *NVT* and *NPT* ensembles. Details about these simulations and calculations are given in Appendix B (essential reading[a]) All simulations were performed using the software package LAMMPS[27] (v. 3 March 2020).

3.3 Results and discussion

All statistical uncertainties reported in this chapter correspond to the 95% confidence interval, unless specified otherwise.

3.3.1 Equation of state and phase diagram

Fig. 3.1(a) shows the equation of state of the mixture as a function of x_1. The equilibrium-*NPT* and NEMD results are in excellent agreement, indicating that the local equilibrium hypothesis is fulfilled in the NEMD simulations. The mixture is expected to have a solid-solution phase diagram,[28] and the thermodynamically stable phase for $x_1 = 0$ is a solid (see Appendix B.11). Therefore, the mixture crosses three regions of the phase diagram along the (x_1; $P = 0.46\ \epsilon\sigma^{-3}$, $T = 0.62\ \epsilon k_\mathrm{B}^{-1}$) line: a homogeneous liquid mixture for $x_l < x_1 < 1$ where x_l corresponds to the liquidus; a liquid-solid coexistence region $x_s \leq x_1 \leq x_l$ where x_s corresponds to the solidus; and a solid-solid mixture for $0 < x_1 < x_s$. All the results presented in this work correspond to a liquid mixture, including $x_1 \leq x_l$ for which our simulations are of the metastable supercooled liquid mixture. Thus, it is necessary to estimate x_l in order to gauge the range of validity of our results.

For an ideal solution the phase diagram can be estimated using the equations[29,30]

$$\ln \frac{x_{s,1}}{x_{l,1}} = \frac{\Delta H_{\mathrm{fus},1}}{k_\mathrm{B}} \left(\frac{1}{T_{m,1}} - \frac{1}{T} \right) \tag{3.5}$$

$$\ln \frac{1 - x_{s,1}}{1 - x_{l,1}} = \frac{\Delta H_{\mathrm{fus},2}}{k_\mathrm{B}} \left(\frac{1}{T_{m,2}} - \frac{1}{T} \right) \tag{3.6}$$

where $T_{m,i}$ and $\Delta H_{\mathrm{fus},i}$ are the melting temperature and enthalpy of fusion, respectively, of species i; and $x_{l,1}$ and $x_{s,1}$ are the mole fractions of the liquidus and solidus for end-member 1. Eqs. 3.5&3.6 further assume that there is no difference in isobaric heat capacity between the supercooled liquid

[a] Appendix B is necessary to understand the methods used in this chapter. Many calculations have been performed, and we have placed this material in an appendix in order to avoid burdening the following discussion with interspersed technical details, which we believe would distract from our main findings.

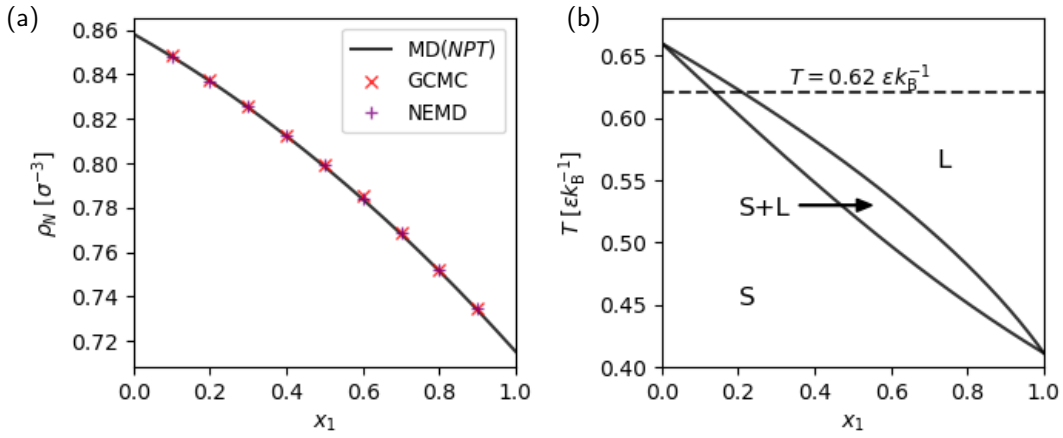


FIGURE 3.1: Equation of state and phase diagram of the LJ mixture. (a) The number density ρ_N for ($P = 0.46\ \epsilon\sigma^{-3}$, $T = 0.62\ \epsilon k_B^{-1}$) as a function of mole fraction x_1, as predicted by MD(NPT), GCMC and NEMD simulations. All simulated systems correspond to a liquid, which is metastable for $x_1 \leq x_l$, where x_l is the mole fraction of the liquidus shown in (b). (b) The estimated solid solution phase diagram of the mixture at $P = 0.46\ \epsilon\sigma^{-3}$. The symbols are: S = solid solution; L = liquid mixture; S+L = solid and liquid coexistence.

and pure solid of species 1 at T.[30] The predicted phase diagram is shown in Fig. 3.1(b), with $x_l \approx 0.21$ at $T = 0.62\ \epsilon k_B^{-1}$. The mixture is near-ideal at $x_1 \approx 0.21$ with thermodynamic factor $\Gamma \approx 0.8$, and the assumption of ideal mixing is therefore expected to be a good approximation. The S_T and Γ minima at $x_1 \sim 0.5$ (see the next section) are safely within the liquid mixture region of the phase diagram.

3.3.2 Soret coefficient minimum and its physical origin

Fig. 3.2(a) contains the main result of this chapter: S_T features a minimum as a function of composition at $x_1^{\min(S_T)} \sim 0.5$. Fitting cubic functions to the data give $x_1^{\min(S_T)} = 0.5 \pm 0.1$ for all four methods: NEMD, GK+FEP, GK+KBI(RDF) and GK+KBI(GCMC). The thermodiffusion response at the minimum is significantly enhanced with respect to diluted mixtures, by ∼30-40% relative to $x_1 = 0.1, 0.9$, and by ∼60-80% when compared to the extrapolated value of S_T at $x_1 = 1$. For all compositions, $S_T < 0$ which indicates that species 1 (the low-boiling component) is thermophilic and preferentially collects in the hot region. The S_T values calculated from NEMD and all three EMS methods are in excellent agreement: all values agree within their statistical uncertainties. Accepting that the Green-Kubo integrals are sufficiently well converged (as shown in Appendix B.5), and that finite-size effects are similar between methods, the agreement indicates that the NEMD results are within the linear regime. This is expected since $\nabla T T^{-1} \sigma \lesssim 0.007 \ll 1$. Explicit verification of linear response is provided in Appendix B.1.2 for two mole fractions ($x_1 = 0.5, 0.9$).

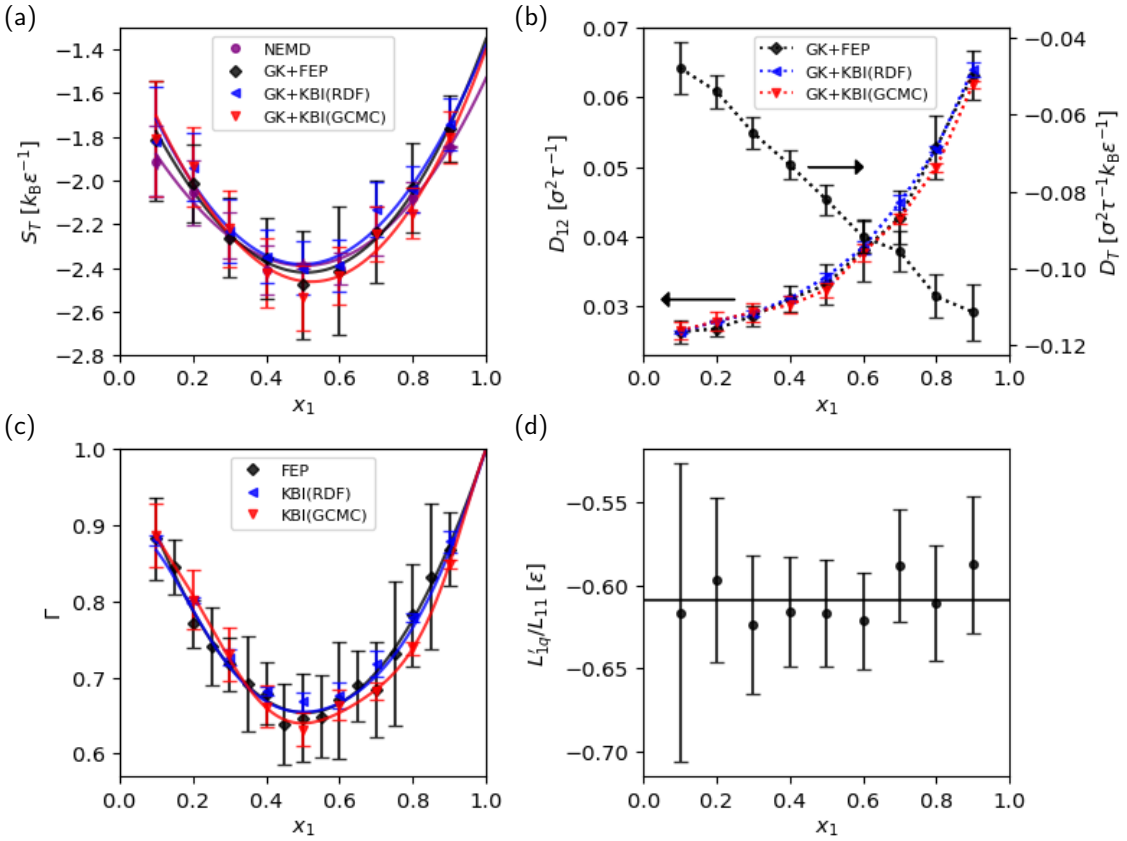


FIGURE 3.2: The Soret coefficient and related properties of the LJ mixture as a function mole fraction x_1. (a) The Soret coefficient S_T; the solid lines show cubic functions fit to the $S_T(x_1)$ data. (b) The mutual diffusion coefficient D_{12} (left axis) and thermal diffusion coefficient D_T (right axis). (c) The thermodynamic factor Γ; the solid lines show polynomial functions fit to $\Gamma(x_1)$ with the infinite-dilution constraint $\Gamma(1) = 1$. (d) The ratio of phenomenological coefficients L'_{1q}/L_{11}; the solid line shows the weighted arithmetic mean.

S_T is determined by D_{12} and D_T (see Eq. 3.2), which monotonically increase and decrease with x_1, respectively (Fig. 3.2(b)). Thus, the S_T minimum arises from a balance of D_T and D_{12}, as opposed to being carried through only by one of the transport coefficients.

The Soret coefficient S_T can be written in terms of the phenomenological coefficients and the thermodynamic factor Γ, as[25]

$$S_T = \frac{L'_{1q}}{L_{11} T w_1} \left(\frac{\partial \mu_{s,1}}{\partial w_1} \right)^{-1}_{P,T} = \frac{1}{k_B T^2} \frac{L'_{1q}}{L_{11}} \frac{m_1}{\Gamma} \tag{3.7}$$

$$\Gamma = \frac{x_1}{k_B T} \left(\frac{\partial \mu_1}{\partial x_1} \right)_{P,T} \tag{3.8}$$

where $m_1 = m_2 \Leftrightarrow x_1 = w_1$. The analysis of the different contributions to the RHS of Eq. 3.7 offers microscopic insight into the mechanisms determining the minimum in S_T. We find that the ratio L'_{1q}/L_{11} is essentially constant for all compositions (Fig. 3.2(d)). This suggests that the minimum

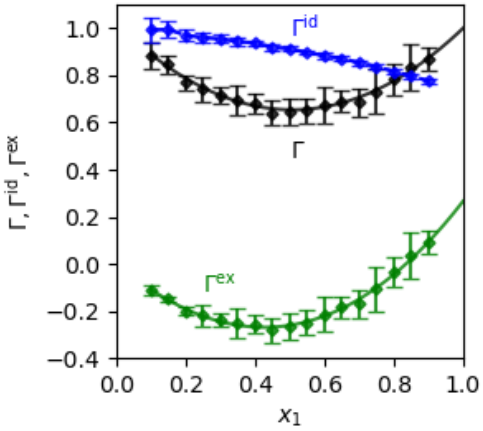


FIGURE 3.3: The thermodynamic factor Γ, and its ideal Γ^{id} and excess Γ^{ex} contributions, as a function of mole fraction x_1. All results correspond to the FEP data.

arises from the $w_1(\partial\mu_1/\partial w_1)_{P,T}$ term. As shown in Fig. 3.2(c), Γ features a distinctive minimum at $x_1^{\min(\Gamma)} \sim 0.5$. All three EMS methods (FEP, KBI(RDF) and KBI(GCMC)) predict $x_1^{\min(\Gamma)}$ values in good agreement with each other. *The minimum in S_T is connected to the minimum in the thermodynamic factor, and therefore signals the composition at which the mixture features the largest non-ideality,* $\max|1-\Gamma|$. The S_T and Γ minima coincide nearly exactly, due to the weak composition dependence of L'_{1q}/L_{11}.

We note that in our work, the minimum in Γ leads to a minimum in S_T since $L'_{1q} < 0 \Leftrightarrow D_T < 0$ ($L_{11} \geq 0$ and a stable single-phase binary mixture requires $\Gamma > 0$). For $L'_{1q} > 0 \Leftrightarrow D_T > 0$, the minimum in Γ leads to a maximum in S_T. Indeed, since S_T and D_T change sign under the permutation of components in a binary mixture ($S_{T,1} = -S_{T,2}$ and $D_{T,1} = -D_{T,2}$), the Γ minimum leads to a maximum in the Soret coefficient of species 2.

The results presented above indicate that the non-ideal contribution dominates at conditions near the minimum. This can be visualised by splitting Γ into its excess and ideal gas contributions, Γ^{ex} and Γ^{id} respectively (Fig. 3.3). $\Gamma^{id} = x_1(\partial\mu_1^{id}/\partial x_1)_{P,T}/(k_BT) = (x_1/\rho_N)(\partial\rho_N/\partial x_1)_{P,T} + 1$ depends only on x_1, the total number density ρ_N and its derivative, while $\Gamma^{ex} = x_1(\partial\mu_1^{ex}/\partial x_1)_{P,T}/(k_BT)$ depends on the excess chemical potential μ_1^{ex} and therefore the inter-particle interactions in the system. Γ^{id} monotonically decreases with increasing x_1, while Γ^{ex} possesses a minimum at $x_1^{\min(\Gamma^{ex})} = 0.4 \pm 0.1$ as determined by fitting a cubic function. Thus, the minimum arises through Γ^{ex}, although its position is shifted by ~ 0.1 (to $x_1 \sim 0.5$) due to the Γ^{id} contribution.

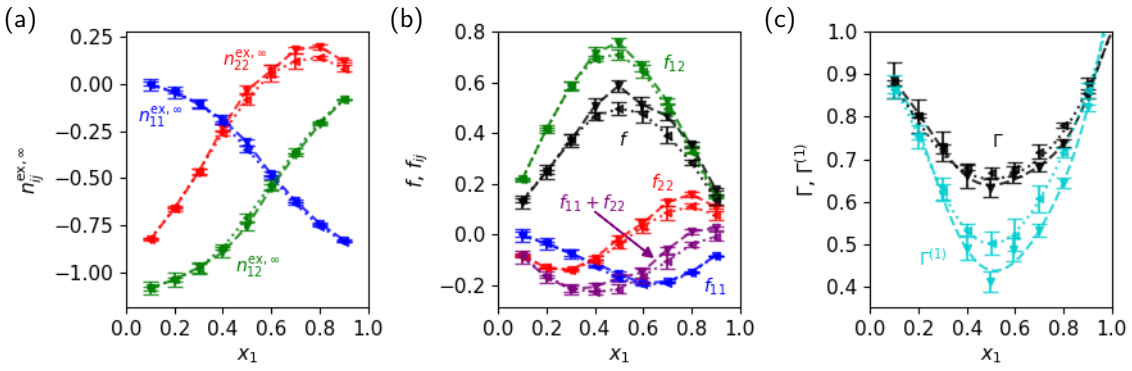


FIGURE 3.4: Analysis of the thermodynamic factor Γ as a function of mole fraction x_1 using Kirkwood-Buff theory. (a) Excess coordination numbers $n_{ij}^{ex,\infty}$ and (b) related functions f and f_{ij}. (c) Γ and its first-order approximation $\Gamma^{(1)}$ (see main text for additional details). Symbols: sideways triangles and dotted lines (··◁··) denote the KBI(RDF) data; downwards triangles (--▽--) and dashed lines denote the KBI(GCMC) data. In (c), dotted and dashed lines show polynomial functions fit to the KBI(RDF) and KBI(GCMC) data respectively. Fits to $\Gamma(x_1)$ were performed with the infinite-dilution constraint $\Gamma(0) = 1$.

To gain insight into the microscopic origins of the minimum in Γ and S_T, we turn to Kirkwood-Buff theory, which connects Γ to the structural properties of the binary mixture,

$$\Gamma = 1 - \frac{x_1 x_2 \rho_N (G_{11} + G_{22} - 2G_{12})}{1 + x_1 x_2 \rho_N (G_{11} + G_{22} - 2G_{12})} \tag{3.9}$$

where ρ_N is the total number density of the mixture. The Kirkwood-Buff integral (KBI) G_{ij} is defined as the spatial integral over $g_{ij}^{\mu VT}(r) - 1$, and quantifies the excess (or deficiency) of species j around i. $g_{ij}^{\mu VT}(r)$ is the pair correlation function in the grand canonical ensemble. The KBIs can be expressed in terms of the excess coordination numbers $n_{ij}^{ex}(r') = n_{ij}(r') - n_{ij}^{id}(r')$ where n_{ij} is the total coordination number, obtained from an integral over the pair correlation function, and $n_{ij}^{id} = (4\pi/3)\rho_{N,j} r_c'^3$ is the ideal coordination number. $\rho_{N,j}$ is the number density of species j. Hence, the KBIs are given by $\rho_{N,j} G_{ij} = \lim_{r' \to \infty} n_{ij}^{ex}(r') = n_{ij}^{ex,\infty}$, and the thermodynamic factor by $\Gamma = (1 + f)^{-1}$ where $f = (1 - x_1) n_{11}^{ex,\infty} + x_1 n_{22}^{ex,\infty} - 2x_1 n_{12}^{ex,\infty} = f_{11} + f_{22} + f_{12}$.

In order to disentangle the contributions from $n_{11}^{ex,\infty}$, $n_{22}^{ex,\infty}$ and $n_{12}^{ex,\infty}$ we take the first-order approximation to the thermodynamic factor, $\Gamma^{(1)} = 1 - f$. As shown in Fig. 3.4(c), $\Gamma^{(1)}$ results in underestimations of 1-35% across the range of compositions, with larger errors for more non-ideal mixtures, but nevertheless provides insight into the relative importance of the f_{ij} terms. f_{12} features a maximum at $x_1 \sim 0.5$ (Fig. 3.4(b)), indicating that the cross-species contribution is responsible for the minimum in $\Gamma^{(1)}$ and Γ. $|(f_{11} + f_{22})/f_{12}| =$ 0-0.41 making the cross-species contribution much more significant, and ∼3-4 times larger in the region of the $\Gamma^{(1)}$ and Γ minima. Consequently, the phenomenology of $\Gamma^{(1)}$ and Γ are primarily determined by f_{12}. *Thus, the composition dependence of* $n_{12}^{ex,\infty}$ *(Fig. 3.4(a)), which represents a net depletion of species* 2 *around*

1 *relative to the ideal state, and increases monotonically with* x_1*, is the primary microscopic origin of the minimum in* Γ *and therefore* S_T*.*

3.3.3 Theoretical models

Now we examine the accuracy of existing theoretical approaches to predict the S_T minimum reported above. We note that existing theoretical models do not accurately predict S_T in general.[31–37] In some cases, even the sign of S_T is not predicted correctly.[32–37] Especially in earlier works, the discrepancies can, at least in part, be attributed to inaccuracies in experimentally determined properties. For example the Haase[34,38] and Kempers[34] models are very sensitive to partial molar properties, and therefore the equation of state used.[34,35] In computer simulations all the required quantities can be accurately calculated, and as shown here using an exact model, all the theories examined herein feature noticeable deviations from the S_T values obtained by direct simulation. Previous simulations have shown that the theories are accurate only in a very limited number of cases, even for simple LJ mixtures and hard-sphere mixtures.[21,36,37] We have tested the standard theoretical models against our simulation data. We calculate the Soret coefficient according to the models of Haase[34,38] (S_T^{H}), Kempers[34] (S_T^{K}) Shukla and Firoozabadi[33] (S_T^{SF}), and Artola, Rousseau and Galliéro[36] (S_T^{ARG}):

$$TS_{T,1}^{\mathrm{H}} = \frac{m_1 m_2}{m_1 x_1 + m_2 x_2} \frac{(h_2 - h_2^0)/m_2 - (h_1 - h_1^0)/m_1}{x_1(\partial\mu_1/\partial x_1)_{P,T}} + \frac{k_{\mathrm{B}} T^2}{x_1(\partial\mu_1/\partial x_1)_{P,T}} S_T^0 \tag{3.10}$$

$$TS_{T,1}^{\mathrm{K}} = \frac{v_1 v_2}{v_1 x_1 + v_2 x_2} \frac{(h_2 - h_2^0)/v_2 - (h_1 - h_1^0)/v_1}{x_1(\partial\mu_1/\partial x_1)_{P,T}} + \frac{k_{\mathrm{B}} T^2}{x_1(\partial\mu_1/\partial x_1)_{P,T}} S_T^0 \tag{3.11}$$

$$TS_{T,1}^{\mathrm{SF}} = \frac{u_1/\tau_1 - u_2/\tau_2}{x_1(\partial\mu_1/\partial x_1)_{P,T}} + \frac{(v_2 - v_1)(x_1 u_1/\tau_1 + x_2 u_2/\tau_2)}{(x_1 v_1 + x_2 v_2) x_1(\partial\mu_1/\partial x_1)_{P,T}} \tag{3.12}$$

$$TS_{T,1}^{\mathrm{ARG}} = \frac{\Delta G_2^{\ddagger} - \Delta G_1^{\ddagger}}{k_{\mathrm{B}} T} + \frac{m_2 - m_1}{m_2 + m_1} \frac{\Delta G_2^{\ddagger} + \Delta G_1^{\ddagger}}{k_{\mathrm{B}} T} \tag{3.13}$$

where h_i, u_i and v_i are the partial molar enthalpy, internal energy and volume of species $i = 1, 2$. The Kempers model was derived by considering a non-isothermal two-bulb system, with the main assumption that the stationary state is the macroscopic state with the maximum number of microstates. Within this model, S_T^{K} corresponds to the centre-of-volume frame of reference, while Haase's earlier educated guess S_T^{H} can be derived in the centre-of-mass frame.[34] h_i^0 and S_T^0 correspond to an ideal gas state at the same temperature (calculated from kinetic theory), and capture the kinetic contribution to S_T. The Shukla-Firoozabadi model was developed with its origins in linear non-equilibrium thermodynamics (LNET), along the same lines as earlier models[39,40] that all correlate the net heat of transport with the activation energy for viscous flow $\Delta U_\eta^{\ddagger}$. The parameter $\tau_i = \Delta U_{c,i}/\Delta U_{\eta,i}^{\ddagger}$, where ΔU_c is the cohesive energy, is related to the size of

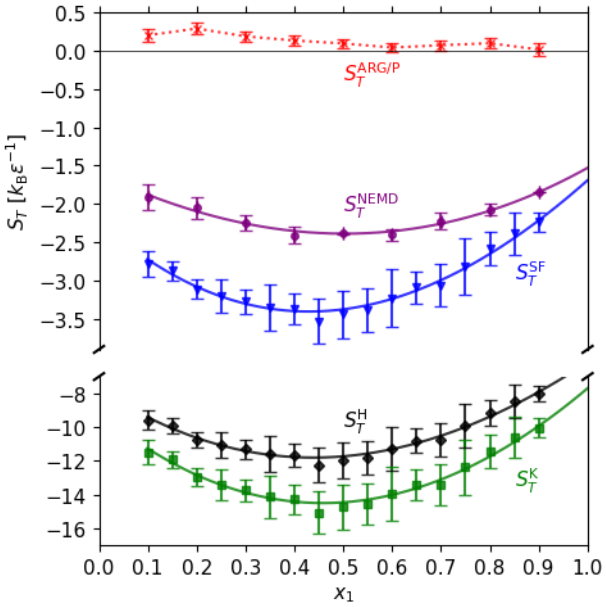


FIGURE 3.5: Soret coefficient S_T as a function of x_1 as predicted by various models, as defined in the main text. The NEMD values S_T^{NEMD} are shown for reference. The solid lines show cubic functions fit to the $S_T(x_1)$ data.

the hole required for viscous flow (from the hole theory of liquids). The Artola-Rousseau-Galliéro model is Prigogine's model (S_T^{P}) modified to include the mass contribution; for $m_1 = m_2$ it reduces to $S_{T,1}^{\mathrm{ARG}} = S_{T,1}^{\mathrm{P}} = (\Delta G_2^{\ddagger} - \Delta G_1^{\ddagger})/k_{\mathrm{B}}T^2$, where $\Delta G_i^{\ddagger}$ is the activation energy for the self-diffusion of species i. In these two kinetic models, thermal diffusion is described as a coupled diffusion-activated process, for which the elementary process can be summarized as a swap between two particles of different species along a temperature gradient. The molecular motion of a component through the mixture is better identified with self-diffusion rather than viscous flow; the use of the latter was historically motivated by the scarcity of self-diffusion data, even for pure components, and justified by the similar activation energies expected from Eyring's rate theory applied to liquids.[41] By using self-diffusion data, the Artola-Rousseau-Galliéro model represents a step forward in the modelling of thermal diffusion.

We show in Fig. 3.5 the Soret coefficients predicted by these models, alongside the NEMD values for reference. Out of the four models, the Shukla-Firoozabadi model is the most accurate: it overestimates $|S_T|$ by ∼20-50%. The Kempers and Haase models overestimate $|S_T|$ by ∼400-500% and ∼300-400% respectively. The Artola-Rousseau-Galliéro/Prigogine model underestimates $|S_T|$ by ∼100-110%, predicting values $\sim 10^{-1}\ k_{\mathrm{B}}\epsilon^{-1}$. Furthermore, the model predicts the wrong sign: $S_T^{\mathrm{ARG/P}} > 0$ or straddles 0 when accounting for the associated uncertainties.

S_T^{H}, S_T^{K} and S_T^{SF} all possess a minimum because they contain $x_1(\partial\mu_1/\partial x_1)_{P,T} = k_{\mathrm{B}}T\Gamma$ in the

denominator. The $x_1(\partial\mu_1/\partial x_1)_{P,T}$ term in S_T^{SF} originates directly from the phenomenological equations for thermodiffusion from linear non-equilibrium thermodynamics (LNET), which the model uses as a starting point for its derivation. For S_T^{K}, the $x_1(\partial\mu_1/\partial x_1)_{P,T}$ term arises naturally from the statistical thermodynamics approach employed by Kempers. Originally an educated guess, S_T^{H} can be derived more rigorously within the framework of Kempers[34]. In contrast, $S_T^{\mathrm{ARG/P}}$ does not predict a minimum: it features a weak concentration dependence, and generally decreases with increasing x_1. $S_T^{\mathrm{ARG/P}}$ contains $k_{\mathrm{B}}T$ (as opposed to $k_{\mathrm{B}}T\Gamma$) in the denominator, which is only valid for ideal mixtures. Indeed the Artola-Rousseau-Galliéro/Prigogine model does not explicitly consider a concentration gradient along the reaction coordinate; doing so would result in a similar "non-ideality" term in the denominator.[42]

3.3.4 Thermal conductivity

Here we show how the Soret coefficient minimum affects the phenomenology of the thermal conductivity. It is well established that the Soret effect reduces the thermal conductivity of the mixture.[25] From LNET, the thermal conductivity λ is given in terms of the phenomenological coefficients $L_{\alpha\beta}$ and $L'_{\alpha\beta}$ as (see Sec. 2.2.2)

$$\lambda = \frac{1}{T^2}\left(L_{qq} - \frac{L_{1q}L_{q1}}{L_{11}}\right)_{\boldsymbol{J}_1=0} = \frac{1}{T^2}\left(L'_{qq} - \frac{L'_{1q}L'_{q1}}{L_{11}}\right)_{\boldsymbol{J}_1=0} \tag{3.14}$$

where the enthalpic terms in the primed coefficients cancel exactly to give the same thermal conductivity as for the unprimed coefficients. λ can therefore be split into two contributions: (1) the thermal conductivity in the absence of coupling effects, $\lambda_0 = L_{qq}/T^2$ or $\lambda'_0 = L'_{qq}/T^2$, and (2) the mass-heat coupling term, $\delta\lambda = -L_{1q}L_{q1}/(L_{11}T^2)$ or $\delta\lambda' = -L'_{1q}L'_{q1}/(L_{11}T^2)$, such that $\lambda = \lambda_0+\delta\lambda = \lambda'_0+\delta\lambda'$. The Soret effect should always decrease λ, and thus $\lambda = \lambda_0-|\delta\lambda| = \lambda'_0-|\delta\lambda'|$.

We show in Fig. 3.6 the thermal conductivity of the mixture, and the contribution due to heat-mass coupling. The thermal conductivities calculated via NEMD and equilibrium-MD (EMD) are in excellent agreement. The thermal conductivity of the mixture decreases with increasing x_1. λ increases with density, consistent with the trend observed for simple fluids, including LJ fluids, along an isotherm. However, the density dependence of the mixture slightly deviates from the $\lambda \propto \rho_N^{2/3}$ scaling reported[43] for pure LJ fluids. The $|\delta\lambda|$ and $|\delta\lambda'|$ terms both feature a maximum, which is a direct consequence of the minimum in S_T and Γ (indeed, $\delta\lambda' = -L'_{1q}S_T\Gamma k_{\mathrm{B}}/m_1$ for $m_1 = m_2$). $|\delta\lambda|$ amounts to a reduction of ∼1-3% relative to λ for $0.1 \leq x_1 \leq 0.9$, while $|\delta\lambda'|$ is an order of magnitude smaller with values from 0 to 0.3%. The result that heat-mass coupling reduces the thermal conductivity by at most a few percent is consistent with previous studies[44] examining different LJ mixtures.

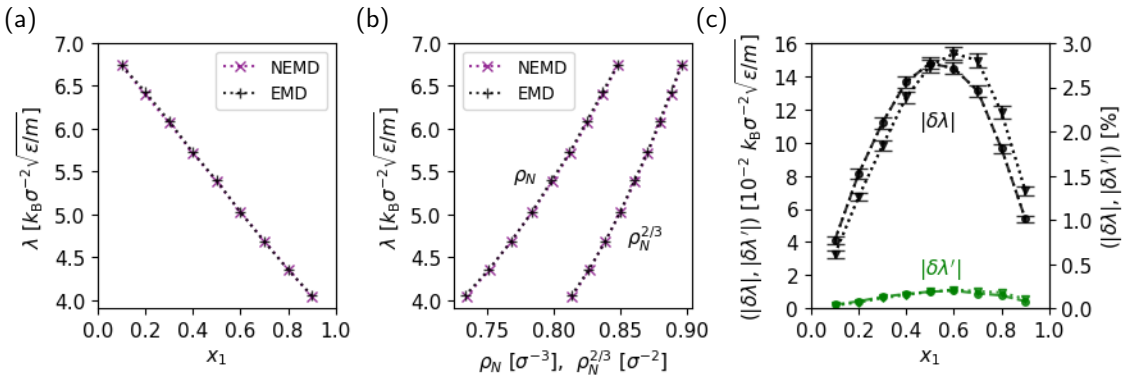


FIGURE 3.6: Thermal conductivity λ as a function of (a) mole fraction x_1 and (b) number density ρ_N as well as $\rho_N^{2/3}$. (c) The decrease in λ due to heat-mass coupling, $|\delta\lambda|$ and $\delta\lambda'$. In (c), circles with dashed lines (--○--) show the absolute values (left axis) and downward triangles with dotted lines ($\cdots\nabla\cdots$) show the values as a percentage of λ (right axis). Where error bars have not been shown, uncertainties are smaller than the size of the symbols.

3.4 Closing remarks and summary

We close this chapter with a discussion of our results in the context of recent literature. While the S_T minimum examined in this work originates from a coincident minimum in Γ, for $LiCl_{(aq)}$, Γ increases monotonically in the concentration range of the S_T minimum.[14] Furthermore, simulations have highlighted the importance of ion solvation structure on the existence of the minimum in $LiCl_{(aq)}$.[45] In contrast, local structural changes in the LJ mixture are minor (see Appendix B.3). We note that many simple salts are thought to have a D_{12} minimum at low concentrations ($\sim 10^{-1}$ mol dm^{-3}) often attributed to ion-pair formation and solute-solvent association.[15,46–48] Recent experiments observed S_T minima in $NaSCN_{(aq)}$, $KSCN_{(aq)}$, $K_2CO_{3(aq)}$ and $CH_3COOK_{(aq)}$ that are carried through D_T.[15,16] S_T minima have been observed in mixtures of polar organic solvents with water. Ethanol/water and acetone/water mixtures have S_T minima at $x_1 \sim 0.6$ and $x_1 \sim 0.5$, respectively, roughly coincident with minima in D_{12} and Γ for both mixtures.[7,17–20,49,50] Hence, the physical origin of the minima in aqueous solutions and mixtures may be quite different to the one reported here for non-polar liquids, since the LJ mixtures do not feature extrema in either D_{12} or D_T, which instead change monotonically with composition (see Fig. 3.2(b)).

LJ mixtures are more representative of mixtures of non-polar organic solvents, in which intermolecular interactions are governed by van der Waals forces. At 25°C, cyclohexane/cis-decalin possesses a S_T maximum at $x_1 \approx 0.2$ but $\Gamma \approx 1.0$ for the entire $0 \leq x_1 \leq 1$ range (there is a very shallow Γ minimum at $x_1 \approx 0.8$),[22] indicative of a different origin compared to the LJ mixture. Also in contrast with the LJ mixture, cyclohexane/benzene features a monotonic increase of S_T with x_1 at 25°C, but does have a strong minimum in Γ at $x_1 \approx 0.5$.[22]

It is evident that the physical origins of S_T minima/maxima must be considered on a case-by-case basis for different mixtures, even those belonging to the same class of mixture (aqueous solution, non-polar organic solvent mixtures, etc.). We provide here a proof of principle and demonstrate that S_T minima can exist in even the simplest of mixtures, as exemplified by a binary LJ mixture in which the components differ by only the interaction parameter ϵ. The concentration dependence of the S_T is, at least for simple mixtures, typically attributed to the cross-interactions between unlike particles[21] – a notion sustained in recent reviews[9,51,52]. For dense supercritical LJ mixtures with cross-interactions given by $\epsilon_{12} = k_{12}\sqrt{\epsilon_{11}\epsilon_{22}}$ it was found that $S_T(x_1) \approx bx_1 + c$, with the slope b controlled by k_{12}.[21] Greater $|1 - k_{12}|$ values resulted in greater $|b|$ values. In this work, we identify a mixture with $k_{12} = 1$ that nevertheless features a strong composition dependence and more complex phenomenology (the S_T minimum). Clearly, further work is required to explain the composition dependence of S_T in liquid mixtures and different thermodynamic conditions.

In summary, we identify a subcritical LJ mixture that features a minimum in S_T as a function of x_1. This S_T minimum arises due to a coincident minimum in the thermodynamic factor Γ, and is therefore connected to the non-ideality of the mixture. It also leads to a maximal decrease in thermal conductivity due to heat-mass coupling effects, although this decrease amounts to at most a few percent. The microscopic origin of the S_T and Γ minima can be traced back primarily to the composition dependence of the excess coordination number $n_{12}^{\mathrm{ex},\infty}$, which represents the net depletion of species 2 around 1 relative to the ideal gas state. Theoretical models that do not include the $x_1(\partial\mu_1/\partial x_1) = k_{\mathrm{B}}T\Gamma$ term, or otherwise account for the non-ideality of the mixture, fail to reproduce the S_T minimum.

Bibliography

[1] C. Ludwig, *Sitzber. Akad. Wiss. Wien Math.-naturw. Kl.*, 1856, **20**, 539.

[2] C. Soret, *Arch. Sci. Phys. Nat. Genève*, 1879, **2**, 48.

[3] S. Duhr and D. Braun, *Phys. Rev. Lett.*, 2006, **96**, 168301.

[4] S. Duhr and D. Braun, *Proc. Natl. Acad. Sci. U.S.A.*, 2006, **103**, 19678–19682.

[5] S. N. Rasuli and R. Golestanian, *Phys. Rev. Lett.*, 2008, **101**, 108301.

[6] A. Würger, *Phys. Rev. Lett.*, 2008, **101**, 108302.

[7] S. Wiegand, *J. Phys.: Condens. Matter*, 2004, **16**, R357–R379.

[8] R. Piazza, *Soft Matter*, 2008, **4**, 1740–1744.

[9] W. Köhler and K. I. Morozov, *J. Non-Equilib. Thermodyn.*, 2016, **41**, 151–197.

[10] K. F. Alexander, *Z. Phys. Chem. (Leipzig) 1*, 1954, **203**, 213–227.

[11] F. S. Gaeta, G. Perna, G. Scala and F. Bellucci, *J. Phys. Chem.*, 1982, **86**, 2967–2974.

[12] F. Römer, Z. Wang, S. Wiegand and F. Bresme, *J. Phys. Chem. B*, 2013, **117**, 8209–8222.

[13] J. Colombani, J. Bert and J. Dupuy-Philon, *J. Chem. Phys.*, 1999, **110**, 8622–8627.

[14] S. Di Lecce, T. Albrecht and F. Bresme, *Sci. Rep.*, 2017, **7**, 44833.

[15] S. Mohanakumar, J. Luettmer-Strathmann and S. Wiegand, *J. Chem. Phys.*, 2021, **154**, 084506.

[16] S. Mohanakumar and S. Wiegand, *Eur. Phys. J. E*, 2022, **45**, 10.

[17] A. Königer, B. Meier and W. Köhler, *Philos. Mag.*, 2009, **89**, 907–923.

[18] L. Zhang, Q. Wang, Y.-C. Liu and L.-Z. Zhang, *J. Chem. Phys.*, 2006, **125**, 104502.

[19] H. Ning and S. Wiegand, *J. Chem. Phys.*, 2006, **125**, 221102.

[20] H. Cabrera, L. Martí-López, E. Sira, K. Rahn and M. García-Sucre, *J. Chem. Phys.*, 2009, **131**, 031106.

[21] P.-A. Artola and B. Rousseau, *Phys. Rev. Lett.*, 2007, **98**, 125901.

[22] S. Hartmann, G. Wittko, F. Schock, W. Groß, F. Lindner, W. Köhler and K. I. Morozov, *J. Chem. Phys.*, 2014, **141**, 134503.

[23] J. N. Agar, C. Y. Mou and J. L. Lin, *J. Phys. Chem.*, 1989, **93**, 2079–2082.

[24] M. Thol, G. Rutkai, R. Span, J. Vrabec and R. Lustig, *Int. J. Thermophys.*, 2015, **36**, 25–43.

[25] S. R. de Groot and P. Mazur, *Non-Equilibrium Thermodynamics*, Dover, 1984.

[26] P. Krüger, S. K. Schnell, D. Bedeaux, S. Kjelstrup, T. J. H. Vlugt and J.-M. Simon, *J. Phys. Chem. Lett.*, 2013, **4**, 235–238.

[27] A. P. Thompson, H. M. Aktulga, R. Berger, D. S. Bolintineanu, W. M. Brown, P. S. Crozier, P. J. in 't Veld, A. Kohlmeyer, S. G. Moore, T. D. Nguyen, R. Shan, M. J. Stevens, J. Tranchida, C. Trott and S. J. Plimpton, *Comp. Phys. Comm.*, 2022, **271**, 108171.

[28] M. R. Hitchcock and C. K. Hall, *J. Chem. Phys.*, 1999, **110**, 11433–11444.

[29] C. Galvin, R. Grimes and P. Burr, *Comput. Mater. Sci.*, 2021, **186**, 110016.

[30] C. D. Thurmond, *J. Phys. Chem.*, 1953, **57**, 827–830.

[31] M. Eslamian and M. Z. Saghir, *J. Non-Equilib. Thermodyn.*, 2009, **34**, 97–131.

[32] L. J. T. M. Kempers, *J. Chem. Phys.*, 1989, **90**, 6541–6548.

[33] K. Shukla and A. Firoozabadi, *Ind. Eng. Chem. Res.*, 1998, **37**, 3331–3342.

[34] L. J. T. M. Kempers, *J. Chem. Phys.*, 2001, **115**, 6330–6341.

[35] M. G. Gonzalez-Bagnoli, A. A. Shapiro and E. H. Stenby, *Philos. Mag.*, 2003, **83**, 2171–2183.

[36] P.-A. Artola, B. Rousseau and G. Galliéro, *J. Am. Chem. Soc.*, 2008, **130**, 10963–10969.

[37] H. Hoang and G. Galliero, *Eur. Phys. J. E*, 2022, **45**, 42.

[38] R. Haase, *Zeitschrift für Physik*, 1949, **127**, 1–10.

[39] E. L. Dougherty and H. G. Drickamer, *J. Chem. Phys.*, 1955, **23**, 295–309.

[40] E. L. Dougherty and H. G. Drickamer, *J. Phys. Chem.*, 1955, **59**, 443–449.

[41] L. J. Tichacek, W. S. Kmak and H. G. Drickamer, *J. Phys. Chem.*, 1956, **60**, 10963–10969.

[42] W. M. Rutherford and H. G. Drickamer, *J. Chem. Phys.*, 1954, **22**, 1157–1165.

[43] N. Ohtori, Y. Ishii, Y. Togawa, T. Oono and K. Takase, *Phys. Rev. E*, 2014, **89**, 022129.

[44] J. Armstrong and F. Bresme, *Phys. Chem. Chem. Phys.*, 2014, **16**, 12307–12316.

[45] S. Di Lecce, T. Albrecht and F. Bresme, *Phys. Chem. Chem. Phys.*, 2017, **19**, 9575–9583.

[46] G.-H. Gao, H.-B. Shi and Y.-X. Yu, *Fluid Phase Equilib.*, 2007, **256**, 105–111.

[47] J. P. Mitchell, J. B. Butler and J. G. Albright, *J. Solution Chem.*, 1992, **21**, 1115–1129.

[48] A. Katz and S. Ben-Yaakov, *Mar. Chem.*, 1980, **8**, 263–280.

[49] M. T. Tyn and W. F. Calus, *J. Chem. Eng. Data*, 1975, **20**, 310–316.

[50] R. Taylor and H. A. Kooijman, *Chem. Eng. Commun.*, 1991, **102**, 87–106.

[51] P.-A. Artola and B. Rousseau, *Mol. Phys.*, 2013, **111**, 3394–3403.

[52] K. Harstad, *Ind. Eng. Chem. Res.*, 2009, **48**, 6907–6915.

Chapter 4

Mass dipole contribution to the isotopic Soret effect in molecular mixtures

4.1 Introduction

Thermal diffusion was not "theoretically discovered" until the 1910s, and one can speculate that it was overlooked by the original pioneers of kinetic theory because the Soret coefficient vanishes for Maxwellian molecules (point particles that repel each other with a force $F \propto r^{-5}$, where r is the inter-particle distance).[1] These equations of Enskog and Chapman already implied that components of a mixture could be separated based solely on their mass,[1] and in 1924 Chapman was the first to suggest[2] the use of thermal diffusion for separating isotopes. Isotope fractionation by thermal diffusion was first experimentally achieved in 1938 by Clusius and Dickens,[3] and subsequently received considerable theoretical treatment by Furry, Jones and Osager, among others.[1,4]

The pseudo-isotopic Soret effect refers to the contribution to the Soret coefficient S_T from the mass and mass distribution of the particles. For molecular mixtures the empirical equation

$$S_T = S_T^{\text{chem}} + S_T^{\text{iso}} \tag{4.1}$$

is usually a good approximation (see Sec. 1.2.2); S_T^{chem} and S_T^{iso} are the chemical and isotopic contributions, respectively.

To date, all models (empirical and theoretically derived) represent S_T^{iso} as a function of the total masses of the particles M_i and their moments of inertia I_i. For binary mixtures,

$$S_T^{\text{iso}} = S_T^{\text{iso}}(M_1, M_2, I_1, I_2) \tag{4.2}$$

and for mixtures consisting of species with the same mass,

$$M_1 = M_2 = M \quad \Longrightarrow \quad S_T^{\mathrm{iso}} = S_T^{\mathrm{iso}}(I_1, I_2; M) \tag{4.3}$$

where three assumptions are implicit in Eqs. 4.2 and 4.3: (1) the effect of the internal mass distribution can be modelled using only the moment of inertia; (2) rigid body moments of inertia are applicable to flexible molecules; and (3) rigid body moments of inertia $\boldsymbol{I}_i$ (3×3 matrices) can be reduced to scalars I_i. Assumptions (1) and (2) are justified for rigid linear molecules, such as diatomic molecules. Small polyatomic molecules have typically been characterized by a single principal moment of inertia $I_{i,k}$ or $I_i = 3/\sum_k I_{i,k}^{-1}$.[5–12] A recent study on halobenzene/n-alkane mixtures used $S_T^{\mathrm{iso}}(M_1, M_2)$ because the moment of inertia is not well defined for flexible alkanes.[7] To the best of our knowledge, assumption (1) has not been tested, or discussed in the literature.

How best to characterize the internal mass distribution of a molecule? The moments $\boldsymbol{\mu}_n$ of the mass distribution are a natural extension to using the total mass and moment of inertia. For a rigid body with mass density $\rho(\boldsymbol{r})$:

$$\boldsymbol{\mu}_n = \int_V \rho(\boldsymbol{r}) \boldsymbol{r}^{\otimes n} d^3\boldsymbol{r} \tag{4.4}$$

where $\boldsymbol{r}^{\otimes n} = \boldsymbol{r} \otimes \boldsymbol{r} \otimes ... \otimes \boldsymbol{r}$ (n times) and $\otimes$ denotes the Kronecker product of two matrices. The zeroth moment $\mu_0 = M$ is the total mass of the body (scalar). The first moment $\boldsymbol{\mu}_1 = \boldsymbol{D}$ is the mass dipole (3×1 vector), which gives the centre of mass when normalized by the total mass, $\boldsymbol{D}/M = \boldsymbol{r}_{\mathrm{com}}$. The second moment $\boldsymbol{\mu}_2$ corresponds to the moment of inertia $\boldsymbol{I}$ (3×3 matrix). Higher order moments, $\boldsymbol{\mu}_{n>2}$, do not affect rigid body dynamics, and thus the mass distribution of a rigid body can be completely represented by $\boldsymbol{\mu}_{n=0,1,2}$, i.e., by M, r_{com} and $\boldsymbol{I}$. While M and $\boldsymbol{I}$ appear frequently in models of thermal diffusion, the impact of the mass dipole on the Soret coefficient of molecular mixtures has not been considered. Indeed, the mass dipole was introduced only very recently in the context of thermal diffusion, when studying the thermal orientation and thermophoresis of anisotropic colloids.[13–15] We show here that the mass dipole is part of a more general description of the mass distribution, which adds additional contributions to the formulation summarized by Eq. 4.2.

In this chapter we investigate the effect of the mass dipole on the Soret coefficient of isotopic mixtures of rod-like molecules. The model we employ allows for the systematic change of the moments of the mass distribution, making it possible to isolate the M, $\boldsymbol{D}$ and $\boldsymbol{I}$ contributions to the Soret coefficient. We provide a proof of principle for the mass dipole contribution in isotopic mixtures. However, the main conclusions of this work are applicable to non-isotopic mixtures as well, conveniently through Eq. 4.1.

4.2 Methods

4.2.1 Particle model

We investigate the thermal diffusion of mixtures of rod-like molecules, in which the components differ only by their internal mass distribution. The molecules were modelled using the shish-kebab model, a rigid chain of tangent spherical monomers of effective diameter σ, of length $N = 7$. The mass m_i of monomer i is given by a point mass at its interaction site. All intermolecular interactions were modelled using the WCA potential

$$\mathcal{V}_{\mathrm{WCA}}(r) = \begin{cases} 4\epsilon\left[\left(\frac{\sigma}{r}\right)^{12} - \left(\frac{\sigma}{r}\right)^{6}\right] + \epsilon, & \text{if } r \leq 2^{1/6}\sigma \\ 0, & \text{if } r > 2^{1/6}\sigma \end{cases} \tag{4.5}$$

where r is the distance between two monomers and ϵ represents the strength of the purely repulsive pairwise interaction. These parameters, ϵ and σ, together with the unit of mass m are used to define the usual Lennard-Jones units, which are adopted in this work.

The total mass of each molecule was set to $M = 56m$. Noting that the total mass has been held constant, we report the reduced mass dipole $\boldsymbol{d} = \boldsymbol{D}/M$, which has a more intuitive physical meaning than $\boldsymbol{D}$: it is the displacement of the centre of mass from the geometric centre, $\boldsymbol{d} = d \cdot \hat{\boldsymbol{u}}_d = \boldsymbol{r}_{\mathrm{com}} - \boldsymbol{r}_g$. The geometric centre $\boldsymbol{r}_g$ was chosen as the centre of symmetry of the molecule (i.e., the inversion centre given the $D_{\infty h}$ point group). Since we consider freely rotating rigid bodies, their rotation is characterized by the moments of inertia I about the axes through the centre of mass. The moments of mass for this model (Fig. 4.1) are given by (for the rod oriented along the x-axis),

$$M = \sum_{i=0}^{7} m_i = 56m, \quad d = \frac{1}{M}\sum_{i=0}^{7} m_i(x_i - x_g), \quad I = \sum_{i=0}^{7} m_i(x_i - x_{\mathrm{com}})^2 \tag{4.6}$$

where x_i is the distance of monomer i along the molecular axis. There are no analytical solutions to Eqs. 4.6 for a given set $\{N, M, d, I\}$ without applying additional constraints. We use numerical optimization methods to generate the mass distributions that give the desired $\{N, M, d, I\}$. Each mixture is characterized by the mass dipoles d_i and moments of inertia I_i of species $i = 1, 2$. By

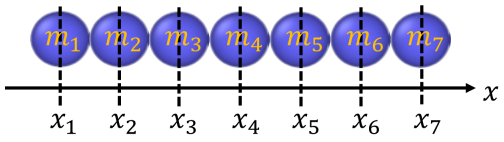


FIGURE 4.1: The shish-kebab model of length $N = 7$.

convention we assign species 1 according to $I_1 > I_2$, and $d_1 > d_2$ if $I_1 = I_2$.

4.2.2 Simulation details

We performed both equilibrium and non-equilibrium molecular dynamics simulations of equimolar (mole fractions $x_1 = x_2 = 0.5$) binary mixtures targeting temperature $T = 3.0\ \epsilon k_{\mathrm{B}}^{-1}$ and pressure $P = 1.121\ \epsilon\sigma^{-3}$, which correspond to a monomer number density of $\rho_{N,\mathrm{mon}} = 0.398\ \sigma^{-3}$ (molecule number density $\rho_{N,m} = \rho_{N,\mathrm{mon}}/7 = 0.0568\ \sigma^{-3}$) and volume fraction $\phi = 0.208$. The molecules were modelled as rigid bodies; their translational and rotational degrees of freedom were integrated using the method of quaternions[16,17]. A timestep of $\delta t = 0.002\tau$ was used for all simulations. All simulations were performed using LAMMPS[18] (v. 3 March 2020).

Non-equilibrium molecular dynamics simulations

Boundary-driven non-equilibrium molecular dynamics (NEMD) simulations of the mixtures were performed at an average density of $\rho_{N,\mathrm{mon}} = 0.4\sigma^{-3}$. An elongated (tetragonal) simulation cell of dimensions $(L_x, L_y, L_z) = (50, 50, 100)\sigma$ was used, with 3D periodic boundary conditions. Two thermostatting regions, hot and cold, were located in the centre and edges of the simulation, respectively (see Fig. 4.2). The thermostatting regions had a width $\Delta z = 7\sigma$ and extended over the entire (x, y) plane, such that the temperature gradients were generated along the z-direction. For the thermostatting procedure, a Langevin thermostat with a time constant (damping parameter) of 1τ was applied to the hot and cold regions at temperatures T_h and T_c, respectively. The thermostat temperatures were set to $T_c = 2.5\ \epsilon k_{\mathrm{B}}^{-1}$ and $T_h = 3.5\ \epsilon k_{\mathrm{B}}^{-1}$, unless specified otherwise. The Langevin thermostats do not conserve linear momentum, so the system's centre-of-mass velocity was subtracted from each particle at every timestep in order to ensure linear momentum conservation. In the stationary state, this set-up results in two equal but opposite temperature gradients, and therefore in equal and opposite heat fluxes, such that the system is completely periodic. In order to avoid potential artefacts associated with the dynamics of the Langevin-thermostated particles,[19,20] only data pertaining to rods with a centre of geometry a minimum distance of $(N/2)\sigma = 3.5\sigma$ from either thermostatting region were used for analysis. For each system, 10 statistically independent replicas were generated, each consisting of an initial $5 \times 10^4\tau$ to establish the stationary state, followed by production runs of equal length, between 10-30$\times 10^4\tau$.

Equilibrium simulations

Equilibrium molecular dynamics (EMD) simulations of the mixtures were performed in the NVT ensemble. A cubic simulation cell of length $L \approx 56.05\sigma$ containing 10^4 rods was used. The temperature was controlled by the Nosé-Hoover chain thermostat, with 3 chains, and a time constant of

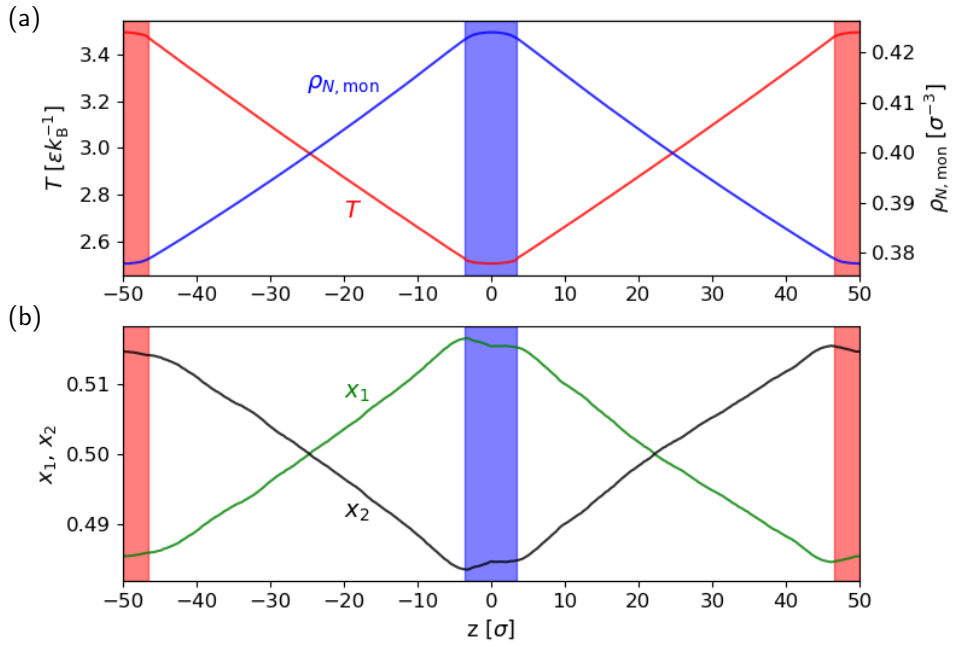


FIGURE 4.2: Representative (a) temperature T and monomer number density $\rho_{N,\mathrm{mon}}$ profiles, and (b) mole fraction, x_1 and x_2, profiles for the NEMD simulations. The blue (cold) and red (hot) indicate the location of the thermostatting regions in the simulation cell. The profiles correspond to the $(I_1 = I_2, d_1, d_2) = (80m\sigma^2, 2.7\sigma, 0)$ mixture.

10τ. Sampling consisted of 10-30 replicas for each system; each replica was equilibrated for 10^3 τ followed by 2×10^4 τ of production.

Simulations of the pure fluid (same particle model, but with the mass distribution given by $m_i = m$ for all monomers) in the NPT ensemble were performed to determine the phase coexistence diagram. These simulations used cubic cells with 3×10^4 molecules. Temperature (pressure) was controlled using a Nosé-Hoover chain thermostat (barostat), with 3 chains, and a time constant of 1τ (10τ). To ensure that hysteresis effects[21] were not significant, two replicas were performed for each (P, T) state point; only systems where the S_2 order parameter (see Sec. 4.3.1) of the two replicas agreed to within their statistical uncertainties were included. Along each isobar, the two replicas were generated using upward (downward) branches starting from a low-density isotropic (high-density nematic) system, with gradually decreasing (increasing) temperature. Each replica consisted of 0.4-12$\times 10^4$ τ of equilibration starting from a nearby state point, followed by a 2×10^4 τ production run.

4.2.3 Transport properties from simulations

The Soret coefficient S_T was evaluated from the NEMD simulations at the zero-mass-flux ($\boldsymbol{J}_1 = 0$) stationary state as

$$S_T = -\left(\frac{1}{w_1 w_2}\frac{\nabla w_1}{\nabla T}\right)_{\boldsymbol{J}_1=0} = -\left(\frac{1}{x_1 x_2}\frac{\nabla x_1}{\nabla T}\right)_{\boldsymbol{J}_1=0} \tag{4.7}$$

where x_i and w_i are the mole and mass fractions of component i. The local gradients ∇T and ∇x_1 were determined by fitting a straight line to their profiles within a range of $\pm 10\sigma$ around the selected state point at $T = 3.0\epsilon k_\mathrm{B}^{-1}$. Verification of linear response is given in Appendix C.1.

The mutual diffusion coefficient D_{12} was calculated from

$$D_{12} = \frac{L_{11}}{\rho(1-w_1)T}\left(\frac{\partial \mu_{s,1}}{\partial w_1}\right)_{P,T} \tag{4.8}$$

where $\mu_{s,1}$ is the specific chemical potential of component 1. For ideal mixtures, such as the isotopic mixtures considered here with the same intermolecular interactions between different components,[22]

$$\left(\frac{\partial \mu_{s,1}}{\partial w_1}\right)_{P,T} = \frac{k_\mathrm{B}T}{w_1[M_1 - w_1(M_1 - M_2)]}. \tag{4.9}$$

The phenomenological coefficients L_{11} were calculated using the Green-Kubo integral formula

$$L_{11} = \frac{V}{3k_\mathrm{B}} \lim_{t'\to\infty} \int_0^{t'} \langle \boldsymbol{J}_1(t) \cdot \boldsymbol{J}_1(0)\rangle dt \tag{4.10}$$

where V is the volume of the simulation cell, and the factor of 3 in the denominator averages the contributions from each spatial dimension. The mass flux is given by

$$\boldsymbol{J}_1 = \frac{1}{V}\sum_{i=1}^{N_1}\sum_{j=1}^{7} m_{j,i}\boldsymbol{v}_{j,i} \tag{4.11}$$

where $\boldsymbol{v}$ is the velocity, and the sum runs over all 7 monomers of the N_1 molecules of species 1. Eq. 4.10 was evaluated from the equilibrium-NVT simulations using a correlation time of $t' = 500\tau$ for the upper limit of the integral, which is sufficient for well-converged integrals (see Appendix C.3).

Unlike in Chapter 3, the thermal diffusion coefficient D_T could not be evaluated from equilibrium simulations using the Green-Kubo approach. Owing to the rigid body constraint forces, reliable per-particle virial stress tensor-based instantaneous heat fluxes could not be obtained, even when using the recently derived centroid formulation[23,24] (and using only the x component[a]). The formulation of instantaneous heat flux in rigid body dynamics has long been established.[26]

[a] Due to an implementation detail in LAMMPS the y and z components of the heat flux for rigid bodies are highly unphysical and should not be used.[25]

Further work is required to implement this capability in LAMMPS. Instead, D_T was calculated from $D_T = S_T D_{12}$. This approach relies on the fact that finite-size effects associated with S_T from NEMD and D_{12} from equilibrium-NVT simulations, are small and additionally cancel. It has recently been shown that the hydrodynamic correction of Yeh and Hummer [27] for self-diffusion coefficients can also be applied to D_{12}.[28] This correction amounts to an increase in D_{12}, D_1 and D_2 of $< 4\%$ (Appendix C.4), which is smaller than the uncertainties associated with D_{12}, S_T and therefore D_T. Regarding S_T from NEMD, extrapolating the simulation cell lengths $L_x = L_y \to \infty$ decreases S_T by $\sim 4\%$ (Appendix C.2). Thus, finite-size effects in S_T and D_{12} are expected to at least partially cancel when calculating D_T. This is because finite-size effects in $S_T \equiv D_T/D_{12}$ include those from D_{12}; based on our finite-size analysis of D_{12} and S_T, we expect finite-size effects of $\sim 1\%$ in D_T, which is smaller than its associated uncertainties. Thus, we use and report the uncorrected D_{12}, D_1 and D_2 values, which give more internally consistent values for S_T, D_{12} and D_T. We note that using the infinite-size D_{12}, D_1 and D_2 does not change any of the qualitative trends reported in this work (Appendix C.4).

Self-diffusion coefficients were calculated using the Einstein relation (Appendix C.4). Rotational diffusion coefficients and shear viscosities were calculated from their Green-Kubo equations using an upper integration limit of 200τ and 500τ, respectively (Appendix C.3). As with D_{12}, these transport properties were calculated from equilibrium-NVT simulations that use a global Nosé-Hoover chain thermostat. Global thermostats have been shown to give transport properties that are statistically indistinguishable from those of the NVE ensemble.[20] Especially given the weak coupling strength (large time constant), the thermostat is not expected to significantly affect the correlation functions and transport properties calculated in this work.

4.3 Results and Discussion

All statistical uncertainties reported in this work refer to the 95% confidence interval of the mean, unless stated otherwise.

4.3.1 Equation of state and phase diagram

The simulated fluid exhibits an isotropic-nematic phase transition, and we are interested in the behaviour of the mixtures in the isotropic phase. Choosing the aspect ratio of the molecules is a compromise: the maximum mass dipole achievable is determined by the length N of the shish-kebab molecule, but the nematic phase is shifted to lower volume fractions for greater aspect ratios. It is therefore necessary to map out the phase coexistence diagram to determine which thermodynamic conditions correspond to the isotropic phase.

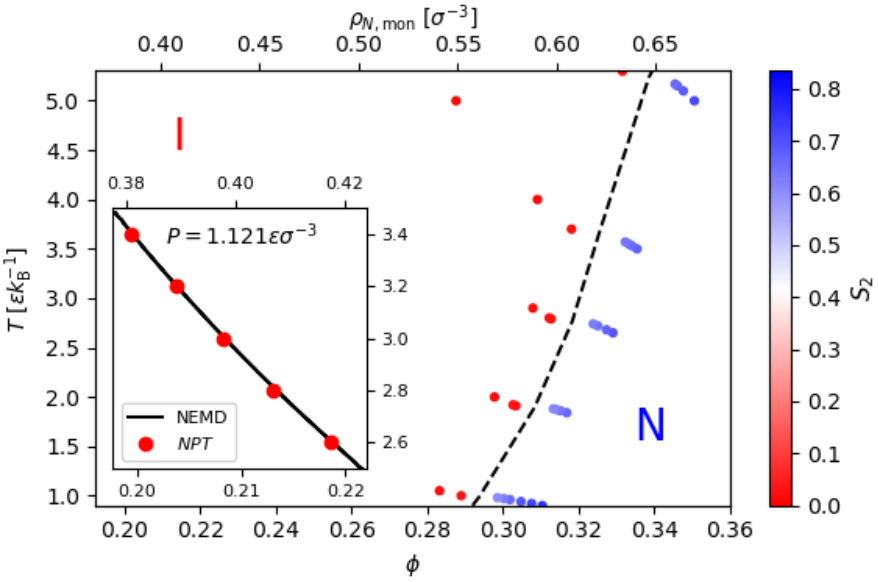


FIGURE 4.3: Phase diagram and equation of state (EOS). T, $\rho_{N,\mathrm{mon}}$ and ϕ are the temperature, monomer number density and volume fraction, respectively. The data is colour coded according to the uniaxial (orientational) order parameter S_2. The dashed isotropic-nematic coexistence line is to guide the eye. The inset shows the EOS at pressure $P = 1.121\epsilon\sigma^{-3}$, as predicted by equilibrium-NPT and NEMD simulations. Symbols: I=isotropic; N=nematic.

The uniaxial orientational order parameter S_2 is zero for an isotropic fluid and unity for a perfectly aligned system. S_2 is the ensemble average of the largest positive eigenvalue P_2 of the $\boldsymbol{Q}$ tensor

$$\boldsymbol{Q}_{\alpha\beta} = \frac{1}{N_m}\sum_{i=1}^{N_m}\left(\frac{3}{2}\hat{\boldsymbol{u}}_{i,\alpha}\hat{\boldsymbol{u}}_{i,\beta} - \frac{1}{2}\delta_{\alpha\beta}\right), \quad \alpha,\beta = x,y,z \tag{4.12}$$

$$S_2 = \langle P_2(\boldsymbol{n}\cdot\hat{\boldsymbol{u}})\rangle = \langle P_2(\cos\theta_n)\rangle = \frac{3}{2}\langle\cos\theta_n\rangle - \frac{1}{2} \tag{4.13}$$

where the director $\boldsymbol{n}$ is the eigenvector associated with P_2, and $\hat{\boldsymbol{u}} = \hat{\boldsymbol{u}}_d$ is the unit vector along the long molecular axis. Numerical data for the estimated isotropic-nematic coexistence temperatures and upper/lower bounds on the coexistence densities are given in Appendix C.5.

The phase diagram of the pure fluid is shown in Fig. 4.3. In classical systems, ensemble averages over thermodynamic observables are independent of the mass and mass distribution of the particles, and the phase diagram is therefore applicable to the isotopic mixtures under equilibrium conditions. All the NEMD simulations correspond to thermodynamic conditions, $T \geq 2.0\ \epsilon k_B^{-1}$ and $\phi < 0.24$, that are safely within the isotropic region of the phase diagram. Each set of NEMD profiles corresponds to the equation of state (EOS) at the simulated pressure, as defined by the component (P_{zz}) parallel to the heat flux vector. The inset of Fig. 4.3 shows the that NEMD simulations reproduce the equilibrium EOS at $P = 1.121\epsilon\sigma^{-3}$, and therefore that local equilibrium is fulfilled.

4.3.2 Mass dipole contribution and its microscopic origin

In this section we consider mixtures with $I = I_1 = I_2$ but $d_1 \neq d_2$, for which all current models of thermal diffusion predict $S_T = 0$ (see, e.g., the reviews Refs. 29–33 and the references contained therein). Fig. 4.4(a)(i)&(b)(i) contains the main result of this work: mixtures with components that differ only by their mass dipole have non-zero Soret coefficients. The mole fraction profiles for one such mixture is shown in Fig. 4.2, providing clear evidence for species separation in the thermal field. In all cases, $S_T > 0$ which indicates that the species with the greater mass dipole is thermophobic and preferentially collects in the cold region. Assigning an interaction strength typical of simple molecular fluids, $\epsilon/k_\mathrm{B} = 10^2$ K, gives S_T =1-15$\times 10^{-3}$ K^{-1} at $T = 300$ K ($T = 3.0\ \epsilon k_\mathrm{B}^{-1}$) for the mass dipole contribution. This is of comparable magnitude to the entire (pseudo-)isotopic Soret effect in many molecular mixtures.[5–7]

We probe the phenomenology of $S_T \equiv D_T/D_{12}$ by considering the thermal diffusion coefficient D_T and mutual diffusion coefficient D_{12}. As shown in Fig. 4.4(a)(iii), D_{12} decreases with increasing I for mixtures with $I = I_1 = I_2$ and $d_2 = 0$, but is essentially constant with d_1. Furthermore, the constant value of D_{12} determined by fitting to the $D_{12}(d_1; I = 80m\sigma^2, d_2 = 0)$ data accurately predicts the D_{12} values for mixtures with $d_2 \neq 0$ as well (Fig. 4.4(b)(iii)), indicating that D_{12} does not significantly depend on either mass dipole, d_1 or d_2, at least relative to the statistical uncertainties associated with the data.

With regards to D_T, all the data for the $I = I_1 = I_2$ and $d_2 = 0$ mixtures can be accurately described by a power law dependence $D_T = a(d_1 - d_2)^k$ (Fig. 4.4(a)(ii)), indicating that D_T is only weakly dependent on the moment of inertia. The exponent $k = k_{d_2=0} = 1.6 \pm 0.1$ was determined by fitting the equation $\ln D_T = k \ln(d_1 - d_2) + \ln a$ to the $d_2 = 0$ data (see Appendix C.6). Considering mixtures with $d_2 \neq 0$, fits to the equation $D_T = a(d_1 - d_2)^{k_{d_2=0}}$ accurately reproduces the simulation data (Fig. 4.4(b)(ii)). Thus, the effect of changing d_2 while keeping $d_1 - d_2$ constant can be captured by the prefactor a, which increases with increasing d_2, as shown explicitly in the inset of Fig. C.8 in Appendix C.6.

Finally, we return to S_T, which we predict with the equation

$$S_T[d_1, d_2, I = I_1 = I_2] = \frac{D_T[d_1, d_2]}{D_{12}[I]} = \frac{a(d_1 - d_2)^k}{c_I[I]} \tag{4.14}$$

where $k = k_{d_2=0}$ describes the whole data set, and a and c_I were determined by the fits to D_T and D_{12}, respectively. We show in Fig. 4.4(a)(i)&(b)(i) that Eq. 4.14 accurately predicts S_T, and captures its weak dependence on I, which can be discerned for large values of $d_1 - d_2$, as shown in the inset of Fig. 4.4(a)(i).

We additionally calculate D_{12} using the Darken approximation $D_\mathrm{MS} \approx D_\mathrm{MS}^\mathrm{Darken} = x_2 D_1 + x_1 D_2$ where D_MS is the Maxwell-Stefan diffusion coefficient, related to the Fickian D_{12} via $D_{12} = \Gamma D_\mathrm{MS}$,

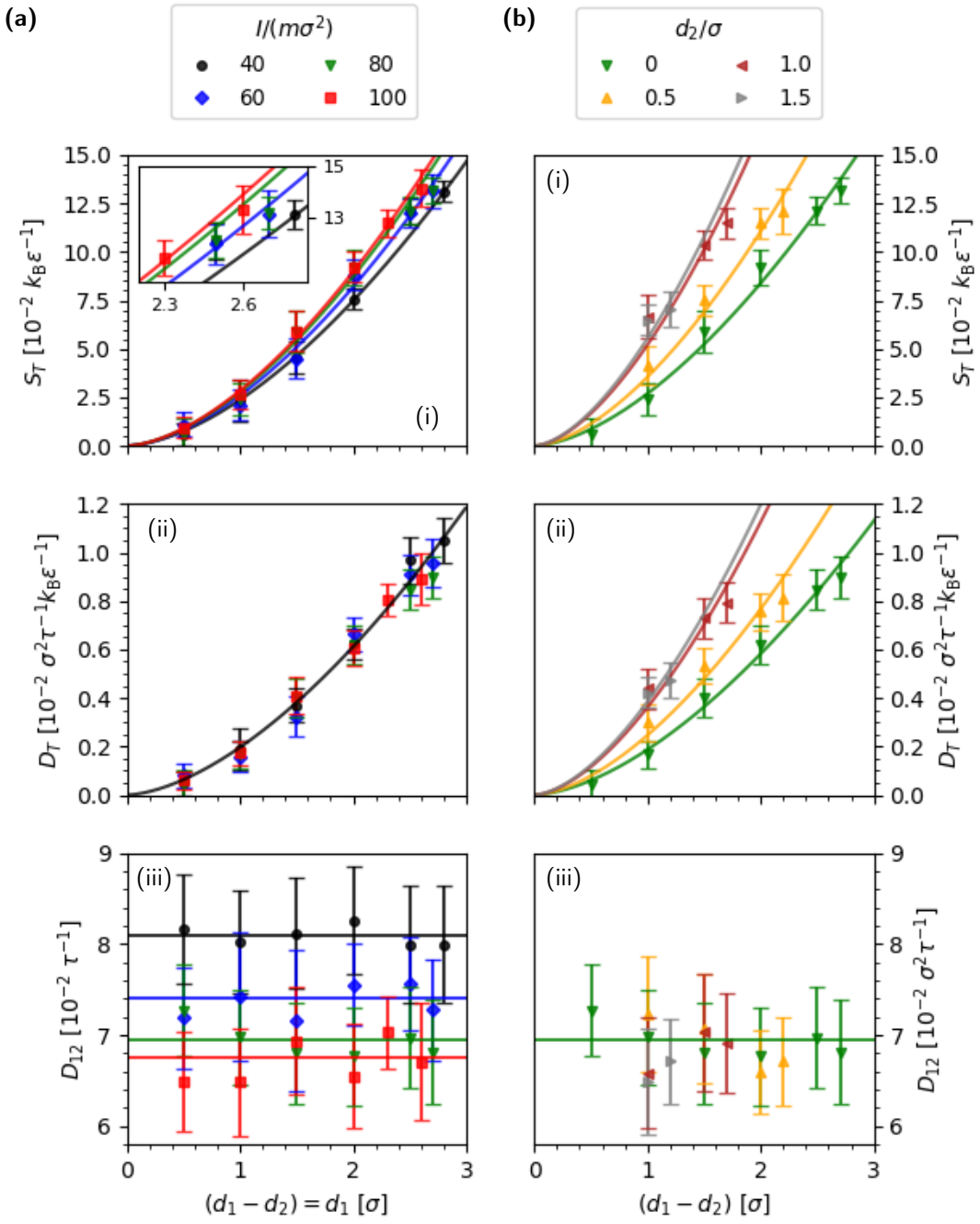


FIGURE 4.4: Transport coefficients for the isotopic mixtures with: (a) $I = I_1 = I_2$ and $d_2 = 0$; and (b) $I = I_1 = I_2 = 80m\sigma^2$ and $d_1 \neq d_2$. The (i) Soret coefficient, (ii) thermal diffusion coefficient D_T and (iii) mutual diffusion coefficient D_{12}, as a function of $d_1 - d_2$. d_i and I_i are the mass dipole and moment of inertia of species $i = 1, 2$, respectively. The solid lines show equations that model the data: see the main text for details.

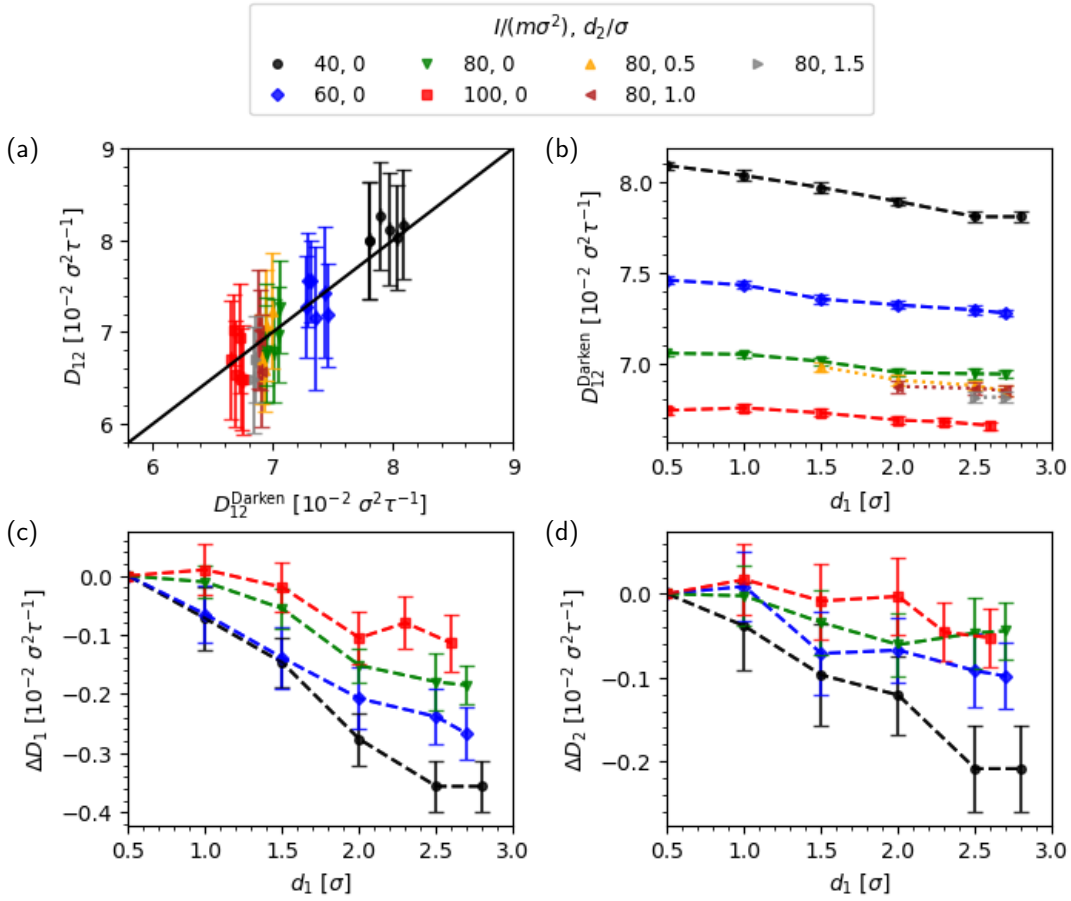


FIGURE 4.5: (a) The mutual diffusion coefficient D_{12} *vs.* the Darken approximation D_{12}^{Darken}. (b) D_{12}^{Darken}, (c) ΔD_1 and (d) ΔD_2 as a function of the mass dipole, d_1, of species 1. $\Delta D_i = D_i - D_i(d_1 = 0.5\sigma)$ is the change in self-diffusion coefficient D_i of species $i = 1, 2$ relative to the corresponding mixture with $d_1 = 0.5\sigma$.

where Γ is the thermodynamic factor ($\Gamma = 1$ for the ideal mixtures considered here). The Darken approximation D_{12}^{Darken} predicts values in excellent agreement with the (non-approximate) D_{12} values (Fig. 4.5(a)), indicating that displacement cross-correlations between particles do not play an important role in determining D_{12}. Thus, the behaviour of D_{12} can be rationalized in terms of the self-diffusion coefficients D_1 and D_2. As shown in Fig. 4.5(b), D_{12}^{Darken} features a weak but discernible dependence on d_1 (and therefore $d_1 - d_2$), which was masked by the greater uncertainties associated with D_{12} calculated from the Green-Kubo integral formula. D_1 and D_2 also depend weakly on the mass dipole d_1 (Fig. 4.5(c)&(d)). Unsurprisingly, the impact of d_1 on D_1 is greater than on D_2, with $\Delta D_1/\Delta D_2$ ~1-4, where $\Delta D_i = D_i(d_1) - D_i(d_1 = 0.5\sigma)$. Thus the weak dependence of D_{12} on the mass dipoles d_1 and d_2 can be primarily attributed to the effect of d_i on D_i. (See Appendix C.4 for additional data on the diffusion coefficients and related quantities).

The mass dipole also affects the rotational diffusion of the rod-like molecules. We show in

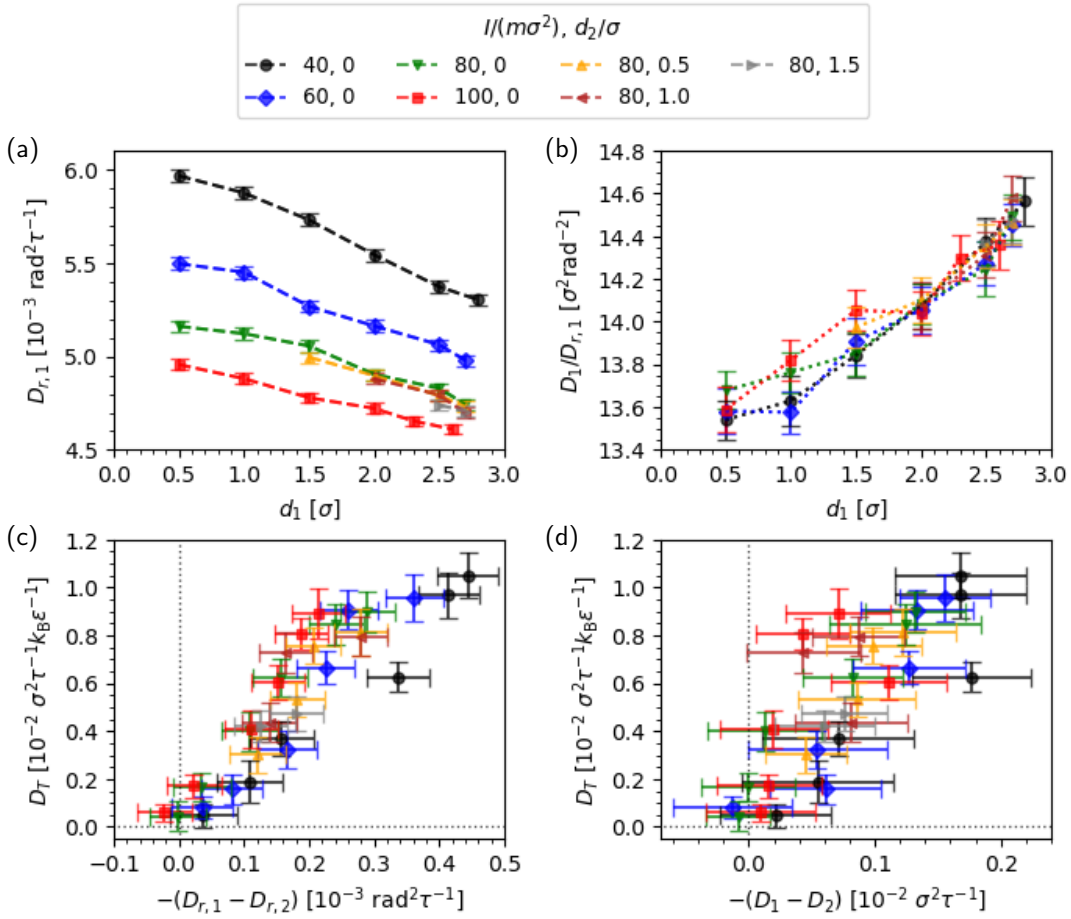


FIGURE 4.6: Rotational and translational diffusion coefficients, and their correlation with the thermal diffusion coefficient D_T. (a) $D_{r,1}$ as a function of the mass dipole d_1 of species 1. (b) The ratio $D_1/D_{r,1}$ as a function of d_1. (c) D_T *vs.* $-(D_{r,1}-D_{r,2})$. (d) D_T *vs.* $-(D_1-D_2)$. $D_{r,i}$ and D_i are the rotational and translational diffusion coefficients, respectively, of species $i=1,2$.

Fig. 4.6(a) that the rotational diffusion coefficient $D_{r,1}$ decreases with increasing mass dipole d_1. $D_{r,i}$ is the rotational diffusion coefficient of species $i=1,2$. The rotational diffusion coefficient decreases with increasing moment of inertia, as expected. The translational and rotational diffusion coefficients are coupled, with $15 > (D_i/D_{r,i})/(\sigma^2\text{rad}^{-2}) > 13$ for all the mixtures considered in this section. As shown in Fig. 4.6(b), the ratio $D_1/D_{r,1}$ increases with the mass dipole d_1, but is statistically independent of I within the statistical uncertainties of our data. We note that comparing to previous simulations[34] of systems of the same WCA shish-kebab model but at the different temperature $T=1\ \epsilon k_B^{-1}$, the ($N=7$, $\rho_{N,m}=0.0568\ \sigma^{-3}$) state point studied in this work is expected to be in the semidilute regime, where the translational and rotational diffusion are known to be coupled[35].

We conclude from Fig. 4.4 that the Soret coefficient depends on the mass dipoles mainly through D_T. We show in Fig. 4.6(c)&(d) that D_T is positively correlated with the differences in rotational

diffusion coefficients, $-(D_{r,1} - D_{r,2})$, and translational diffusion coefficients, $-(D_1 - D_2)$. We expect the rotational correlation reflects librational modes that influence the thermal transport and therefore D_T.

Hence, to probe the microscopic mechanism associated with librational modes, and its dependence on the molecular internal degrees of freedom, we calculate the power spectra of various velocity autocorrelation functions (VACFs). We consider the "all-atom" VACF, C_{atom}, as well as the rotational and translational centre-of-mass VACFs of the rigid molecules, C_{rot} and C_{trans}, respectively:

$$C_{\text{atom}}(t) = \frac{\langle \boldsymbol{v}_i(t) \cdot \boldsymbol{v}_i(0) \rangle}{\langle v_i^2(0) \rangle} \tag{4.15}$$

$$C_{\text{rot}}(t) = \frac{\langle \boldsymbol{\omega}_j(t) \cdot \boldsymbol{\omega}_j(0) \rangle}{\langle \omega_j^2(0) \rangle} \tag{4.16}$$

$$C_{\text{trans}}(t) = \frac{\langle \boldsymbol{v}_{\text{COM},j}(t) \cdot \boldsymbol{v}_{\text{COM},j}(0) \rangle}{\langle v_{\text{COM},j}^2(0) \rangle} \tag{4.17}$$

where $\boldsymbol{v}_i$ is the velocity of monomer i, $\boldsymbol{\omega}_j$ is the angular velocity of rigid molecule j, $v_{\text{COM},j}$ is the centre-of-mass velocity of rigid molecule j, and t is the elapsed time from an arbitrary starting time. The power spectrum is then given by the Fourier transform of the corresponding VACF:

$$I_X(\nu) = \lim_{t' \to \infty} \int_{-t'}^{t'} C_X(t) e^{-i2\pi\nu t} dt \tag{4.18}$$

where I_X is the intensity and ν is the frequency.

The power spectra of species 1 in the $I = I_1 = I_2 = 80m\sigma^2$ and $d_2 = 0$ mixtures are shown in Fig. 4.7. For large mass dipoles, I_{atom} features a peak at $\sim 0.5\tau^{-1}$ indicative of a librational mode. Increasing the mass dipole increases the frequency of the librational mode. This librational mode is also reflected in I_{rot}. For low mass dipoles, a single peak is observed at $\sim$0.2-0.3τ^{-1}, which contains contributions from both the libration and a lower frequency mode. Upon increasing d, the librational mode is blue-shifted and two distinct peaks are observed.

In order to disentangle contributions from the different modes, we fit the rotational power spectra I_{rot} using the equations:

$$I_{\text{fit}} = I_{\text{L}} + I_{\text{DHO}} \tag{4.19}$$

$$I_{\text{L}} = \frac{a_{\text{L}}}{1 + \left(\frac{\nu - \nu_{\text{L}}}{c_{\text{L}}}\right)^2} \tag{4.20}$$

$$I_{\text{DHO}} = \frac{D\gamma}{(\nu_0^2 - \nu^2)^2 + \gamma^2\nu^2} \tag{4.21}$$

where the Lorentzian-like function I_{L} captures the low frequency peak at $\nu \sim 10^{-2}\tau^{-1}$. In spectroscopy, librations are typically modelled as damped harmonic oscillators (DHO). In Eq. 4.21 for

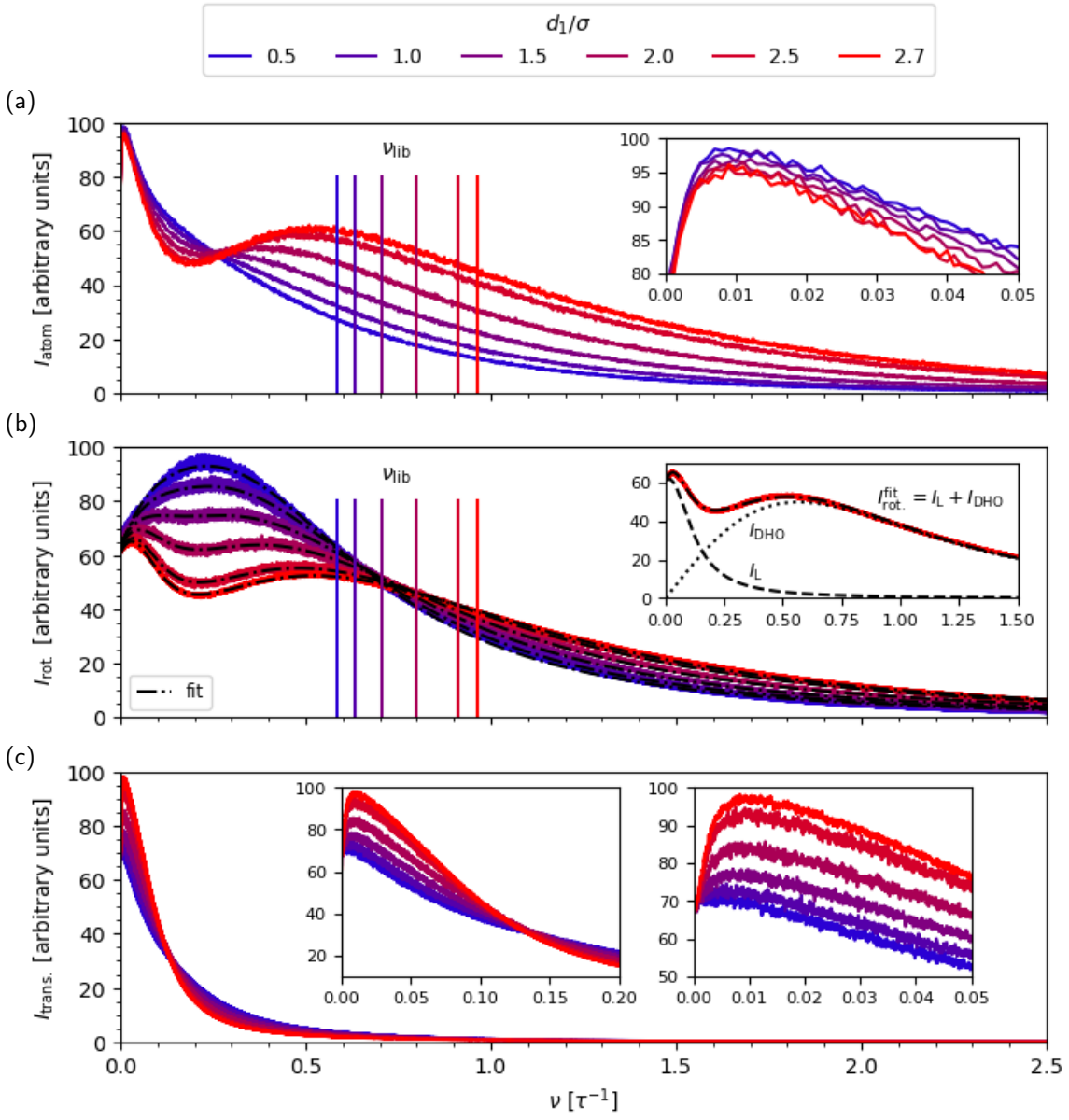


FIGURE 4.7: Power spectra of species 1 of the $(I_1 = I_2, d_1, d_2) = (80m\sigma^2, d_1, 0)$ mixtures. The intensity I_X *vs.* frequency ν for the (a) "all-atom" (I_{atom}) (b) rotational (I_{rot}) and (c) translational centre-of-mass (I_{trans}) power spectra. In (a) and (b), the vertical solid lines show the librational mode frequencies ν_{lib}. In (b), the dash-dot (-.) lines denote the fitted spectra I_{fit} and the inset shows the individual fitted functions for the $(I_1 = I_2, d_1, d_2) = (80m\sigma^2, 2.7\sigma, 0)$ mixture.

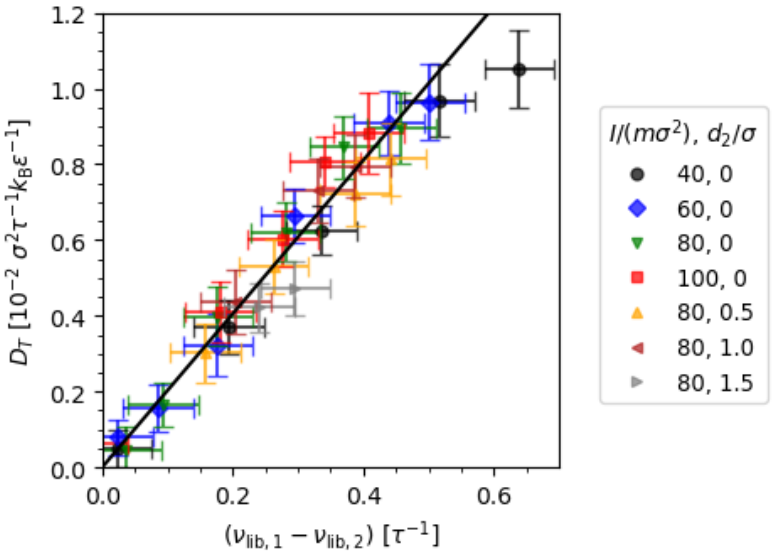


FIGURE 4.8: Thermal diffusion coefficient D_T as a function of $\nu_{\text{lib},1} - \nu_{\text{lib},2}$, where $\nu_{\text{lib},i}$ is the librational frequency of species i. The solid line shows the fit to $D_T = b(\nu_{\text{lib},1} - \nu_{\text{lib},2})$. Error bars correspond to maximum/minimum values based on the sensitivity of the fitting procedure for Eqs. 4.19,4.20&4.21.

the DHO, D is the oscillator intensity constant, γ is the damping constant, and ν_0 is its frequency (band position). Using the $I = I_1 = I_2 = 80m\sigma^2$ and $d_2 = 0$ mixtures as an example, we show in Fig. 4.7(b) that fitting Eq. 4.19 accurately reproduces I_{rot}. Extracting the librational frequencies $\nu_{\text{lib}} = \nu_0$ from the fits, it is evident that ν_{lib} increases with d_1 (Fig. 4.7).

In Fig. 4.8 we show that D_T is highly correlated with the difference in librational frequencies of species 1 ($\nu_{\text{lib},1}$) and species 2 ($\nu_{\text{lib},2}$). The effect of the mass dipole on ν_{lib} can be large; we observe $\nu_{\text{lib},1} - \nu_{\text{lib},2}$ values of up to $\sim 100\%$ of $\nu_{\text{lib},2}$. We fit the data to the equation $D_T = b(\nu_{\text{lib},1} - \nu_{\text{lib},2})$, demonstrating a direct proportionality relationship with D_T. Given their statistical uncertainties, all data points agree with the fitting except for the $(I_1 = I_2, d_1, d_2) = (40m\sigma^2, 2.8\sigma, 0)$ mixture, which corresponds to the greatest $\nu_{\text{lib},1} - \nu_{\text{lib},2}$ value of all the mixtures considered in this section. This suggests that D_T may saturate at sufficiently large $\nu_{\text{lib},1} - \nu_{\text{lib},2}$ values, beginning from $\sim 0.5\tau^{-1}$. We conclude that the librational frequency is sensitive to the mass dipole, and that the mass dipole contribution to D_T is highly correlated with the modification of the librational mode, and therefore short-time dynamics of the rod-like molecules.

4.3.3 Coupling with the moment of inertia contribution

In this section, we examine how the mass dipoles affect the Soret coefficient of mixtures with non-zero moment of inertia contributions. We consider mixtures with components that differ only in

their moments of inertia ($I_1 \neq I_2$, $d_1 = d_2$), with I_1, I_2 =10-270 $m\sigma^2$ and ratios I_1/I_2 =1-27, then mixtures with $I_1 \neq I_2$ and $d_1 \neq d_2$.

First we consider the simplest case of mass-symmetric molecules: $I_1 \neq I_2$ and $d_1 = d_2 = 0$. The Soret coefficients for these mixtures are shown in Fig. 4.9(a)&(b). In all cases $S_T > 0$, indicating that the component with the greater moment of inertia (species 1) is thermophobic. For molecular mixtures, the pseudo-isotopic Soret effect is usually modelled by the empirical equation

$$S_T = S_T^{\text{chem}} + S_T^{\text{iso}} = S_T^{\text{chem}} + a_M \frac{M_1 - M_2}{M_1 + M_2} + b_I \frac{I_1 - I_2}{I_1 + I_2} \tag{4.22}$$

where S_T^{iso} was originally taken by analogy to the description of gaseous mixtures,[1,8,36] and adjusted for liquids by the prefactors a_M and b_I.[9,30] For the mixtures considered here, Eq. 4.22 reduces to

$$S_T = b_I \frac{I_1 - I_2}{I_1 + I_2} \tag{4.23}$$

which is also retrieved from the theoretical model[37] of Villain-Guillot and Würger (derived by considering velocity fluctuations in a hard-bead model with elastic collisions) when setting $M_1 = M_2$. As shown in Fig. 4.9(a), Eq. 4.23 is in relatively good agreement with our simulation results. However, it is unable to predict all data points within their associated uncertainties. Previous simulations of binary isotopic mixtures of Lennard-Jones dumbbells with I_1/I_2 =1-40 have shown very good agreement with the moment of inertia contribution given by Eq. 4.23.[38,39] These simulations did not account for the mass dipole, but this contribution is likely to be small with $d_1 - d_2 \leq 1\sigma$ for the dumbbells. More generally, Eq. 4.22 has been able to accurately model the experimental Soret coefficients of relatively low molecular mass non-polar mixtures[5] and isotope mixtures[5,8–12]. However $M_1 + M_2$ and $I_1 + I_2$ in these mixtures were almost constant; the terms in Eq. 4.22 could also be written in terms of absolute differences $M_1 - M_2$ and $I_1 - I_2$. Indeed, Wittko and Köhler found that the isotopic substitution C_6H_{12} to C_6D_{12} results in a constant shift in S_T, irrespective of the nature of the other component.[6] This trend is not reproduced by Eq. 4.22. Thus, we also fit our simulation data to

$$S_T = b_I (I_1 - I_2) \tag{4.24}$$

which similarly reproduces the S_T values relatively well, as shown in Fig. 4.9(b).

We emphasize that Eqs. 4.23 & 4.24 are empirical equations, and how accurately they model the moment of inertia contribution must be considered on a case-by-case basis for each mixture. Additionally, b_I is typically fit simultaneously with multiple other coefficients,[5,6] making it difficult to isolate the moment of inertia term. Isotopic substitution changes both the mass and inertia of a molecule. Thus, even for isotopic mixtures, the moment of inertia must be considered together with the total mass (and the mass dipole). Only recently, in simulations of isotopic mixtures

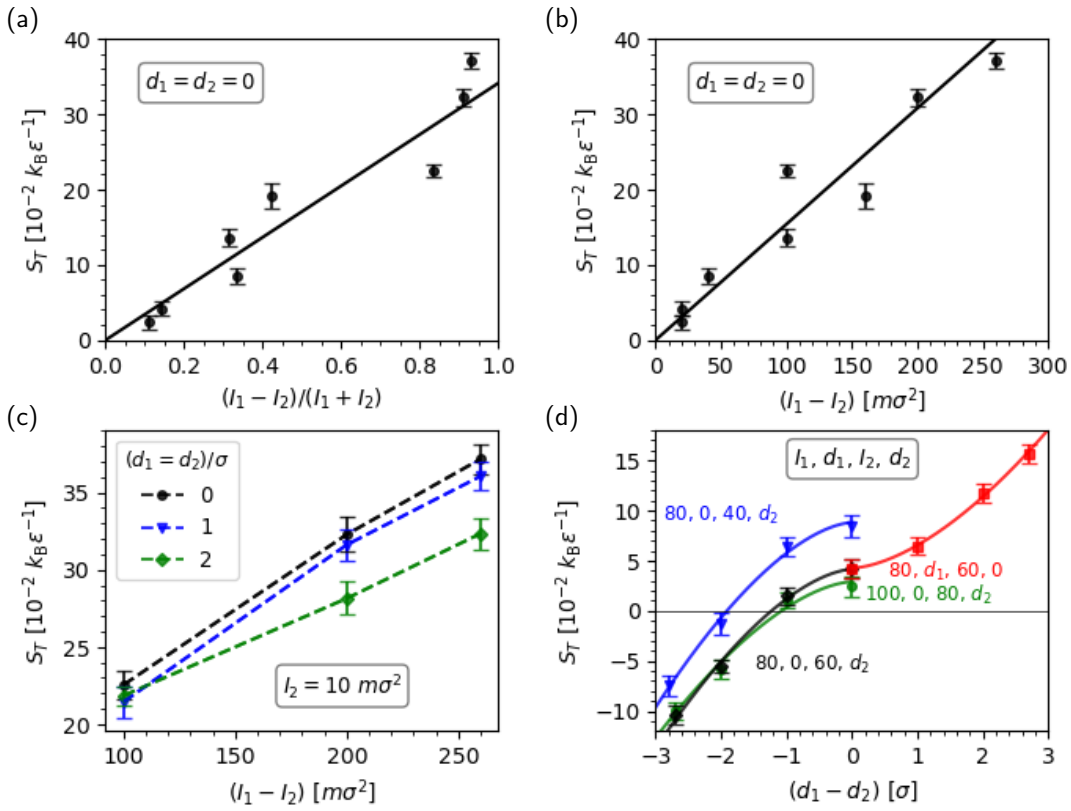


FIGURE 4.9: The Soret coefficient S_T as a function of: (a) the relative $(I_1 - I_2)/(I_1 + I_2)$ and (b) absolute $(I_1 - I_2)$ differences in moment of inertia I_i of species $i = 1, 2$ for mixtures with mass dipoles $d_1 = d_2 = 0$; (c) $(I_1 - I_2)$ for mixtures with $d_1 = d_2$; and (d) $(d_1 - d_2)$ for mixtures with (I_1, d_1, I_2, d_2). In (d), the solid lines show fits to Eq. 4.25, and the label units for I_i and d_i are $m\sigma^2$ and σ, respectively.

of Lennard-Jones dumbbells with $M_1 = M_2$, has the moment of inertia contribution been studied independently from total mass contribution.[39] The shish-kebab model used in this work allows us to isolate the moment of inertia contribution from both the total mass and mass dipole contributions.

Next we consider mixtures with $I_1 \neq I_2$ and $d_1 = d_2 \neq 0$. As shown in Fig. 4.9(c), increasing $d_1 = d_2$ while holding I_1 and $I_2 = 10m\sigma^2$ constant decreases S_T, and this decrease is more pronounced when I_1 (i.e., $I_1 - I_2$) and S_T are larger. In terms of its relative magnitude, S_T decreases by $\sim 15\%$ when increasing $d_1 = d_2$ from 0 to 2σ for the entire $100 \leq (I_1 - I_2)/(m\sigma^2) \leq 260$ range (15% is comparable to the uncertainties for $I_1 - I_2 = 100m\sigma^2$). This demonstrates that the moment of inertia contribution is coupled with the mass dipole, even when $d_1 = d_2$.

Finally we consider mixtures with $I_1 \neq I_2$ and $d_1 \neq d_2$. As shown in Fig. 4.9(d), S_T can be tuned by the mass dipoles d_1 and d_2 when holding I_1 and I_2 constant. In all cases, S_T increases with $d_1 - d_2$, and the mass dipole contribution can both enhance or compete with the moment of inertia contribution. All current models of thermal diffusion predict that when the components differ by only their internal mass distribution, the component with the greater moment

of inertia is thermophobic ($S_T > 0$). Crucially, we demonstrate that by increasing $-(d_1 - d_2)$, the competing mass dipole contribution causes a reversal in sign of S_T, and species 1 ($I_1 > I_2$) becomes thermophilic ($S_T < 0$), or can lead to inhibition of thermal diffusion ($S_T = 0$).

Following from the power law dependence of the mass dipole contribution (Eq. 4.14) described in Sec. 4.3.2, we model the $I_1 \neq I_2$ and $d_1 \neq d_2$ mixtures using the equation

$$S_T = a(d_1 - d_2)|d_1 - d_2|^{k-1} + c_I \tag{4.25}$$

where $k = k_{d_2=0} = 1.6 \pm 0.1$ as determined in Sec. 4.3.2. The prefactor a accounts for the strength of the mass dipole contribution including the coupling with the moments of inertia, while the constant $c_I(I_1, I_2)$ represents only the inertia contribution. As shown in Fig. 4.9(d), Eq. 4.25 is in excellent agreement with our simulation data; all data points agree to within their statistical uncertainties. a depends on both I_1 and I_2, indicating that the mass dipole contribution is coupled with the moments of inertia.

4.3.4 An empirical equation for the isotopic Soret effect

In this section we propose an empirical equation for the isotopic Soret effect that includes the mass dipole contribution. Building on the success of equations of the form $S_T^{\text{iso}} = S_T^M(M_1, M_2) + S_T^I(I_1, I_2)$ for modelling experimental[5,6,8–12,40] and simulation[38] data, we assume that contributions from the different moments of the mass distribution are only weakly coupled, and seek an equation of the form

$$S_T^{\text{iso}}(M_1, M_2, d_1, d_2, I_1, I_2) = S_T^M(M_1, M_2) + S_T^d(d_1, d_2) + S_T^I(I_1, I_2) \tag{4.26}$$

All mixtures considered in this work correspond to $M_1 = M_2$ and thus $S_T^M = 0$. However, we note that $S_T^M \propto (M_1 - M_2)/(M_1 + M_2)$, $S_T^M \propto (M_1 - M_2)$ and $S_T^M \propto -(M_1^{-1} - M_2^{-1})$ have been used to model a range of molecular mixtures.[5–7,40] For S_T^d we propose

$$S_T^d(d_1, d_2) = (a_1 d_s + a_2)(d_1 - d_2)|d_1 - d_2|^{k-1} \tag{4.27}$$

where $d_s = \min\{d_1, d_2\}$ is the smaller mass dipole, a_1 and a_2 are constants, and $k = k_{d_2=0} = 1.6 \pm 0.1$ as determined in Sec. 4.3.2. The $(a_1 d_s + a_2)$ term stems from the observation that a in Eq. 4.14 is approximately linear with d_s ($d_2 = d_s$ for the $I_1 = I_2$ mixtures considered in Sec. 4.3.2), as evident from the inset of Fig. C.8(b) in Appendix C.6. For S_T^I we test both Eq. 4.23 (model A) and Eq. 4.24 (model B). Thus for the isotopic mixtures studied in this work the empirical equations

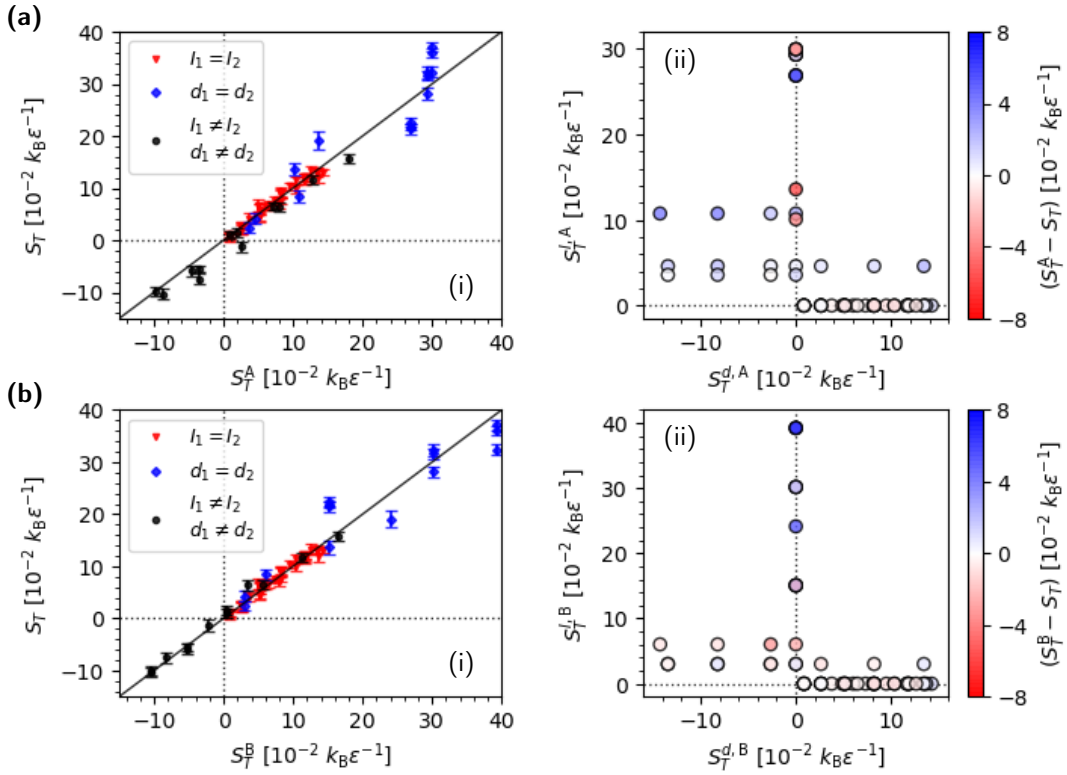


FIGURE 4.10: Empirical models (a) A (Eq. 4.28) and (b) B (Eq. 4.29) for the isotopic Soret effect. (i) S_T *vs.* S_T^{X} for model $\mathrm{X} = \mathrm{A}, \mathrm{B}$, where S_T^{X} and S_T are the predicted and reference (simulated) Soret coefficients, respectively. (ii) The error $S_T^{\mathrm{X}} - S_T$ as a function of the mass dipole contribution $S_T^{d,\mathrm{X}}$ and moment of inertia contribution $S_T^{I,\mathrm{X}}$ of model $\mathrm{X} = \mathrm{A}, \mathrm{B}$. Data are colour coded according to the error $S_T^{\mathrm{X}} - S_T$.

are: model A,

$$S_T^{\mathrm{A}} = S_T^d(d_1, d_2) + b_I \frac{I_1 - I_2}{I_1 + I_2} \tag{4.28}$$

and model B,

$$S_T^{\mathrm{B}} = S_T^d(d_1, d_2) + b_I(I_1 - I_2) \tag{4.29}$$

For the mass dipole contribution S_T^d, the parameters a_1 and a_2 were fit using only the $I_1 = I_2$ mixtures. Analogously, for the moment of inertia contribution S_T^I, the parameters b_I were fit using only the $d_1 = d_2$ mixtures. The ($I_1 \neq I_2$, $d_1 \neq d_2$) mixtures were not used in the fitting procedure, and $S_T^{\mathrm{X=A,B}}$ values for these mixtures are therefore true predictions.

We show in Fig. 4.10 that both models are in relatively good agreement with our simulation data. For the $d_1 = d_2$ mixtures, $S_T^{\mathrm{X}} = S_T^I$ have *maximum* absolute errors (MAEs) of 7.2×10^{-2} $k_B\epsilon^{-1}$ and 7.6×10^{-2} $k_B\epsilon^{-1}$ for models A and B, respectively. These are ~ 4 times greater than the MAE of 1.8×10^{-2} $k_B\epsilon^{-1}$ for the $I_1 = I_2$ mixtures, for which $S_T^{\mathrm{X}} = S_T^d$. Thus, Eqs 4.28 & 4.29 more accurately model the mass dipole contribution compared to the moment

of inertia contribution. For the ($I_1 \neq I_2$, $d_1 \neq d_2$) mixtures, models A and B have MAEs of $4.0 \times 10^{-2}\ k_B\epsilon^{-1}$ and $3.0 \times 10^{-2}\ k_B\epsilon^{-1}$, respectively. We note that while a full range of mass dipoles ($d_i \leq 3$ for this particle model) has been explored, the simulated ($I_1 \neq I_2$, $d_1 \neq d_2$) mixtures correspond to a more limited range of moments of inertia (see Fig. 4.9(d)). Using the same range of (I_1, I_2) as the $d_1 = d_2$ mixtures would presumably result in higher MAEs for the ($I_1 \neq I_2$, $d_1 \neq d_2$) mixtures. For the mixtures studied in this work, the accuracy of the empirical models are limited by the (in)accuracy of the S_T^I term, rather than the assumption that the moments of the mass distribution are uncoupled.

Next we consider the validity of the weak coupling approximation. As shown in Fig. 4.4(a)(iii), D_{12} increases (S_T decreases) by $\sim 20\%$ when decreasing $I = I_1 = I_2$ from $100m\sigma^2$ to $40m\sigma^2$, which corresponds to the largest change in the mass dipole contribution due to the coupling with the moments of inertia. The a_1 and a_2 coefficients in S_T^d (Eq. 4.27) include an average over the effect of I on D_{12}; we therefore expect a maximum error of $\sim 10\%$ in S_T^d due to the coupling with I_1 and I_2. With regards to the moment of inertia contribution (as discussed in Sec. 4.3.3), S_T decreases by $\sim 15\%$ when increasing $d_1 = d_2$ from 0 to 2σ for the ($I_2 = 10m\sigma^2$, $d_1 = d_2$) mixtures. Extrapolating this result to the entire range of mass dipoles $d_i \leq 3\sigma$ and moments of inertia, $I_i \leq 260m\sigma^2$, we expect coupling effects in S_T^I of $\lesssim 30\%$ for the mixtures considered in this work.

4.3.5 Thermal orientation

The molecules with $d_i \neq 0$ exhibit thermal orientation[41] (TO): they adopt an average orientation with respect to the heat flux vector, quantified by $\langle \cos\theta_i \rangle = \hat{\boldsymbol{u}}_{d,i} \cdot \hat{\boldsymbol{u}}_{J_q}$ for species $i = 1, 2$, where $\hat{\boldsymbol{u}}_{d,i}$ and $\hat{\boldsymbol{u}}_{J_q}$ are the unit vectors in the directions of the mass dipole and heat flux, respectively. Representative $\langle \cos\theta_{z,i} \rangle = \hat{\boldsymbol{u}}_{d,i} \cdot \hat{\boldsymbol{z}}$ profiles from the NEMD simulations are shown in Fig. 4.11(a). In all cases, $\langle \cos\theta_i \rangle \geq 0$, indicating that on average the mass dipole points towards the hot source (i.e., the heavy side points towards the cold source). This is consistent with simulations of mass-asymmetric diatomic molecules, for which the heavier atom preferentially orients towards the cold source,[41] and follows the trend in the isotopic Soret effect of binary mixtures where the heavier component migrates towards the cold source (assuming the components are otherwise identical). As shown in Fig. 4.11(b)(i), $\langle \cos\theta_1 \rangle / |\nabla T|$ increases then begins to saturate with d_1. Holding d_1 constant, $\langle \cos\theta_1 \rangle / |\nabla T|$ increases with decreasing $I = I_1 = I_2$. $\langle \cos\theta_1 \rangle / |\nabla T|$ also depends on d_2, as demonstrated for the $I = 80m\sigma^2$ mixtures, increasing d_2 decreases $\langle \cos\theta_1 \rangle / |\nabla T|$. However, the effects of I and d_2 on $\langle \cos\theta_1 \rangle$ are an order of magnitude smaller than its dependence on d_1.

Does thermal orientation have an effect on the Soret coefficient? Based on the general formalism of linear non-equilibrium thermodynamics[22] (LNET), as a coupling effect, it does. We will show in

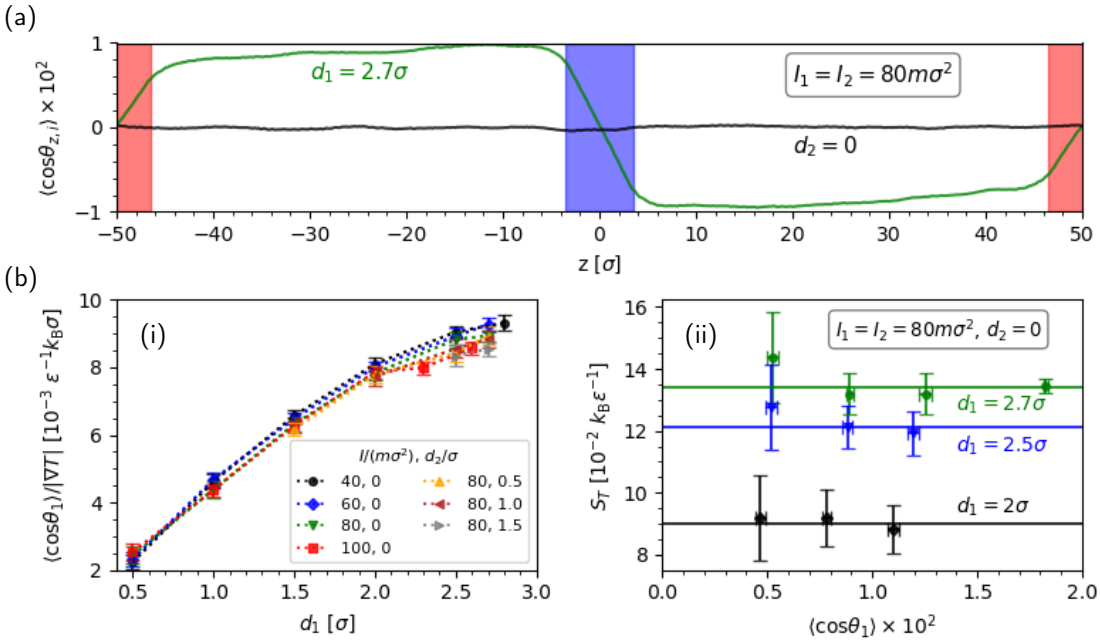


FIGURE 4.11: Thermal orientation of the rod-like molecules. (a) The average orientation $\langle \cos\theta_{z,i} \rangle$ of species $i = 1, 2$ as a function of position z in the NEMD simulations. The blue (cold) and red (hot) indicate the location of the thermostatting regions in the simulation cell. The profiles correspond to the same system shown in Fig. 4.2. (b) Average orientation $\langle \cos\theta_1 \rangle$ of species 1 for different mixtures: (i) $\langle \cos\theta_1 \rangle / |\nabla T|$ *vs.* the mass dipole d_1; (ii) the Soret coefficient S_T *vs.* $\langle \cos\theta_1 \rangle$ for different temperature gradients ∇T.

Chapter 5 that for rigid rod-like colloids in the dilute regime, the TO effect decreases $S_T = D_T/D$ primarily by increasing the diffusion coefficient D of the colloid. TO also impacts the Soret coefficient of Janus particles.[15] However, we show in Fig. 4.11(b) that, for the molecular mixtures studied here, the effect of TO is smaller than the uncertainties associated with our S_T data. As exemplified by three different mixtures, S_T does not show a significant dependence on $\langle \cos\theta_i \rangle$. (For each mixture, greater/smaller $|\langle \cos\theta_i \rangle|$ values were achieved by increasing/decreasing ∇T in additional NEMD simulations; see Appendix C.1 for details). The $|\langle \cos\theta \rangle / \nabla T|$ values observed in this work and in other[41] molecular fluids are ∼2-3 orders of magnitude smaller than those observed in the colloidal regime[13,15]. This suggests that TO effects large enough to significantly impact S_T may be more difficult to achieve in molecular mixtures. However, we will show in Chapter 6 that thermal polarization, which emerges from the thermal orientation of polar molecules, can give rise to measurable electrostatic fields in molecular fluids. As a coupling effect, it leads to a reduction in the thermal conductivity of the polar fluid, as described by LNET.[42] Thermal polarization can play an important role in determining the thermoelectric response of aqueous solutions.[43] The impact of thermal polarization on the thermal diffusion of polar molecular mixtures remains an open question.

4.4 Conclusions

We have uncovered the mass dipole contribution to the isotopic Soret effect, showing that mixtures of components that differ only by the first moment of their mass distributions can have non-zero Soret coefficients. All current models of thermal diffusion describe the isotopic contribution S_T^{iso} in terms of only the total mass (the zeroth moment) and moments of inertia (the second moment) of the components. Our results demonstrate that other moments of the mass distribution must be included for a complete description of the (pseudo-)isotopic Soret effect in fluid mixtures.

For the isotopic mixtures of rigid linear molecules examined in this work, the dependence of S_T on the mass dipole arises mainly through the thermal diffusion coefficient D_T. In turn, D_T is correlated with both long-time dynamics—differences in rotational and translational diffusion coefficients, and short-time dynamics—the modification of a librational mode. Regarding the latter, greater mass dipoles give rise to higher frequency librations (of frequency ν_{lib}) with changes of up to 100%, and we find that $D_T \propto \nu_{\text{lib},1} - \nu_{\text{lib},2}$. Through the self-diffusion coefficients $D_{i=1,2}$, the mutual diffusion coefficient D_{12} features a very weak dependence of the mass dipoles, which can be attributed primarily to the effect of d_i on D_i. However, D_{12} does depend significantly on the moment of inertia, which together with $D_T(d_1, d_2)$, affects how S_T varies with the mass dipoles. Indeed, in mixtures with $d_1 \neq d_2$ and $I_1 \neq I_2$, the mass dipole contribution depends on both moments of inertia.

The mass dipole contribution can both enhance or compete with the moment of inertia contribution, giving rise to new phenomenology. For example, it is possible to design isotopic mixtures with $M_1 = M_2$ where the component with a greater moment of inertia is thermophilic. Additionally, the moment of inertia contribution depends on the mass dipoles, even when $d_1 = d_2$ and the mass dipole contribution vanishes. Our results show that changes in the internal mass distribution can be used to tune S_T, including its sign and the thermophilicity of the components.

Building on the success of previous empirical models, we show that the mass dipole contribution can be incorporated as an additional additive contribution to the (pseudo-)isotopic Soret effect. This approach is valid when the contributions are only weakly coupled. For the mixtures considered in this work, the weak coupling assumption leads to estimated errors of $\lesssim 10\%$ and $\lesssim 30\%$ for the mass dipole and moment of inertia contributions, respectively. Indeed, the accuracy of the models are limited by the (in)accuracy of the moment of inertia term rather than the weak coupling assumption. Overall, the proposed empirical equations reproduce our simulation data well.

Our work highlights the importance of internal degrees of freedom, such as the mass dipole, in determining the thermodiffusion response of binary mixtures. Further work is required to assess the magnitude of the mass dipole contribution in other molecular mixtures, and determine how it affects the phenomenology of these mixtures under the influence of thermal fields.

Bibliography

[1] R. C. Jones and W. H. Furry, *Rev. Mod. Phys.*, 1946, **18**, 151–224.

[2] S. Chapman and W. Hainsworth, *The London, Edinburgh, and Dublin Philosophical Magazine and Journal of Science*, 1924, **48**, 593–607.

[3] K. Clusius and G. Dickel, *Naturwiss.*, 1938, **26**, 546.

[4] W. H. Furry, R. C. Jones and L. Onsager, *Phys. Rev.*, 1939, **55**, 1083–1095.

[5] C. Debuschewitz and W. Köhler, *Phys. Rev. Lett.*, 2001, **87**, 055901.

[6] G. Wittko and W. Köhler, *J. Chem. Phys*, 2005, **123**, 014506.

[7] B. Pur, W. Köhler and K. I. Morozov, *J. Chem. Phys.*, 2020, **152**, 054501.

[8] J. Schirdewahn, A. Klemm and L. Waldmann, *Z. Naturforsch. A*, 1961, **16**, 133–144.

[9] W. M. Rutherford, *J. Chem. Phys.*, 1984, **81**, 6136–6139.

[10] W. M. Rutherford, *J. Chem. Phys.*, 1987, **86**, 5217.

[11] W. M. Rutherford, *J. Chem. Phys.*, 1987, **86**, 397–399.

[12] W. M. Rutherford, *J. Chem. Phys.*, 1989, **90**, 602–603.

[13] J. Olarte-Plata, J. M. Rubi and F. Bresme, *Phys. Rev. E*, 2018, **97**, 052607.

[14] O. R. Gittus, J. D. Olarte-Plata and F. Bresme, *Eur. Phys. J. E.*, 2019, **42**, 90.

[15] F. Bresme, J. D. Olarte-Plata, A. Chapman, P. Albella and C. Green, *Eur. Phys. J. E*, 2022, **45**, 59.

[16] T. F. Miller, M. Eleftheriou, P. Pattnaik, A. Ndirango, D. Newns and G. J. Martyna, *J. Chem. Phys.*, 2002, **116**, 8649–8659.

[17] H. Kamberaj, R. J. Low and M. P. Neal, *J. Chem. Phys.*, 2005, **122**, 224114.

[18] A. P. Thompson, H. M. Aktulga, R. Berger, D. S. Bolintineanu, W. M. Brown, P. S. Crozier, P. J. in 't Veld, A. Kohlmeyer, S. G. Moore, T. D. Nguyen, R. Shan, M. J. Stevens, J. Tranchida, C. Trott and S. J. Plimpton, *Comp. Phys. Comm.*, 2022, **271**, 108171.

[19] D. D. Daub, A. Per-Olof and F. Bresme, *Phys. Chem. Chem. Phys.*, 2014, **16**, 22097–22106.

[20] J. E. Basconi and M. R. Shirts, *J. Chem. Theory Comput.*, 2013, **9**, 2887–2889.

[21] A. Kowaguchi, P. E. Brumby and K. Yasuoka, *Molecules*, 2021, **26**, year.

[22] S. R. de Groot and P. Mazur, *Non-Equilibrium Thermodynamics*, Dover, 1984.

[23] D. Surblys, H. Matsubara, G. Kikugawa and T. Ohara, *Phys. Rev. E*, 2019, **99**, 051301.

[24] D. Surblys, H. Matsubara, G. Kikugawa and T. Ohara, *J. Appl. Phys.*, 2021, **130**, 215104.

[25] LAMMPS Development Team, *LAMMPS Documentation (accessed: 1st July 2022)*, https://docs.lammps.org/compute_heat_flux.html.

[26] D. J. Evans and S. Murad, *Mol. Phys.*, 1989, **68**, 1219–1223.

[27] I.-C. Yeh and G. Hummer, *J. Phys. Chem. B*, 2004, **108**, 15873–15879.

[28] S. H. Jamali, L. Wolff, T. M. Becker, A. Bardow, T. J. H. Vlugt and O. A. Moultos, *J. Chem. Theory Comput.*, 2018, **14**, 2667–2677.

[29] W. Köhler and K. I. Morozov, *J. Non-Equilib. Thermodyn.*, 2016, **41**, 151–197.

[30] D. Niether and S. Wiegand, *J. Phys.: Condens. Matter*, 2019, **31**, 503003.

[31] S. Wiegand, *J. Phys.: Condens. Matter*, 2004, **16**, R357–R379.

[32] P.-A. Artola and B. Rousseau, *Mol. Phys.*, 2013, **111**, 3394–3403.

[33] M. Eslamian and M. Z. Saghir, *J. Non-Equilib. Thermodyn.*, 2009, **34**, 97–131.

[34] D. M. Heyes, *J. Chem. Phys.*, 2019, **150**, 184503.

[35] M. Doi and S. F. Edwards, *The Theory of Polymer Dynamics*, Clarendon Press, 1986.

[36] J. M. Kincaid, E. G. D. Cohen and M. López de Haro, *J. Chem. Phys.*, 1987, **86**, 963–975.

[37] S. Villain-Guillot and A. Würger, *Phys. Rev. E*, 2011, **83**, 030501.

[38] G. Galliero, B. Duguay and J. Caltagirone, *Fluid Phase Equilib.*, 2003, **208**, 171–188.

[39] Hoang, Hai and Galliero, Guillaume, *Eur. Phys. J. E*, 2022, **45**, 42.

[40] S. Hartmann, W. Köhler and K. I. Morozov, *Soft Matter*, 2012, **8**, 1355–1360.

[41] F. Römer, F. Bresme, J. Muscatello, D. Bedeaux and J. M. Rubí, *Phys. Rev. Lett.*, 2012, **108**, 105901.

[42] F. Bresme, A. Lervik, D. Bedeaux and S. Kjelstrup, *Phys. Rev. Lett.*, 2008, **101**, 020602.

[43] S. Di Lecce and F. Bresme, *J. Phys. Chem. B*, 2018, **122**, 1662–1668.

Chapter 5

Thermophoresis and thermal orientation of anisotropic colloids

5.1 Introduction

In Chapters 3 and 4 we saw how temperature gradients induce mass transport in molecular mixtures. An analogous effect is observed in colloidal suspensions: thermal fields rectify the Brownian motion of colloids, which move either towards the hot or cold sources. This phenomenon, called thermophoresis, has been a matter of intense investigation in recent years. It is now well established that the thermophoretic drift of colloids varies with the colloid-solvent interactions, ionic strength and colloid properties, such as size, mass, moment of inertia or charge.[1–4] Consequently, the Soret effect has been exploited to manipulate mixtures of nanoscopic particles and biomolecules.[4–10] Notwithstanding these advances, it remains difficult to predict whether a colloid will be thermophobic or thermophilic at a specific temperature or composition of the solution.

The thermophoretic response of axially symmetric, elongated particles has previously been studied in aerosols and suspensions, using kinetic theory[11] and hydrodynamic simulations[12]. These works concluded that freely rotating colloids undergo an anisotropic thermophoresis, with non-vanishing Soret coefficients in the direction perpendicular to the temperature gradient. Recently, it was shown that the internal degrees of freedom of particles can couple with thermal fluxes, inducing a preferred orientation in a molecular fluids (e.g., in Chapter 4) and colloids.[13–15] This thermal orientation (TO) effect opens new avenues to manipulate anisotropic colloids in solution. Colloids and nanoparticles can possess much larger mass dipoles (mass anisotropy) and aspect ratios (shape anisotropy) compared to molecules, and therefore one might expect that much stronger orientation effects can be achieved in these materials.

In this chapter, we connect the thermal orientation and thermophoresis of rod-like colloids in the dilute regime. Using both theory and simulation, we show how the Soret coefficient of these

colloids can be tuned by their internal mass distributions. The analysis in this chapter was done in collaboration with Juan D. Olarte-Plata.

5.2 Theoretical model

In this section, we derive equations that relate the Soret coefficient S_T of the colloid to its internal mass distribution. (In Sec. 5.4.3 this objective is furthered by directly linking S_T with the average orientation.) The orientation of the colloid w.r.t. the thermal field is defined by $\cos\theta = \hat{\boldsymbol{u}}_c \cdot \hat{\boldsymbol{u}}_{J_q}$, where the unit vectors $\hat{\boldsymbol{u}}_c$ and $\hat{\boldsymbol{u}}_{J_q}$ are the direction of the colloid and heat flux, respectively (see Fig. 5.1). We start with the framework introduced in Ref. 15, where the TO effect was modelled using the von Mises probability distribution. In that work, the interaction between the colloid and the thermal field is described by the potential well

$$\mathcal{V}_E(\theta) = -\frac{k_E}{2}\cos(\theta - \theta_0) \tag{5.1}$$

which is a minimum when the colloid reaches mechanical equilibrium at the preferred orientation θ_0. The curvature of the potential about the minimum is defined by the force constant k_E. The normalized probability distribution for the colloid adopting a given angle θ is given by the von Mises distribution on the half circle:

$$p(\theta) = \frac{\exp\big(\kappa\cos(\theta - \theta_0)\big)}{\pi I_0(\kappa)} \tag{5.2}$$

where $\kappa = k_E/(2k_BT)$ and I_0 is the modified Bessel function of first kind. Once the probability distribution is known, the average over property $\mathcal{A}(\theta)$ can be calculated from

$$\langle\mathcal{A}\rangle = \frac{\int_0^\pi \mathcal{A}(\theta)\sin\theta p(\theta)\,\mathrm{d}\theta}{\int_0^\pi \sin\theta p(\theta)\,\mathrm{d}\theta} \tag{5.3}$$

where $\sin\theta$ is the angular weighting factor that follows from the Jacobian in spherical coordinates. The solution to Eq. 5.3 for $\mathcal{A} = \cos\theta$ and $\theta_0 = \pi$ is the negative of the well-known Langevin function $\mathcal{L}(\kappa)$:

$$\langle\cos\theta\rangle = -\mathcal{L}(\kappa) = \frac{1}{\kappa} - \coth\kappa \tag{5.4}$$

To obtain an equation for the Soret coefficient, we consider a colloid with a constant drift velocity $\boldsymbol{v}$ such that it experiences equal and opposite thermophoretic, $\boldsymbol{F}_T$, and friction, $\boldsymbol{F}_\zeta = -\zeta\boldsymbol{v}$, forces: $\boldsymbol{F}_T + \boldsymbol{F}_\zeta = 0$. ζ is the friction coefficient of the colloid. Decomposing (in the body frame of

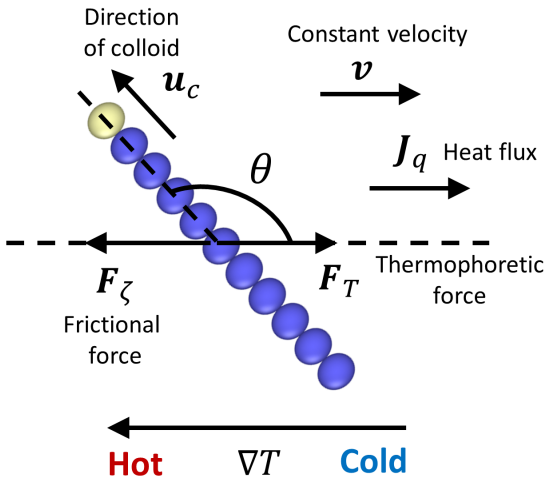


FIGURE 5.1: Free body diagram of the anisotropic colloid in a thermal field.

reference) the component of the drifting velocity and frictional force in the direction of heat flux, v_{J_q} and F_{ζ,J_q} respectively, into parallel and perpendicular components leads to:

$$v_\parallel = v_{J_q}\cos\theta \tag{5.5}$$

$$v_\perp = v_{J_q}\sin\theta \tag{5.6}$$

$$F_\parallel = -\zeta_\parallel v_{J_q}\cos\theta \tag{5.7}$$

$$F_\perp = -\zeta_\perp v_{J_q}\sin\theta \tag{5.8}$$

$$\begin{aligned} F_{\zeta,J_q}(\theta) &= F_\parallel\cos\theta + F_\perp\sin\theta \\ &= -\zeta_\parallel v_{J_q}\cos^2\theta - \zeta_\perp v_{J_q}\sin^2\theta = -\zeta(\theta)v_{J_q} \end{aligned} \tag{5.9}$$

$$\implies \zeta(\theta) = \zeta_\parallel\cos^2\theta + \zeta_\perp\sin^2\theta \tag{5.10}$$

where we have obtained an expression for the friction coefficient ζ in terms of the angle θ of the colloid w.r.t. the thermal field. Using Eq. 5.3 the average friction coefficient $\langle\zeta\rangle = \zeta_\parallel\langle\cos^2\theta\rangle + \zeta_\perp\langle\sin^2\theta\rangle$ is given by

$$\langle\zeta\rangle = \zeta_\parallel\left(\frac{\kappa^2 - 2\kappa\coth\kappa + 2}{\kappa^2}\right) + \zeta_\perp\left(\frac{2\kappa\coth\kappa - 2}{\kappa^2}\right) \tag{5.11}$$

For no net orientation, given by the limit $\kappa \to 0$, we recover the well-known[16] friction coefficient of a rigid rod:

$$\langle\zeta_{\text{sym}}\rangle = \frac{1}{3}\zeta_\parallel + \frac{2}{3}\zeta_\perp \tag{5.12}$$

where $\langle\zeta_{\text{sym}}\rangle$ is the average friction coefficient of the *mass*-symmetric colloid.

It has been shown in previous work[14] that the Soret coefficient of mass-symmetric rods varies with the colloid mass M according to $S_T \propto (M - m_s)/(M + m_s)$, where m_s is the mass of a

solvent molecule. This equation is similar to the equation derived from kinetic theory for mixtures of elastic spheres interacting through r^{-12} repulsive potentials.[17,18] Here, we assume that the thermal diffusion coefficient D_T follows a similar dependence with the colloid/solvent mass ratio,

$$D_T = B\left(\frac{M - m_s}{M + m_s}\right) + C \tag{5.13}$$

where B and C are constants. It has been assumed in Eq. 5.13 that D_T does not depend on the orientation of the colloid. Advancing the discussion below, we find that this assumption leads to equations that accurately reproduce our simulations results.

Combining Eqs. 5.11 and 5.13, and using the Einstein-Smoluchowski relation for the diffusion coefficient, $D = k_\mathrm{B}T/\zeta$, we arrive at the following expression for the Soret coefficient $S_T = D_T/D$ in terms of the von Mises parameter κ:

$$S_T = \frac{1}{k_\mathrm{B}T}\left[B\left(\frac{M - m_s}{M + m_s}\right) + C\right]\left[\zeta_\perp\left(\frac{2\kappa\coth\kappa - 2}{\kappa^2}\right) + \zeta_\parallel\left(\frac{\kappa^2 - 2\kappa\coth\kappa + 2}{\kappa^2}\right)\right] \tag{5.14}$$

In Sec. 5.4.2, we simplify this equation further for the specific case of the shish-kebab model, and test its accuracy against data obtained from simulations.

5.3 Methods

We investigated the response of rod-like colloids with varying degrees of mass asymmetry. The colloids were modelled using the shish-kebab model, i.e., a rigid chain of tangent spheres of diameter σ. Asymmetric mass distributions were achieved by varying the position and mass m_a of a single bead, dubbed the “asymmetric" bead, while all other beads had a mass m equal to the mass of the solvent m_s. The degree of mass asymmetry in this model is quantified through the mass dipole $d \cdot \boldsymbol{u}_c = \boldsymbol{r}_\mathrm{com} - \boldsymbol{r}_g$, where $\boldsymbol{r}_\mathrm{com}$ is the centre of mass of the colloid and $\boldsymbol{r}_g$ is its geometric centre. For this particular model (see Fig. 5.2(b)), the mass dipole of a colloid composed of N particles can be written as

$$d = a\frac{\gamma - 1}{N + \gamma - 1}\sigma \tag{5.15}$$

where $\gamma = m_a/m$ and $a = 0, 1, ..., (N-1)/2$ is the position of the asymmetric bead when N is odd. We show in Fig. 5.2(a) the mass dipole as a function of the mass ratio, γ, and position, a, for a colloid of size $N = 11$.

Boundary-driven non-equilibrium molecular dynamics (NEMD) simulations of a colloid suspended in a particle-based fluid at infinite dilution were carried out using LAMMPS[19] (v. 11 Aug. 2017). The fluid was modelled at an average number density $\rho_{N,s} = 1.0\sigma^{-3}$ characteristic

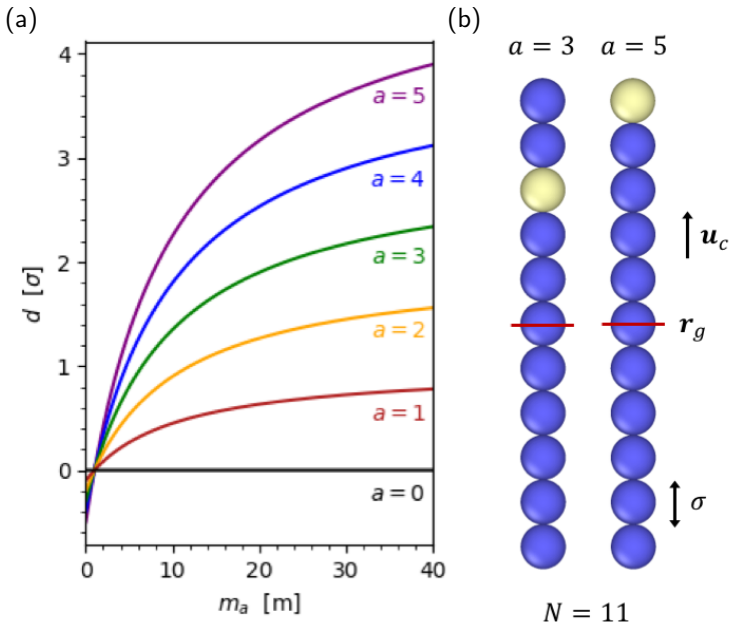


FIGURE 5.2: The shish-kebab model. (a) Range of mass dipoles d as a function of the mass m_a of the single asymmetric bead at position a. (b) Graphical representations of colloids with $a = 3$ and $a = 5$. The bead of mass m_a is shown in yellow.

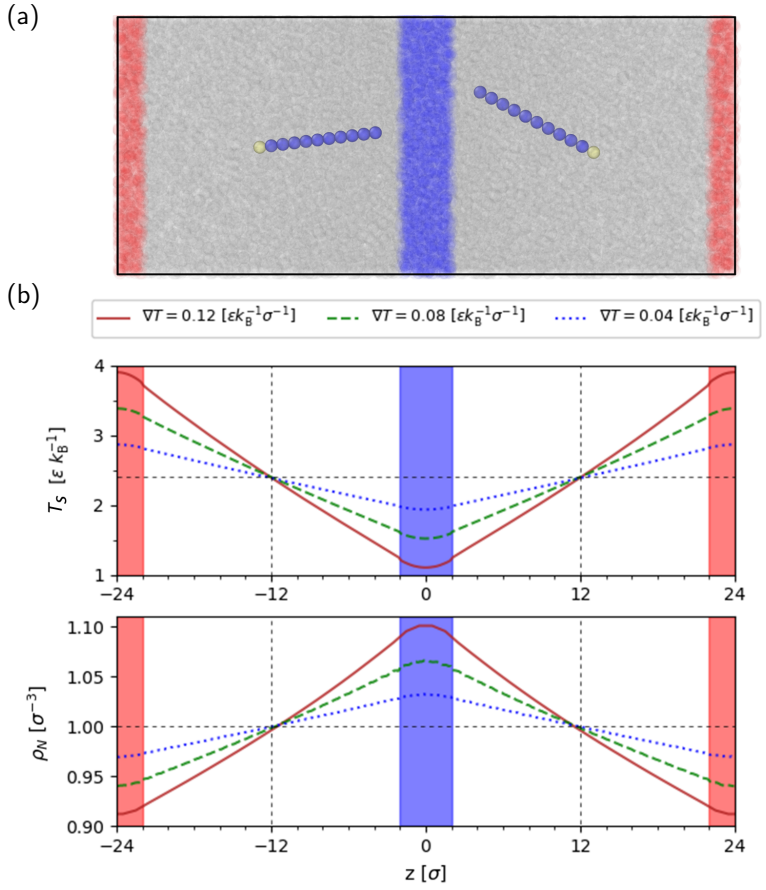


FIGURE 5.3: Simulation methodology. (a) Snapshot of the simulation setup for a colloid with with $a = 5$. (b) Representative solvent temperature T_s (top) and number density $\rho_{N,s}$ (bottom) profiles for different temperature gradients ∇T. Thermostatting regions are shaded red (hot) and blue (cold).

of a liquid. A simulation cell of dimensions $(L_x, L_y, L_z) = (20, 20, 48)\sigma$ was used. Thermostatting regions of width 4σ were located in the edges and centre of the simulation cell (see Fig. 5.3). A temperature gradient was established by applying the simple velocity rescaling algorithm to solvent particles in the hot and cold regions, while ensuring linear momentum conservation. A colloid particle was placed in the centre $\boldsymbol{r}_c$ of each compartment, its centre of mass tethered using a harmonic potential $\mathcal{V}_r(\boldsymbol{r}) = k_r(\boldsymbol{r}_{\mathrm{com}} - \boldsymbol{r}_c)^2/2$, with a force constant $k_r = 2 \times 10^3\ \epsilon\sigma^{-2}$. 3D periodic boundary conditions were applied.

All inter-particle interactions were modelled using the WCA potential

$$\mathcal{V}_{\mathrm{WCA}}(r) = \begin{cases} 4\epsilon\left[\left(\frac{\sigma}{r}\right)^{12} - \left(\frac{\sigma}{r}\right)^{6}\right] + \epsilon, & \text{if } r \leq 2^{1/6}\sigma \\ 0, & \text{if } r > 2^{1/6}\sigma \end{cases} \tag{5.16}$$

where r is the distance between two particles and ϵ represents the strength of the purely repulsive pair-wise interaction. The equations of motion of the solvent particles were integrated using the velocity Verlet algorithm, while the translational and rotational degrees of freedom of the colloids were integrated using the method of quaternions for rigid bodies.[20] A timestep of $\delta t = 0.0025\tau$ was used. 20-120 statistically independent replicas were performed for each system. Each replica consisted of an initial 50τ to establish the stationary state followed by $5 \times 10^4\tau$ of production.

The thermophoretic force on each colloid was computed using $\boldsymbol{F}_T = -\langle \boldsymbol{F}_r \rangle = k_r \langle (\boldsymbol{r}_{\mathrm{com}} - \boldsymbol{r}_c) \rangle$.[21,22] The Soret coefficient was then calculated from

$$S_T = \frac{\boldsymbol{F}_s - \boldsymbol{F}_T}{k_{\mathrm{B}} T \nabla T} \tag{5.17}$$

where $\boldsymbol{F}_s$ is the thermophoretic force on the solvent (see Ref. 22) and T is the average temperature of the colloid. $\boldsymbol{F}_s$ was calculated by averaging over the forces experienced by particles in a system of pure solvent, using the same NEMD setup. The temperature of the colloid T was measured by averaging the kinetic energy associated with each translational and rotational degree of freedom of the rigid body, and is not necessarily equal to the average temperature at the centre of the compartment, to which the centre of mass of the colloid was tethered. In our simulations, colloids with greater mass dipoles preferentially sample lower temperature regions. In all cases, we set the temperature of the hot and cold thermostats to give $T = 2.4\ \epsilon k_{\mathrm{B}}^{-1}$.

5.4 Results and discussion

All statistical uncertainties reported in this chapter correspond to the standard error of the mean, unless specified otherwise.

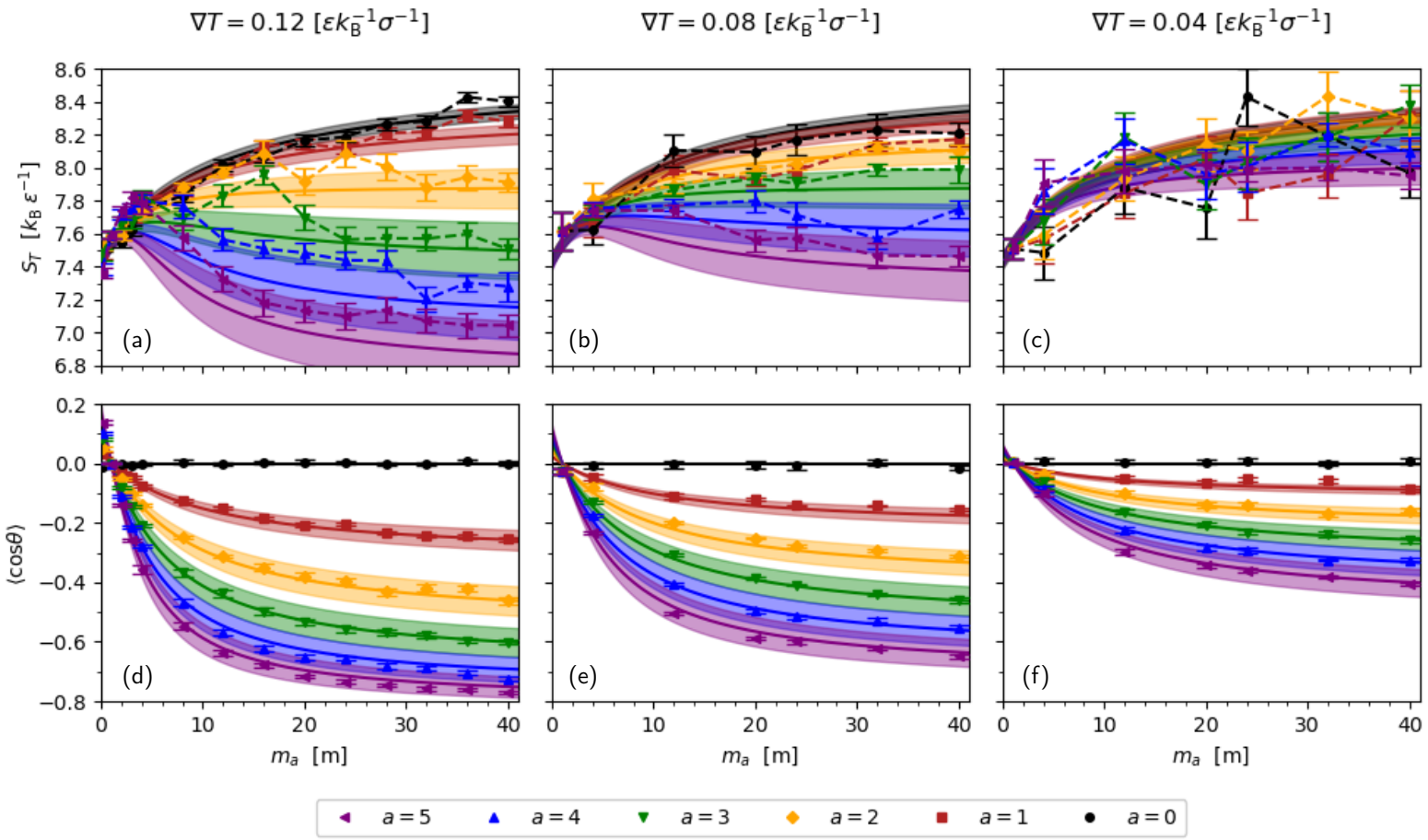


FIGURE 5.4: Soret coefficient S_T (a-c) and average orientation $\langle\cos\theta\rangle$ (d-f) of the colloids as a function of the mass m_a of the asymmetric bead at position a. Predictions from phenomenological equations (Eq. 5.4 and Eq. 5.22, with Eq. 5.18) are shown by solid lines, with the shaded area representing the associated uncertainty.

5.4.1 Thermal orientation

The thermal field induces a net orientation in the colloid. Fig. 5.4 shows that colloids of the same total mass but with different internal mass distributions can exhibit very different thermal orientation responses. For $\nabla T = 0.12\ \epsilon k_{\mathrm{B}}^{-1}\sigma^{-1}$ and holding m_a constant, $\langle\cos\theta\rangle$ can be increased by a factor of ~ 4 just by shifting the position of the asymmetric bead along the axis of the colloid.

We identify three regimes for our model: one in which there is a heavy bead ($\gamma > 1 \Rightarrow d > 0$) and $\langle\cos\theta\rangle < 0$; the symmetric rod ($\gamma = 1 \Rightarrow d = 0$) for which there is no net orientation; and the case of a light bead ($\gamma < 1 \Rightarrow d < 0$) and $\langle\cos\theta\rangle > 0$. In the case of a heavy bead, $\langle\cos\theta\rangle < 0$ indicates that the heavy bead points towards the hot region. This is consistent with the results obtained previously for similar colloid models.[14,15] However, the opposite behaviour is observed in molecular fluids: diatomic molecules[13] and even the rod-like molecules encountered in Chapter 4 (which use the same WCA shish-kebab model but with $N = 7$) orient with the heavy side pointing towards the cold source.

As discussed in previous work,[14,15] the TO effect can be modelled using the von Mises distribution and Eq. 5.4, with κ being given by the phenomenological relation

$$\kappa = \alpha \frac{N d \nabla T}{T}. \tag{5.18}$$

where α is a constant that depends on the nature of the solvent. For our model, the only unknown variable in Eq. 5.18 is α; we determined $\alpha = 1.9 \pm 0.3$ by fitting the simulation data for the smallest gradient $\nabla T = 0.04\ \epsilon k_{\mathrm{B}}^{-1}\sigma^{-1}$ to Eq. 5.4 via Eq. 5.18. Our theoretical results for $\nabla T/(\epsilon k_{\mathrm{B}}^{-1}\sigma^{-1}) = 0.08, 0.12$ are therefore true predictions. We show in Fig. 5.4(c)-(f) and Fig. 5.5 that this theoretical framework accurately reproduce the dependence of the $\langle\cos\theta\rangle$ with m_a and d. In addition, our simulation results corroborate the validity of Eq. 5.18, as shown explicitly in Fig. 5.6.

The approach used here to obtain κ relies only on $\langle\cos\theta\rangle$. κ can then give the entire angular probability distribution (Eq. 5.2), and is related to experimental conditions (∇T and T) as well as properties of the colloid and solvent (N, d and α). Thus, our analysis suggests an experimental route to quantify the orientation probability distribution and colloidal properties from measurements of the average orientation of the colloids.

In this work, we examine under what conditions a linear relationship holds between $\langle\cos\theta\rangle$ and the aforementioned variables. Taking the Taylor series expansion of the Langevin function gives

$$\langle\cos\theta\rangle = -\frac{\kappa}{3} + \frac{\kappa^3}{45} + \mathcal{O}(\kappa^5) + \ldots \tag{5.19}$$

$$\approx -\frac{\kappa}{3} = -\frac{\alpha N d \nabla T}{3T}, \qquad |\kappa| \ll 1 \tag{5.20}$$

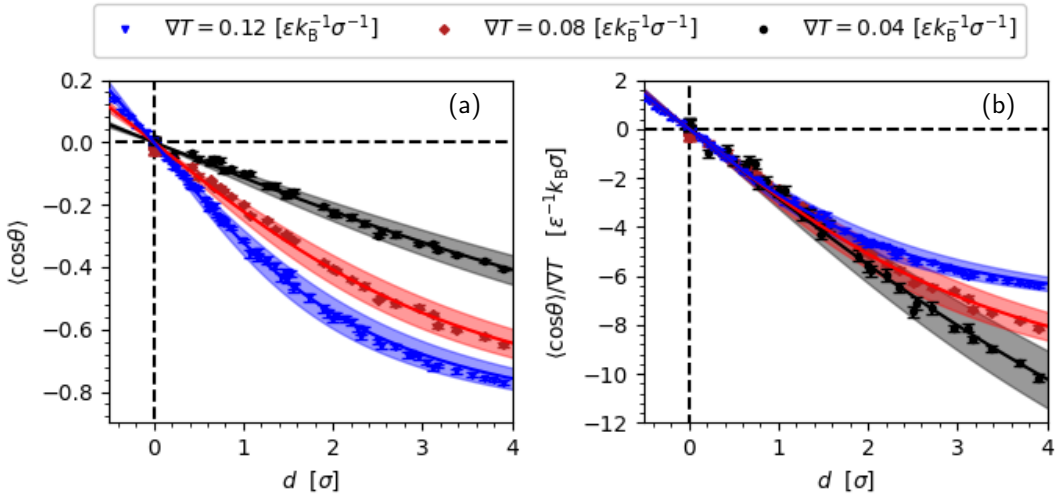


FIGURE 5.5: Average orientation (a) $\langle\cos\theta\rangle$ and (b) $\langle\cos\theta\rangle/\nabla T$ as a function of mass dipole d for different temperature gradients ∇T. Predictions made using the phenomenological equation (Eq. 5.4 with Eq. 5.18) are shown by solid lines, with the shaded area representing the associated uncertainty.

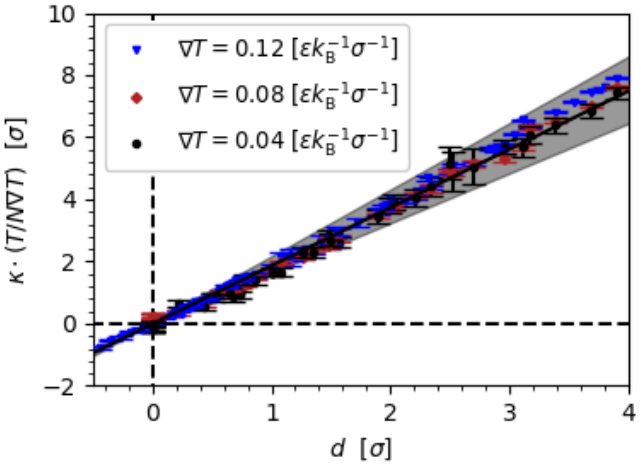


FIGURE 5.6: The "reduced" von Mises parameter $\kappa \cdot (T/N\nabla T)$ as a function of the mass dipole d. The solid line represents the prediction made using the phenomenological Eq. 5.18. The shaded area represents the associated uncertainty.

which applies for small κ and therefore small orientations. Noting that N, α and T have been held constant throughout the simulations, $\langle\cos\theta\rangle/\nabla T \propto d$ for $|\kappa| \ll 1$. We test this prediction in Fig. 5.5(b); the results do indeed collapse onto a single master curve at small dipole values, $d \to 0$. Furthermore the approximation for small κ provides a good estimate for $\langle\cos\theta\rangle$ at relatively large mass dipoles, $d \sim 1$, corresponding to $\langle\cos\theta\rangle/\nabla T \sim -3\ \sigma k_B \epsilon^{-1}$. In the context of pure fluids of

anisotropic particles, linear relationships similar to Eq. 5.20 have been derived by adopting a local equilibrium, mean-field theory approach.[23–25]

5.4.2 Thermophoresis

The Soret coefficients of the colloidal particles are shown in Fig. 5.4(a)-(c). In all cases, $S_T < 0$ indicating that the colloid is thermophobic and experiences a thermophoretic force in the direction of the cold region. $S_T \sim$ 7-8 $k_\mathrm{B}\epsilon^{-1}$ which corresponds to ∼0.07-0.08 K^{-1} using typical interaction strengths for simple fluids ($\epsilon/k_B = 10^2$ K). These values are intermediate between the Soret coefficients typically obtained for molecular binary mixtures and for small colloids.

We now apply the theoretical model derived in Sec. 5.2 in order to explain the phenomenology shown in Fig. 5.4(a)-(c). According to Kirkwood theory, the parallel and perpendicular friction coefficients of the shish-kebab model are given by[16]

$$\zeta_\perp = 2\zeta_\parallel = \frac{4\pi\eta N\sigma}{\ln\left(N/2\right)} \tag{5.21}$$

where η is the shear viscosity of the solvent. It follows that the friction coefficient can be written in terms of $\zeta_\parallel$ (or $\zeta_\perp$) only. This allows Eq. 5.14 to be simplified to

$$S_T = \frac{D_T\zeta_\parallel}{k_\mathrm{B}T}\left[1 + \frac{2}{\kappa}\left(\coth\kappa - \frac{1}{\kappa}\right)\right] \tag{5.22}$$

The viscosity $\eta = (4.24 \pm 0.01)\ m\sigma^{-1}\tau^{-1}$ was obtained using the Green-Kubo approach.[a] Since D_T is assumed to be independent of the orientation, we use the simulation results for the mass-symmetric ($a = 0$) colloid with $\gamma = 1$ at $\nabla T = 0.12\ \epsilon k_\mathrm{B}^{-1}\sigma^{-1}$ to fit the constants $B = (5.2 \pm 0.1) \times 10^{-2}\ \sigma^2\tau^{-1}k_\mathrm{B}\epsilon^{-1}$ and $C = (2.0 \pm 0.1) \times 10^{-2}\ \sigma^2\tau^{-1}k_\mathrm{B}\epsilon^{-1}$ appearing in Eq. 5.13. For the smallest temperature gradient $\nabla T = 0.04\ \epsilon k_\mathrm{B}^{-1}\sigma^{-1}$, the simulation results for S_T have large statistical uncertainties despite extensive computational effort (at least 16 μs of sampling for each data point using the Lennard-Jones parameters for argon[26]). This highlights the need for a theoretical approach to extrapolate our results to the magnitude of temperature gradients easily accessible in experiments.

For the mass-symmetric colloid ($a = 0 \Rightarrow d = 0$), S_T increases monotonically with the total mass of the colloid. S_T begins to saturate at the largest colloid masses considered in this work. In contrast, the mass-asymmetric colloids do not necessarily feature a monotonic increase. Instead, maxima in S_T as a function of m_a are observed for sufficiently large values of ∇T and a (and

[a] Two statistically independent equilibrium-NVT molecular dynamics simulations of a WCA fluid ($T_s = 2.4\ \epsilon k_\mathrm{B}^{-1}$, $\rho_{N,s} = 1.0\ \sigma^{-3}$) in a $(25, 25, 25)\sigma$ simulation cell were performed, each with 0.25τ of equilibration followed by $8.72 \times 10^5\tau$ of production. Temperature was controlled using the Nosé-Hoover chain thermostat with three chains and a time constant of 0.25τ. See, e.g., Sec. B.7 for details on the Green-Kubo integral formula; a correlation time of 2.5τ was used as the upper limit for integration.

therefore d). This occurs because the TO effect couples with the thermophoretic response; greater $|\langle\cos\theta\rangle|$ values imply that the colloid is more likely to be aligned parallel to $\boldsymbol{u}_{J_q}$ such that $\zeta_{\parallel}$ contributes a greater proportion of ensemble average, reducing $\langle\zeta\rangle$ and increasing D, which in turn decreases S_T. Consequently, the Soret coefficient of very heavy colloids can be smaller than that of lighter colloids. Another key message is that the Soret coefficient of mass-asymmetric colloids depend on $\langle\cos\theta\rangle$ and therefore on the temperature gradient ∇T. The Soret coefficients of mass-symmetric colloids are independent of ∇T.

The theoretical model captures and rationalizes the main phenomenology shown in Fig. 5.4. Predictions lie mostly within the statistical uncertainties for $m_a > 20m$, although systematic deviations between simulation and theory are observed for some branches of a. Inaccuracies in the coefficients entering Eq. 5.22 may lead to systematic deviations, while more fundamentally, possible sources of error include the approximations inherent in Eq. 5.22 (discussed in the following paragraphs).

Firstly, the underlying assumption that D_T does not depend on the internal mass distribution of the colloid, only its total mass. The orientation dependence of D_T for spherocylinders in a dilute solvent of Knudsen number $\mathrm{Kn} \gg 1$ (free-molecular flow regime) has previously been investigated using kinetic theory.[11] Ybarra and Rosner found that the thermophoretic velocity v_T had a maximum difference of 52% between the parallel and perpendicular orientations w.r.t. the thermal field. This maximum difference corresponds to the limiting case of a sphero-cylindrical particle of infinite aspect ratio (i.e., length/radius $\to \infty$) and a maximal momentum accommodation coefficient of 1.0. Smaller lengths and aspect ratios correspond to smaller differences in v_T. While that study finds a significant orientation dependence of D_T, it corresponds to very different conditions to the dense fluid ($\mathrm{Kn} < 1$) studied here. Taking as a reference the colloid with the greatest mass dipole ($a = 5, \gamma = 40$) under the largest temperature gradient $\nabla T = 0.12\ \epsilon k_{\mathrm{B}}^{-1}\sigma^{-1}$, the difference between theory and simulation amounts to a relative error of 3%. This suggests that the orientation dependence of D_T is small for the conditions used here.

Secondly, we note that the application of Kirkwood theory (and thus Eq. 5.21) is valid in the continuum limit, while in our simulations, each colloid "bead" is the same characteristic size of a solvent particle. Thirdly, the solvent viscosity η was calculated for a WCA fluid with an average temperature $T = 2.4\ \epsilon k_{\mathrm{B}}^{-1}$ and density $\rho_{N,s} = 1.0\ \sigma^{-3}$. In a thermal field, the average solvent density sampled by a mass-asymmetric colloid may differ from this value due to the TO effect. Additional work is required to determine how significant each of these approximations are.

5.4.3 Linking the Soret coefficient and average orientation

The coupling between thermal orientation and thermophoresis can be made more explicit by expressing S_T in terms of $\langle \cos\theta \rangle$, which can in principle be measured using optical techniques.[27] We use Eq. 5.4 to rewrite S_T (Eq. 5.22) as a function of $\langle \cos\theta \rangle$:

$$S_T = \frac{D_T \zeta_\parallel}{k_\mathrm{B} T} \left[1 - \frac{2\langle \cos\theta \rangle}{\mathcal{L}^{-1}(-\langle \cos\theta \rangle)} \right] \tag{5.23}$$

where $\mathcal{L}$ is again the Langevin function. The inverse Langevin function does not have an analytical expression, and approximations to $\mathcal{L}^{-1}$ are an active area of research.[28] The Puso approximation[29]

$$\mathcal{L}^{-1}(x) \approx \frac{3x}{1 - x^3} \tag{5.24}$$

for $x \in [0, 1]$, has a maximum relative error of 5%, and offers a favourable compromise between accuracy and complexity. Using this approximation Eq. 5.23 becomes

$$S_T = \frac{D_T \zeta_\parallel}{k_\mathrm{B} T} \left[\frac{5 + 2\langle \cos\theta \rangle^3}{3} \right] \tag{5.25}$$

which now defines the S_T in terms of variables that can be fixed or measured in experiments. In the case of a mass-symmetric colloid (no net orientation), $S_T^{\mathrm{sym}} = (5/3) D_T \zeta_\parallel / (k_\mathrm{B} T)$. The Soret coefficient of a mass-asymmetric colloid S_T^{asym} relative to that of a mass-symmetric colloid S_T^{sym} of the same total mass is given by

$$\frac{S_T^{\mathrm{asym}}}{S_T^{\mathrm{sym}}} = 1 - \frac{2}{5} |\langle \cos\theta \rangle|^3 \tag{5.26}$$

This equation shows that the impact of the TO effect on S_T can be represented on a single master curve, as shown in Fig. 5.7, which includes all our data for $\nabla T / (\epsilon k_\mathrm{B}^{-1} \sigma^{-1}) = 0.08, 0.12$. Eq. 5.26 implies that $S_T^{\mathrm{asym}} / S_T^{\mathrm{sym}} < 1$, that the TO effect always decreases S_T. However, we observe a minority of data points with $S_T^{\mathrm{asym}} / S_T^{\mathrm{sym}} \geq 1$ even when accounting for their statistical uncertainties. Deviations from the simulation results can be attributed to the approximations discussed in Sec. 5.4.2. Overall, we find good agreement with the simulation results for both the Puso approximation (Eq. 5.26) and when using the exact $\mathcal{L}^{-1}$. This confirms the explicit link between the TO effect and Soret coefficient established in our work.

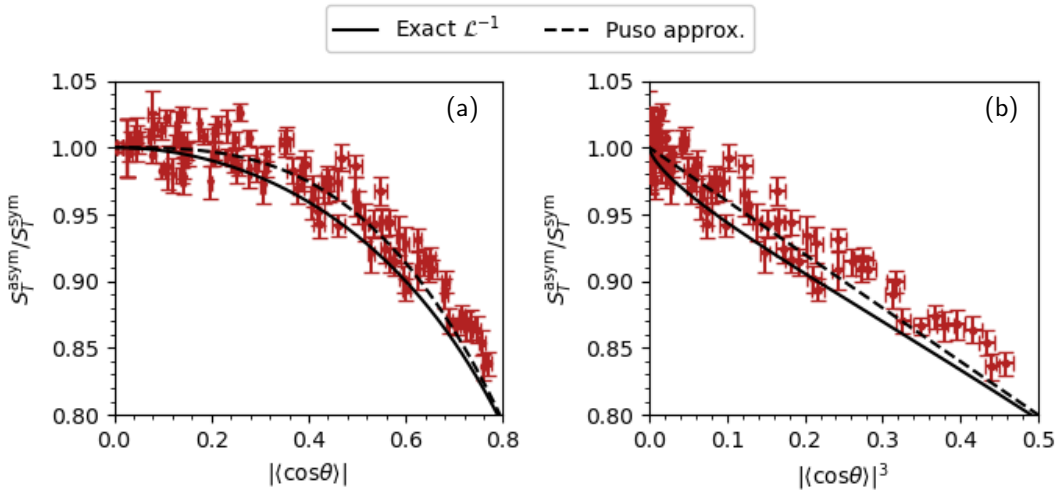


FIGURE 5.7: Ratio of the Soret coefficient of mass-asymmetric S_T^{asym} and mass-symmetric S_T^{sym} colloids as a function of the average orientation (a) $|\langle\cos\theta\rangle|$ and (b) $|\langle\cos\theta\rangle|^3$. Theoretical predictions from Eq. 5.23 and Eq. 5.26 are shown by solid and dashed lines respectively.

5.5 Conclusions

Using both theory and simulation, we have shown that the Soret coefficient of colloids can depend significantly on not just their total mass, but also their internal mass distribution. For the rod-like colloids examined in this work, the thermal orientation effect reduces $S_T = D_T/D$ by increasing D, while our results suggest that D_T features only a weak orientation dependence. For the largest mass dipoles ($d \approx 4\sigma$) and thermal gradients ($\nabla T = 0.12\ \epsilon k_{\text{B}}^{-1}\sigma^{-1}$) explored in this study, the Soret coefficient of mass-asymmetric colloids decreases by ~20% relative to a mass-symmetric colloid of the same total mass. This observation suggests an approach to identify internal colloidal compositions using thermal gradients as sensing probes.

The TO effect also gives rise to novel phenomenology. The Soret coefficient of a colloid can feature a maximum as a function of its total mass. Thus, for two colloids that differ only in their mass and mass distribution, it is possible for the lighter colloid to have a greater Soret coefficient. Another key message is that, through the TO effect, S_T can depend on the temperature gradient ∇T. Thus, understanding the coupling between TO and thermophoresis opens new avenues to manipulate anisotropic colloids. We have directly linked S_T and $\langle\cos\theta\rangle$ (accessible through optical techniques[27]), providing an attractive route for the experimental verification of our findings.

Bibliography

[1] A. Würger, *Rep. Prog. Phys.*, 2010, **73**, 126601.

[2] R. Piazza and A. Parola, *J. Phys.: Condens. Matter*, 2008, **20**, 153102.

[3] S. Wiegand, *J. Phys.: Condens. Matter*, 2004, **16**, R357–R379.

[4] D. Niether and S. Wiegand, *J. Phys.: Condens. Matter*, 2019, **31**, 503003.

[5] S. Duhr and D. Braun, *Proc. Natl. Acad. Sci. U. S. A.*, 2006, **103**, 19678–19682.

[6] C. J. Wienken, P. Baaske, U. Rothbauer, D. Braun and S. Duhr, *Nat. Commun.*, 2010, **1**, 100.

[7] Y. T. Maeda, T. Tlusty and A. Libchaber, *Proc. Natl. Acad. Sci. U. S. A.*, 2012, **109**, 17972–17977.

[8] F. Huang, P. Chakraborty, C. C. Lundstrom, C. Holmden, J. J. G. Glessner, S. W. Kieffer and C. E. Lesher, *Nature*, 2010, **464**, 396–400.

[9] F. M. Richter, E. B. Watson, R. A. Mendybaev, F.-Z. Teng and P. E. Janney, *Geochim. Cosmochim. Acta*, 2008, **72**, 206–220.

[10] A. Lervik and F. Bresme, *Phys. Chem. Chem. Phys.*, 2014, **16**, 13279–13286.

[11] P. Garcia-Ybarra and D. E. Rosner, *AIChE J.*, 1989, **35**, 139–147.

[12] Z. Tan, M. Yang and M. Ripoll, *Soft Matter*, 2017, **13**, 7283–7291.

[13] F. Römer, F. Bresme, J. Muscatello, D. Bedeaux and J. M. Rubí, *Phys. Rev. Lett.*, 2012, **108**, 105901.

[14] J. Olarte-Plata, J. M. Rubi and F. Bresme, *Phys. Rev. E*, 2018, **97**, 052607.

[15] J. D. Olarte-Plata and F. Bresme, *Phys. Chem. Chem. Phys.*, 2019, **21**, 1131–1140.

[16] M. Doi and S. F. Edwards, *The Theory of Polymer Dynamics*, Clarendon Press, 1986.

[17] W. H. Furry, R. C. Jones and L. Onsager, *Phys. Rev.*, 1939, **55**, 1083–1095.

[18] R. C. Jones and W. H. Furry, *Rev. Mod. Phys.*, 1946, **18**, 151–224.

[19] A. P. Thompson, H. M. Aktulga, R. Berger, D. S. Bolintineanu, W. M. Brown, P. S. Crozier, P. J. in 't Veld, A. Kohlmeyer, S. G. Moore, T. D. Nguyen, R. Shan, M. J. Stevens, J. Tranchida, C. Trott and S. J. Plimpton, *Comp. Phys. Comm.*, 2022, **271**, 108171.

[20] T. F. Miller, M. Eleftheriou, P. Pattnaik, A. Ndirango, D. Newns and G. J. Martyna, *J. Chem. Phys.*, 2002, **116**, 8649–8659.

[21] G. Galliero and S. Volz, *J. Chem. Phys.*, 2008, **128**, 064505.

[22] M. Yang and M. Ripoll, *J. Phys.: Condens. Matter*, 2012, **24**, 195101.

[23] A. A. Lee, *Soft Matter*, 2016, **12**, 8661–8665.

[24] P. Wirnsberger, C. Dellago, D. Frenkel and A. Reinhardt, *Phys. Rev. Lett.*, 2018, **120**, 226001.

[25] A. Gardin and A. Ferrarini, *Phys. Chem. Chem. Phys.*, 2019, **21**, 104–113.

[26] J. A. White, *J. Chem. Phys.*, 1999, **111**, 9352–9356.

[27] P. V. Ruijgrok, N. R. Verhart, P. Zijlstra, A. L. Tchebotareva and M. Orrit, *Phys. Rev. Lett.*, 2011, **107**, 037401.

[28] R. Jedynak, *Rheol. Acta*, 2015, **54**, 29–39.

[29] M. Puso, *PhD Thesis*, University of California, Davis, 2003.

Chapter 6

Thermal polarization and thermal conductivity of acetonitrile

6.1 Introduction

Polar fluids generate an electrostatic field when exposed to a thermal flux. This phenomenon, termed *thermal polarization*, occurs because the polar molecules adopt a net orientation with respect to the thermal field. It is therefore a type of thermal orientation, which we encountered in Chapters 4 and 5 for non-polar molecules and colloids. Thermal polarization was first observed in water,[1] where it is particularly strong at supercritical conditions.[2] It has since been studied using models of simple polar fluids,[3–5] but not yet examined in any other real molecular fluids. Investigating the response of different fluids is necessary to explain more generally the behaviour of polar fluids under thermal fields, and is the first step in rationalizing correlations between molecular structure and thermal polarization.

In this chapter we investigate the thermal polarization effect in acetonitrile (ACN). ACN is a highly polar fluid, and widely used as aprotic solvent in synthesis and energy applications. ACN also features a strong response to electromagnetic fields, e.g., the Optical Kerr Effect, with a Kerr constant about half that of o-nitrotoluene, which is amongst the liquids featuring the strongest birefringence response.[6] Experimental measurements of the depolarized hyper-Rayleigh scattering spectra of ACN were originally interpreted as indicative of a ferroelectric transition with the formation of small ferroelectric domains.[7] This motivated computer simulation studies to test the existence of such domains.[8] It was concluded that ACN does not feature local ferroelectric domains, in disagreement with the conclusions of the experimental studies. However, these simulations were performed under equilibrium conditions. The impact of transient or stationary thermal fields on ACN is unknown.

6.2 Methods

We performed equilibrium and non-equilibrium molecular dynamics simulations of acetonitrile at thermodynamic conditions ranging from standard to supercritical. ACN molecules were modelled as rigid bodies using the TraPPE force field (see Fig. 6.1(a)), which predicts thermophysical properties in good agreement with experimental results.[9] The equations of motion were integrated using the velocity Verlet algorithm and a timestep of 2 fs. Rigid body dynamics were evolved using two virtual sites located along the ACN axis[10,11], whose distance was kept constant using the LINCS[12] algorithm. The coordinates of the CH_3, C and N interaction sites were represented relative to the position of these virtual sites, such that the total force and the total torque are conserved.[10,11] Electrostatic interactions were calculated using the Particle Mesh Ewald method.[13] A cutoff of 1.06 nm was used for the Lennard-Jones potentials. All simulations were performed using Gromacs (v. 2020).[11,14]

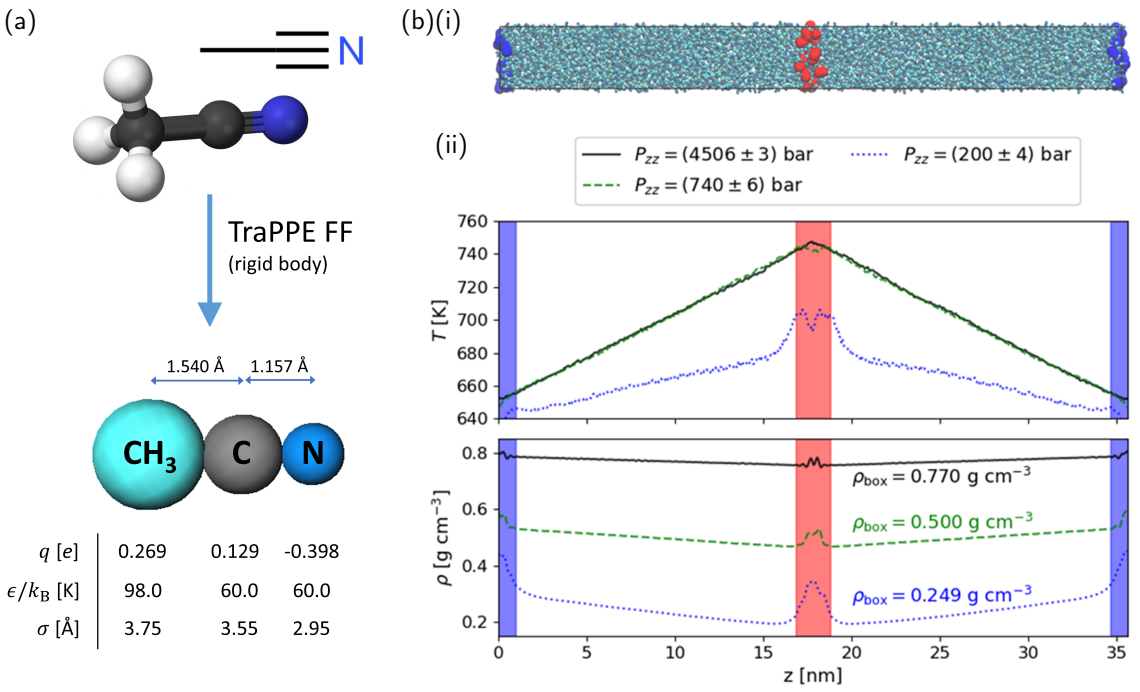


FIGURE 6.1: Simulation methods. (a) Graphical representation of the TraPPE force field of acetonitrile. The charge q and Lennard-Jones parameters ϵ and σ are shown under their corresponding species, while rigid bond distances are shown above the molecule. (b) NEMD simulations: (i) snapshot of the simulation cell, thermostat regions are represented by enlarged red (hot) and cold (blue) molecules; (ii) representative temperature T and density ρ profiles for pressures P_{zz}.

6.2.1 Non-equilibrium molecular dynamics simulations

Boundary-driven non-equilibrium molecular dynamics (NEMD) simulations, using a restraint approach, was used to model the fluids in the stationary state. A tetragonal simulation cell of dimensions $(L_x, L_y, L_z) = (3.564, 3.564, 35.639)$ nm was used, with 3D periodic boundary conditions. The two thermostatting regions, hot and cold, were located in the centre and edges of the box, respectively (see Fig. 6.1). The thermostatting regions extend in the (x, y) plane, such that the temperature gradients are generated along the z-direction. In the stationary state, this set-up results in two equal but opposite temperature gradients, and therefore in equal and opposite heat fluxes, such that the system is completely periodic.

The thermostats were applied to ACN molecules located in the thermostatting regions. We restrained the position of the carbon atom bonded to nitrogen to its initial z-coordinate using a harmonic potential with a force constant of 10^3 kJ mol^{-1} nm^{-2}. The restraint was applied only in the z-direction; the molecules were free to rotate, and also translate in the x- and y-directions. The temperature difference between the hot and cold thermostats was set to 100 K for all NEMD simulations.

The thermostatting process was implemented using the Nosé-Hoover thermostat.[15,16] A single thermostat, using one chain, was applied to each of the thermostatting regions, while the trajectories of all other molecules were generated following standard Newtonian dynamics. The Nosé-Hoover equations include an equation of motion for the dynamic variable p_ξ, which models the dynamic exchange of heat of the system at temperature T, with a reservoir that is set to the desired temperature T_r:

$$\frac{d\mathbf{v}_i}{dt} = \frac{\mathbf{f}_i}{m_i} - \frac{p_\xi}{Q}\mathbf{v}_i \tag{6.1}$$

$$\frac{dp_\xi/Q}{dt} = \frac{(T - T_r)}{Q} \tag{6.2}$$

where $Q = \tau_T^2 T_r/(4\pi^2)$, τ_T defines the period of the temperature fluctuations, which was set to 1 ps. $\mathbf{r}_i$, $\mathbf{v}_i$ and $\mathbf{f}_i$ are the position, velocity and the force acting on particle i with mass m_i. The Nosé-Hoover Hamiltonian incorporates the contributions due to the reservoir:

$$H(\mathbf{r}^N, \mathbf{p}, \xi) = \sum_{i=1} \frac{\mathbf{p}_i^2}{2m_i} + U(\mathbf{r}^N) + \frac{p_\xi^2}{2Q} + N_{dof} k_B T \xi \tag{6.3}$$

where $\mathbf{r}^N = (\mathbf{r}_1, \mathbf{r}_2, \cdots, \mathbf{r}_N)$, $\dot{\xi} \equiv \mathrm{d}\xi/dt = p_\xi/Q$ and N_{dof} is the total number of degrees of freedom of the region being thermostatted. The last two terms in Eq. 6.3 represent the energy exchanged with the reservoir. The heat flux, $\boldsymbol{J}_q = (0, 0, \pm J_q)$, can be obtained from the time-average value

of $\dot{\xi}$ using the continuity equation:

$$J_q = -\frac{\langle \dot{\xi} \rangle N_{dof} k_B T}{A} \tag{6.4}$$

where $A = (L_x \times L_y)^2 = 3.564^2$ nm^2 ($L_x = L_y$) is the cross sectional area of the simulation box. The simulated systems consisted of 1590-5050 molecules to target different densities. Each thermostat was coupled to 33 molecules, giving $N_{dof} = 165$ (5 degrees of freedom per molecule).

After the stationary state was established, sampling consisted of 5 (up to 25) replicas, each 4 ns (8 ns) in length, for the high density (low density, $\rho = 0.249$ g cm^{-3}) systems. Fluctuations for the low density systems are large, particularly as the critical temperature is approached. Extensive sampling (up to 200 ns) was needed to obtain averages within acceptable statistical uncertainty.

6.2.2 Equilibrium simulations

We also performed MD simulations in the NVT and NPT ensembles, with temperature and pressure controlled by the CSVR thermostat[17] and Parrinello-Rahman barostat[18], respectively. A typical simulation consisted of 1000 molecules, 1 ns of equilibration time and 9 ns of production, with typically 6-10 statistically independent replicas. Equilibrium-NVT simulations were performed to compute: (1) coexistence lines from simulations of explicit liquid-vapour interfaces, using the direct coexistence method;[19] and (2) dielectric properties and Debye relaxation times. A smaller timestep of 1 fs was used to calculate the dipole moment correlation functions.

6.3 Results and discussion

All statistical uncertainties reported in this chapter correspond to the standard error of the mean, unless specified otherwise.

6.3.1 Equation of state and phase diagram

The thermodynamic states investigated in this work are shown in Fig. 6.2. We targeted the standard state, high temperature/density systems, and states along the critical isochore. It has previously been shown that the TraPPE force field accurately reproduces the phase diagram of acetonitrile, including the critical point.[9] Our coexistence densities, obtained using the direct coexistence method, are in good agreement with these previous[9] simulations. With regards to the NEMD data, we show in Fig. 6.1(b) representative temperature and density profiles for selected thermodynamic states. In order to exclude any possible artefacts arising from the thermostats, only spatial bins located at least 4 nm from the centre and edges of the simulation cell were used. Each set of profiles corresponds to the equation of state (EOS) at the simulated pressure, as defined by

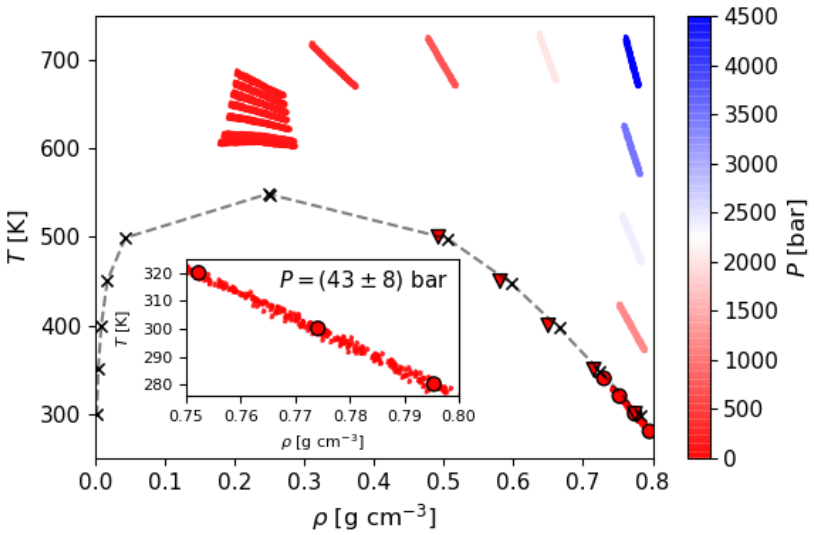


FIGURE 6.2: Thermodynamic states investigated in this work with reference to the coexistence curve of acetonitrile: coexistence densities from this work (▽) and previous simulations[9] (--×); NEMD (dots ·, which may appear as thick lines) and equilibrium-NPT (○) data. Our data is colour coded according to the pressure P of the system.

the component (P_{zz}) parallel to the heat flux vector. The EOS obtained from NEMD (see Fig. 6.2) reproduces the behaviour of the fluid at equilibrium. This is equivalent to stating that the NEMD simulations generate a collection of states that fulfill local equilibrium, a key assumption in linear non-equilibrium thermodynamics (LNET).

6.3.2 Thermal polarization

The phenomenological description of thermal polarization (TP) within the framework of LNET is given in Sec. 2.2.4. The application of temperature gradient ∇T induces a stationary electrostatic field $\boldsymbol{E}$ given by[1]

$$\boldsymbol{E} = \left(1 - \frac{1}{\varepsilon_r}\right) \frac{L_{pq}}{L_{pp}} \frac{\nabla T}{T} \tag{6.5}$$

where ε_r is the static relative permittivity of the fluid, and $L_{\alpha\beta}$ are the phenomenological coefficients, with L_{pq} measuring the strength of the heat-polarization coupling, and L_{pp} is connected to the relaxation time of the polarization. The strength of the TP effect can be quantified using the *thermal polarization coefficient*[2]

$$S_{\mathrm{TP}} = \frac{E}{\nabla T} = \left(1 - \frac{1}{\varepsilon_r}\right) \frac{L_{pq}}{L_{pp}} \frac{1}{T}, \tag{6.6}$$

The phenomenological coefficient L_{pp} is related to the Debye relaxation time, τ, via[20]

$$\boldsymbol{P}(t) = \kappa \boldsymbol{E} \left(1 - \exp(-t/\tau)\right) \tag{6.7}$$

where $\boldsymbol{P}$ is the polarization, which in the absence of free charges is given by $\boldsymbol{P} = -\varepsilon_0 \boldsymbol{E}$, and $\kappa = (\varepsilon_r - 1)\varepsilon_0$. An approximation to phenomenological coefficient L_{pp} within the assumptions of the Debye model is then given by

$$L_{pp} = \frac{\kappa T}{\tau}. \tag{6.8}$$

Once L_{pp} is known, it is possible to extract L_{pq} from Eq. 6.5, provided $\boldsymbol{E}$, ε_r, ∇T and T are known. All these quantities are either defined in our simulation set-up (∇T and T) or are accessible through the NEMD or equilibrium simulations ($\boldsymbol{E}$ and ε_r).

The electrostatic field induced by the thermal gradient was calculated by integrating the total charge density along the direction of the heat flux,

$$E(z) = \frac{1}{\varepsilon_0} \int_0^z \rho_q(z') dz' \tag{6.9}$$

where ε_0 is the vacuum permittivity, and $\rho_q(z) = \left(\sum_{i=1}^{N_q} \delta(z - z_i) q_i\right) / A$ is the charge density, and N_q is the number of charges in the system. We also calculated the dipolar field

$$E_P(z) = \frac{-1}{\varepsilon_0} \int_0^z \frac{dP_z(z')}{dz'} dz', \tag{6.10}$$

with

$$P_z(z) = \frac{1}{A} \left\langle \sum_{i=1}^{N_m} \delta(z - z_i) \left[\sum_{j=1}^{j \in m} q_{j,m} z_{j,m} \right] \right\rangle \tag{6.11}$$

where the first and second sums in Eq. 6.11 run over the number of molecules N_m, and the number of atoms in molecule m, respectively, and for z_i we used the position of the central atom in each molecule. The thermal polarization coefficient can be split into dipolar and higher order (HO) contributions: $S_{\mathrm{TP}} = (E_P + E_{\mathrm{HO}})/\nabla T = S_{\mathrm{TP}}^{P} + S_{\mathrm{TP}}^{\mathrm{HO}}$.

Clear polarization fields across the simulation cells are observed, as evidenced by the slope of the potentials shown in Fig. 6.3(a).[a] The strength of the TP effect depends on the thermodynamic conditions. At high densities, $\rho = 0.770$ g cm^{-3}, the polarization is strongest at near-standard conditions, and decreases with temperature: by ∼60% from 300 K to 700 K. Similarly, $|S_{\mathrm{TP}}|$ decreases with temperature along the critical isochore, decreasing by ∼70% from 600 K to 660 K. The enhancement in TP as the system approaches the critical temperature resembles the behaviour reported[2] for water. At 607 K ($T/T_c - 1 \sim 0.1$), $S_{\mathrm{TP}} = -(0.3 \pm 0.1)$ mV K^{-1} (see Appendix D)

[a] Numerical data from the NEMD simulations, including the electrostatic fields, are given in Appendix D.

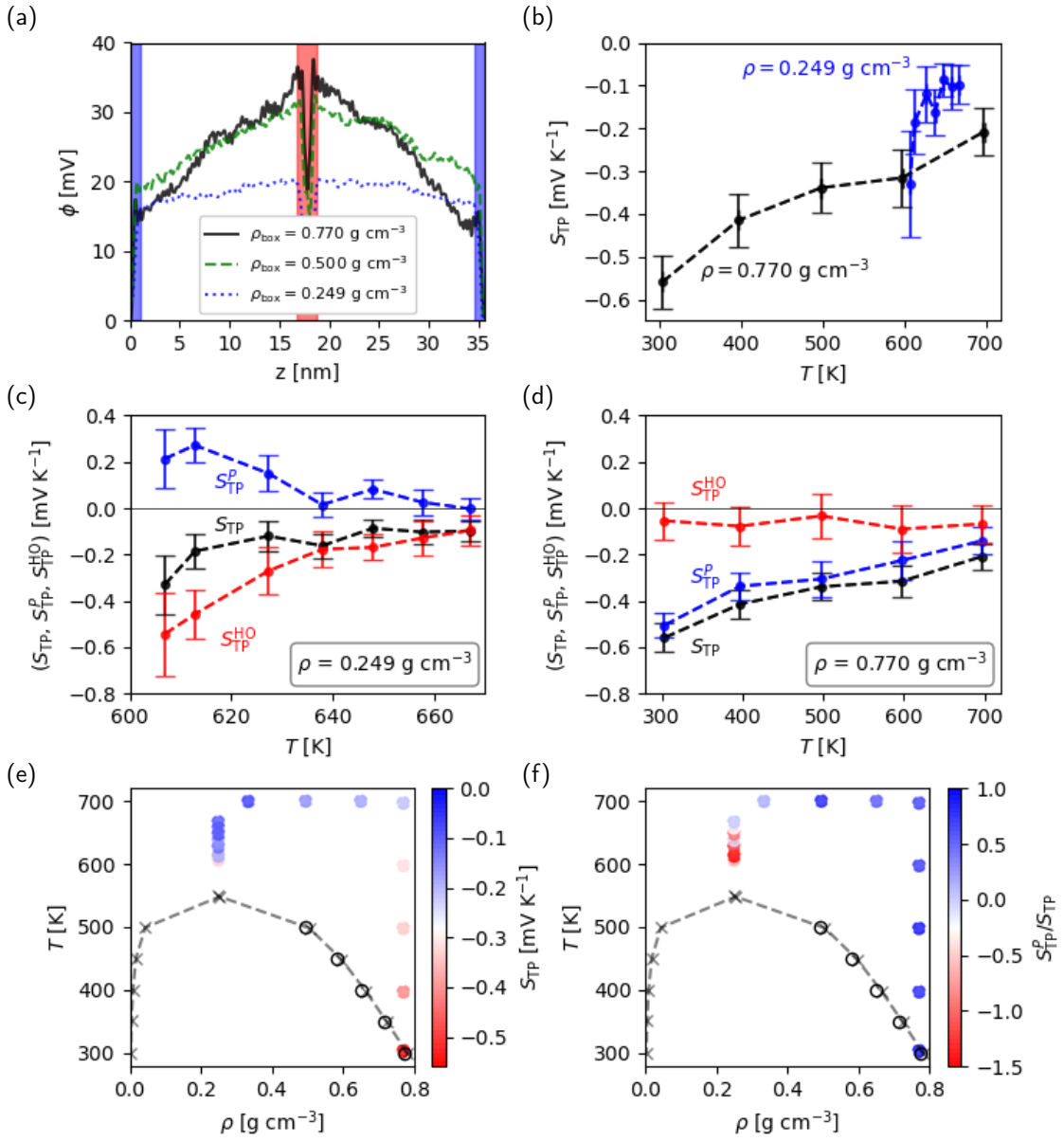


FIGURE 6.3: Thermal polarization of acetonitrile. (a) Electrostatic potential ϕ across the simulation cell. (b-d) Total S_{TP}, dipolar S^{P}_{TP} and higher-order $S^{\mathrm{HO}}_{\mathrm{TP}}$ thermal polarization coefficients along the high density and critical isochores. (e) S_{TP} and (f) $S^{P}_{\mathrm{TP}}/S^{\mathrm{HO}}_{\mathrm{TP}}$ with reference to the phase diagram.

has a similar magnitude to that near-standard conditions. This value is one order of magnitude lower than that obtained for water at the same $T/T_c - 1$, -2.5 mV K^{-1},[2] highlighting differences in the TP response of these two polar fluids. We also note that $|S_{\mathrm{TP}}|$ increases with density along the $T = 700$ K isotherm: by ∼200% from 0.333 g cm^{-3} to 0.770 g cm^{-3}.

For all the systems investigated in this work, the thermal polarization coefficient of acetonitrile is negative, $S_{\mathrm{TP}} < 0$. This is in contrast with the TP effect in water, where a field inversion is observed.[2] This inversion phenomenon in water is connected to the balance of dipolar and quadrupolar contributions to the electrostatic field, with the latter dominating at high temperatures and low densities when the fluid features greater thermal expansion. We report in Fig. 6.3 the dipolar and higher order contributions to the total thermal polarization field of acetonitrile. At high densities, $\rho = 0.770$ g cm^{-3}, the dipolar term is negative for all temperatures investigated, and is the dominant contribution (∼70-90%, noting the high uncertainties of ∼10-30% associated with these percentages) to the total field. $E_P < 0$ indicates that the molecules orient preferentially with the dipole pointing toward the hot region. The small impact of higher order terms in determining the field explains the lack of inversion at this high density. Along the critical isochore the situation is more complex. In all cases, $E_P > 0$ (or straddles 0 given the uncertainty) indicating that the molecules orient preferentially with the dipole pointing toward the cold region. At high temperatures, the dipolar and higher order term contributions have similar values, but opposite signs, while the higher order terms dominate the TP response upon approaching the critical temperature. This result follows previous observations for water, where contributions beyond the dipolar term become dominant near critical conditions, mirroring the increase of the thermal expansion coefficient.[2]

Next, we briefly consider the relative importance of the parameters given in Eq. 6.5 to S_{TP}. As shown in Table 6.1, ε_r features only a weak dependence with temperature: at a density of $\rho = 0.770$ g cm^{-3} ($\rho = 0.249$ g cm^{-3}), ε_r decreases by ∼8% (∼ 1%) from 300 K to 700 K (610 K to 670 K), while S_{TP} changes by ∼60% (∼70%). These small changes in ε_r correspond to even smaller differences of $< 1\%$ in $(1 - 1/\varepsilon_r)$. Since TS_{TP} is not constant with T, S_{TP} must be interpreted in terms of changes in both T and L_{pq}/L_{pp}. We address the latter in the following, by calculating L_{pq} and L_{pp}.

The phenomenological coefficients can be obtained using Eqs. 6.5 & 6.8. To calculate L_{pp} we computed the static relative permittivity ε_r, and Debye relaxation time τ of acetonitrile. ε_r was calculated from the analysis of the total dipolar fluctuations in the simulation box:

$$\varepsilon_r - 1 = \frac{\langle \mathbf{P}^2 \rangle - \langle \mathbf{P} \rangle^2}{3Vk_BT\varepsilon_0}, \tag{6.12}$$

where $\mathbf{P} = \sum_{i=1}^{N} q_i \mathbf{r}_i$, V is the volume of the simulation box, and the brackets <> denote an ensemble average. The Debye relaxation time τ was calculated from the normalized total dipole moment

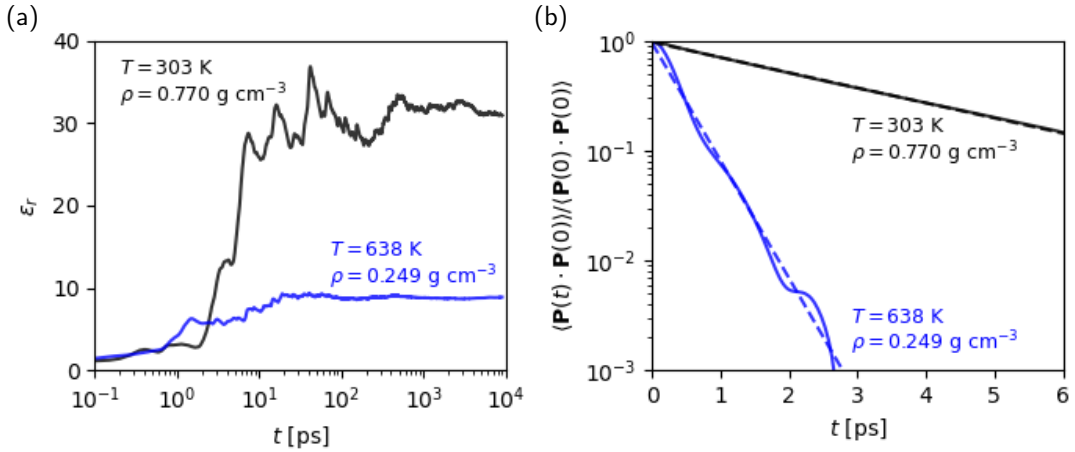


FIGURE 6.4: Dielectric properties of acetonitrile. (a) Convergence of the static relative permittivity ε_r with time t for the thermodynamics states $(\rho, T) = (0.770 \text{ g cm}^{-3}, 303 \text{ K})$ and $(0.249 \text{ g cm}^{-3}, 638 \text{ K})$. (b) Total dipole correlation functions, $\langle \mathbf{P}(t) \cdot \mathbf{P}(0) \rangle / \langle \mathbf{P}(0) \cdot \mathbf{P}(0) \rangle$, for the same thermodynamic states. Dashed lines show the fit to the exponential function $f(t) = A \exp\{(-t/\tau_P\}$.

TABLE 6.1: Properties related to the thermal polarization of acetonitrile at selected thermodynamic conditions (density ρ and temperature T): thermal polarization coefficient S_{TP}; static relative permittivity ε_r; dipolar relaxation times τ_P (total) and τ_p (averaged molecular); L_{pp} and L_{pq} are the phenomenological coefficients; $\delta\lambda$ is the difference between the total thermal conductivity λ and that in the absence of the thermal polarization coupling effect $\lambda_{L_{pq}=0}$. Statistical uncertainties in the least significant figure are given in parenthesis.

ρ [g cm^{-3}]	T [K]	S_{TP} [mV K^{-1}]	ε_r	τ_p [ps]	τ_P [ps]	$L_{pp} \times 10^{-4}$ [C^2 K/(J m s)]	$L_{pq} \times 10^{-4}$ [C K/(m s)]	L_{pq}/L_{pp} [V]	λ [W/(K m)]	$\lambda_{L_{pq}=0}$ [W/(K m)]	$\delta\lambda$ [W/(K m)]	$\delta\lambda$ [%]
0.770	303	-0.56(6)	31.3(1)	3.061(2)	3.13(2)	2.59(2)	-0.45(5)	-0.18(2)	0.239(7)	0.248(7)	-0.009(2)	-3.6(8)
0.770	498	-0.34(6)	30.0(1)	1.462(1)	1.51(3)	8.5(1)	-1.5(3)	-0.17(3)	0.236(5)	0.246(6)	-0.010(4)	-4(2)
0.770	697	-0.21(6)	28.94(9)	0.929(1)	0.98(2)	17.6(3)	-2.6(7)	-0.15(4)	0.234(9)	0.24(1)	-0.008(4)	-3(2)
0.249	607	-0.3(1)	8.78(1)	0.367(1)	0.47(1)	8.9(2)	-2.0(8)	-0.23(9)	0.26(2)	0.27(2)	-0.012(9)	-5(4)
0.249	638	-0.15(5)	8.81(2)	0.348(1)	0.42(2)	10.5(4)	-1.2(4)	-0.12(4)	0.121(5)	0.125(6)	-0.004(2)	-3(2)
0.249	667	-0.10(5)	8.84(2)	0.325(1)	0.40(1)	11.6(4)	-0.9(4)	-0.07(3)	0.088(4)	0.090(5)	-0.001(1)	-2(1)

correlation functions: $\langle \mathbf{P}(t) \cdot \mathbf{P}(0) \rangle / \langle \mathbf{P}(0) \cdot \mathbf{P}(0) \rangle$ and $N_m^{-1} \sum_{i=1}^{N_m} \langle \mathbf{p}_m(t) \cdot \mathbf{p}_m(0) \rangle / \langle \mathbf{p}_m(0) \cdot \mathbf{p}_m(0) \rangle$ respectively, where $\mathbf{p}_m$ is the dipole moment vector of a single molecule. The correlation functions feature a typical exponential decay such that their initial decay could be fit to a single exponential curve $f(t) = A \exp(-t/\tau_\alpha)$; we used upper cutoffs of 5 and 2 ps when fitting the high (0.770 g cm^{-3}) and low (0.249 g cm^{-3}) density states, respectively. The exception to this is the $(\rho, T) = (0.770$ g cm$^{-3}, 697$ K) point, with a cutoff of 3.5 ps. This model assumes the simplest treatment considering a single relaxation time, consistent with Eq. 6.7.

Our results for the static relative permittivity and dipolar correlation times are reported in Table 6.1. At 303 K and 0.770 g cm^{-3} the simulated static relative permittivity is close to the experimental value,[21] with a relative deviation -13%, which is acceptable considering the simplicity of the model and slight difference in thermodynamic conditions. The Debye relaxation time is also consistent with experimental estimates of 3.5 ps[21] and 3.7 ps[22]. Similar relaxation times are obtained using the total (τ_P) or molecular (τ_p) dipole moments, indicating a small impact from cross-correlations. τ_p values are systematically lower. At high density, increasing the temperature results in a small decrease of the static relative permittivity, while the relaxation time becomes significantly shorter. This is expected, as the rotational diffusion increases with temperature. The static relative permittivity is much smaller along the critical isochore, and changes only marginally for the temperature interval investigated. These supercritical states feature shorter relaxation times for dipole correlations, ~ 0.5 ps, as expected given the higher temperatures.

The values for L_{pp} and L_{pq} are collected in Table 6.1. The coefficients depend strongly on the temperature. In the case of L_{pp}, the rapid increase with temperature is due to the significant speed-up of rotational dynamics, reflected in shorter relaxation times, τ_P. Interestingly, $|L_{pq}|$ increases with temperature at 0.770 g cm^{-3}, but decreases with temperature along the critical isochore as one moves away from the critical temperature. At both densities, the ratio $|L_{pq}/L_{pp}|$ decreases with temperature; however, the values in each isochore overlap considering their associated statistical uncertainty. As mentioned previously, the S_{TP} coefficients at (607 K, 0.249 g cm^{-3}) (approximately 10% above the critical point) and (303 K, 0.770 g cm^{-3}), are similar. The ratio $|L_{pq}/L_{pp}|$ in Eq. 6.6 in the supercritical states is about 30% larger than that of the low temperature/high density system. For the latter system, the strong polarization response is driven by a significantly higher static relative permittivity and lower temperature, which enhance the TP effect (see Eq. 6.6).

6.3.3 Thermal conductivity

We demonstrated in Sec. 6.3.1 that locally the NEMD simulations reproduce the equation of state of the fluids. We took advantage of this to calculate the thermal conductivity of acetonitrile at different thermodynamic conditions using Fourier's law ($\lambda = -\boldsymbol{J}_q / \nabla T$) and the local temperature

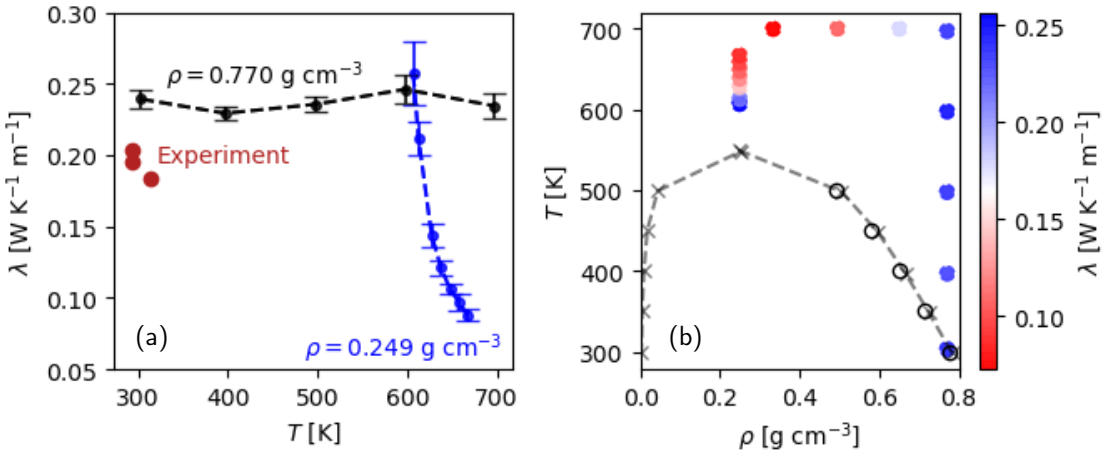


FIGURE 6.5: Thermal conductivity λ of acetonitrile: (a) along the high density and critical isochores, with experimental values measured at ambient pressure (see text for discussion); and (b) with reference to the phase diagram.

gradient, at the temperature and density of interest. The temperature gradient was determined by fitting a straight line to the temperature profile within a range of ± 2 nm around the selected state point. We note that the calculation of the thermal conductivity via NEMD includes all possible coupling effects, and we discuss later in this section how the coupling between heat and polarization fluxes affects the thermal conductivity of acetonitrile.

The thermal conductivities computed in this work are shown in Fig. 6.5 (and given in Appendix D). The TraPPE force field predicts $\lambda = (0.239 \pm 0.007)$ W K^{-1} m^{-1} at 303 K and 0.770 g cm^{-3}, corresponding to a pressure of $P = (43 \pm 8)$ bar. This result is on the order of the thermal conductivity reported experimentally at 293.15 K and ambient pressure: 0.195 W K^{-1} m^{-1} and 0.2034 W K^{-1} m^{-1}.[23,24] In the latter case, a density of 0.7897 g cm^{-3} was also reported.[24] Note that it is also comparable to the experimental value of 0.183 W K^{-1} m^{-1} obtained at 313.15 K at ambient pressure.[23]

As shown in Fig. 6.5, the thermal conductivity does not change significantly with temperature along the 0.770 g cm^{-3} isochore. In contrast, the critical isochore features a strong increase with temperature as the critical point is approached. This behavior is consistent with the enhancement discussed previously by Sengers[25]. We have not attempted to fit our data to a power law since our temperatures are well above the critical temperature. Moving along the $T = 700$ K isotherm, we observe an increase in thermal conductivity with density (see Fig. 6.5(b)).

The phenomenological coefficients can be used to assess the impact of the TP effect on the thermal conductivity. It is well established that coupling effects impact transport properties, for example the Soret effect, where heat-mass flux coupling decreases the thermal conductivity (as shown in Sec. 3.3.4).[20,26] However, the impact of TP remains unexplored. In this case, the thermal

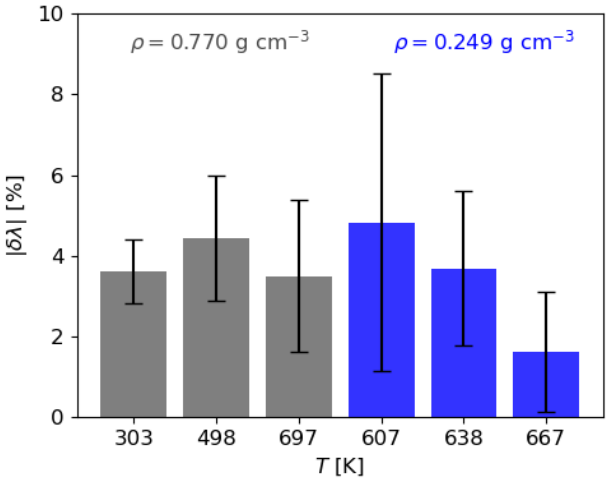


FIGURE 6.6: The decrease $|\delta\lambda|$ in thermal conductivity of acetonitrile due to thermal polarization.

conductivity in the stationary state characterized by zero displacement current can be written in terms of the phenomenological coefficients as (see Sec. 2.2.4)

$$\lambda = \frac{1}{T^2}\left(L_{qq} - \frac{L_{pq}L_{qp}}{L_{pp}}\right) \tag{6.13}$$

where L_{qq} is the phenomenological coefficient associated with the heat flux and $L_{pq} = L_{qp}$ are the cross-coupling coefficients. Following LNET (Sec. 2.2.4), $L_{qp}L_{pq}/L_{pp} = L_{qp}^2/L_{pp} \geq 0$, hence $L_{pq} \neq 0$ implies that the TP coupling effect should always decrease λ. The NEMD thermal conductivities include the effect of the TP coupling. Equation 6.13 thus provides a route to estimate the reduction of the thermal conductivity associated with the cross-coupling of heat and polarization fluxes. When $L_{pq} = 0$ such coupling does not exist, and we obtain the corresponding thermal conductivity, $\lambda_{L_{pq}=0}$. Thus, $\lambda = \lambda_{L_{pq}=0} + \delta\lambda$, where we compute $\delta\lambda = -L_{pq}^2/(T^2 L_{pp})$ directly from variables T, S_{TP}, τ_P and ε_r, according to

$$\delta\lambda = -\frac{S_{\mathrm{TP}}^2 T}{\tau}\left(\frac{\varepsilon_0\varepsilon_r^2}{\varepsilon_r - 1}\right) \tag{6.14}$$

As shown in Fig. 6.6, the TP effect reduces the thermal conductivity by ∼2-5% for the thermodynamics states investigated in this work. (In all cases, S_{TP} carries the largest relative uncertainty.) This result confirms the notion that fluids that become polarized under a thermal gradient become worse heat conductors.

6.4 Conclusions

We have shown that thermal fields polarize liquid and supercritical acetonitrile. This effect can be significant at near-standard conditions, with TP coefficients $S_{\mathrm{TP}} \sim -0.6$ mV K^{-1}. Large temperature gradients, 10^6 to 10^8 K m^{-1}, can be obtained using plasmonic systems,[27] corresponding to measurable fields, 10^2 to 10^5 V m^{-1}, and thus opening a route to the experimental observation of the TP effect. The TP effect might be relevant in thermo-plasmonics, where local polarization effects and the refractive index of the surrounding medium influence the plasmonic response.

Electrostatic fields of similar magnitude are obtained at near-standard and supercritical conditions. The analysis of the phenomenological coefficients defining S_{TP} shows that at near-standard conditions, large static relative permittivities and the low temperatures are major factors in contributing to the field strength. In contrast, the TP strength at supercritical conditions is connected to the enhanced rotational diffusion, and the stronger cross-coupling between the heat and polarization fluxes. At standard conditions, the TP electrostatic field is dominated by dipolar contributions, while higher order terms become the largest contributors for the supercritical fluid (as is the case for water[2]). Unlike the physical behaviour observed in water,[2] the TP field of acetonitrile does not feature a reversal in sign.

We have demonstrated, for the first time, that the TP effect has a measurable impact on the thermal conductivity of polar fluids. We find that the coupling of heat and polarization fluxes leads to a reduction in thermal conductivity of ∼2-5%, both at near-standard and supercritical conditions. While differences in thermal conductivities obtained from non-equilibrium and equilibrium simulation techniques might be masked by statistical uncertainties, these thermal conductivities must be different due the coupling of polarization and heat fluxes. Equilibrium approaches relying on linear response theory and Green-Kubo equations would thus need to include the cross coefficients to obtain reliable thermal conductivities, in a similar fashion to what has been done before (see Chapter 3) for the Soret effect.

Bibliography

[1] F. Bresme, A. Lervik, D. Bedeaux and S. Kjelstrup, *Phys. Rev. Lett.*, 2008, **101**, 020602.

[2] I. Iriarte-Carretero, M. A. Gonzalez, J. Armstrong, F. Fernandez-Alonso and F. Bresme, *Phys. Chem. Chem. Phys.*, 2016, **18**, 19894–19901.

[3] C. D. Daub, P.-O. Åstrand and F. Bresme, *Phys. Chem. Chem. Phys.*, 2014, **16**, 22097–22106.

[4] A. A. Lee, *Soft Matter*, 2016, **12**, 8661–8665.

[5] P. Wirnsberger, C. Dellago, D. Frenkel and A. Reinhardt, *Phys. Rev. Lett.*, 2018, **120**, 226001.

[6] R. J. W. Le Fèvre, B. J. Orr and G. L. D. Ritchie, *J. Chem. Soc.*, 1965, 2499–2505.

[7] D. P. Shelton, *J. Chem. Phys.*, 2005, **123**, 084502.

[8] M. A. Pounds and P. A. Madden, *J. Chem. Phys.*, 2007, **126**, 104506.

[9] C. D. Wick, J. M. Stubbs, N. Rai and J. I. Siepmann, *J. Phys. Chem. B*, 2005, **109**, 18974–18982.

[10] H. J. C. Berendsen and W. F. van Gunsteren, in *Molecular dynamics simulations: Techniques and approaches*, Reidel, Dordrecht, The Netherlands, 1984, ch. 8, pp. 475–500.

[11] Gromacs Development Team, *GROMACS Documentation: Release 2020*, https://doi.org/10.5281/zenodo.3562512.

[12] B. Hess, H. Bekker, H. J. C. Berendsen and J. G. E. M. Fraaije, *J. Comp. Chem.*, 1997, **18**, 1463–1472.

[13] T. Darden, D. York and L. Pedersen, *J. Chem. Phys.*, 1993, **98**, 10089.

[14] M. J. Abraham, T. Murtola, R. Schulz, S. Páll, J. C. Smith, B. Hess and E. Lindahl, *SoftwareX*, 2015, **1–2**, 19–25.

[15] S. Nosé, *Mol. Phys.*, 1984, **52**, 255–268.

[16] W. G. Hoover, *Phys. Rev. A*, 1985, **31**, 1695–1697.

[17] G. Bussi, D. Donadio and M. Parrinello, *J. Chem. Phys.*, 2007, **126**, 014101.

[18] M. Parrinello and A. Rahman, *J. Appl. Phys.*, 1981, **52**, 7182–7190.

[19] G. A. Chapela, G. Saville, S. M. Thompson and J. S. Rowlinson, *J. Chem. Soc., Faraday Trans. 2*, 1977, **73**, 1133–1144.

[20] S. R. de Groot and P. Mazur, *Non-Equilibrium Thermodynamics*, Dover, 1984.

[21] D. S. Venables and C. A. Schmuttenmaer, *J. Chem. Phys.*, 1998, **108**, 4935–4944.

[22] A. Sugitani, S.-I. Ikawa and S. Konaka, *Chem. Phys.*, 1990, **142**, 423–430.

[23] R. J. Hulse, M. W. Anderson, M. D. Bybee, D. D. Gonda, C. A. Miller, J. L. Oscarson, R. L. Rowley and W. V. Wilding, *J. Chem. Eng. Data*, 2004, **49**, 1433–1435.

[24] L. Qun-Fang, L. Rui-Sen, N. Dan-Yan and H. Yu-Chun, *J. Chem. Eng. Data*, 1997, **42**, 971–974.

[25] J. V. Sengers, *Ber. Bunsenges. Phys. Chem.*, 1972, **76**, 234–249.

[26] J. Armstrong and F. Bresme, *Phys. Chem. Chem. Phys.*, 2014, **16**, 12307–12316.

[27] C. R. Crick, P. Albella, B. Ng, A. P. Ivanov, T. Roschuk, M. P. Cecchini, F. Bresme, S. A. Maier and J. B. Edel, *Nano Lett.*, 2015, **15**, 553–559.

Chapter 7

Thermophysical properties of water using reactive force fields

7.1 Introduction

7.1.1 Motivation

Water plays a central role in our lives: it is ubiquitous in nature and industry, and by definition hosts the entirety of aqueous chemistry. It is therefore unsurprising that an accurate description of water is a long-standing goal of computational chemistry and physics. To this end a vast number of water models have been developed, each with its own set of strengths, limitations and scope.

ReaxFF force fields incorporate many characteristics desirable for modelling aqueous systems: molecular flexibility, polarization, and chemical reactivity (bond formation and breaking). From the impetus of this thesis, our interest in ReaxFF stems from its potential application to model gold nanoheaters[1] (plasmonic nanoparticles), where the explicit inclusion of atomic polarization can have a significant effect on the interfacial thermal conductance.[2–4] ReaxFF has previously been used to study aqueous systems of gold nanoparticles,[5] but not at the elevated temperatures nanoheaters reach. Accurate ReaxFF water models would also pave the way for simulation studies of $H^+_{(aq)}/OH^-_{(aq)}$ transport under thermal fields, including thermally-driven pH gradients.[6]

The water-2017 and CHON-2017_weak ReaxFF force fields have been used to model a wide range of phenomena in water and water-containing systems, for example: hydrogen bonding in supercritical water[7]; water isotope dynamics[8]; water-graphene/graphene oxide interfaces[9–12]; anion exchange membranes[13,14]; and polymer biodegradation[15]. Benchmarks of CHON-2017_weak water at higher than ambient temperatures and pressures (sub- and supercritical) have already been performed.[16] However, many important thermodynamic and transport properties have not been calculated at “ambient" (300 K) conditions, and astoundingly few along the standard pressure 1 bar

isobar. Additionally, there have been recent efforts to refine the predicted thermodynamic properties of ReaxFF water through the improved description of electrostatics and long-range dispersion interactions.[17,18] More comprehensive benchmarks may help direct these efforts. Hence, we report herein a comprehensive analysis of the thermophysical properties of state-of-the-art ReaxFF models of water, and analyze the performance of these force fields against non-dissociative and non-polarizable empirical force fields that are widely used in the literature.

7.1.2 ReaxFF in the context of state-of-the-art water models

Despite their simplicity, empirical force fields have achieved great success in reproducing the structural, thermodynamic and transport properties of liquid water over a broad range of temperatures and pressures. Arguably the most successful general purpose water model for thermodynamic properties,[19] TIP4P/2005[20] reproduces the phase diagram and anomalous properties of water fairly accurately.[19] Another rigid force field, SPC/E[21] remains one of the most popular models for liquid water, and predicts a dielectric constant in better agreement with experiment. Flexible models such as TIP4P/2005f, SPC/Fw[22] and mSPCFw[23] incorporate intramolecular degrees of freedom through O-H bond and H-O-H angle potentials. Early central force models of water incorporated for the first time self-dissociation effects and flexibility in an empirical force field. These force fields predict thermophysical properties that are in general, in good agreement with experiments.[24,25] Explicitly including polarization in water simulations remains an open challenge, with classical approaches either modelling charge redistribution within each atom (e.g., induced dipole and Drude oscillator methods), or charge flow between atoms (e.g., fluctuating charge models).[26–29] A key motivation for incorporating polarization effects is the accurate description of water's dipole moment in both the vapour and liquid phases using a single force field. Many-body potentials go beyond the pairwise approximation, explicitly considering higher-order terms in the interaction energy.[30] The mW model is a widely used coarse grained model of water that explicitly incorporates three body terms[31]. The majority of the empirical water models developed to date, with the exception of central force models, are non-dissociative; they are unable to describe the formation and breaking of chemical bonds.

Ab initio methods are able to model bond dissociation, but remain prohibitively expensive for many applications. Even so, the accurate description of water by DFT is a work in progress, with the Jacob's ladder of approximations providing more accurate but costly descriptions at each progressive rung.[32] Many popular GGAs underestimate the bulk density of water,[32] and predict that the density of ice is higher than water (ice sinks in water).[32–34] When modelling water at the experimental density of 1 g cm^{-3}, GGA functionals typically predict an overstructured liquid with

a low self-diffusion coefficient.[32] These problems persist even for hybrid functionals and when accounting for nuclear quantum effects (NQEs).[32,33,35] Dispersion corrections help ameliorate these deficiencies because semi-local functionals do not describe the long-range electron correlations that gives rise to the asymptotic r^{-6} decay in interaction energy.[32] meta-GGA functionals can offer an improved description of structure and dynamics,[34,36,37] and the SCAN functional notably predicts the correct order of water and ice densities.[34] A proportion of exact exchange (i.e., hybrid functionals) together with a well-chosen treatment of dispersion may provide an accurate description of liquid water at ambient conditions, but this level of theory is limited to simulations of around 100s of atoms for 10s of picoseconds, even with today's state-of-the-art supercomputers.

Semi-empirical methods (e.g., DFTB and MOPAC) and reactive force fields (RFFs) (also called dissociative force fields) offer more computationally feasible routes to modelling chemical reactivity. Of the latter, ReaxFF models can accommodate simulations of many (10s of) thousands of atoms on the nanosecond timescale using (state-of-the-art) high-performance computing facilities. The first-generation ReaxFF water force field was parameterized against DFT (X3LYP/6-311G**) data, primarily fitting to energetic benchmarks (such as dissociation curves, binding energies and reaction barriers) for single molecules, dimers, clusters and ice, while also targetting properties of the bulk liquid when deciding on the final parameter set.[38] The first-generation ReaxFF force field describes water dissociation and the structural migration of solvated protons (the Grotthus mechanism), but underestimates the bulk density of liquid water by ∼8% at 298 K and ambient pressure,[39] and predicts the incorrect order of $H_2O/H_3O^+/OH^-$ diffusion coefficients.[38] The second-generation ReaxFF force field (water-2017) remedied these deficiencies by including the experimental density and $H_2O/H_3O^+/OH^-$ diffusion coefficients as training data in the reparameterization of the first-generation force field.[39] Additional DFT reference data was also included to improve the structure of the hydrated OH^- ion. Another ReaxFF force field designed to model water, CHON-2017_weak is a reparameterization of the protein-2013[40] RFF (and thus indirectly of the first-generation water RFF) that improves the description of weak interactions in condensed phase functionalized hydrocarbon/water systems.[41]

7.2 Methods

7.2.1 ReaxFF models

This chapter focuses on structural, dynamic and thermodynamic properties of two ReaxFF water models: water-2017[39] and CHON-2017_weak[41]. ReaxFF employs a bond-order formalism in conjunction with a fluctuating charge description of polarization.[42] A fundamental assumption of ReaxFF is that the bond-order BO_{ij} between atom pairs (i, j) is a function of their interatomic

distance r_{ij}, and distinguishes between contributions

$$BO_{ij} = BO_{ij}^{\sigma} + BO_{ij}^{\pi} + BO_{ij}^{\pi\pi} \tag{7.1}$$

from σ-, π-, and double π-bonds. The ReaxFF potential energy E_P^{total} is given by the additive terms

$$E_P^{\text{total}} = E_P^{\text{bond}} + E_P^{\text{val}} + E_P^{\text{tor}} + E_P^{\text{over}} + E_P^{\text{under}} + E_P^{\text{vdW}} + E_P^{\text{Coulomb}} + E_P^{\text{specific}} \tag{7.2}$$

which are the bond-order dependent energies associated with two-body bonds E_P^{bond}, three-body valence angle strain E_P^{val}, four-body torsional angle strain E_P^{tor}, overcoordination E_P^{over}, and undercoordination E_P^{under}. E_P^{specific} encompasses system-specific contributions. For water these are the lone-pair E_P^{lp} and hydrogen-bonding E_P^{HB} energies, which are also bond-order dependent. The van der Waals, E_P^{vdW}, and Coulomb, E_P^{Coulomb}, energies are given by bond-order independent shielded and tapered pair potentials. Atomic partial charges are assigned on-the-fly using a charge equilibration method, traditionally (and for the RFFs considered in this work) the electronegativity equalization method[43] (EEM),[42,44] although methods such as ACKS2 and eReaxFF have been developed in order to address some of the deficiencies of EEM and extend its range of application.[45] Thus, ReaxFF accounts for polarizability through atomic charge fluctuations. Variations in molecular geometry and interactions with the environment translate into changes in the electrostatic moments.

ReaxFF force fields can be categorised as three-centre, flexible, polarizable, and dissociative within the typical classifications of water models. We additionally benchmark the mSPCFw force field[23] , which models water as a three-site molecule with flexible bonds and H-O-H angle. Hence, it provides a more direct connection with the geometry of the ReaxFF water molecules, while mSPCFw does not explicitly include electronic polarization or bond dissociation. We will also compare the ReaxFF benchmarks with data from the literature for state-of-the-art rigid models, specifically TIP4P/2005.

7.2.2 Simulation details

We performed both equilibrium and non-equilibrium molecular dynamics (MD) simulations. All simulations were carried out using the open-source software package LAMMPS (v. 7Aug2019).[44,46,47] The equations of motion were integrated using the velocity Verlet algorithm and a timestep of $\delta t = 0.2$ fs (unless stated otherwise). 3D periodic boundary conditions were applied in all simulations, except for those of a single molecule in vacuum for which finite (non-periodic) boundary conditions were used. In the ReaxFF charge equilibration procedure, a relative residual norm tolerance of 10^{-6} was used for the employed Preconditioned Conjugate Gradient method.[44]

We note in passing that due to poor energy conservation, it is difficult to perform sufficiently long simulations using ReaxFF force fields in the NVE ensemble. For CHON-2017_weak and water-2017 we observed temperature drifts of (15.1 ± 0.2) K ns^{-1} and (17.2 ± 0.2) K ns^{-1}, corresponding to 0.997 g cm^{-3} and the temperature windows 304-313 K and 297-307 K, respectively. The reasons behind this have recently been addressed.[48,49] We therefore relied on the mSPCFw force field to assess the extent to which the employed temperature-control algorithms affected dynamic properties, as compared to the NVE results.

Simulations of bulk liquid water

Equilibrium simulations of bulk liquid water were performed in the NVT and NPT ensembles. NVT simulations were carried out at 300 K and the corresponding experimental density of 0.997 g cm^{-3}, while NPT simulations were performed at 1 bar and temperatures ranging from 180-370 K. Temperature was controlled by the Nosé-Hoover chain thermostat, with 3 chains, and a time constant of 0.5 ps. Pressure was controlled with a Nosé-Hoover chain barostat, also with 3 chains, and a time constant of 2 ps. Unless stated otherwise (e.g., for the finite-size analyses) a cubic simulation box containing 521 water molecules was used. For the 521-molecule NVT systems, sampling consisted of 7-10 statistically independent replicas, each equilibrated for 200 ps followed by a 2 ns production run. For the NPT simulations, a single replica was performed for each temperature, with at least 200 ps of equilibration followed by a 10-15 ns production run for the ReaxFF force fields, and 10-20 ns for mSPCFw. Additional details are reported in section 7.3.

For mSPCFw, the electrostatic interactions were handled using the P^{3}M implementation[50] of the Ewald summation method, with a root mean square (RMS) error in per-atom forces of 10^{-6} relative to the force two point charges of elementary charge exert on each other at a distance of 1 Å. A cutoff of 9.8 Å was used for the oxygen-oxygen Lennard-Jones (LJ) potential, and tail corrections[51] were applied to the total potential energy and pressure.

Simulations of the liquid-vapour interface

Direct coexistence simulations of the liquid-vapour interface were carried out in order to calculate the surface tension. An elongated (tetragonal) simulation cell with dimensions $(L_x, L_y, L_z) = (30, 30, 200)$ Å and containing 1024 water molecules stabilised a liquid slab surrounded by vacuum, with two symmetrical interfaces perpendicular to L_z. Simulations were performed in the NVT ensemble at 300 K using the Nosé-Hoover chain thermostat, with 3 chains, and a time constant of 0.5 ps. A single replica was run for each force field, consisting of 200 ps of equilibration followed by 3 ns of production from which data was collected.

For mSPCFw, both electrostatic and dispersion interactions were calculated using the standard 3D Ewald summation method, with a relative RMS per-atom force error of 10^{-6}. The long-range dispersion interactions are required to obtain coexistence densities consistent with the densities obtained using NPT simulations that include tail corrections for the Lennard-Jones potential.

Non-equilibrium molecular dynamics simulations

Boundary-driven non-equilibrium molecular dynamics (NEMD) simulations were used to model water in the stationary state, and thereby calculate the thermal conductivity. An elongated (tetragonal) simulation cell of dimensions $L_x = L_y = 25$ Å was used, while L_z was varied to investigate finite-size effects (see Sec. 7.3.13). In all cases the number of molecules was chosen to give an average density of $\rho_{\text{box}} = 0.997$ g cm^{-3}. Two thermostatting regions, hot and cold, of width 5 Å were located at the edges and centre of the box, respectively (see Fig. 7.15). The thermostatting regions extended in the (x, y) plane such that the temperature gradients were generated along the z-direction. A Langevin thermostat with a damping parameter of 20 fs was applied to all atoms within these regions, while the trajectories of all other atoms were evolved using standard Newtonian dynamics. The system's centre-of-mass velocity was subtracted from each atom at every timestep in order to ensure good linear momentum conservation. In the stationary state, this setup results in two equal but opposite temperature gradients, such that the system is completely periodic. The heat flux across the system, $\boldsymbol{J}_q = (0, 0, \pm J_q)$, can be obtained from the continuity equation

$$J_q = \frac{|\langle \Delta U \rangle|}{2\delta t A} \tag{7.3}$$

where $A = L_x \times L_y$ is the cross-sectional area of the simulation box, δt is the timestep, and ΔU is the internal energy exchanged at each timestep, between each thermostatting region and its thermal reservoir. The factor of 2 in the denominator accounts for the two heat fluxes (equal magnitude and opposite direction) generated in this setup.

To ensure adequate sampling, 10 statistically independent replicas were run for each set of simulation conditions. Each replica consisted of at least an initial 200 ps to establish the stationary state, followed by trajectories spanning 1-2 ns for data collection.

For mSPCFw, the electrostatic interactions were handled using the P^{3}M method[50], again with a relative RMS per-atom force error of 10^{-6}. A cutoff of 9.8 Å was used for the oxygen-oxygen Lennard-Jones potential.

TABLE 7.1: Thermophysical properties of water at 300 K and 0.997 g cm^{-3}, as predicted by ReaxFF and mSPCFw force fields. Symbol meanings are given in the main text. Parentheses contain the statistical uncertainties or estimated errors in the least significant figure.

	CHON-2017_weak	water-2017	mSPCFw	Experiment
P [bar]	138(3)	−178(3)	−214(2)	11 [a]
$\langle r_{\mathrm{OH}}^{\mathrm{bond}} \rangle$ [Å]	0.981(1)	0.989(1)	1.034(1)	-
$\langle \theta_{\mathrm{HOH}}^{\mathrm{angle}} \rangle$ [°]	105.2(1)	105.7(1)	109.1(1)	-
$r_{\mathrm{OO}}^{\mathrm{max},1}$ [Å], $g_{\mathrm{OO}}^{\mathrm{max},1}$, $n_{\mathrm{OO}}^{\mathrm{max},1}$	2.85(3), 2.33(1), 1.8(2)	2.68(1), 3.62(2), 0.9(1)	2.73(1), 3.200(5), 1.26(8)	2.80(1), 2.57(5), 1.48(7) [b]
$r_{\mathrm{OO}}^{\mathrm{min},1}$ [Å], $g_{\mathrm{OO}}^{\mathrm{min},1}$, $n_{\mathrm{OO}}^{\mathrm{min},1}$	3.39(1), 0.681(3), 4.7(1)	3.49(2), 0.813(2), 5.1(1)	3.27(2), 0.738(2), 4.2(1)	3.45(4), 0.84(2), 5.0(2) [b]
$n_{\mathrm{OO}}(r_{\mathrm{OO}} = 3.30$ Å)	4.44(1)	4.36(1)	4.30(1)	4.3(1) [b]
($\langle q_{\mathrm{O}} \rangle$, $\sigma(q_{\mathrm{O}})$) [e]	−0.7122(2), 0.0210(4)	−0.7435(2), 0.0250(8)	−0.82, 0	-
($\langle q_{\mathrm{H}} \rangle$, $\sigma(q_{\mathrm{H}})$) [e]	0.3561(1), 0.0203(3)	0.3718(1), 0.0246(5)	0.41, 0	-
($\langle \mu_{\mathrm{COM}} \rangle$, $\sigma(\mu_{\mathrm{COM}})$) [D]	2.0382(6), 0.1153(9)	2.1322(6), 0.1305(9)	2.3602(6), 0.1382(9)	2.9(6) [c] and 2.95(10) [d]
($\langle \mu_{\mathrm{GC}} \rangle$, $\sigma(\mu_{\mathrm{GC}})$) [D]	2.0386(6), 0.1055(9)	2.1329(6), 0.1165(9)	2.3602(6), 0.1382(9)	-
μ_{rigid} [D]	2.038(3)	2.133(3)	2.361(4)	-
$Q_{T,\mathrm{rigid}}$ [D Å]	1.559(4)	1.667(4)	2.097(5)	-
$\mu_{\mathrm{rigid}}/Q_{T,\mathrm{rigid}}$ [Å^{-1}]	1.307(4)	1.280(3)	1.126(3)	-
$\Delta_{\mathrm{l}}^{\mathrm{g}}\mu$ [D]	−0.370(1) [e(ii)], −0.371(1) [e(ii)]	−0.387(1) [e(i)], −0.388(1) [e(ii)]	−0.155(2)	−1.1(1) [f]
O-H stretch, $\tilde{\nu}$ [cm^{-1}]	3000(20), 3260(40)	3170(20), 3390(40)	3420(20)	3404 [g]
H-O-H bend, $\tilde{\nu}$ [cm^{-1}]	1900(20)	1840(20)	1650(10)	1644 [g]
Librations (A_2, B_2, B_1), $\tilde{\nu}$ [cm^{-1}]	440(10)	490(30)	520(30)	400-800 [h] (430, 650, 794) [i]
Intermolecular stretch, $\tilde{\nu}$ [cm^{-1}]	∼120-240 [j]	-	∼140-280 [j]	162 [i], 172-175 [k]
Cage vibrations, $\tilde{\nu}$ [cm^{-1}]	40(10)	40(10)	50(10)	65 [i], 60 [k]
(C_V, C_V^{qc}) [J K^{-1} mol^{-1}]	104.5(9), 68(1)	98(1), 61(1)	111.1(6), 73.8(8)	74.41(7) [l]
C_V^{Δ} [J K^{-1} mol^{-1}], $C_V^{\Delta,\mathrm{intra}}$ [%]	−36.1(4), 68(1)	−37.5(5), 66(1)	−37.3(5), 66(1)	-
D_0 [10^{-5} cm^2 s^{-1}]	2.93(5)	3.64(5)	2.40(3)	2.41(2) [m]
(η_{GK}, η_{YH}) [mPa s]	0.70(7), 0.60(9)	0.54(2), 0.50(7)	0.85(1), 0.9(1)	0.854(9) [n]
λ [W K^{-1} m^{-1}]	0.826(4) [o]	0.839(7) [o]	0.873(1) [o]	0.609(4) [p]

[a] IAPWS-95 formulation[52] from the NIST database for 0.99700 g cm^{-3}. Note that the experimental density corresponding to 300 K and 1 bar is 0.997 g cm^{-3} to 3 decimal places. [b] From Ref. 53, or calculated from the RDF (and associated error) if not provided in text. Corresponds to 295 K and ambient pressure. [c] From Ref. 54. Corresponds to (297.60 ± 0.05) K and ambient pressure. [d] From Ref. 55. Corresponds to 300 K. Extracted from experimental refractive index data with the support of classical and *ab initio* simulations. [e] Using (i) $\langle \mu_{\mathrm{COM}} \rangle$ and (ii) $\langle \mu_{\mathrm{CG}} \rangle$ for the dipole moment of liquid water. [f] Using the liquid and gas phase dipole moments from Ref. 33 and Refs. 56,57, respectively. [g] From Refs. 58,59. Corresponds to room temperature and ambient pressure, with measurements in Ref. 59 being carried out at 298 K. [h] From Refs. 58,60,61 corresponding to room temperature and ambient pressure. [i] From Ref. 60 corresponding to 297 K and 128 bar. [j] Shoulder in the oxygen atom power spectrum (see Sec. 7.3.3) [k] From Ref. 61 and works cited therein. Corresponds to room temperature and ambient pressure conditions. [l] IAPWS-95 formulation[52] from the NIST database. The uncertainties in C_P are ±0.1%. Usually the C_V uncertainties in the liquid region follow from those given for C_P, so uncertainties of ±0.1% have also been assumed. However, owing to the unclear data situation, a more conservative estimate of ±0.75% has also been given in Ref. 52. [m] From Ref. 62. The stated absolute error limit of ≤ 1% is given in parentheses. [n] From Ref. 63. Corresponds to 300 K and 1 bar. [o] The linear response (LR) values corresponding to 300 K and 1.00 g cm^{-3} (see Sec. 7.3.13). [p] From Ref. 64. Corresponds to 300 K and 1 bar. The uncertainty corresponds to the maximum deviation of 0.7% from primary experimental data.

TABLE 7.2: Thermodynamic properties of water at standard pressure, as predicted by ReaxFF water and mSPCFw force fields. All properties correspond to 300 K and/or 1 bar, except for coexistence properties (ΔH_{vap} and Π) which correspond to the vapour pressure at 300 K. Symbol meanings are given in the main text. Parentheses contain the statistical uncertainties or estimated errors in the least significant figure.

	CHON-2017_weak	water-2017	mSPCFw	Experiment
ρ [g cm^{-3}]	0.9921(2)	1.0032(1)	1.0067(1)	0.99656(1) [a]
α_P [10^{-4} K^{-1}]	2.0(2)	3.3(2)	4.4(1)	2.7 [b]
T_{MD} [K]	255(3)	205(6)	252(3)	277 [b]
ΔH_{vap} [kJ mol^{-1}]	49.27(5)	52.09(6)	52.49(6)	43.908(7) [c]
Π [mN m^{-1}]	67(2)	59(1)	63(1)	71.7(4) [d]
β_T [Mbar^{-1}]	38.2(3)	31.8(1)	42.5(2)	45.1 [b]
$T_{\min(\beta_T)}$ [K]	260(40)	None	None	319 [b]
(C_P, C_P^{qc}) [J K^{-1} mol^{-1}]	106(1), 70(2)	100.9(6), 63(1)	115(1), 78(2)	75.32(8) [e]
(C_V, C_V^{qc}) [J K^{-1} mol^{-1}]	105(1), 69(2)	99.0(7), 62(1)	113(1), 75(2)	74.41(7) [e]
C_V^{Δ} [J K^{-1} mol^{-1}], $C_V^{\Delta,\mathrm{intra}}$ [%]	−36.0(5), 68(1)	−37.4(5), 66(1)	−37.3(4), 66(1)	-
γ, γ^{qc}	1.006(1), 1.008(2)	1.019(2), 1.031(3)	1.022(1), 1.032(1)	1.012(1) [e]
($T_{\min(C_P)}$, $T_{\min(C_P^{\mathrm{qc}})}$) [K]	None, None	270(30), None [f]	None, None	310(10) [e]
(c_S, c_S^{qc}) [m s^{-1}]	1629(7), 1632(7)	1789(4), 1799(4)	1551(4), 1559(4)	1501.5 [g]
($T_{\max(c_S)}$, $T_{\max(c_S^{\mathrm{qc}})}$) [K]	260(40), 260(40)	None, None	None	347 [b]

[a] IAPWS-95 formulation[52] from the NIST database. Uncertainty of 0.001%.

[b] Determined from the IAPWS-95 formulation from the NIST database. The associated uncertainty is less than the stated level of precision.

[c] IAPWS-95 formulation[52] from the NIST database. Uncertainty from Ref. 65.

[d] From Ref. 66. Uncertainties are estimated based on the reliability of the experimental data.

[e] IAPWS-95 formulation[52] from the NIST database. The uncertainties in C_P are ±0.1%. Usually the C_V uncertainties in the liquid region follow from those given for C_P, so uncertainties of ±0.1% have also been assumed. However, owing to the unclear data situation, a more conservative estimate of ±0.75% has also been given in Ref. 52.

[f] Or moved to a lower temperature: $T_{\min(C_P)} > T_{\min(C_P^{\mathrm{qc}})}$.

[g] IAPWS-95 formulation[52] from the NIST database. Uncertainty of ±0.005%.

7.3 Results and discussion

All statistical uncertainties reported for quantities calculated in this work refer to the standard error of the mean, unless stated otherwise.

7.3.1 Radial distribution functions

Radial distribution functions (RDFs), $g(r)$, and coordination numbers n were calculated using a bin width of 0.01 Å. Oxygen-oxygen $g_{\mathrm{OO}}(r_{\mathrm{OO}})$, oxygen-hydrogen $g_{\mathrm{OH}}(r_{\mathrm{OH}})$ and hydrogen-hydrogen $g_{\mathrm{HH}}(r_{\mathrm{HH}})$ RDFs are shown in Fig. 7.1, and numerical values for the first maxima/minima are reported in Table. 7.1. The O-O RDF is a primary figure of merit for the structure of water models. While nuclear quantum effects (NQEs) soften the first peaks of g_{OO}, g_{OH} and g_{HH},[67,68] the g_{OO} is much less affected by NQEs, and therefore provides a fairer comparison for simulations with classical nuclear dynamics.

Regarding the experimental reference, there has been controversy about the height of the first peak (see literature cited in Ref. 53), but the high-energy x-ray diffraction measurements[53] we compare to are generally accepted to supersede earlier work. Compared to our simulations these measurements correspond to slightly different thermodynamic conditions, 295 K and ambient pressure, while the experimental reference for g_{OH} and g_{HH} from neutron diffraction measurements[69] correspond to 298 K and 1 bar. We additionally show the g_{OO} from Ref. 69, noting that the qualitative comparisons to the shape of the first peak do not change. More recent x-ray measurements[70–72] extend the temperature range examined, and report ambient condition O-O RDFs in very good agreement with Ref. 53.

The CHON-2017_weak O-O RDF features a broader peak and underestimated first maximum $g_{\mathrm{OO}}^{\mathrm{max},1}$. In contrast, the water-2017 O-O RDF possesses a narrower peak, and an overestimated $g_{\mathrm{OO}}^{\mathrm{max},1}$. Although slightly overestimated, CHON-2017_weak has a peak position $r_{\mathrm{OO}}^{\mathrm{max},1} = (2.85 \pm 0.03)$ Å in better agreement with the experimental value of (2.80 ± 0.01) Å than water-2017, which underestimates the position of the first maximum with $r_{\mathrm{OO}}^{\mathrm{max},1} = (2.68 \pm 0.01)$ Å. Likewise, CHON-2017_weak better predicts the position of the first minimum $r_{\mathrm{OO}}^{\mathrm{min},1}$, but the depth of the minimum is exaggerated. water-2017 better reproduces the first minimum, but slightly overestimates $r_{\mathrm{OO}}^{\mathrm{min},1}$. Both RFFs accurately reproduce the second peak, which is characteristic of tetrahedral order.

Classical force fields, including TIP4P/2005, SPC/E and mSPCFw (this work), typically underestimate $r_{\mathrm{OO}}^{\mathrm{max},1}$ and overestimate $g_{\mathrm{OO}}^{\mathrm{max},1}$, while the longer range structure is more accurately reproduced (although TIP4P/2005 underestimates the position of the second peak $r_{\mathrm{OO}}^{\mathrm{max},2}$ by ~ 0.6 Å at 300 K and 1 bar).[73] However, with $g_{\mathrm{OO}}^{\mathrm{max},1} = (3.62 \pm 0.02)$ Å, the over-structuring of the first maximum exhibited by water-2017 is more severe. DFT descriptions beyond GGA functionals (e.g., meta-GGAs, hybrid functionals, possibly with dispersion corrections and accounting for

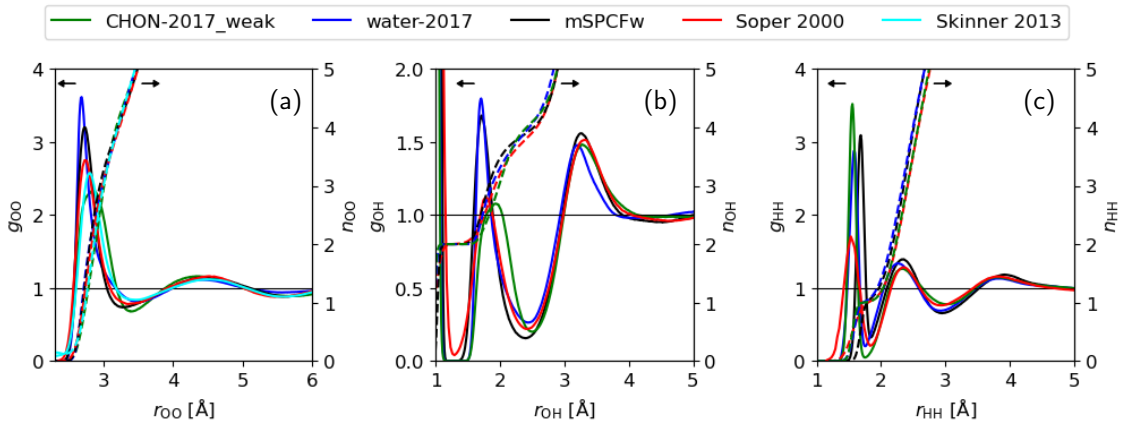


FIGURE 7.1: Radial distribution functions (RDFs) of liquid water at 300 K and 0.997 g cm^{-3} as predicted by selected force fields. (a) Oxygen-oxygen RDFs g_{OO} and coordination numbers n_{OO}. (b) Oxygen-hydrogen RDFs g_{OH} and coordination numbers n_{OH}. (c) Hydrogen-hydrogen RDFs g_{HH} and coordination numbers n_{HH}. $r_{\alpha\beta}$ is the radial distance between species α and β. Experimental RDFs are from Refs. 53,69.

NQEs)[32,34,36,74] and many-body potentials, for example MB-pol[73,75], can offer more accurate predictions of the first O-O RDF peak at ambient temperatures than the RFFs and classical models.

Both RFFs are in relatively good agreement with the experimental value[53] of $n_{OO}(R_c/\text{Å} = 3.30) = 4.3 \pm 0.1$, which corresponds to the first minimum in $r_{OO}^2 g_{OO}(r_{OO})$; water-2017 agrees within the associated uncertainties, while CHON-2017_weak slightly overestimates $n_{OO}(R_c/\text{Å} = 3.30)$. These are inline with popular empirical models which typically give $n_{OO}(R_c/\text{Å} = 3.30)$ values of 4.3-4.4.[22] The agreement in the coordination numbers shows the local structure is well reproduced by the classical force fields, the main deficiency being the lack of delocalization of water molecules in the hydrogen bonding network, as reflected in the over-structured g_{OO} first maximum. This deficiency can, at least in part,[68] be attributed to NQEs, which are not explicitly accounted for.

The O-H RDF is instructive because its maximum at $r_{OH} \simeq 1.75$-1.80 Å directly probes the hydrogen bond between donor H and acceptor O. For CHON-2017_weak the height of this peak is in good agreement with experiment[69], while water-2017 and mSPCFw overestimate the height of the peak by ∼50-60%. The coordination numbers for these three models, the two RFFs and mSPCFw, are very similar (see Fig. 7.1(b)), showing that the key difference between CHON-2017_weak and water-2017 is the delocalization of the hydrogen bond structure, reflected in the lower and wider first maximum of CHON-2017_weak. The position of the first intermolecular maximum is slightly overestimated (underestimated) by CHON-2017_weak (water-2017 and mSPCFw) with $r_{OH} \simeq 1.94$ Å ($r_{OH} \simeq 1.70$-1.72 Å), indicative of a longer (shorter) and therefore weaker (stronger) hydrogen bond. Overall these results indicate that CHON-2017_weak predicts weaker hydrogen bonding. Advancing the discussion below, we will see that this is reflected in the enthalpy of

vaporization, which is also lower for CHON-2017_weak.

The H-H RDFs show different trends. In this instance, the position of the first maximum is very similar for both RFFs, and lower than the mSPCFw prediction since the RFFs have shorter average bond lengths $\langle r_{\mathrm{OH}}^{\mathrm{bond}} \rangle$ and smaller average bond angles $\langle \theta_{\mathrm{HOH}}^{\mathrm{angle}} \rangle$ (see Table 7.1). Beyond the intramolecular peak ($r_{\mathrm{HH}} \simeq$ 1.5-1.7 Å) the intermolecular long-range structure ($r_{\mathrm{HH}} > 2$ Å) agrees reasonably well with the experiments for all the models, both in phase and height of the maxima/minima.

We note that the water-2017 RDFs reported herein are consistent with Ref. 17, while those in Ref. 39 are in better agreement with experiment. We are able to reproduce the RDFs in Ref. 39 using a bin width of 0.1 Å, and therefore attribute this discrepancy to the different bin width employed in our work (0.01 Å), which results in the better resolution of the RDF maxima.

7.3.2 Atomic charges and electrostatic moments

In EEM, atomic partial charges are assigned on-the-fly with the view of minimizing the total electrostatic energy of the system under constraints of net system charge.[43,44] The atomic charge distributions of the ReaxFF water models at 300 K and 0.997 g cm^{-3} are shown in Fig. 7.2; averages and standard deviations are given in Table 7.1. Both RFFs predict atomic charges with smaller magnitudes compared to the classical mSPCFw model, and indeed all models in the SPC family (SPC, SPC/E, SPC/Fw, SPC/Fd), which are arguably the most successful (certainly the most popular) 3-site models of water. In 3-site models, partial charges are assigned to each atom, making them the most suitable for comparison to the RFFs.

In our simulations, the global charge neutrality constraint in EEM ensures that the whole system has a net-zero charge,[44] but no such condition is imposed on individual molecules. Consequently, we observe molecule charge distributions centred on zero, but with non-zero standard deviations of (0.0378 ± 0.0008) e and (0.0452 ± 0.0008) e for CHON-2017_weak and water-2017, respectively. Only the lowest-order non-zero electric multipole moment of a charge distribution is translationally invariant. For ReaxFF water molecules this is the total charge, and dipole moments are therefore origin dependent. In order to gauge the sensitivity of molecular dipole moment on the choice of origin, we compare the dipole moments defined relative to the centre of mass μ_{COM} and centre of geometry μ_{GC}. These dipole distributions are shown in Fig. 7.2(c), and are characterised by means that differ by only $\sim 10^{-3} - 10^{-4}$ D due to the choice of origin. However, standard deviations differ more appreciably, by $\sim 10^{-2}$ D. The instantaneous differences $\mu_{\mathrm{COM}} - \mu_{\mathrm{GC}}$ (Fig. 7.2d) are slightly more significant, with $\langle |\mu_{\mathrm{COM}} - \mu_{\mathrm{GC}}| \rangle = (0.0479 \pm 0.0008)$ D and $\langle |\mu_{\mathrm{COM}} - \mu_{\mathrm{GC}}| \rangle = (0.0578 \pm 0.0008)$ D for CHON-2017_weak and water-2017, respectively.

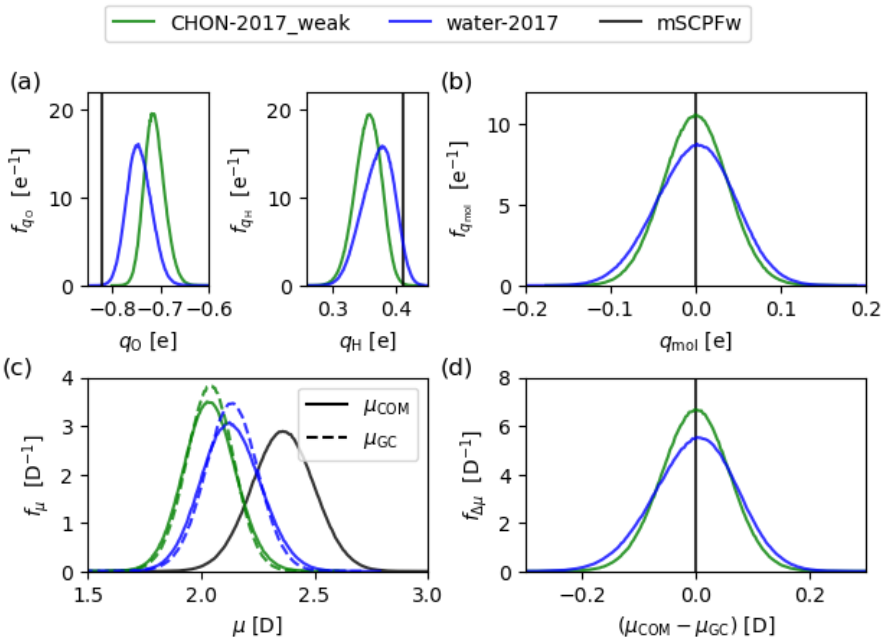


FIGURE 7.2: Atomic charge and molecular multipole moment probability density functions f_X (where X is the variable) for liquid water at 300 K and 0.997 g cm^{-3}, as predicted by selected force fields: (a) Oxygen (left) and hydrogen (right) atomic charges q_O and q_H, respectively; (b) total molecular charge q_{mol}; (c) molecular dipole moment μ as measured relative to the centre of mass, μ_{COM}, and centre of geometry, μ_{GC}; and (d) the instantaneous difference $\Delta\mu = \mu_{COM} - \mu_{GC}$.

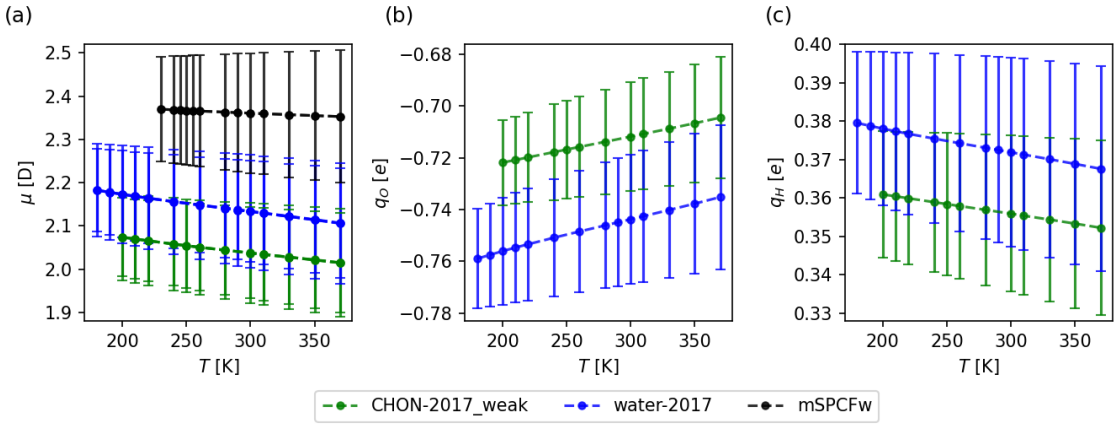


FIGURE 7.3: (a) Molecular dipole moments μ, (b) oxygen atomic charges q_O, and (c) hydrogen atomic charges q_H of liquid water at temperatures T along the 1 bar isobar, as predicted by selected force fields. In all cases the error bars represent the standard deviation σ. In (a), both $\sigma(\mu_{COM})$ and $\sigma(\mu_{GC})$ are shown with $\sigma(\mu_{COM}) > \sigma(\mu_{GC})$, while $\langle\mu_{GC}\rangle$ and $\langle\mu_{GC}\rangle$ cannot be distinguished on the scale of the plot.

For both RFFs, the smaller atomic charges translate into smaller average dipole moments of ∼2.04 D and ∼2.13 D for CHON-2017_weak and water-2017, respectively, which are underestimated compared to the experimental value[54,55] of ∼2.95 D, but of the same order as the dipole

moment of central force models[25]. The mSPCFw dipole moment of ∼2.36 D is also underestimated compared to experiment, and is similar to the dipole of state-of-the-art 4-site models, namely TIP4P/2005 and OPC (see Table 7.3). The atomic charges and dipole moments along the 1 bar isobar are shown in Fig. 7.3. For the dipole (atomic charge) distributions, average magnitudes increase (decrease) with temperature. The standard deviations increase with temperature, with $\sigma(\mu_{\mathrm{COM}}) > \sigma(\mu_{\mathrm{GC}})$ for the dipole moment.

The multipole moments of water are crucial for building accurate water models. For non-polarizable rigid models $2.4 \leq \mu/\mathrm{D} \leq 2.6$ and $2.2 \leq Q_T/(\mathrm{D\ \AA}) \leq 2.4$ have been shown to produce the highest quality models for liquid water,[76] and a $\mu/Q_T \sim 1.0\ \mathrm{\AA}^{-1}$ ratio is particularly important for reproducing the phase diagram of water, specifically the right order of stability for the phases of ice.[77,78] $Q_T = (Q_{xx} - Q_{yy})/2$ is a convenient measurement of the quadrupole moment; it is an origin-independent scalar in the frame of reference where the z-axis bisects the H-O-H angle and the x-axis is parallel to the line joining the two hydrogen atoms. The reduction of the quadrupole moment tensor to Q_T relies on the $C_{2\mathrm{v}}$ symmetry imposed at all times by rigid models, but not by flexible and/or polarizable models. For the flexible models at finite temperature, we therefore calculate $Q_{T,\mathrm{rigid}}$, and additionally μ_{rigid}, as if the molecules were rigid, using the average bond length, bond angle and atomic partial charges obtained from the MD simulations. This approach assumes that the charge and geometry contributions to the multipole moments are decoupled, and that fluctuations from the average values do not have a significant impact. In the liquid phase (Table 7.1) μ_{rigid} agrees with the MD estimates to within their associated uncertainties, while differences $\sim 10^{-2}$-10^{-3} D are observed for the RFF water molecules in vacuum (Table 7.3), indicating that these are good approximations. At 300 K and 0.997 g cm^{-3}, the RFFs have much lower quadrupole moments of $Q_T \approx$ 1.5-1.6 D Å, and greater ratios $\mu/Q_T \approx 1.3\ \mathrm{\AA}^{-1}$, while mSPCFw has values inline with popular rigid force fields.

The RFFs and mSPCFw are able to model the shift in dipole moment $\Delta^{\mathrm{g}}_{\mathrm{l}}\mu$ when going from the liquid to vapour phase. At 300 K, and approximating the vapour phase by a water molecule in vacuum, we obtain $\Delta^{\mathrm{g}}_{\mathrm{l}}\mu$ values between −0.37 D and −0.39 D for the RFFs, and a smaller $\Delta^{\mathrm{g}}_{\mathrm{l}}\mu \approx -0.16$ D for mSPCFw. In the latter case the change is solely due to the modification of molecular geometry, while for the RFFs we decompose $\Delta^{\mathrm{g}}_{\mathrm{l}}\mu$ into contributions from the change in atomic charge and the change in molecular geometry, again using the average charges and geometries given in Table 7.1 and Table 7.3. For both RFFs, the majority of $\Delta^{\mathrm{g}}_{\mathrm{l}}\mu$ originates from the charge contribution: 88-90% for CHON-2017_weak and 92-93% for water-2017. The dipole moment of a water molecule in vacuum has been experimentally determined to be 1.855 D.[56,57] CHON-2017_weak and water-2017 underestimate this value by 10% and 6%, respectively, while in contrast mSPCFw overestimates it by 18%. All three force fields greatly underestimate the shift in dipole moment of $\Delta^{\mathrm{g}}_{\mathrm{l}}\mu \sim -1.1$ D expected from experiment[54–57].

TABLE 7.3: Molecular geometry and multipole moments of a water molecule in vacuum for selected force fields. $r_{\mathrm{OH}}^{\mathrm{bond}}$ and $\theta_{\mathrm{HOH}}^{\mathrm{angle}}$ are the O-H bond length and H-O-H bond angle, respectively; q_{H} is the atomic partial charge for hydrogen; μ and Q_T are the dipole and quadrupole moment, respectively. Statistical uncertainties in the least significant figure are given in parentheses.

Model	$r_{\mathrm{OH}}^{\mathrm{bond}}$ [Å]	$\theta_{\mathrm{HOH}}^{\mathrm{angle}}$ [°]	q_{H} [e]	μ [D]	Q_T [D Å]	μ/Q_T [Å^{-1}]
CHON-2017_weak	0.953[a], 0.956(1)[b]	104.14[a], 104.8(1)[b]	0.2989[a], 0.2986(1)[b]	1.6824[a], 1.668(1)[b], 1.674(3)[c]	1.2170[a], 1.233(3)[c]	1.3824[a], 1.357(4)[c]
water-2017	0.950[a], 0.954(1)[b]	103.16[a], 103.8(1)[b]	0.3108[a], 0.3102(1)[b]	1.7631[a], 1.745(1)[b], 1.754(3)[c]	1.2413[a], 1.261(3)[c]	1.4203[a], 1.391(4)[c]
mSPCFw	1.012[a], 1.015(1)[b]	113.24[a], 113.1(1)[a]	0.41	2.1930[a], 2.205(2)[b], 2.201(4)[c]	2.1095[a], 2.118(5)[c]	1.0396[a], 1.039(3)[c]
SPC/E	1.0	109.47	0.4238	2.3505	2.0356	1.1547
TIP4P/2005	0.9572, 0.1546[d]	104.52	0.5564	2.3052	2.2969	1.0036
OPC	0.8724, 0.1594[d]	103.6	0.6791	2.4797	2.2997	1.0782
Experiment[56,57,83]	-	-	-	1.855	2.56(1)	0.723(4)

[a] Geometrically optimised molecules (0 K).

[b] Average (mean) at 300 K. The canonical distribution was sampled using the Nosé-Hoover chain thermostat, with 3 chains, and a time constant of 0.5 ps.

[c] Calculated using the average molecular geometry and atomic partial charges at 300 K.

[d] The distance r_{OM} between the oxygen atom and the massless M site that carries the negative charge in these 4-site models. M is coplanar with the O and H sites and bisects the H-O-H angle.

Comparing to DFT, many functionals of varying levels of theory (semi-local, van der Waals and hybrid functionals) are able to reproduce the experimental dipole moment of a water molecule in vacuum to within 3%.[79] Estimates of the liquid phase dipole moment, using maximally localized Wannier functions to spatially partition electron density, typically range from 2.8-3.3 D depending on the functional,[79,80] with the SCAN functional giving[80] (2.94 ± 0.28) D at 330 K (an elevated temperature was used to crudely[36] approximate NQEs) in good agreement with experimental[54,55] values. Thus, despite being parameterized primarily using DFT data, the RFFs predict dipole moments much less accurately. Indeed, the first generation ReaxFF water model (on which CHON-2017_weak and water-2017 are based) used Mulliken charges as target parameters, although a relatively low weight was placed on these. Although still widely used, the Mulliken population analysis is (among other problems) extremely sensitive to basis set choice, and care must be taken to ensure the obtained partial charges are chemically meaningful. For this reason, Mulliken charges for a single water molecule have been shown to be unreliable, irrespective of the electronic structure method used.[81,82] Recent benchmarks have shown that the Mulliken population analysis performs relatively poorly compared to other charge partitioning schemes for the assignment of atomic partial charges and dipole moments in water systems including the isolated water molecule, dimer, and clusters.[82]

7.3.3 Vibrational power spectrum

The unambiguous assignment of spectral features to the molecular-scale dynamics of liquid water remains a challenge due to the fluctuating nature of the hydrogen bonding network in which hydrogen bonds are continually broken and reformed, and the presence of both intra- and intermolecular couplings between vibrational modes.[84–87] In order to probe key dynamics, we calculate the vibrational power spectrum from the Fourier transform of the velocity autocorrelation function (VACF) of all atoms,

$$I(\nu) \propto \lim_{t' \to \infty} \int_{-t'}^{t'} \langle \boldsymbol{v}_j(t) \cdot \boldsymbol{v}_j(0) \rangle e^{-i2\pi\nu t} dt \tag{7.4}$$

where I is the intensity, ν is the vibrational frequency, $\boldsymbol{v}_j$ is the velocity of atom j, and t is the elapsed time from an arbitrary starting time. The power spectrum allows an investigation of vibrational frequencies independently of infrared (IR) and Raman selection rules, while the calculation of these spectra would be required for direct comparisons with experiment.[88] We additionally calculate the vibrational frequencies of a single water molecule in vacuum (Table 7.4) from the eigenvalues of the dynamical matrix. The dynamical matrix (mass-weighted Hessians) of the geometrically optimised molecules were calculated using the finite-difference method, using a displacement of 10^{-4} Å.

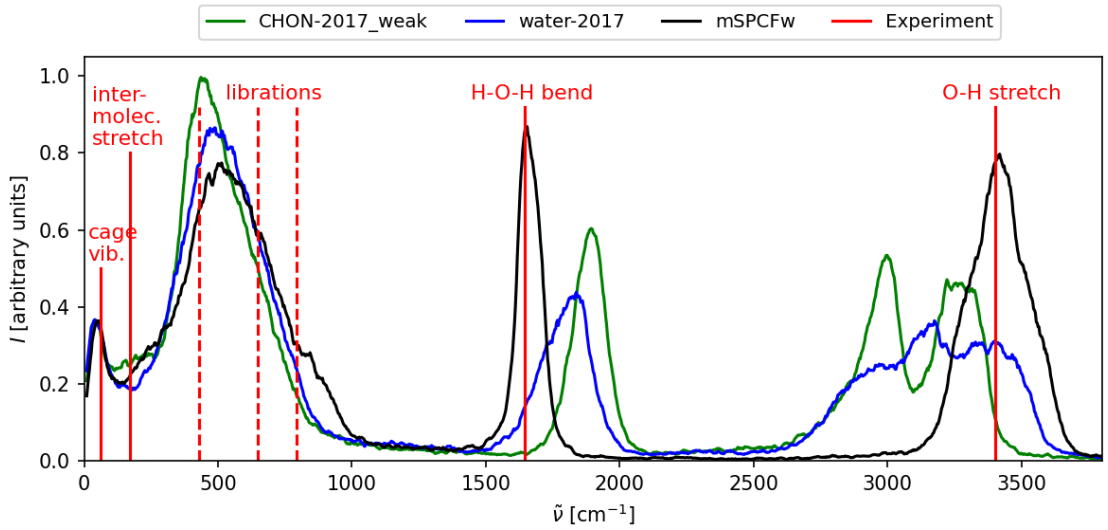


FIGURE 7.4: Vibrational power spectrum of liquid water at 300 K and 0.997 g cm^{-3}, as predicted by selected force fields. I is the intensity at wavenumber $\tilde{\nu}$. Power spectra share the same normalization condition $\int_0^\infty I(\tilde{\nu})d\tilde{\nu} = C$, where C is a constant. Experimental lines are from Refs. 58–61.

The power spectra at 300 K and 0.997 g cm^{-3} are shown in Fig. 7.4, and the peak positions are given in Table 7.1. The IR spectrum of liquid water at ambient conditions features a broad and asymmetric O-H stretching peak at ∼3400 cm^{-1}. The RFFs possess red-shifted stretching regions, and do not reproduce the single peak: CHON-2017_weak predicts two distinct maxima, while water-2017 predicts two maxima and a shoulder. This peak splitting has previously been observed for CHON-2017_weak, and was attributed to the large difference between gas phase symmetric ν_1 and asymmetric ν_3 stretching frequencies.[8] We also find this to be the case, with CHON-2017_weak and water-2017 yielding differences of 228 cm^{-1} and 156 cm^{-1}, respectively, compared to 99 cm^{-1} from experiment. mSPCFw predicts $\tilde{\nu}_1 - \tilde{\nu}_3 = 85$ cm^{-1} in better agreement with experiment, and reproduces the single O-H stretching peak in its liquid power spectrum. Indeed, classical force fields that employ Morse potentials for the O-H bond, such as mSPCFw and TIP4P/2005f, feature this single peak, while harmonic potentials neglect bond anharmonicity and often lead to peak splitting. This peak splitting has been also observed in central force type models.[25] The introduction of anharmonicity results in an additional red-shift in the stretching modes, and eventually a single stretching peak.[89] Additionally, both RFFs possess a H-O-H bending frequency blue-shifted relative to experiment: by ∼ 260 cm^{-1} for CHON-2017_weak and ∼ 200 cm^{-1} for water-2017.

Red-shifts in the O-H stretching frequency and blue-shifts in the H-O-H bending frequency are positively correlated with the strength of the H_2O-HOH hydrogen bond.[84,87,91–93] Comparing the frequency shifts moving from vacuum to the liquid phase for CHON-2017_weak, water-2017

TABLE 7.4: Normal mode frequencies of a water molecule in vacuum for selected force fields. $\tilde{\nu}_1$, $\tilde{\nu}_2$ and $\tilde{\nu}_3$ denote the wavenumbers of the symmetric stretch, bend and asymmetric stretch, respectively.

Model	$\tilde{\nu}_1$ [cm^{-1}]	$\tilde{\nu}_2$ [cm^{-1}]	$\tilde{\nu}_3$ [cm^{-1}]	$(\tilde{\nu}_3 - \tilde{\nu}_1)$ [cm^{-1}]
CHON-2017_weak	3128	1783	3356	228
water-2017	3331	1576	3487	156
mSPCFw	3649	1584	3734	85
Experiment[90]	3657	1594	3756	99

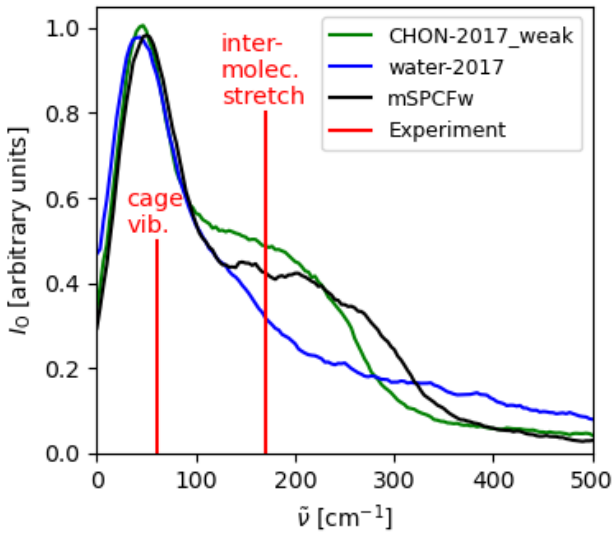


FIGURE 7.5: Oxygen atom power spectra of liquid water at 300 K and 0.997 g cm^{-3} as predicted by selected force fields. I_O is the intensity at wavenumber $\tilde{\nu}$. Power spectra share the same normalization condition $\int_0^\infty I_O(\tilde{\nu})d\tilde{\nu} = C$, where C is a constant. Experimental lines are from Refs. 60,61.

and mSPCFw, the O-H stretching (H-O-H bending) frequencies are red-shifted (blue-shifted) upon hydration by ∼110 cm^{-1} (∼120 cm^{-1}), ∼130 cm^{-1} (∼260 cm^{-1}) and ∼270 cm^{-1} (∼70 cm^{-1}), respectively. The experimental red-shift (blue-shift) in stretching (bending) frequency is ∼ 300 cm^{-1} (∼ 50 cm^{-1}). Both RFFs underestimate (overestimate) the shift in stretching (bending) frequency, while mSPCFw predicts shifts in good agreement with experiment. The RFFs predict gas phase stretching frequencies ∼270-530 cm^{-1} lower than experiment, and the CHON-2017_weak ν_2 bend is additionally blue-shifted by ∼ 190 cm^{-1}. It is therefore impossible for the RFFs investigated here to predict both accurate liquid phase frequencies and shifts from the gas phase.

The vibrational spectra of liquid water feature a broad band spanning 400-800 cm^{-1} corresponding to the three libration modes;[58,60,61] this is reproduced by the RFFs, as well as mSPCFw and TIP4P/2005f[94], which all predict a maximum located between the experimental A_2 and B_2 mode peaks[60,61] (as determined[60] by Guassian deconvolution). Intermolecular stretching is not observed as a peak in the power spectrum for both the RFFs and mSPCFw. However, a shoulder

centred around 200 cm^{-1} is observed in the oxygen atom power spectrum $I_O(\nu)$ (Fig. 7.5) for CHON-2017_weak and mSPCFw, but not for water-2017, indicating[95] the presence of this O-O stretch along the H-bond direction. Interestingly, TIP4P/2005f does display this peak in the power spectrum of hydrogen velocities relative to oxygen velocities, albeit at a slightly higher frequency of 230 cm^{-1}.[94] Both RFFs, as well as mSPCFw and TIP4P/2005f[94], have a peak ∼40-50 cm^{-1} corresponding to cage vibrations[95], close to the Raman peak[60,61] near 60 cm^{-1}.

7.3.4 Potential energy curves of the water monomer and dimer

The ReaxFF force field parameterization procedure included fitting various potential energy curves (PECs) to those predicted by quantum-mechanical methods.[38,39,41] In Fig. 7.6 we compare the PECs predicted by the RFFs and mSPCFw, for bond dissociation and angle strain in the isolated water molecule, and hydrogen bonding in the water dimer.

For the intramolecular PECs, only the single oxygen-hydrogen distance r_{OH} or H-O-H angle θ^{angle}_{HOH} parameter was varied; all other degrees of freedom were constrained to the values of the minimum-energy geometry, which has potential energy E_P^{min}. The O-H bond dissociation energy D_0^{bond} of both RFFs are in good agreement with the experimental value[96] of 492.21 kJ mol^{-1} for H_2O[16] (which includes NQEs); with values (percent errors) of 465.60 kJ mol^{-1} (−5%) and 497.52 kJ mol^{-1} (1%) for CHON-2017_weak and water-2017 respectively, CHON-2017_weak slightly underestimates D_0^{bond}. mSPCFw reproduces the experimental D_0^{bond} because it was parameterized to do so.[23]

The insets in Fig. 7.6 show the intramolecular PECs close to their minima, where the harmonic approximation is valid. Fitting harmonic potentials of the form $E_P(r_{OH}) - E_P^{min} = k_b(r_{OH} - r_0)^2/2$ to the region $r_0 \pm 0.01$ Å gives O-H bond force constants k_b/(kJ mol^{-1} $Å^{-2}$) of 3472, 3807 and 4585 for CHON-2017_weak, water-2017 and mSPCFw, respectively. The RFF force constants are smaller than the ∼ 4400 kJ mol^{-1} $Å^{-2}$ typically employed in classical models with harmonic bonds,[22,97,98] and the fitted k_b for mSPCFw. Similarly, fitting harmonic potentials $E_P(\theta^{angle}_{HOH}) - E_P^{min} = k_a(\theta^{angle}_{HOH} - \theta_0)^2/2$ to the region $\theta_0 \pm 0.5$ ° gives k_a/(kJ mol^{-1} rad^{-2}) of 480 and 367 for CHON-2017_weak and water-2017, respectively. These RFF force constants k_a are comparable to the ∼300-400 kJ mol^{-1} rad^{-2} typically[22,23,94] used in classical models ($k_a \approx$ 424 kJ mol^{-1} rad^{-2} for mSPCFw[23]). Further reductions in the regions used to fit the force constants may lead to changes on the order of 10^0-10^1 kJ mol^{-1} $Å^{-2}$ for k_b and 10^0 kJ mol^{-1} rad^{-2} for k_a. The force constants are consistent with the order of stretching ($\tilde{\nu}$(mSPCFw) > $\tilde{\nu}$(water-2017) > $\tilde{\nu}$(CHON-2017_weak)) and bending ($\tilde{\nu}_2$(CHON-2017_weak) > $\tilde{\nu}_2$(mSPCFw) > $\tilde{\nu}_2$(water-2017)) normal mode frequencies, as given in Table 7.4.

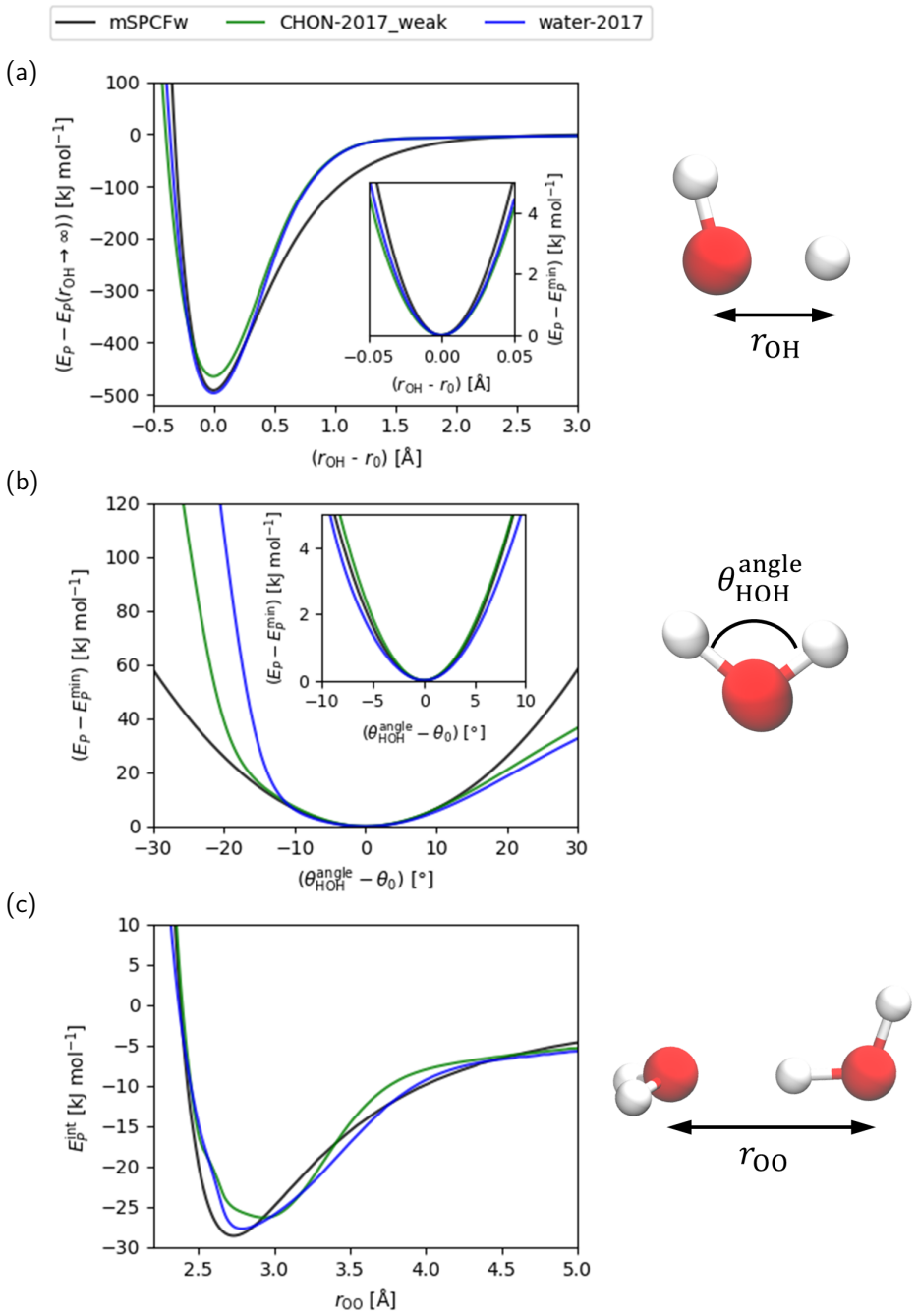


FIGURE 7.6: Potential energy curves (PECs) of the water monomer and dimer as predicted by selected force fields. (a) The water monomer bond dissociation PEC: the potential energy E_P as a function of $r_{OH} - r_0$, where r_{OH} is the oxygen-hydrogen distance and r_0 is the distance at the minimum-energy geometry; E_P is shifted relative to its value at infinite separation $E_P(r_{OH} \to \infty)$. The inset shows E_P relative to that of the minimum-energy geometry E_P^{min}, close to r_0. (b) The angle-strain PEC: $E_P - E_P^{min}$ as a function of $\theta_{HOH}^{angle} - \theta_0$, where θ_{HOH}^{angle} is the H-O-H angle, and θ_0 is θ_{HOH}^{angle} at the minimum-energy geometry. (c) The interaction energy $E_P^{int} = E_P^{min}((H_2O)_2) - 2E_P^{min}(H_2O)$ of the C_s water dimer as a function of oxygen-oxygen distance r_{OO}.

The water dimer interaction energy $E_P^{\text{int}} = E_P^{\text{min}}((H_2O)_2) - 2E_P^{\text{min}}(H_2O)$ as a function of oxygen-oxygen distance r_{OO}, for each force field, is shown in Fig. 7.6(c). Only the distance r_{OO} was constrained, and each configuration was geometrically optimized. This cut through the potential energy surface corresponds to a hydrogen-bonded structure of C_s symmetry, and passes through the global minimum. mSPCFw, CHON-2017_weak and water-2017 predict water dimer binding energies of 28.60 kJ mol^{-1}, 26.32 kJ mol^{-1} and 27.66 kJ mol^{-1}, respectively. These values are around double the experimental value[99] of $D_0^{\text{dim}} = (13.2 \pm 0.1)$ kJ mol^{-1} (including NQEs), or if comparing the potential energy surface without NQEs, ∼30-50% higher than the $D_e^{\text{dim}} \sim 20$ kJ mol^{-1} predicted by high-level *ab initio* calculations[100–102]. The RFF training data included DFT (X3LYP/6-311++G**) water dimer PECs that also give $D_e^{\text{dim}} \sim 20$ kJ mol^{-1}.[38,39] The order of dimer hydrogen bonding strength conveyed by the binding energies, mSPCFw > water-2017 > CHON-2017_weak, is consistent with the predicted enthalpies of vaporization of bulk water (see Sec. 7.3.9). The dimer PEC for CHON-2017_weak features a broader and shallower minimum, similar to the first intermolecular maximum of the O-O RDF of liquid water, which reflects the strength of the hydrogen bonds. However, the RDFs include n-body terms arising from interactions of several molecules with a central one and between themselves (see Sec. 7.3.1). Indeed, care must be taken when relating the properties of the (single C_s) water dimer to the structure and thermodynamics of bulk water, as many-body effects and configurations other than the optimal hydrogen bonding arrangement contribute to the sampled potential energy surface of bulk water at finite temperature.

7.3.5 Density and thermal expansion

The equation of state at 1 bar is shown in Fig. 7.7. The CHON-2017_weak and water-2017 RFFs give average densities of (0.9921 ± 0.0002) g cm^{-3} and (1.0032 ± 0.0001) g cm^{-3} at 300 K, respectively; these are in good agreement with the experimental value[52] of 0.9966 g cm^{-3} at the same temperature and pressure. Our results are consistent with those previously reported at 298.15 K: 0.99 g cm^{-3} for CHON-2017_weak[41] and 1.01 g cm^{-3} for water-2017[39]. mSPCFw predicts a water density of (1.0067 ± 0.0001) g cm^{-3} at 300 K, this is ∼ 2% higher than the value of 0.991 g cm^{-3} at 298 K and 1 atm reported[23] by Smirnov, and is closer to the (1.012 ± 0.016) g cm^{-3} of the original SPC/Fw model (which shares the same intermolecular potentials) at 298.15 K and 1 atm.[22] SPC/E predicts a density of 0.994 g cm^{-3} at 298.15 K and 1 atm;[103] the experimental value[52] is 0.9971 g cm^{-3}. Thus, the RFFs are of comparable accuracy to these three-point, non-polarizable force fields. Additionally, the RFFs are only marginally less accurate than the TIP4P/2005 model, which predicts 0.9972 g cm^{-3} (0.9979 g cm^{-3}) at 300 K (298 K) and 1 bar,[20,104] within 0.1% of the experimental values.

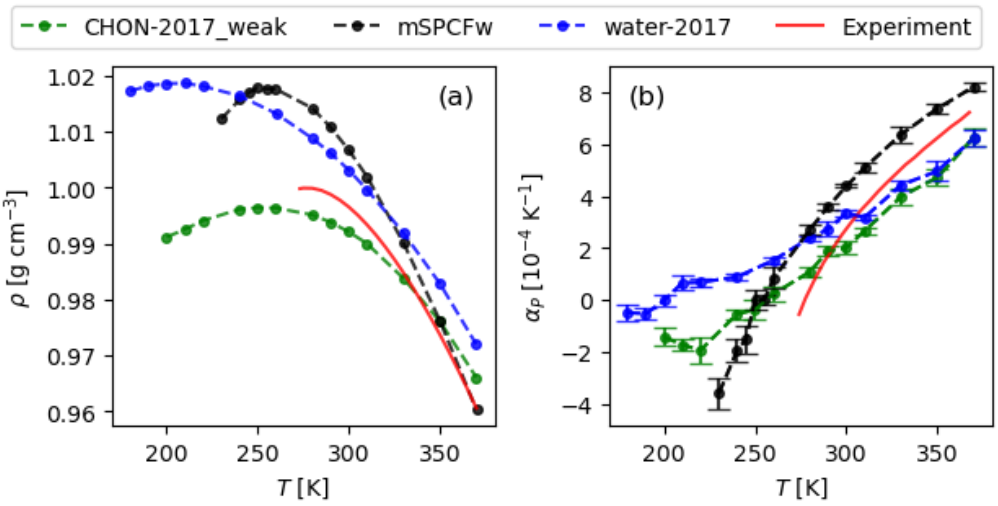


FIGURE 7.7: Density ρ (a) and thermal expansion coefficient α_P (b) of liquid water at temperatures T along the 1 bar isobar, as predicted by selected force fields. In (a), uncertainties associated with ρ are smaller than the size of the symbols. Experimental values are from Ref. 52.

We additionally compute the volumetric thermal expansion coefficient $\alpha_P = (1/V)(\partial V/\partial T)_P$ using the fluctuation relation $\langle \delta V \delta H \rangle_{NPT} = k_B T^2 V \alpha_P$, where T is temperature, V is volume, H is enthalpy, and k_B is the Boltzmann constant. $\delta\mathcal{A} = \mathcal{A} - \langle \mathcal{A} \rangle_{ens}$ where $\langle \mathcal{A} \rangle_{ens}$ is the ensemble average of variable $\mathcal{A}$. At 300 K we obtain $\alpha_P/(10^{-4}\ \mathrm{K}^{-1})$ values of 2.0 ± 0.2, 3.3 ± 0.2 and 4.4 ± 0.1 for CHON-2017_weak, water-2017 and mSPCFw, respectively; these can be compared to the experimental value of $2.7 \times 10^{-4}\ \mathrm{K}^{-1}$ calculated from the numerical derivative of the $\rho(T)$ curve[52] shown in Fig. 7.7. TIP4P/2005 predicts $\alpha_P = 2.8 \times 10^{-4}\ \mathrm{K}^{-1}$ at 298 K and 1 atm, within 10% of the experimental value of $2.56 \times 10^{-4}\ \mathrm{K}^{-1}$.[20]

The competition between hydrogen bond formation and thermal expansion leads to liquid water's anomalous density maximum, which at 1 bar occurs at 277 K.[52] Work by Paschek[105] highlighted the importance of $\rho(T)$ and $\alpha_P(T)$ for describing the hydrophobic effect in water, and in part motivated the emphasis placed on T_{MD} as a target parameter when fitting TIP4P/2005.[20] Both RFFs underestimate the temperature of maximum density T_{MD}, which were estimated by interpolating ρ and α_P: CHON-2017_weak and water-2017 predict (255 ± 3) K and (205 ± 6) K, respectively. mSPCFw also underestimates T_{MD} giving (252 ± 3) K, similar to SPC/E with T_{MD} = 240-241 K.[19,73] TIP4P/2005 was fit to closely reproduce T_{MD}, even at the expense of a more accurate melting temperature;[20] it therefore unsurprisingly achieves $T_{MD} = (277 \pm 3)$ K in agreement with the experimental value.[19,20,73,104]

7.3.6 Enthalpy of vaporization

The enthalpy of vaporization ΔH_{vap} is the change in enthalpy required to transform n mols of substance from liquid to gas phase, where each phase is under the coexistence pressure (i.e., the vapour pressure of the liquid). $\Delta H_{\text{vap}} = H_{\text{g}}(P,T) - H_{\text{l}}(P,T)$ can be written as $\Delta H_{\text{vap}} = (U_{\text{g}} - U_{\text{l}}) + P(V_{\text{g}} - V_{\text{l}})$ where $U = K + E_P$ is the internal energy, K is the kinetic energy and E_P is the potential energy. Noting that $V_{\text{g}} \gg V_{\text{l}}$ and assuming that the gas is ideal ($PV_g = nRT$ and $E_{P,\text{g}}^{\text{inter}} = 0$), one obtains $\Delta H_{\text{vap}} \approx (E_{P,\text{g}} - E_{P,\text{l}}) + nRT$ where R is the gas constant. Using experimental data, corrections to ΔH_{vap} accounting for the non-ideality of the gas phase have been estimated to be approximately -0.02 kJ mol^{-1} at 298 K, increasing in magnitude with temperature to -0.22 kJ mol^{-1} at 370 K, which is the highest temperature investigated in this work.[106] These corrections have not been taken into account in our ΔH_{vap} values. From our MD simulations we calculate:

$$\Delta H_{\text{vap}} \approx \langle E_{P,\text{g}}^{\text{intra}} \rangle - \langle E_{P,\text{l}} \rangle + nRT \tag{7.5}$$

Simulations of liquid water were carried out at an external pressure of 1 bar, rather than the vapour pressure. This should introduce a minor change in $E_{P,\text{l}}$ compared to the potential energy at the state corresponding to the vapour pressure. The difference is expected to be within the uncertainty of the simulation results, $\lesssim 2 \times 10^{-3}$ kJ mol^{-1} using Ref. 106 as a guideline. The gas-phase intramolecular potential energies $E_{P,\text{g}}^{\text{intra}}$ were from simulations of a molecule in vacuum in the NVT ensemble. We do not include a correction for NQEs, as these have been estimated to be small.[106] Nevertheless, the increase of ΔH_{vap} for isotopologues D_2O (45.48 kJ mol^{-1}) and T_2O (45.73 kJ mol^{-1}) observed experimentally indicate that NQEs are appreciable.[20] NQEs are implicitly included in classical models fit to experimental data (especially since ΔH_{vap} is often used as a target parameter), while this is not the case for RFFs if they are parameterized using only *ab initio* data.

Our results for the enthalpy of vaporization are shown in Fig. 7.8. All three force fields overestimate ΔH_{vap} compared to the experimental values, water-2017 more severely than CHON-2017_weak for the RFFs. At 300 K CHON-2017_weak, water-2017 and mSPCFw predict ΔH_{vap}/(kJ mol^{-1}) values of 49.27 ± 0.05, 52.09 ± 0.06 and 52.49 ± 0.06, while the experimental value[52,65] is 43.908 ± 0.007. We also compare ΔH_{vap}/(kJ mol^{-1}) at 300 K and 0.997 g cm^{-3}, which is the corresponding experimental density at saturation pressure: 49.30 ± 0.05, 52.05 ± 0.06 and 52.44 ± 0.06 for CHON-2017_weak, water-2017 and mSPCFw, respectively. Unsurprisingly, these constant-volume values are similar to their constant-pressure counterparts as all three force fields reproduce the experimental density at 300 K and 1 bar fairly well (see Sec. 7.3.5).

Popular rigid non-polarizable models perform much better than the ReaxFF (and mSPCFw) models investigated in this work. Models such as TIP3P, TIP4P and TIP5P reproduce ΔH_{vap}

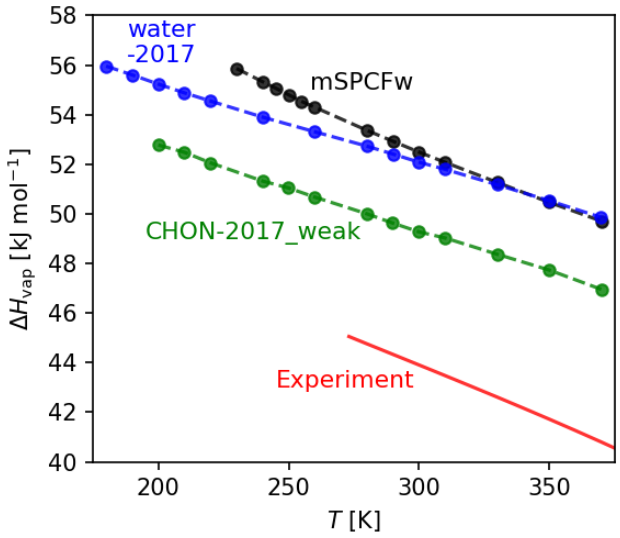


FIGURE 7.8: Enthalpy of vaporization ΔH_{vap} at temperatures T predicted by selected force fields. Uncertainties are smaller than the size of the symbols. Experimental values are from Ref. 52.

(without a polarization correction) by design and do so to within 5% at 298 K.[19,20] TIP4P/2005 includes the dipole-corrected[21] enthalpy of vaporization $\Delta H'_{vap}$ as a target parameter, but its reproduction is a compromise with other target parameters, primarily T_{MD}.[20] Similarly, SPC/E is a reparameterization of SPC accounting for this dipole correction term.[21] Thus at 298 K, TIP4P/2005 and SPC/E predict higher ΔH_{vap}/(kJ mol^{-1}) values, 50.17 and 49.33, but $\Delta H'_{vap}$/(kJ mol^{-1}) values, 45.56 and 44.12, in better agreement with experimental value[52,65] of $\Delta H_{vap} = (43.994 \pm 0.007)$ kJ mol^{-1}.[19–21] The dipole correction[21] used in these models amounts to ~ -5 kJ mol^{-1}, and accounts for the intramolecular rearrangement energy required to give the correct gas phase dipole moment. However, recent work has shown that taking into account both multipole distortion and purely electronic polarization effects, up to the quadrupole moment, results in a smaller total correction close to zero.[107] We decided not to include additional corrections since the reference systems in the vapour phase are well defined for each force field. By construction, all three force fields incorporate changes in molecular multipole moments between the liquid and vapour phases: mSPCFw through changes in molecular geometry, and the ReaxFF models through changes in geometry and atomic partial charges.

7.3.7 Surface tension

The surface tension Π is defined as the work required to create one unit area of the interface. In the NVT ensemble, this is given by $\Pi = (\partial F/\partial A)_{NVT}$ where F is the Helmholtz free energy and A is the surface area. We calculate Π based on the mechanical definition for a planar interface

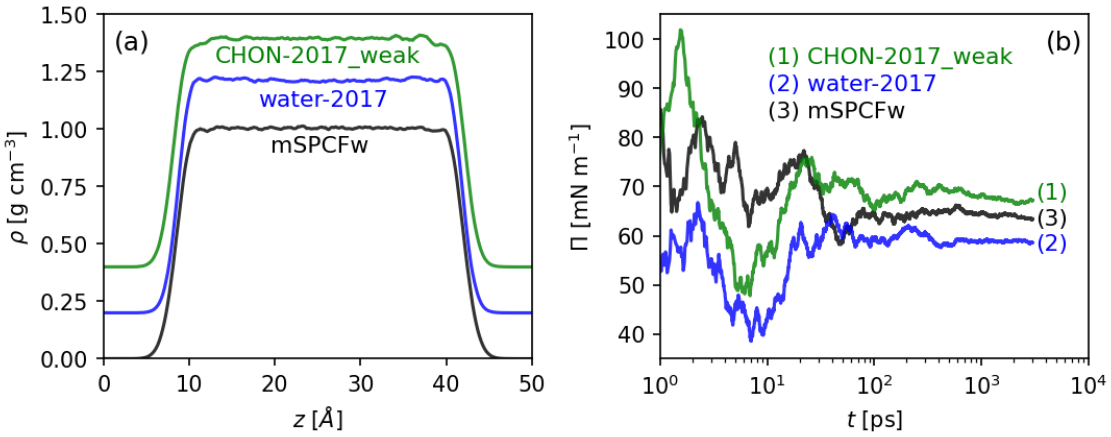


FIGURE 7.9: (a) Density ρ profiles of the liquid-vapour interface systems along the z-axis perpendicular to the interface. For clarity, the density profiles of water-2017 and CHON-2017_weak have been shifted vertically by 0.2 g cm^{-3} and 0.4 g cm^{-3}, respectively. (b) Convergence of the the surface tension Π with simulation time t.

perpendicular to the z-axis:

$$\Pi = \int_{-\infty}^{\infty} [P_N(z) - P_T(z)]dz \tag{7.6}$$

where $P_N(z)$ and $P_T(z)$ are the normal and tangential (local) components of the pressure tensor, respectively. For a planar interface, P_N is equal to the vapour pressure and is independent of position z. From our MD simulations (see Sec. 7.2.2), which stabalize two liquid-vapour interfaces, Π can be calculated as

$$\Pi = \frac{L_z}{2}\left(\langle P_{zz}\rangle + \frac{\langle P_{xx}\rangle + \langle P_{yy}\rangle}{2}\right) \tag{7.7}$$

where $P_{\alpha\alpha}$, with $\alpha = x, y, z$, are the diagonal components of the pressure tensor.

Density profiles of the interfacial systems and the convergence of Π are shown in Fig. 7.9. At 300 K, CHON-2017_weak, water-2017 and mSPCFw predict Π/(mN m^{-1}) values (percent errors) of 67 ± 2 ($-$4-9%), 59 ± 1 ($-$17-20%) and 63 ± 1 ($-$9-14%) compared to the experimental value[66] of 71.7 ± 0.4. TIP4P/2005 predicts Π = 68-69 mN m^{-1} ($-$4-5%) at 300 K, with simulation uncertainties of $\pm$1 mN m^{-1} typically being reported.[19,108–110] Thus, while water-2017 substantially underestimates Π, CHON-2017_weak predicts Π in relatively good agreement with experiment: only $\sim$3% lower than TIP4P/2005, and more accurately than many[19,109–112] classical force fields.

Since the liquid-vapour interface simulations were carried out using a single box with dimensions $(30, 30, 200)$ Å, it is not possible to perform a finite-size analysis for the surface tension values. However, the lateral dimensions $L_x = L_y = 30$ Å$\approx 9.5\sigma_{OO}$ (σ_{OO} is the characteristic diameter of the water molecule, and the "size" parameter of the oxygen-oxygen LJ potential for mSPCFw and other classical models) were chosen to ensure finite-size effects are small if not insignificant; for TIP4P/2005, Π values calculated with lateral dimensions of $7\sigma_{OO}$, $9.5\sigma_{OO}$ and $11.3\sigma_{OO}$ were found

to agree with each other to within their associated uncertainties of ≤ 1.3 mN m^{-1}. Regarding the finite slab thickness, all three systems possess Gibbs dividing surfaces separated by 33-34 Å of liquid, as determined fitting hyperbolic tangent functions to the density profiles. Negative vapour pressures $P_{\text{vap}} = P_{zz}$ were obtained for all three force fields: (-0.64 ± 0.02) bar, (-0.67 ± 0.05) bar and (-0.71 ± 0.02) bar for CHON-2017_weak, water-2017 and mSPCFw, respectively. This has previously[108,109] been observed for temperatures as low as 300 K, and is presumably due to the disjoining pressure that arises from the attractive forces between the two surfaces. The measured surface tensions are therefore systematically underestimated by 0.6-0.8 mN m^{-1} (assuming $P_{\text{vap}} \sim 10^{-2}$ bar), which is within their associated statistical uncertainties.

7.3.8 Isothermal compressibility

Water is generally approximated as an incompressible fluid at ambient temperature and pressure conditions. The isothermal compressiblity $\beta_T = -(1/V)(\partial V/\partial P)_T$ was calculated from our MD simulations using the fluctuation relation $\langle \delta V^2 \rangle_{NPT} = V k_{\text{B}} T \beta_T$. Our results for β_T are shown in Fig. 7.10 and Table 7.2. The RFFs both underestimate β_T for the temperature range investigated. At 300 K, this underestimation is by ∼15% for CHON-2017_weak (β_T/Mbar^{-1} = 38.2 ± 0.3) and ∼29% for water-2017 (β_T/Mbar^{-1} = 31.8 ± 0.1), compared to the experimental value[52] of 45.1 Mbar^{-1}. For mSPCFw, β_T values coincide with experiment at ∼315 K, with departing agreement at both higher and lower temperatures. At 300 K, mSPCFw predicts $\beta_T = (42.5 \pm 0.2)$ Mbar^{-1}, in good agreement with experiment. Indeed, popular classical models seem to offer more accurate β_T predictions compared to the RFFs, with TIP4P/2005 and SPC/E giving 46.5 Mbar^{-1} and 46.1 Mbar^{-1}, respectively, at 298 K and 1 bar,[20,104] which can be compared to the experimental value[52] of 45.3 Mbar^{-1}.

The decrease in isothermal compressibility with increasing temperature until a minimum at $T_{\min(\beta_T)}$, and the minimum itself, are considered two of the anomalous properties of water. At 1 bar, this β_T minimum occurs at 319 K.[52] Some classical models of water are able to reproduce this minimum, such as TIP4P/2005 and SPC/E, while others such as TIP5P are not.[73,104] TIP4P/2005 predicts $T_{\min(\beta_T)}$ around 310-320 K,[73,104] while SPC/E predicts a value of ∼280 K.[73] Fitting a cubic function to the $\beta_T(T)$ data for CHON-2017_weak suggests that a minimum exists at $T_{\min(\beta_T)} = (260 \pm 40)$ K, in close proximity to its temperature of maximum density. However, owing to the statistical uncertainty associated with β_T values for $T \leq 250$ K, we do not discount the possibility that the minimum disappears upon more exhaustive sampling. As shown in Fig. 7.10, water-2017 features a monotonic increase in β_T with temperature, and thus does not capture the minimum, nor the decreasing β_T for $T < T_{\min(\beta_T)}$. Likewise, a minimum is not observed for mSPCFw; as temperature is decreased along the isobar, β_T decreases then plateaus near T_{MD}.

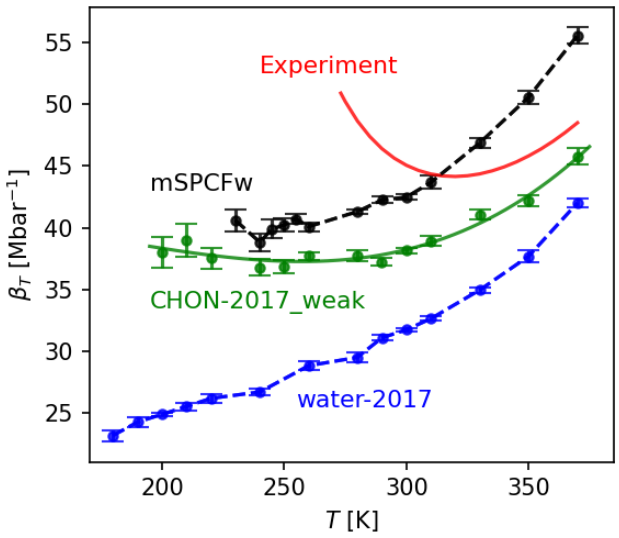


FIGURE 7.10: Isothermal compressibility β_T of liquid water at temperatures T along the 1 bar isobar, as predicted by selected force fields. Experimental values are calculated from Ref. 52.

High energy x-ray diffraction experiments show a continuous structural transition associated with the second g_{OO} peak position concomitant with the compressibility minimum, with greater tetrahedral order being observed at and below $T_{\min(\beta_T)}$.[70] The increase from near-zero intensity at $g_{OO}(r_{OO}/\text{Å} \simeq 11)$ peak from 340-320 K upon cooling further suggests that tetrahedral structures start to appear as well-defined regions around the compressibility minimum.[113] Longer range correlations also indicate a restructuring of the liquid, favouring tetrahedral H-bonding, upon cooling.[114] Two-state models[115–118] (which have garnered increasing support from experimental data) rationalize the anomalous properties of water, including the compressibility minimum, in terms of structural fluctuations between low-density liquid (enthalpy favoured through tetrahedral H-bonding) and high-density liquid (entropy favoured with a more close-packed structure, possessing a fifth neighbour in the interstitial position between the first and second coordination shells).[119] Water models that do not possess a compressibility minimum fail to capture these structural properties of water. The lack of a compressibility minimum for water-2017 indicates that this RFF is missing crucial aspects of the orientational correlations in liquid water, since these are linked to the tetrahedral order of the liquid.

7.3.9 Isobaric and isochoric heat capacity

An unusually high heat capacity is considered one of the anomalous properties of water, and is rationalised in terms of water's strong hydrogen bonding. Under thermodynamic constraints of constant pressure and constant volume, the isobaric $C_P = (\partial H/\partial T)_P$ and isochoric $C_V =$

$(\partial U/\partial T)_V$ heat capacities can be written in terms of thermodynamic potentials H and U. We compute these heat capacities from MD simulations using the fluctuation relations $\langle \delta H^2 \rangle_{NPT} = k_B T^2 C_P$ and $\langle \delta U^2 \rangle_{NVT} = k_B T^2 C_V$. C_V values corresponding to 300 K and 0.997 g cm^{-3} were calculated from NVT simulations (see Table 7.1), while C_P values at 1 bar were calculated from NPT simulations. Additionally, C_V values along the 1 bar isobar were calculated using the relation

$$C_P = C_V + VT\frac{\alpha_P^2}{\beta_T} \tag{7.8}$$

where all variables in Eq. 7.3.9 can be measured from our NPT simulations. We obtain consistent values of C_V at 300 K (corresponding to slightly different average densities) via Eq. 7.3.9 and the $\langle \delta U^2 \rangle_{NVT}$ fluctuation relation.

As evident in Fig. 7.11 values of C_P and C_V are overestimated by ∼30-60%, primarily due to the exclusion of NQEs. At 298 K, D_2O (C_V=84.42 J K^{-1} mol^{-1})[120] has a heat capacity 13% greater than H_2O (C_V=74.55 J K^{-1} mol^{-1})[52], indicating that the overall impact of NQEs is to reduce the heat capacity. Path-integral simulations incorporate NQEs by treating nuclei quantum mechanically, and when paired with a suitable potential energy surface, are able to accurately reproduce the heat capacities of H_2O and D_2O.[121] Extracting "quantum" heat capacities from classical simulations requires further approximations. The most widely adopted approach is to quantum-correct the vibrational density of states $S(\nu)$, as in the 1PT model[122], the 2PT model[123–125] and the correction of Berens[122]. Similar corrections can be applied directly to the VACF and trajectories.[126] These methods have previously been applied to liquid water.[122,126–129] The main advantage of the 2PT model is that only $S(\nu)$ and therefore short MD trajectories are required, while the correction of Berens has been shown to better account for NQEs in liquid water.[126] Additionally, the original 2PT method is not equipped to deal with bond breaking and formation.[130]

In this work we employ the method[122] of Berens, and quantum-correct C_V within a harmonic oscillator approximation.[122]

$$C_V^{qc} = C_V + C_V^{\Delta} \tag{7.9}$$

This involves integrating $S(\nu)$ with a weighting function $W_{C_V}^{\Delta}$, which is the difference between the quantum and classical weighting functions for a set of harmonic oscillators:

$$C_V^{\Delta} = k_B \int_0^{\infty} S(\nu) W_{C_V}^{\Delta} d\nu \tag{7.10}$$

$$W_{C_V}^{\Delta} = \frac{u^2 e^u}{(1-e^u)^2} - 1 \tag{7.11}$$

where $u = h\nu/(k_{\mathrm{B}}T)$ and h is Planck's constant. $S(\nu)$ was obtained from the Fourier transform of the total VACF $C(t)$, defined as the mass-weighted sum of atomic VACFs,

$$C(t) = \sum_{j=1}^{N} m_j \langle \boldsymbol{v}_j(t) \cdot \boldsymbol{v}_j(0) \rangle \tag{7.12}$$

$$S(\nu) = \frac{2}{k_{\mathrm{B}}T} \lim_{t' \to \infty} \int_{-t'}^{t'} C(t) e^{-i2\pi\nu t} dt \tag{7.13}$$

where m_j and $\boldsymbol{v}_j$ are the mass and velocity of atom j, respectively, and t is the elapsed time from an arbitrary starting time. $S(\nu)$ has the normalization $\int_0^\infty S(\nu) dv = 3N$ where N is the total number of degrees of freedom (9 per molecule for flexible water models).

This approach satisfies the correspondence principle $\lim_{\hbar \to 0} C_V^{\mathrm{qc}} = C_V$. While C_V^{Δ} does not incorporate anharmonic effects, they are included through the classical C_V. The quantum correction C_V^{Δ} is based on the division of dynamics in frequency space. The low-frequency region features major anharmonic effects but behaves nearly classically, so while the correction is less accurate, it is small. At higher frequencies, atomic motions are better approximated as harmonic and quantum effects are more significant, so while the correction is large, it is also reasonably accurate. Thus, the quantum correction can be applied over the entire frequency domain.

C_V^{Δ} values were calculated from MD simulations in the NVT ensemble with production runs spanning 500 ps. For simulations corresponding to the 1 bar isobar, the average densities from the NPT simulations were used. We show in Table 7.5 that the thermostat and reducing the timestep do not have an appreciable effect on C_V^{qc} (see Table 7.5 for numerical values).

At 1 bar the quantum-corrected heat capacities C_P^{qc} (C_V^{qc}) of the RFFs are systematically underestimated: for example, by ∼7% (∼7%) for CHON-2017_weak and ∼16% (∼17%) for water-2017 at 300 K. Similarly C_V^{qc} at 300 K and 0.997 g cm^{-3} is underestimated by ∼9% and ∼18% for CHON-2017_weak and water-2017, respectively. Once quantum-corrected, mSPCFw predicts heat capacities that are in relatively good agreement with experiment in the temperature range corresponding to liquid water. C_P^{qc} deviates from experiment by just ∼3% at 300 K and 1 bar, and the C_V^{qc} values corresponding to 300 K (both at 1 bar and 0.997 g cm^{-3}) agree with experiment withing their associated uncertainties. The C_P^{qc} values agree with experiment considering their associated uncertainties for $310 \leq T/\mathrm{K} \leq 370$. With $C_P = 88.3$ J K^{-1} mol^{-1} at 298 K and 1 bar, TIP4P/2005 overestimates C_P by ∼7%;[20] quantum-corrections bring C_V^{qc} to within ∼3% of the experimental value.[128] Rigid models are expected to have smaller heat capacities and quantum corrections than their flexible counterparts, as intramolecular modes are frozen out. Path-integral simulations with TIP4PQ/2005 underestimate C_P by ∼6% at 300 K.[121]

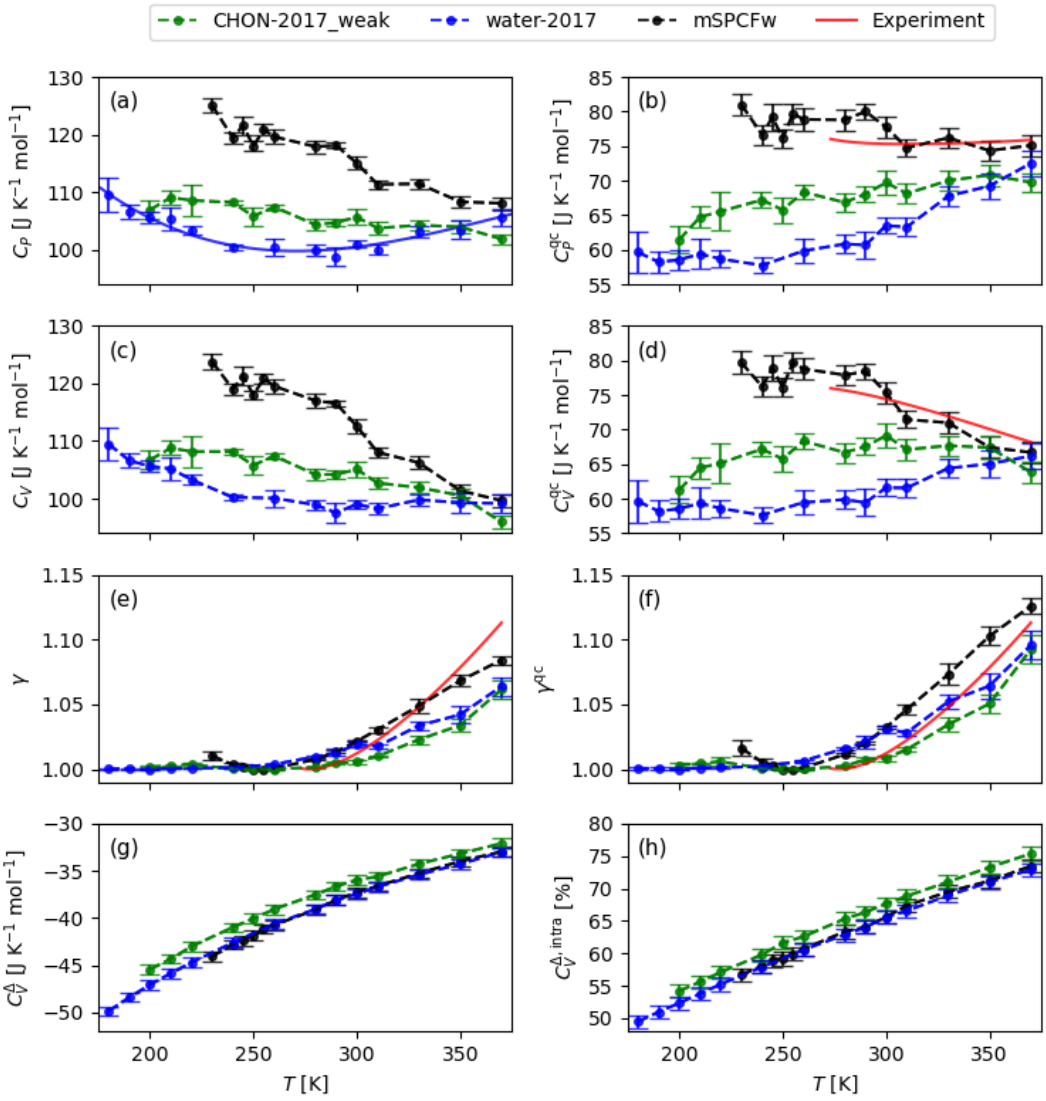


FIGURE 7.11: Heat capacities and related quantities of liquid water at temperature T along the 1 bar isobar, as predicted by selected force fields: (a) isobaric heat capacity C_P, the solid line is a cubic function fit to the water-2017 data; (b) quantum-corrected isobaric heat capacity C_P^{qc}; (c) isochoric heat capacity C_V; (d) quantum-corrected isochoric heat capacity C_V^{qc}; (e) heat capacity ratio $\gamma = C_P/C_V$; (f) quantum-corrected ratio $\gamma^{\mathrm{qc}} = C_P^{\mathrm{qc}}/C_V^{\mathrm{qc}}$; (g) quantum correction C_V^{Δ}; and (h) intramolecular contribution $C_V^{\Delta,\mathrm{intra}}$ to the quantum-correction. Experimental values are from or calculated from Ref. 52.

At 1 bar, the isobaric heat capacity of water has a minimum at ∼310 K.[52] Interestingly, water-2017 features a shallow minimum in C_P at $T_{\min(C_P)} = (270 \pm 30)$ K as determined by fitting a cubic function. This minimum is either lost or moved to a lower temperature, upon applying the quantum correction. mSPCFw and CHON-2017_weak do not possess a discernible minimum in either C_P or C_P^{qc} in the temperature interval considered here.

$|C_V^\Delta|$ increases with decreasing temperature primarily through $W_{C_V}^\Delta$ (Eq. 7.3.9); the temperature dependence of $S(\nu)$ also serves to decrease $|C_V^\Delta|$, but to a much lesser extent. The quantum corrections C_V^Δ differ by at most ∼2 J K^{-1} mol^{-1} between the RFFs and mSPCFw, while corrections for rigid models are substantially smaller.[128] We partition C_V^Δ into intramolecular and intermolecular contributions by dividing $S(\nu)$ at frequency ν_{cut} corresponding to the minimum between the libration peak and bending peak of a smoothed $S(\nu)$. The value of ν_{cut} therefore depends on the force field and thermodynamic conditions, and falls in the range 1200-1600 cm^{-1} for the thermodynamic states considered in this work. This partitioning method incurs some systematic error since intermolecular (intramolecular) interactions contribute to $S(\nu > \nu_{\text{cut}})$ ($S(\nu < \nu_{\text{cut}})$). However, this systematic error is likely small since $S(\nu_{\text{cut}}) \approx 0$, and owing to the expected cancellation of errors. The intramolecular contribution $C_V^{\Delta,\text{intra}}$ constitutes ∼66-68% of C_V^Δ at 300 K, and increases with temperature, again primarily due to the $k_\text{B}T$ terms in $W_{C_V}^\Delta$.

We additionally show the ratios $\gamma = C_P/C_V = 1 + VT\alpha_P^2/\beta_T$ and $\gamma^{\text{qc}} = C_P^{\text{qc}}/C_V^{\text{qc}}$, which show qualitatively the same temperature dependence as experiment. $\gamma^{\text{qc}} > \gamma$ as expected from $C_V^\Delta < 0$.

7.3.10 Speed of sound

In classical mechanics, the speed of sound c is given by $c^2 = dP/d\rho$. The isentropic (adiabatic) speed of sound can therefore be written in terms of the isentropic compressibility β_S as

$$c_S^2 = \frac{1}{\rho\beta_S} \tag{7.14}$$

which we calculate in turn from our NPT simulations at 1 bar using the relation

$$\beta_S = \beta_T - \frac{\alpha_P^2 T}{\rho C_P}. \tag{7.15}$$

where C_P in Eq. 7.15 is the specific quantity. We further calculate c_s^{qc} using the quantum-corrected isobaric heat capacity C_P^{qc} in Eq.7.15. The results are shown in Fig. 7.12. The inability of all three force fields to reproduce the experimental trend in c_S can be attributed primarily to their β_T values, with ρ being fairly well reproduced (see Sec. 7.3.5), and the $\alpha_P^2 T/(\rho C_P)$ term contributing between 0-8% of β_T (0-12% using C_P^{qc}) across the temperature range (e.g., 1-2% at 300 K). This is also evidenced by the $\gamma = C_P/C_V = \beta_T/\beta_S \approx 1$ values shown in Fig. 7.11, and the relatively minor impact quantum-correcting C_P has on c_S. Nevertheless, mSPCFw predicts $c_S = (1551 \pm 4)$ m s^{-1} at 300 K, just 3-4% from the experimental value of 1501.5 m s^{-1}. mSPCFw and CHON-2017_weak predictions coincide with experiment at ∼316 K (in line with β_T, see Sec. 7.3.8) and ∼370 K, respectively. At 300 K, CHON-2017_weak and water-2017 predict c_S/(m s^{-1}) values (percent errors) of 1629±7 (8-9%) and 1789±4 (19%), respectively.

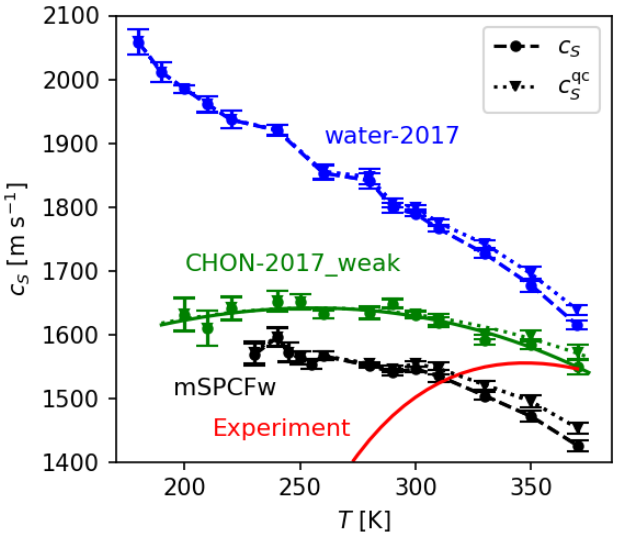


FIGURE 7.12: Isentropic speed of sound of liquid water at temperatures T along the 1 bar isobar, as predicted by selected force fields. c_S and c_S^{qc} are the classical and quantum-corrected speed of sound, respectively. For CHON-2017_weak, the solid and dotted lines show cubic functions fit to the c_S and c_S^{qc} data, respectively. Experimental values are from Ref. 52.

At 1 bar, c_S has a maximum at 347 K, in close proximity to the compressibility minimum. Fitting cubic functions to the $c_S(T)$ and $c_S^{qc}(T)$ data for CHON-2017_weak suggests that a maximum exists at $T_{\max(c_S)} = (260 \pm 40)$ K for both sets of data, coincident with the compressibility minimum. water-2017 predicts monotonically decreasing c_S values with increasing temperature, and a maximum at $T > T_{MD}$ is also not observed for mSPCFw, similar to the β_T minimum. Classical force fields that are better able reproduce β_T along the 1 bar isobar, will presumably also more accurately predict c_S. For example, TIP4P/2005 predicts c_S in excellent agreement with experiment at 1 bar and temperatures close to 300 K.[131,132]

7.3.11 Self-diffusion coefficient

We calculate the self-diffusion coefficients D from the average mean square displacement (MSD) using the Einstein relation

$$D = \frac{1}{2d} \lim_{t\to\infty} \frac{\langle |\boldsymbol{r}(t) - \boldsymbol{r}(0)|^2 \rangle}{t} \tag{7.16}$$

where t is the elapsed time from arbitrary an starting time, and $d = 3$ is the number of spatial dimensions. D was therefore calculated by fitting to the equation $\langle |\boldsymbol{r}(t) - \boldsymbol{r}(0)|^2 \rangle = 6Dt$, excluding the first 10 ps of data to ensure only the diffusive regime was sampled (as opposed to the ballistic regime). In order to account for finite-size effects, we calculate the "infinite-size" diffusion coefficient

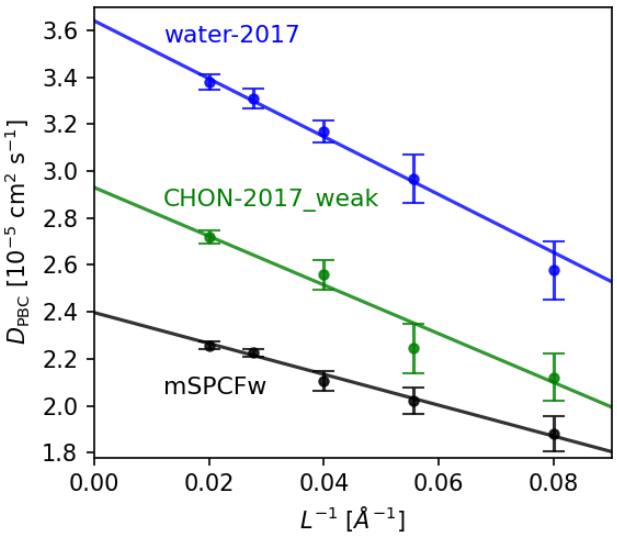


FIGURE 7.13: Finite-size analysis for the self-diffusion coefficients of liquid water at 300 K and 0.997 g cm^{-3}, as predicted by selected force fields. Extrapolation of size-dependent diffusion coefficients D_{PBC} to $L^{-1} = 0$, where L is the length of the cubic simulation box.

D_0 by extrapolation to $L^{-1} = 0$, where L is the length of the cubic simulation box. This finite-size analysis is shown in Fig. 7.13, and follows from the equation derived by Yeh and Hummer[133] using a simple hydrodynamic model of a particle surrounded by a solvent of viscosity η_{YH} in a periodically replicated simulation box,

$$D_{\mathrm{PBC}} = -\frac{\xi k_{\mathrm{B}} T}{6\pi\eta_{\mathrm{YH}}} L^{-1} + D_0 \tag{7.17}$$

where D_{PBC} are the finite-size diffusion coefficients calculated from our MD simulations, and ξ is a dimensionless constant equal to 2.837297 for a cubic simulation box with 3D periodic boundary conditions.[133] The same expression was obtained earlier[134] by Dünweg and Kremer using a closely related derivation. Equation B.14 also provides a route to estimate the shear viscosity η. From the fitted gradients and intercepts in Fig. 7.13, it is evident that force fields that predict higher diffusion coefficients also predict lower viscosities, consistent with $D \propto \eta^{-1}$ implied by the Stokes-Einstein relation.

Values for the diffusion coefficients D_0 are shown in Table. 7.1. We compare our results to a reference value[62] of $(2.41 \pm 0.02) \times 10^{-5}$ cm^2 s^{-1} at 300 K, as determined from a Speedy-Angell power-law fit to experimental data. Both RFFs overestimate the self-diffusion coefficient: by 22% for CHON-2017_weak and 51% for water-2017. This is particularly unfortunate for the water-2017 force field, which was designed in part to predict more accurate $OH^-/H_3O^+/H_2O$ diffusion compared to its predecessor.[38,39] Fitting to Eq. B.14, our value of $D_{\mathrm{PBC}} = (3.0 \pm 0.1) \times 10^{-5}$ cm^2

s^{-1} for $N = 216$ water molecules ($L \approx 18.64$ Å) is consistent with the value of 2.7×10^{-5} cm^2 s^{-1} reported by Ref. 39 – a slightly lower diffusion coefficient is expected at 298.15 K and 1.01 g cm^{-3}. For CHON-2017_weak, a diffusion coefficient of 2.5×10^{-5} cm^2 s^{-1} was previously calculated[41] at 298.15 K and 0.99 g cm^{-3}, but system sizes were not reported alongside this value, so a fair comparison to our results cannot be made. These literature values[39,41] can be compared to the experimental value[62,135] of $(2.299 \pm 0.005) \times 10^{-5}$ cm^2 s^{-1} at 298.15 K, but these simulation results do not account for finite-size effects. However, as demonstrated in this and other[133,136] work, finite-size effects can lead to strong underestimations for small system sizes. The latter are commonly used in *ab initio* MD simulations of liquid water,[32] and care should therefore be exercised when comparing these results with experimental data. For the PBE functional (not accounting for NQEs), D_0 was estimated[137] to be 0.789×10^{-5} cm^2 s^{-1} at 300 K, which is greatly underestimated compared to experiment.

The size-independent D_0 values vary appreciably between traditional classical force fields, but popular models typically outperform the RFFs, or perform similarly to CHON-2017_weak. In this work, we find mSPCFw predicts $D_0 = (2.40 \pm 0.03) \times 10^{-5}$ cm^2 s^{-1} in good agreement with the experimental value. At 300 K and 0.998 g cm^{-3}, TIP4P/2005, SPC/E and the polarizable Dang-Chang model predict $(2.49 \pm 0.05) \times 10^{-5}$ cm^2 s^{-1}, $(2.97 \pm 0.05) \times 10^{-5}$ cm^2 s^{-1} and $(2.72 \pm 0.09) \times 10^{-5}$ cm^2 s^{-1}, respectively, slightly higher than experiment.[136] TIP3P predicts $(6.10 \pm 0.03) \times 10^{-5}$ cm^2 s^{-1} at 298 K and the lower density of 0.987 g cm^{-3}.[133]

In order to target a specific thermodynamic state, the NVT ensemble was sampled using a temperature control algorithm that alters dynamics compared to the Newtonian dynamics of the NVE ensemble. It is therefore necessary to check whether the employed global Nosé-Hoover (3-chains) thermostat affects the computed self-diffusion coefficients. We demonstrate in Table 7.5, using mSPCFw, that it does not: all D_{MD} values calculated at the same temperature (304 K) agree within their associated uncertainty. This is consistent with previous work that shows that "global" velocity scaling thermostats, including the Nosé-Hoover thermostat, do not significantly alter diffusion coefficients or viscosity.[138] We additionally show in Table 7.5 that reducing the timestep to 0.1 fs does not affect the dynamical properties, D and η.

The scope of this work is limited to pure water. However, both the water-2017 and CHON-2017_weak force fields have been used to study the transport of H^+ and OH^- ions.[8,10,11,13,14,39] At room temperature and pressures close to 1 bar, the diffusion coefficient of $H_3O^+_{(aq)}$ ($OH^-_{(aq)}$) were estimated to be 10.4×10^{-5} cm^2 s^{-1} (7.8×10^{-5} cm^2 s^{-1}) and 10.9×10^{-5} cm^2 s^{-1} for water-2017[39] (at 298.15 K) and CHON-2017_weak[8], respectively. Based on the number of molecules and average densities reported in Refs. 8,39, we estimate that the diffusion coefficients correspond to box lengths of $L \approx 18.6$ Å and $L \approx 24.7$ Å for water-2017 and CHON-2017_weak, respectively. These diffusion coefficients appear to be in good agreement with the experimentally determined diffusion

TABLE 7.5: The effect of thermostat and timestep δt on the dynamics of mSPCFw water. Results correspond to a 521-molecule water-box with a density of 0.997 g cm^{-3} and average simulation temperature T. $D_{N=521}$, η_{GK} and C_V^{Δ} are the self-diffusion coefficient, Green-Kubo shear viscosity (Eq. 7.18) and quantum-correction to the isochoric heat capacity (Eq. 7.3.9), respectively. Statistical uncertainties in the least significant figure are given in parentheses.

Ensemble	δt [fs]	T [K]	$D_{N=521}$ [10^{-5} cm^2 s^{-1}]	η_{GK} [mPa s]	C_V^{Δ} [J K^{-1} mol^{-1}] [a]
NVE	0.1	304	2.28(5)	0.76(6)	−37.3(3)
NVE	0.2	304	2.31(3)	0.73(4)	−37.3(4)
NVT[b]	0.2	304	2.30(7)	0.79(6)	−37.2(4)
NVT[b]	0.2	300	2.11(4)	0.85(1)	−37.3(5)

[a] C_V^{Δ} is a thermodynamic property. However, it is calculated from the vibrational density of states, and is consequently determined by the dynamics of the system.
[b] Nosé-Hoover chain thermostat with 3 chains (see Sec. 7.2).

coefficients[139] of 9.3×10^{-5} cm^2 s^{-1} for $H_3O^+_{(aq)}$ and 5.6×10^{-5} cm^2 s^{-1} for $OH^-_{(aq)}$, corresponding to 298.15 K and infinite dilution. However, the simulated values do not account for finite-size effects and correspond to finite concentrations, but with no direct solute-solute interactions. Based on the finite-size analysis presented in Fig. 7.13, the absolute difference in the self-diffusion coefficient of water when going from $L \approx 18.6$ Å for water-2017 and $L \approx 24.7$ Å for CHON-2017_weak, to $L \to \infty$, amount to ∼18% and ∼14% (relative to D_0), respectively. While we do not necessarily expect the same system size dependence for $H_3O^+_{(aq)}$ and $OH^-_{(aq)}$, the changes in bulk water are large enough to warrant further investigation; an extrapolation to infinite system size and infinite dilution would be required to assess the importance of finite-size effects for the diffusion coefficients of these ions.

7.3.12 Shear viscosity

We calculate the shear viscosity η using two methods: the Green-Kubo relation and Eq. B.14 (see Sec. 7.3.11). The former calculates η using the integral formula

$$\eta_{\mathrm{GK}} = \frac{V}{k_{\mathrm{B}}T} \lim_{t' \to \infty} \int_0^{t'} C_{P_{\alpha\beta}}(t) dt \tag{7.18}$$

$$C_{P_{\alpha\beta}}(t) = \langle P_{\alpha\beta}(t) P_{\alpha\beta}(0) \rangle \tag{7.19}$$

where V is the volume of the simulation box, t is the elapsed time from an arbitrary start time, and $C_{P_{\alpha\beta}}(t)$ is the autocorrelation function of off-diagonal components of the pressure tensor $P_{\alpha\beta}$, where $\alpha \neq \beta$. Results were averaged over $(\alpha, \beta) = (x, y)$, (x, z) and (y, z). A correlation time of $t' = 10$ ps was used for the upper limit in the integral given above. Selecting this integration limit is a compromise between sampling efficiency and minimising the resulting truncation error. We show in Fig. 7.14 that 10 ps is sufficiently long to achieve a well-converged integral, while the exhaustive extent of our sampling is reflected in the associated statistical uncertainty.

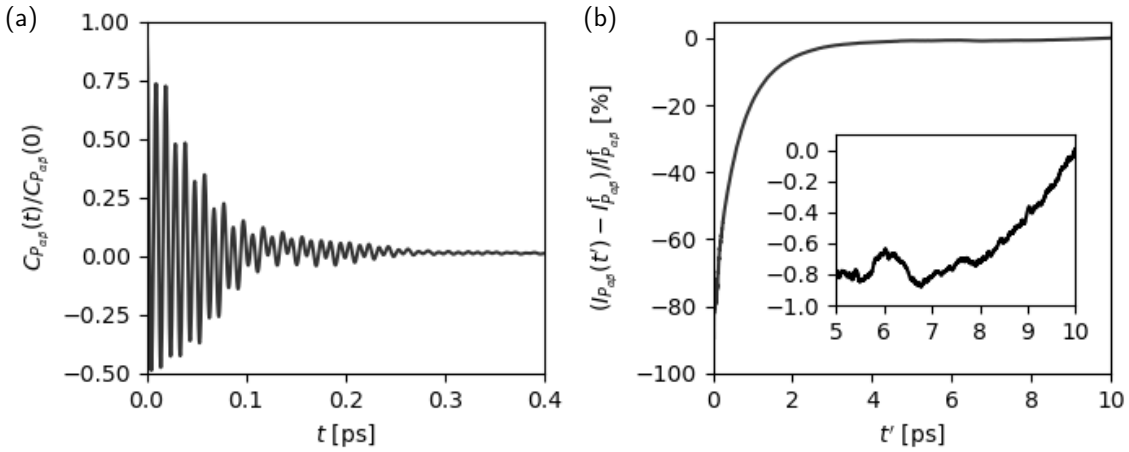


FIGURE 7.14: Shear viscosity of mSPCFw water from the Green-Kubo integral formula. (a) The normalised autocorrelation function $C_{P_{\alpha\beta}}(t)/C_{P_{\alpha\beta}}(0)$, where t is the elapsed time. (b) The convergence of the integral $I_{P_{\alpha\beta}}(t') = \int_0^{t'} C_{P_{\alpha\beta}}(t)dt$ where t' is the correlation time used as the upper limit of the integral; $(I_{P_{\alpha\beta}}(t') - I^{\mathrm{f}}_{P_{\alpha\beta}})/I^{\mathrm{f}}_{P_{\alpha\beta}}$ is the relative deviation of $I_{P_{\alpha\beta}}(t')$ from the final value $I^{\mathrm{f}}_{P_{\alpha\beta}} = I_{P_{\alpha\beta}}(t'/\mathrm{ps} = 10)$ used to calculate the viscosity.

Our calculated values for shear viscosity are shown in Table. 7.1. For all three force fields, the viscosities evaluated using Eq. B.14 and Eq. 7.18, η_{YH} and η_{GK}, respectively, agree with each other given their associated uncertainties. Both RFFs underestimate the viscosity compared to the experimental value[63] of (0.854 ± 0.009) mPa s at 300 K and 1 bar: by ∼19-26% for CHON-2017_weak and ∼34-39% for water-2017, while the mSPCFw values agree with experiment considering their associated uncertainties. Traditional classical force fields typically underestimate η near standard conditions, for example at 298 K and 1 bar with $\eta/(\mathrm{mPa\ s})$ values (percent errors) of 0.321 (−64%) for TIP3P, 0.494 (−45%) for TIP4P, 0.699 (−22%) for TIP5P, 0.855 (−4%) for TIP4P/2005, and 0.729 (−18%) for SPC/E[140], compared to the experimental value[62] of 0.893 ± 0.009. Closer to the thermodynamic conditions used in this work, at 300 K and 0.9965 g cm^{-3}, TIP4P/2005 and SPC/E predict (0.83 ± 0.01) mPa s (−3%) and (0.722 ± 0.005) mPa s (−15%), respectively.[141] The underestimation by the RFFs is comparable to this range.

We demonstrate in Table 7.5, using mSPCFw, that the employed thermostatting procedure does not significantly alter η_{GK} values. Additionally, since the thermostat does not significantly affect the self-diffusion coefficients (see Sec. 7.3.11), it is not expected to affect η_{YH}.

7.3.13 Thermal conductivity

We calculate the thermal conductivity λ from boundary-driven NEMD simulations using Fourier's Law, $\boldsymbol{J}_q = -\lambda \nabla T$, where $\boldsymbol{J}_q$ is the heat flux and ∇T is the local temperature gradient. The computation of thermal conductivity via NEMD includes all possible coupling effects. In the case

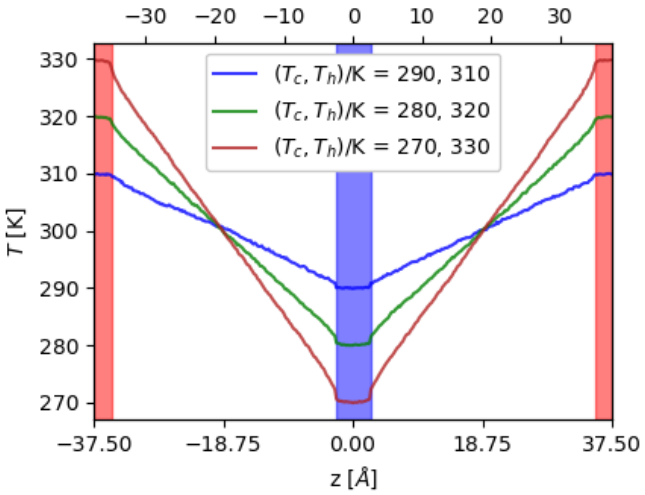


FIGURE 7.15: Representative temperature T profiles for the NEMD simulations. Data corresponds to CHON-2017_weak and $L_z = 75$ Å. The blue (cold) and red (hot) shaded areas indicate the location of the thermostatting regions, set to temperatures T_c and T_h, respectively.

polar fluids, such as water, this includes the coupling between heat and polarization fluxes,[142] as we saw in Chapter 6.

The simulation details and results are summarised in Table 7.6, and representative temperature profiles are shown in Fig. 7.15. Local densities ρ and temperatures T were determined from a 5 Å bin close to the centre of each NVE compartment. The position of the bin was chosen such that $T = 300$ K. The local temperature gradient was determined by fitting a straight line to the temperature profile within a range of ±8 Å around the selected state point; exceptions to this are noted in Table 7.6.

All the NEMD thermal conductivity values calculated in this work, for both ReaxFF and mSPCFw, range from 0.80-0.88 W K^{-1} m^{-1}, and are therefore overestimated by 31-44% relative to the experimental value[64] of (0.609±0.004) W K^{-1} m^{-1} at 300 K and 1 bar. CHON-2017_weak, water-2017 and mSPCFw overestimate λ by 31-36%, 35-39% and 41-44%, respectively. This is consistent with many other traditional classical force fields, which typically overestimate the thermal conductivity by ∼10-50% at temperatures/pressures close to 300 K and 1 bar.[25,141,143–156] Thermal conductivities at 1.00 g cm^{-3} and within 2 K of 300 K have ranged between 0.65-0.91 W K^{-1} m^{-1} for SPC/E[141,145,149,150,154–156] and 0.56-0.91 W K^{-1} m^{-1} for TIP4P/2005[141,154]. However, it was recently shown that the per-atom virial stress tensor-based instantaneous heat flux that has commonly been used in Green-Kubo and some NEMD calculations leads to inaccurate thermal conductivities (it is only rigorous for pairwise interactions).[157–159] Extensive NEMD simulations[153] that calculate $\boldsymbol{J}_q$ from the continuity equation (Eq. 8.1) set the thermal conductivities of SPC/E

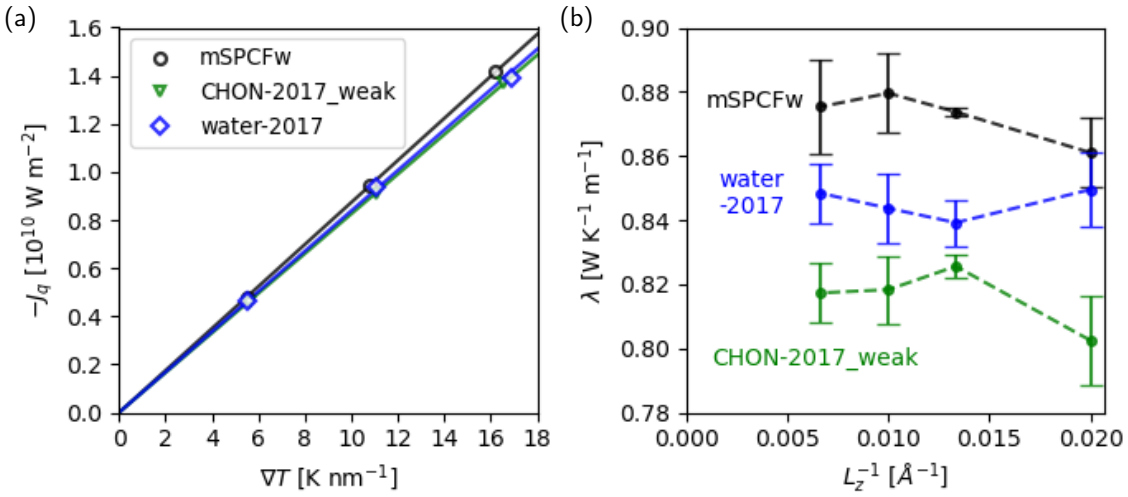


FIGURE 7.16: Thermal conductivity λ at 300 K and 1.00 g cm^{-3} as predicted by selected force fields. (a) The linear response of heat flux J_q with local temperature gradient ∇T. Results correspond to $L_z = 75$ Å. Statistical uncertainties are smaller than the symbols. (b) Finite-size analysis: L_z is the length of the simulation cell parallel to the direction of heat flux. For $L_z = 75$ Å, the results corresponding to the linear response fitted in (a) have been plotted.

and TIP4P/2005 at temperatures close to 300 K in the range 0.8-0.9 W K^{-1} m^{-1}. Comparing to a dissociative force field, the central force model predicts ∼0.63 W K^{-1} m^{-1} at 300 K and 1.00 g cm^{-3},[25] in good agreement with experiment.

The largest temperature gradients used in this work approach magnitudes of $\lesssim 20$ K nm^{-1}. This magnitude of thermal gradient is widely used in computer simulations because larger gradients reduce the noise to signal ratio in T, and the statistical uncertainty associated with λ. While experimental setups at the micro and nanoscale are approaching gradients of this magnitude [160,161], they are large by macroscopic standards. We show in Fig. 7.16(a) that all of our results are within the linear regime, and additionally calculate λ_{LR} by fitting the (∇T, $\boldsymbol{J}_q$) data to Fourier's Law.

Finite-size effects are not expected to be significant for the calculated thermal conductivity values, because the thermal transport mechanism in liquid water is dominated by collisions between nearest neighbours, setting a characteristic length scale for heat transport at around one molecular diameter (≈ 3 Å for water). We show in Fig. 7.16(b) that increasing L_z past 75 Å does not make an appreciable difference; the λ values agree to within their statistical uncertainties.

We note that the thermal conductivities reported in Table 7.6 for the same force field are not expected to be in perfect agreement. This is because they correspond to slightly different thermodynamic conditions, as indicated by the different P_{zz} values. Using the experimental pressure dependence of the thermal conductivity of liquid water along the 300 K isotherm as a guideline, we expect differences $\sim 10^{-3}$ W K^{-1} m^{-1} or less, due to the P_{zz} differences < 40 bar obtained for the same force field. Deviations in λ values are therefore expected to be within their uncertainties.

TABLE 7.6: Non-equilibrium molecular dynamics simulation parameters and results for the calculation of thermal conductivity λ. L_z is the length of the simulation box parallel to the direction of heat flux. ρ_{box}, T_{box} and P_{zz} are the average density, temperature and pressure parallel to the direction of heat flux, respectively. T_h and T_c are the temperatures of the hot and cold thermostats; ∇T is the resulting temperature gradient. All local properties (columns 8-11) were computed at thermodynamic conditions specified by density ρ and temperature T. Statistical uncertainties in the least significant figure are given in parentheses.

	L_z [Å]	ρ_{box} [g cm^{-3}]	T_c [K]	T_h [K]	T_{box} [K]	P_{zz} [bar]	ρ [g cm^{-3}]	T [K]	∇T [K nm^{-1}]	λ [W K^{-1} m^{-1}]
CHON-2017_weak	50	0.997	287	313	300	152(2)	0.998	300	11.2(2)[a]	0.80(1)
	75	0.997	290	310	300	149(3)	0.998	300	5.6(1)	0.81(2)
	75	0.997	280	320	300	156(2)	0.998	300	11.1(1)	0.82(1)
	75	0.997	270	330	300	164(3)	0.998	300	16.5(1)	0.829(7)
	75	-	-	-	-	-	0.998	300	LR[c]	0.826(4)
	100	0.997	274	326	300	150(2)	0.998	300	10.8(1)	0.82(1)
	150	0.997	280	320	300	153(1)	0.998	300	5.43(6)	0.817(9)
water-2017	50	0.997	287	313	300	−173(2)	0.998	300	11.0(1)[a]	0.85(1)
	75	0.997	290	310	300	−172(2)	0.998	300	5.5(1)	0.85(2)
	75	0.997	280	320	300	−168(3)	0.998	300	11.09(7)	0.847(6)
	75	0.997	270	330	300	−160(3)	0.998	300	16.9(1)	0.826(7)
	75	-	-	-	-	-	0.998	300	LR[c]	0.839(7)
	100	0.997	274	326	300	−176(3)	0.998	300	10.8(1)	0.84(1)
	150	0.997	260	340	300	−141(2)	0.998	300	10.7(1)	0.848(9)
mSPCFw	50	0.997	287	313	300	9(2)	0.998	300	10.6(1)[a]	0.86(1)
	75	0.997	290	310	300	9(3)	0.998	300	5.5(2)	0.87(3)
	75	0.997	280	320	300	14(1)	0.998	300	10.77(8)	0.874(9)
	75	0.997	270	330	300	31(4)	0.999	300	16.2(1)	0.875(9)
	75	-	-	-	-	-	1.00	300	LR[c]	0.873(1)
	100	0.997	285	315	300	0(1)	0.998	300	6.02(8)	0.88(1)
	150	0.997	285	315	300	7(1)	0.998	300	3.98(6)[b]	0.88(1)

[a] A range of ±5 Å was used when fitting to the temperature profile.
[b] A range of ±16 Å was used when fitting to the temperature profile.
[c] Linear response (see in text).

7.4 Conclusions

The rich phenomenology and widescale importance of water continue to motivate the development of computational models that are more accurate, cheaper and/or transferable. ReaxFF models are bond-order based reactive force fields that explicitly include polarization effects through a charge equilibration scheme. They offer an intermediate step between the capabilities of quantum-based electronic structure methods and the computational efficiency of traditional (non-reactive) empirical force fields. One of the key motivations for the development of ReaxFF force fields is the ability to model chemical reactions. Nevertheless, ReaxFF force fields should strive to accurately model both chemical reactivity and thermophysical properties. In this work, we have investigated the performance of two ReaxFF models, CHON-2017_weak and water-2017, in predicting the general thermophysical properties of water. Figure 7.17 summarizes some of our key results, presenting the deviation of 15 different properties from their experimental values. We close this article with a brief assessment of the ReaxFF models based on our results, and where possible, recommend potential avenues for improvement.

Structure of liquid water. The RFFs reproduce the RDFs of liquid water at near standard conditions reasonably well. They accurately predict the nearest O-O neighbour distance. water-2017 overestimates the height of the first g_{OO} maximum in line with classical force fields such as mSPCFw and TIP4P/2005, while the CHON-2017_weak prediction is in better agreement with the RDFs extracted from neutron and x-ray diffraction experiments. CHON-2017_weak exhibits weaker hydrogen bonding than water-2017, as reflected in a longer hydrogen bonding distance and slightly lower enthalpy of vaporization. Both RFFs possess coordination numbers corresponding to the first (intermolecular) maxima of g_{OO} and g_{OH} in good agreement with experiment.

Vibrational modes and frequencies. The RFF power spectra show good agreement with experiment and empirical flexible force fields in the low frequency region (< 1000 cm^{-1}), with the exception that water-2017 does not possess a shoulder in the oxygen atom power spectrum corresponding to intermolecular stretching vibrations. However, significant deviations from experiment are observed for the intramolecular modes: the O-H stretching frequencies are red-shifted by ∼100-300 cm^{-1} and the H-O-H bending frequencies are blue-shifted by ∼200-300 cm^{-1}. Furthermore, the RFFs exhibit peak-splitting in the stretching region instead of the single broad peak observed in IR and Raman spectra. This is, at least in part, due to the large differences between gas phase symmetric and asymmetric stretching frequencies. Improving the gas phase frequencies would therefore be the first step in improving the vibrational properties in the liquid phase. Indeed, both RFFs predict gas phase stretching frequencies red-shifted by ∼300-500 cm^{-1}, and the water-2017 bending frequency is blue-shifted by ∼200 cm^{-1}. It is therefore impossible for the RFFs to predict both accurate liquid phase frequencies and shifts from the gas phase, the latter being indicative of

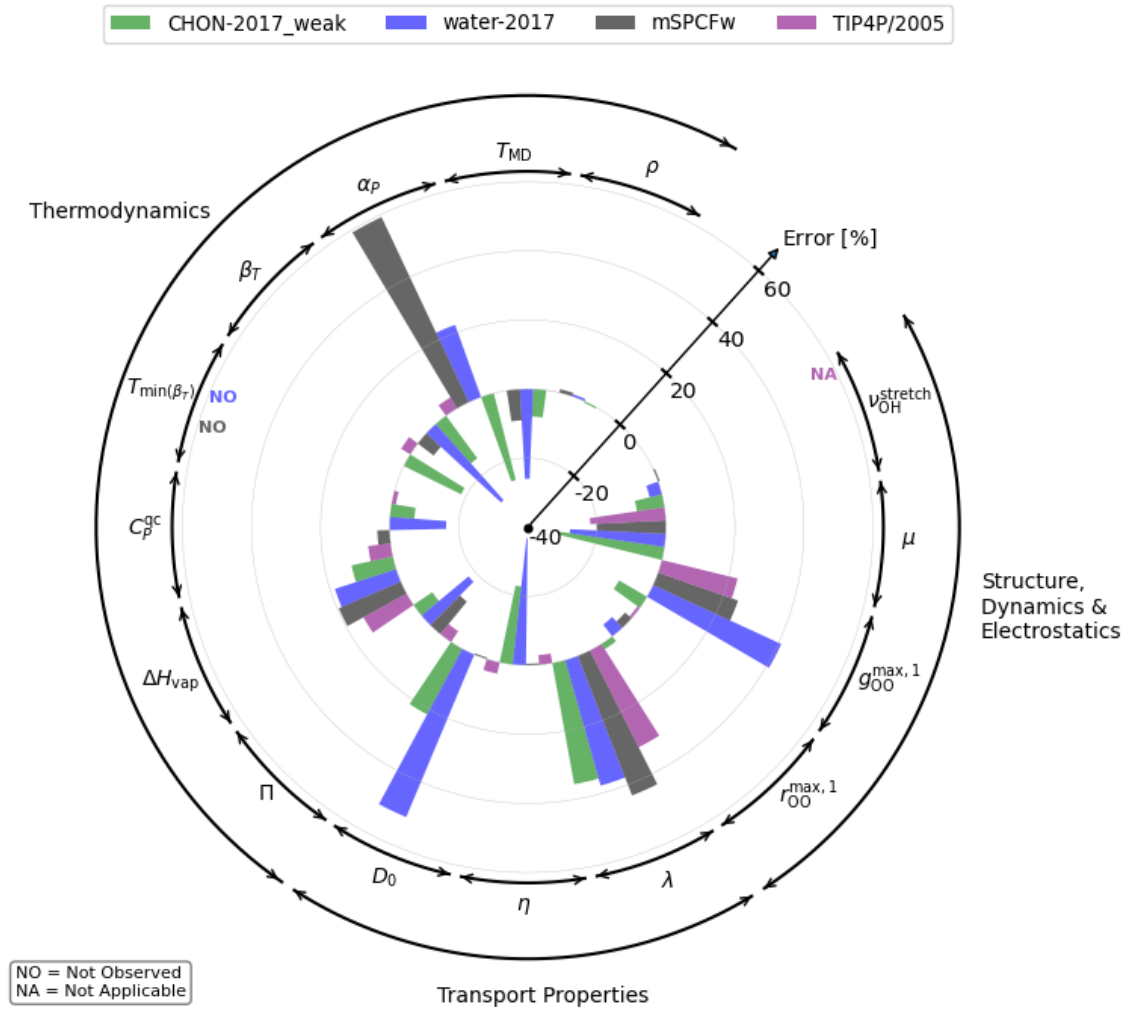


FIGURE 7.17: Deviation from experimental reference values of 15 properties of water predicted by the CHON-2017_weak and water-2017 ReaxFF force fields as well as the classical empirical mSPCFw and TIP4P/2005 force fields. All values correspond to 300 K (where appropriate) and either 1 bar, the vapour pressure for coexistence properties (ΔH_{vap} and Π), or 1.00 g cm^{-3} (see the main text for details). Symbol meanings are given in the main text. Experimental values are from Refs. 52,53,55,58,59,62–64,66 and values for TIP4P/2005 are from Refs. 19,20,73,104,108,128,136, 141,153.

hydrogen bonding strength.

Electrostatic moments. Capturing the electrostatic multipole moments of water is essential for building high quality water models, with work[77,78] by Abascal and Vega bringing to light the importance of the quadrupole moment Q_T and ratio μ/Q_T, on top of the dipole moment μ. In the liquid phase, the RFFs predict μ = 2.0-2.2 D which is substantially lower than the $\mu \sim 2.95$ D expected from experiments[54,55], but only marginally lower than the dipole moments, μ =2.3-2.5 D of most classical force fields. However, the RFFs have a ratio $\mu/Q_T \approx 1.3$ Å^{-1}, which is significantly higher than the $\mu/Q_T \sim 1.0$ Å^{-1} shown to produce high-quality water models for

empirical force fields.[76–78] Improving the μ/Q_T ratio may result in RFFs that predict overall more accurate thermophysical properties. The RFFs predict a shift in dipole moment when going from the liquid to vapour phase of $\Delta_{\mathrm{l}}^{\mathrm{g}}\mu = -0.37$-$0.39$ D, which is greatly underestimated relative to the $\Delta_{\mathrm{l}}^{\mathrm{g}}\mu \sim -1.1$ D expected from experiments[54–57].

Equation of state and thermodynamic response functions. Both RFFs reproduce the density of liquid water at 1 bar fairly accurately. At 300 K, they predict densities to within 1% of the experimental value, and more accurate thermal expansion coefficients than some classical force fields such as mSPCFw (but not TIP4P/2005). Both RFFs feature a density maximum, but greatly underestimate the temperature T_{MD} at which it occurs: CHON-2017_weak and water-2017 predict (255 ± 3) K and (205 ± 6) K respectively, compared to the 277 K observed experimentally. The isothermal compressibility predicted by the RFFs are systematically lower than experiment, with a more severe underestimation by water-2017. Crucially, our results suggest that CHON-2017_weak possesses a compressibility minimum, albeit at lower temperature of (260 ± 40) K near its T_{MD} (compared to the experimental 319 K), while water-2017 does not. This suggests that water-2017 is missing aspects of the orientational correlations that are linked to the tetrahedral order of liquid water. The speed of sound predictions are underestimated and largely limited by the RFF's (in)ability to accurately model the compressibility; CHON-2017_weak possesses a maximum while water-2017 does not. Once quantum-corrected, the isobaric and isochoric heat capacities are systematically underestimated, but nonetheless show relatively good agreement with experiment with deviations comparable to many[126–128] classical force fields.

Liquid-vapour coexistence properties. Both RFFs predict orthobaric liquid densities at 300 K in good agreement with experiment, consistent with the density predictions at 300 K and 1 bar. CHON-2017_weak and water-2017 underestimate the surface tension at 300 K by 4-9% and 17-20%, respectively. CHON-2017_weak therefore predicts Π in good agreement with experiment: only $\sim 3\%$ lower than TIP4P/2005 and more accurately than many other classical force fields. CHON-2017_weak also predicts more accurate enthalpies of vaporization than water-2017, although both RFFs overestimate ΔH_{vap}: by 12% and 19% at 300 K for CHON-2017_weak and water-2017, respectively. These deviations from experiment are in line with TIP4P/2005, SPC/E and mSPCFw, which also overestimate (the uncorrected) ΔH_{vap} by 10-20%. The greater ΔH_{vap} of water-2017 suggests that it predicts stronger hydrogen bonding than CHON-2017_weak.

Transport properties. The RFFs overestimate the self-diffusion coefficients and underestimate the viscosity of liquid water at near standard conditions, water-2017 more severely than CHON-2017_weak. This is particularly unfortunate for the water-2017 force field, which was parameterized to model the diffusion of $H_2O/H_3O^+/OH^-$, and included the diffusion coefficients of

these species as target parameters for fitting. Presumably, the overestimated self-diffusion coefficient is an artefact that arose from not accounting for finite-size effects in the force field parameterization process. This could be remedied by refitting the force field with the "infinite-size" diffusion coefficients D_0. Likewise, previous estimates[8,39] of the $H_3O^+_{(aq)}/OH^-_{(aq)}$ diffusion coefficients for both RFFs have not accounted for finite-size effects. Our results for bulk systems indicate that finite-size effects are significant, with the CHON-2017_weak and water-2017 self-diffusion coefficients increasing by ∼30% when going from a box length of 12.5 Å to a system of infinite size. These finite-size effects motivate further investigations of the dynamic properties of the RFFs. The thermal conductivity predicted by the RFFs are ∼30-40% higher than the experimental value, in line with popular empirical force fields including TIP4P/2005, SPC/E and mSPCFw.

Final remarks and evaluation. We have performed comprehensive benchmarks of two state-of-the-art ReaxFF force fields designed to model water, CHON-2017_weak and water-2017, encompassing structural, electrostatic, vibrational, thermodynamic, coexistence, and transport properties. Our results suggest that overall, CHON-2017_weak more accurately predicts the thermophysical properties of water than water-2017. The CHON-2017_weak oxygen and hydrogen atom parameters are used for both water and functionalized hydrocarbons, while water-2017 is a dedicated water force field parameterized to model $H_2O/H_3O^+/OH^-$ diffusion. Comparing to its predecessors[38,40], the description of water by CHON-2017_weak appears to have benefited greatly from the focus on weak interactions in its reparameterization of the protein-2013 force field[40], which included additional training data ranging from the binding energies of water clusters to the chemical reactions of nitrogen containing systems.[41] However, ReaxFF parameters are highly correlated, and dedicated water force fields such as water-2017 should be able to sacrifice transferability for accuracy. Our results suggest that improving the μ/Q_T ratio, self-diffusion coefficients and gas phase frequencies are first steps towards building ReaxFF models that more accurately describe the thermophysical properties of liquid water. This could be achieved by including these quantities as target parameters in the force field optimization procedure.

Bibliography

[1] G. Baffou, F. Cichos and R. Quidant, *Nat. Mater.*, 2020, **19**, 946–958.

[2] H. Bhattarai, K. E. Newman and J. D. Gezelter, *J. Chem. Phys.*, 2020, **153**, 204703.

[3] J. D. Olarte-Plata and F. Bresme, *J. Chem. Phys.*, 2022, **156**, 204701.

[4] S. A. Shavalier and J. D. Gezelter, *J. Phys. Chem. C*, 2022, **126**, 12742–12754.

[5] S. Monti, J. Jose, A. Sahajan, N. Kalarikkal and S. Thomas, *Phys. Chem. Chem. Phys.*, 2019, **21**, 13099–13108.

[6] L. M. R. Keil, F. M. Möller, M. Kieß, P. W. Kudella and C. B. Mast, *Nat. Commun.*, 2017, **8**, 1897.

[7] L. Ai, Y. Zhou and M. Chen, *J. Mol. Liq.*, 2019, **276**, 83–92.

[8] W. Zhang, X. Chen and A. C. T. van Duin, *J. Phys. Chem. Lett.*, 2018, **9**, 5445–5452.

[9] P. Saidi, L. K. Béland and M. R. Daymond, *J. Phys. Chem. C*, 2020, **124**, 26864–26873.

[10] L. Shi, A. Xu and Y. Cheng, *J. Phys. Chem. C*, 2019, **123**, 27429–27435.

[11] L. Shi, Z. Ying, A. Xu and Y. Cheng, *Chem. Mater.*, 2020, **32**, 6062–6069.

[12] B. R. H. de Aquino, H. Ghorbanfekr-Kalashami, M. Neek-Amal and F. M. Peeters, *Phys. Chem. Chem. Phys.*, 2019, **21**, 9285–9295.

[13] D. Dong, W. Zhang, A. C. T. van Duin and D. Bedrov, *J. Phys. Chem. Lett.*, 2018, **9**, 825–829.

[14] W. Zhang, D. Dong, D. Bedrov and A. C. T. van Duin, *J. Mater. Chem. A*, 2019, **7**, 5442–5452.

[15] N. Dasgupta, D. E. Yilmaz and A. van Duin, *J. Phys. Chem. B*, 2020, **124**, 5311–5322.

[16] H. Manzano, W. Zhang, M. Raju, J. S. Dolado, I. n. López-Arbeloa and A. C. T. van Duin, *J. Chem. Phys.*, 2018, **148**, 234503.

[17] I. Leven, H. Hao, A. K. Das and T. Head-Gordon, *J. Phys. Chem. Lett.*, 2020, **11**, 9240–9247.

[18] K. Heijmans, I. C. Tranca, D. M. J. Smeulders, T. J. H. Vlugt and S. V. Gaastra-Nedea, *J. Chem. Theory Comput.*, 2021, **17**, 322–329.

[19] C. Vega and J. L. F. Abascal, *Phys. Chem. Chem. Phys.*, 2011, **13**, 19663–19688.

[20] J. L. F. Abascal and C. Vega, *J. Chem. Phys.*, 2005, **123**, 234505.

[21] H. J. C. Berendsen, J. R. Grigera and T. P. Straatsma, *J. Phys. Chem.*, 1987, **91**, 6269–6271.

[22] T. Wu, H. L. Tepper and G. A. Voth, *J. Chem. Phys.*, 2006, **124**, 024503.

[23] K. S. Smirnov, *Phys. Chem. Chem. Phys.*, 2017, **19**, 2950–2960.

[24] H. L. Lemberg and F. H. Stillinger, *J. Chem. Phys.*, 1975, **62**, 1677–1690.

[25] F. Bresme, *J. Chem. Phys.*, 2001, **115**, 7564–7574.

[26] Z. Jing, C. Liu, S. Y. Cheng, R. Qi, B. D. Walker, J.-P. Piquemal and P. Ren, *Annu. Rev. Biophys*, 2019, **48**, 371–394.

[27] A. A. Chialvo and P. T. Cummings, *J. Chem. Phys.*, 1996, **105**, 8274–8281.

[28] P. Ren and J. W. Ponder, *J. Phys. Chem. B*, 2003, **107**, 5933–5947.

[29] P. Paricaud, M. Předota, A. A. Chialvo and P. T. Cummings, *J. Chem. Phys.*, 2005, **122**, 244511.

[30] G. A. Cisneros, K. T. Wikfeldt, L. Ojamäe, J. Lu, Y. Xu, H. Torabifard, A. P. Bartók, G. Csányi, V. Molinero and F. Paesani, *Chem. Rev.*, 2016, **116**, 7501–7528.

[31] V. Molinero and E. B. Moore, *J. Phys. Chem. B*, 2009, **113**, 4008–4016.

[32] M. J. Gillan, D. Alfè and A. Michaelides, *J. Chem. Phys.*, 2016, **144**, 130901.

[33] A. P. Gaiduk, F. Gygi and G. Galli, *J. Phys. Chem. Lett.*, 2015, **6**, 2902–2908.

[34] M. Chen, H.-Y. Ko, R. C. Remsing, M. F. Calegari Andrade, B. Santra, Z. Sun, A. Selloni, R. Car, M. L. Klein, J. P. Perdew and X. Wu, *Proc. Natl. Acad. Sci. U. S. A.*, 2017, **114**, 10846–10851.

[35] B. Chen, I. Ivanov, M. L. Klein and M. Parrinello, *Phys. Rev. Lett.*, 2003, **91**, 215503.

[36] L. Ruiz Pestana, N. Mardirossian, M. Head-Gordon and T. Head-Gordon, *Chem. Sci.*, 2017, **8**, 3554–3565.

[37] G. Zhao, S. Shi, H. Xie, Q. Xu, M. Ding, X. Zhao, J. Yan and D. Wang, *Phys. Chem. Chem. Phys.*, 2020, **22**, 4626–4631.

[38] A. C. T. van Duin, C. Zou, K. Joshi, V. Bryantsev and W. A. Goddard, in *Computational Catalysis*, ed. A. Asthagiri and M. J. Janik, The Royal Society of Chemistry, Thomas Graham House, Science Park, Milton Road, Cambridge CB4 0WF, UK, 2013, ch. 6, pp. 223–243.

[39] W. Zhang and A. C. T. van Duin, *J. Phys. Chem. B*, 2017, **121**, 6021–6032.

[40] S. Monti, A. Corozzi, P. Fristrup, K. L. Joshi, Y. K. Shin, P. Oelschlaeger, A. C. T. van Duin and V. Barone, *Phys. Chem. Chem. Phys.*, 2013, **15**, 15062–15077.

[41] W. Zhang and A. C. T. van Duin, *J. Phys. Chem. B*, 2018, **122**, 4083–4092.

[42] A. C. T. van Duin, S. Dasgupta, F. Lorant and W. A. Goddard III, *J. Phys. Chem. A*, 2001, **105**, 9396–9409.

[43] W. J. Mortier, S. K. Ghosh and S. Shankar, *J. Am. Chem. Soc.*, 1986, **108**, 4315–4320.

[44] H. M. Aktulga, J. C. Fogart, S. A. Pandit and A. Y. Grama, *Parallel Comput.*, 2012, **38**, 245–259.

[45] T. P. Senftle, S. Hong, M. M. Islam, S. B. Sylasa, Y. Zheng, Y. K. Shin, C. Junkermeier, R. Engel-Herbert, M. J. Janik, H. M. Aktulga, T. Verstraelen, A. Grama and A. C. T. van Duin, *npj Comput. Mater.*, 2016, **2**, 15011.

[46] A. P. Thompson, H. M. Aktulga, R. Berger, D. S. Bolintineanu, W. M. Brown, P. S. Crozier, P. J. in 't Veld, A. Kohlmeyer, S. G. Moore, T. D. Nguyen, R. Shan, M. J. Stevens, J. Tranchida, C. Trott and S. J. Plimpton, *Comp. Phys. Comm.*, 2022, **271**, 108171.

[47] S. Plimpton, *J. Comput. Phys.*, 1995, **117**, 1–19.

[48] D. Furman and D. J. Wales, *J. Phys. Chem. Lett.*, 2019, **10**, 7215–7223.

[49] D. Furman and D. J. Wales, *J. Chem. Phys.*, 2020, **153**, 021102.

[50] E. Pollock and J. Glosli, *Comput. Phys. Commun.*, 1996, **95**, 93–110.

[51] M. Allen and D. Tildesley, *Computer Simulation of Liquids*, Oxford: Clarendon Pr, 1987.

[52] W. Wagner and A. Pruß, *J. Phys. Chem. Ref. Data*, 2002, **31**, 387–535.

[53] L. B. Skinner, C. Huang, D. Schlesinger, L. G. M. Pettersson, A. Nilsson and C. J. Benmore, *J. Chem. Phys.*, 2013, **138**, 074506.

[54] Y. S. Badyal, M.-L. Saboungi, D. L. Price, S. D. Shastri, D. R. Haeffner and A. K. Soper, *J. Chem. Phys.*, 2000, **112**, 9206–9208.

[55] A. V. Gubskaya and P. G. Kusalik, *J. Chem. Phys.*, 2002, **117**, 5290–5302.

[56] S. A. Clough, Y. Beers, G. P. Klein and L. S. Rothman, *J. Chem. Phys.*, 1973, **59**, 2254–2259.

[57] S. L. Shostak, W. L. Ebenstein and J. S. Muenter, *J. Chem. Phys.*, 1991, **94**, 5875.

[58] C. Chapados and J.-J. Max, *J. Chem. Phys.*, 2009, **131**, 184505.

[59] S. Y. Venyaminov and F. G. Prendergast, *Anal. Biochem.*, 1997, **248**, 234–245.

[60] D. M. Carey and G. M. Korenowski, *J. Chem. Phys.*, 1998, **108**, 2669–2675.

[61] G. E. Walrafen, *J. Chem. Phys.*, 1964, **40**, 3249–3256.

[62] M. Holz, S. R. Heil and A. Sacco, *Phys. Chem. Chem. Phys.*, 2000, **2**, 4740–4742.

[63] M. L. Huber, R. A. Perkins, A. Laesecke, D. G. Friend, J. V. Sengers, M. J. Assael, I. N. Metaxa, E. Vogel, R. Mareš and K. Miyagawa, *J. Phys. Chem. Ref. Data*, 2000, **38**, 101–125.

[64] M. L. Huber, R. A. Perkins, D. G. Friend, J. V. Sengers, M. J. Assael, I. N. Metaxa, K. Miyagawa, R. Hellmann and E. Vogel, *J. Phys. Chem. Ref. Data*, 2012, **41**, 033102.

[65] International Association for the Properties of Water and Steam, *IAPWS AN1-03*, 2003.

[66] N. B. Vargaftik, B. N. Volkov and L. D. Voljak, *J. Phys. Chem. Ref. Data*, 1983, **12**, 817–820.

[67] A. K. Soper and C. J. Benmore, *Phys. Rev. Lett.*, 2008, **101**, 065502.

[68] M. Ceriotti, W. Fang, P. G. Kusalik, R. H. McKenzie, A. Michaelides, M. A. Morales and T. E. Markland, *Chem. Rev.*, 2016, **116**, 7529–7550.

[69] A. K. Soper, *Chem. Phys.*, 2000, **258**, 121–137.

[70] L. B. Skinner, C. J. Benmore, J. C. Neuefeind and J. B. Parise, *J. Chem. Phys.*, 2014, **141**, 214507.

[71] C. Benmore, L. C. Gallington and E. Soignard, *Mol. Phys.*, 2019, **117**, 2470–2476.

[72] H. Pathak, A. Späh, K. H. Kim, I. Tsironi, D. Mariedahl, M. Blanco, S. Huotari, V. Honkimäki and A. Nilsson, *J. Chem. Phys.*, 2019, **150**, 224506.

[73] G. Camisasca, H. Pathak, K. T. Wikfeldt and L. G. M. Pettersson, *J. Chem. Phys.*, 2019, **151**, 044502.

[74] C. Apostolidou, *J. Chem. Phys.*, 2019, **151**, 064111.

[75] S. K. Reddy, S. C. Straight, P. Bajaj, C. Huy Pham, M. Riera, D. R. Moberg, M. A. Morales, C. Knight, A. W. Götz and F. Paesani, *J. Chem. Phys.*, 2016, **145**, 194504.

[76] S. Izadi, R. Anandakrishnan and A. V. Onufriev, *J. Phys. Chem. Lett.*, 2014, **5**, 3863–3871.

[77] J. L. F. Abascal and C. Vega, *Phys. Rev. Lett.*, 2007, **98**, 237801.

[78] J. L. F. Abascal and C. Vega, *J. Phys. Chem. C*, 2007, **111**, 15811–15822.

[79] C. Zhang, J. Wu, G. Galli and F. Gygi, *J. Chem. Theory Comput.*, 2011, **7**, 3054–3061.

[80] L. Zheng, M. Chen, Z. Sun, H.-Y. Ko, B. Santra, P. Dhuvad and X. Wu, *J. Chem. Phys.*, 2018, **148**, 164505.

[81] F. Martin and H. Zipse, *J. Comput. Chem.*, 2005, **26**, 97–105.

[82] B. Han, C. M. Isborn and L. Shi, *J. Chem. Theory Comput.*, 2021, **17**, 889–901.

[83] J. Verhoeven and A. Dymanus, *J. Chem. Phys.*, 1970, **52**, 3222–3233.

[84] H. J. Bakker and J. L. Skinner, *Chem. Rev.*, 2010, **110**, 1498–1517.

[85] F. Perakis, L. De Marco, A. Shalit, F. Tang, Z. R. Kann, T. D. Kühne, R. Torre, M. Bonn and Y. Nagata, *Chem. Rev.*, 2016, **116**, 7590–7607.

[86] K. M. Hunter, F. A. Shakib and F. Paesani, *J. Phys. Chem. B.*, 2018, **122**, 10754–10761.

[87] C.-C. Yu, K.-Y. Chiang, M. Okuno, T. Seki, T. Ohto, X. Yu, V. Korepanov, H.-o. Hamaguchi, M. Bonn, J. Hunger and Y. Nagata, *Nat. Commun.*, 2020, **11**, 5977.

[88] G. R. Medders and F. Paesani, *J. Chem. Theory Comput.*, 2015, **11**, 1145–1154.

[89] P. Bopp, G. Jancsó and K. Heinzinger, *Chem. Phys. Lett.*, 1983, **98**, 129–133.

[90] W. S. Benedict, N. Gailar and E. K. Plyler, *J. Chem. Phys.*, 1956, **24**, 1139–1165.

[91] R. Rey, K. B. Møller and J. T. Hynes, *J. Phys. Chem. A.*, 2002, **106**, 11993–11996.

[92] D. Ojha, K. Karhan and T. D. Kühne, *Sci. Rep.*, 2018, **8**, 16888.

[93] M. Falk, *Spectrochim. Acta*, 1984, **40**, 43–48.

[94] M. A. González and J. L. F. Abascal, *J. Chem. Phys.*, 2011, **135**, 224516.

[95] J. Martí, J. A. Padro and E. Guàrdia, *J. Chem. Phys.*, 1996, **105**, 639–649.

[96] O. V. Boyarkin, M. A. Koshelev, O. Aseev, P. Maksyutenko, T. R. Rizzo, N. F. Zobov, L. Lodi, J. Tennyson and O. L. Polyansky, *Chem. Phys. Lett.*, 2013, **568-569**, 14–20.

[97] U. W. Schmitt and G. A. Voth, *J. Chem. Phys.*, 1999, **111**, 9361–9381.

[98] L. X. Dang and B. M. Pettitt, *J. Phys. Chem.*, 1987, **91**, 3349–3354.

[99] B. E. Rocher-Casterline, L. C. Ch'ng, A. K. Mollner and H. Reisler, *J. Chem. Phys.*, 2011, **134**, 211101.

[100] N. A. Benedek, I. K. Snook, M. D. Towler and R. J. Needs, *J. Chem. Phys.*, 2006, **125**, 104302.

[101] I. G. Gurtubay and R. J. Needs, *J. Chem. Phys.*, 2007, **127**, 124306.

[102] A. Mukhopadhyay, S. S. Xantheas and R. J. Saykally, *Chem. Phys. Lett.*, 2018, **700**, 163–175.

[103] L.-P. Wang, T. J. Martinez and V. S. Pande, *J. Phys. Chem. Lett.*, 2014, **5**, 1885–1891.

[104] H. L. Pi, J. L. Aragones, C. Vega, E. G. Noya, J. L. F. Abascal, M. A. Gonzalez and C. McBride, *Mol. Phys.*, 2009, **107**, 365–374.

[105] D. Paschek, *J. Chem. Phys.*, 2004, **120**, 6674–6690.

[106] H. W. Horn, W. C. Swope, J. W. Pitera, J. D. Madura, T. J. Dick, G. L. Hura and T. Head-Gordon, *J. Phys. Chem.*, 2004, **120**, 9665.

[107] A. W. Milne and M. Jorge, *J. Chem. Theory Comput.*, 2019, **15**, 1065–1078.

[108] J. Alejandre and G. A. Chapela, *J. Chem. Phys.*, 2010, **132**, 014701.

[109] C. Vega and E. de Miguel, *J. Chem. Phys.*, 2007, **126**, 154707.

[110] R. D. Mountain, *J. Phys. Chem. B*, 2009, **113**, 482–486.

[111] P. K. Yuet and D. Blankschtein, *J. Phys. Chem. B*, 2010, **114**, 13786–13795.

[112] A. Ghoufi and P. Malfreyt, *Mol. Simul.*, 2019, **45**, 295–303.

[113] C. Huang, K. T. Wikfeldt, D. Nordlund, U. Bergmann, T. McQueen, J. Sellberg, L. G. M. Pettersson and A. Nilsson, *Phys. Chem. Chem. Phys.*, 2011, **13**, 19997–20007.

[114] D. Schlesinger, K. T. Wikfeldt, L. B. Skinner, C. J. Benmore, A. Nilsson and L. G. M. Pettersson, *J. Chem. Phys.*, 2016, **145**, 084503.

[115] A. Nilsson and L. G. M. Pettersson, *Nat. Commun.*, 2015, **6**, 8998.

[116] J. Russo and H. Tanaka, *Nat. Commun.*, 2014, **5**, 3556.

[117] M. Vedamuthu, S. Singh and G. W. Robinson, *J. Phys. Chem.*, 1995, **99**, 9263–9267.

[118] R. S. Singh, J. W. Biddle, P. G. Debenedetti and M. A. Anisimov, *J. Chem. Phys.*, 2016, **144**, 144504.

[119] A. K. Soper and M. A. Ricci, *Phys. Rev. Lett.*, 2000, **84**, 2881–2884.

[120] M. Nakamura, K. Tamura and S. Murakami, *Thermochim. Acta*, 1995, **253**, 127–136.

[121] C. Vega, M. M. Conde, C. McBride, J. L. F. Abascal, E. G. Noya, R. Ramirez and L. M. Sesé, *J. Chem. Phys.*, 2010, **132**, 046101.

[122] P. H. Berens, D. H. J. Mackay, G. M. White and K. R. Wilson, *J. Chem. Phys*, 1983, **79**, 2375–2389.

[123] S.-T. Lin, M. Blanco and W. A. Goddard, *J. Chem. Phys.*, 2003, **119**, 11792–11805.

[124] S.-T. Lin, P. K. Maiti and W. A. Goddard, *J. Phys. Chem. B*, 2010, **114**, 8191–8198.

[125] T. A. Pascal, S.-T. Lin and W. A. Goddard III, *Phys. Chem. Chem. Phys.*, 2011, **13**, 169–181.

[126] D. Berta, D. Ferenc, I. Bakó and Madarász, *J. Chem. Theory Comput.*, 2020, **16**, 3316–3334.

[127] Q. Waheed and O. Edholm, *J. Chem. Theory Comput.*, 2011, **7**, 2903–2909.

[128] T. A. Pascal, D. Schärf, Y. Jung and T. D. Kühne, *J. Chem. Phys.*, 2012, **137**, 244507.

[129] K.-Y. Yeh, S.-N. Huang, L.-J. Chen and S.-T. Lin, *J. Chem. Phys.*, 2014, **141**, 044502.

[130] M. A. Caro, O. Lopez-Acevedo and T. Laurila, *J. Chem. Theory Comput.*, 2017, **13**, 3432–3441.

[131] F. Bresme, J. W. Biddle, J. V. Sengers and M. A. Anisimov, *J. Chem. Phys.*, 2014, **140**, 161104.

[132] V. Holten, J. V. Sengers and M. A. Anisimov, *J. Phys. Chem. Ref. Data*, 2014, **43**, 043101.

[133] I.-C. Yeh and G. Hummer, *J. Phys. Chem. B*, 2004, **108**, 15873–15879.

[134] B. Dünweg and K. Kremer, *J. Chem. Phys.*, 1993, **99**, 6983–6997.

[135] R. Mills, *J. Phys. Chem.*, 1973, **77**, 685–688.

[136] S. Tazi, A. Boţan, M. Salanne, V. Marry, P. Turq and B. Rotenberg, *J. Phys.: Condens. Matter*, 2012, **24**, 284117.

[137] T. D. Kühne, M. Krack and M. Parrinello, *J. Chem. Theory Comput.*, 2009, **5**, 235–241.

[138] J. E. Basconi and M. R. Shirts, *J. Chem. Theory Comput.*, 2013, **9**, 2887–2899.

[139] T. S. Light, S. Licht, A. C. Bevilacqua and K. R. Morash, *Electrochem. Solid-State Lett.*, 2005, **8**, E16.

[140] M. A. González and J. L. F. Abascal, *J. Chem. Phys.*, 2010, **132**, 096101.

[141] S. H. Lee and J. Kim, *Mol. Phys.*, 2019, **117**, 1926–1933.

[142] F. Bresme, A. Lervik, D. Bedeaux and S. Kjelstrup, *Phys. Rev. Lett.*, 2008, **101**, 020602.

[143] T. Ohara, *J. Chem. Phys.*, 1999, **111**, 6492–6500.

[144] D. Bedrov and G. D. Smith, *J. Chem. Phys.*, 2000, **113**, 8080–8084.

[145] M. Zhang, E. Lussetti, L. E. S. de Souza and F. Müller-Plathe, *J. Phys. Chem. B*, 2005, **109**, 15060–15067.

[146] T. Terao and F. Müller-Plathe, *J. Chem. Phys.*, 2005, **122**, 081103.

[147] W. Evans, J. Fish and P. Keblinski, *J. Chem. Phys.*, 2007, **126**, 154504.

[148] E. J. Rosenbaum, N. J. English, J. K. Johnson, D. W. Shaw and R. P. Warzinski, *J. Phys. Chem. B*, 2007, **111**, 13194–13205.

[149] H. Jiang, E. M. Myshakin, K. D. Jordan and R. P. Warzinski, *J. Phys. Chem. B*, 2008, **112**, 10207–10216.

[150] S. Kuang and J. D. Gezelter, *J. Chem. Phys.*, 2010, **133**, 164101.

[151] J. Muscatello and F. Bresme, *J. Chem. Phys.*, 2011, **135**, 234111.

[152] J. Muscatello, F. Römer, J. Sala and F. Bresme, *Phys. Chem. Chem. Phys.*, 2011, **13**, 19970–19978.

[153] F. Römer, A. Lervik and F. Bresme, *J. Chem. Phys.*, 2012, **137**, 074503.

[154] Y. Mao and Y. Zhang, *Chem. Phys. Lett.*, 2012, **542**, 37–41.

[155] T. W. Sirk, S. Moore and E. F. Brown, *J. Chem. Phys.*, 2013, **138**, 064505.

[156] S. H. Lee, *Mol. Phys.*, 2014, **112**, 2155–2159.

[157] P. Boone, H. Babaei and C. E. Wilmer, *J. Chem. Theory Comput.*, 2019, **15**, 5579–5587.

[158] D. Surblys, H. Matsubara, G. Kikugawa and T. Ohara, *Phys. Rev. E*, 2019, **99**, 051301.

[159] D. Surblys, H. Matsubara, G. Kikugawa and T. Ohara, *J. Appl. Phys.*, 2021, **130**, 215104.

[160] A. O. Govorov, W. Zhang, T. Skeini, H. Richardson, J. Lee and N. A. Kotov, *Nanoscale Res. Lett.*, 2006, **1**, 84.

[161] C. R. Crick, P. Albella, B. Ng, A. P. Ivanov, T. Roschuk, M. P. Cecchini, F. Bresme, S. A. Maier and J. B. Edel, *Nano Lett.*, 2015, **15**, 553–559.

Chapter 8

On the anomalous thermal conductivity of water

8.1 Introduction

Thermal conductivity is considered one of water's anomalous properties. Apart for liquid metals,[1] it is the highest of any liquid at room temperature and ∼1 bar.[2] Unlike for simple liquids, it features a strong temperature dependence at constant density. At near-atmospheric pressure, it possesses a maximum[3] at ∼400 K (10 bar) and controversially[4–6] a minimum at ∼220 K (1 bar) in the super-cooled region. Despite its significance, the physical origin of water's anomalous thermal conductivity remains an open question.

In this chapter, we assess the ability of molecular force fields to reproduce the thermal conductivity of water at near-standard temperature and pressure, along the "standard liquid" 0.997 g cm^{-3} isochore, and along different isobars for pressures $P < 1500$ bar. Taking advantage of the (in)ability of different molecular force fields to accurately model the thermal conductivity, we correlate its anomalous temperature dependence with other thermophysical properties, namely the speed of sound, compressibility, sound attenuation coefficient, and kinematic longitudinal viscosity.

8.2 Methods

We performed molecular dynamics (MD) simulations of water modelled using the following molecular force fields: the classical rigid force fields TIP3P[7], TIP3P-FB[8], SPC[9], SPC/E[10], OPC3[11], TIP4P[7], TIP4P/2005[12], TIP4P-FB[8], OPC[13], TIP5P[14] and TIP5P/2018[15]; the classical flexible force fields TIP3P/Fs[16], SPC/Fw[17] and mSPCFw[18]; and the ReaxFF force fields water-2017[19] and CHON-2017_weak[20]. In this chapter, we refer to empirical, all-atom, non-polarizable, non-reactive N-site classical models as "traditional" classical force fields (i.e., all the non-ReaxFF force

fields used in this work). All simulations were carried out using LAMMPS[21] (v. 7Aug2019). The equations of motion were integrated using the velocity Verlet algorithm, except for the 5-site rigid models (TIP5P and TIP5P/2018), for which the method of quaternions[22] for rigid bodies was used. A timestep of $\delta t = 1$ fs and $\delta t = 0.2$ fs were used for the rigid and flexible force fields, respectively. For the rigid models, the RATTLE[23] algorithm was used to maintain the holonomic constraints, except for in the *NPT* simulations where SHAKE[24] was used (we find that RATTLE, as implemented in LAMMPS, does not reproduce the correct volume fluctuations; see Appendix E.1). For the classical force fields, a cutoff of 13 Å was used for the oxygen-oxygen Lennard-Jones (LJ) potential unless specified otherwise, and tail corrections[25] were *not* applied in order for the isotropic equilibrium simulations to be fully consistent with the non-isotropic non-equilibrium simulations. Electrostatic interactions were handled using the P^{3}M implementation[26] of the Ewald summation method, with a root mean square (RMS) error in per-atom forces of 10^{-5} relative to the force two point charges of elementary charge exert on each other at a distance of 1 Å. For the ReaxFF charge equilibration procedure, a relative residual norm tolerance of 10^{-6} was used for the employed Preconditioned Conjugate Gradient method.[27] The ReaxFF models use an interaction cutoff of 10 Å, which is part of the force field parameterization. 3D periodic boundary conditions were applied in all simulations.

8.2.1 Non-equilibrium molecular dynamics simulations

Boundary-driven non-equilibrium molecular dynamics (NEMD) simulations were performed to calculate the thermal conductivity. Two sets of simulations were performed: (1) "small" systems from which the thermal conductivity at a single (P, T, ρ) state point was extracted, and (2) "large" systems that target a wide temperature range over an isobar. In all cases, an elongated (tetragonal) simulation cell of dimensions (L_x, L_y, L_z), where $L_x = L_y = L_\parallel$, was used. Two thermostatting regions, set to temperatures T_c (cold) and T_h (hot), of width Δz were located in the centre and edges of the box, respectively, and extended in the (x, y) plane. Depending on the force field, either the CSVR or Langevin thermostat, with a time constant τ, was used. The system's centre-of-mass velocity was subtracted from each atom at every timestep in order to ensure linear momentum conservation. For each system, sampling consisted of N_{rep} statistically independent replicas, which were run for a time t_{stat} in order to establish the stationary state, followed by t_{prod} for data collection. The number of molecules, N_{mol}, in the simulation cell was also varied. The simulation details are summarized in Table 8.1.

In the stationary state, the heat flux across the system, $\boldsymbol{J}_q = (0, 0, \pm J_q)$, can be obtained from the continuity equation

$$J_q = \frac{|\langle \Delta U \rangle|}{2\delta t A} \tag{8.1}$$

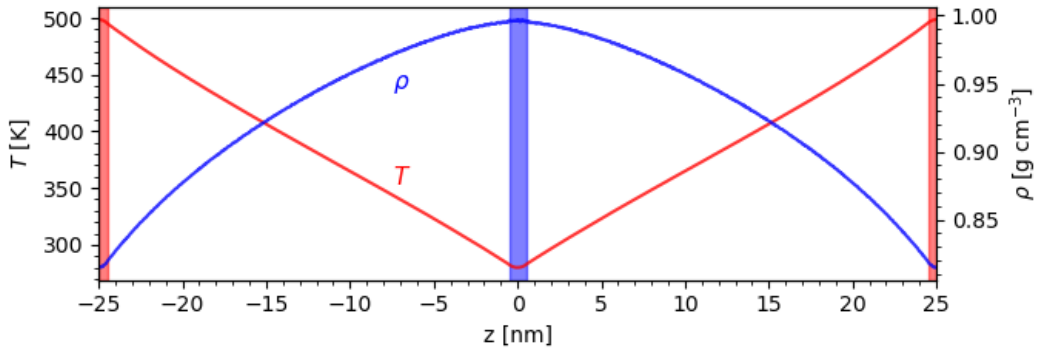


FIGURE 8.1: Representative temperature T and density ρ profiles for the NEMD simulations. The blue (cold) and red (hot) indicate the location of the thermostatting regions in the simulation cell. The profiles correspond to TIP4P/2005 and $P = (10 \pm 1)$ bar.

TABLE 8.1: NEMD simulation parameters. Symbol meanings are defined in the main text.

Type	Force field	N_{mol}	$L_{\parallel}$, L_z [Å]	T_c, T_h [K]	$T_h - T_c$ [K]	Δz [Å]	Thermostat (τ [fs])	N_{rep}	t_{stat}, t_{prod} [ns]
Small	Rigid[a]	4266	40, 80	variable	40	10	CSVR(50)	10	1,10
Small	5-site[b]	4266	40, 80	variable	40	10	Langevin(100)	10	1, 5
Small	Flexible[c]	4266	40, 80	variable	40	10	CSVR(50)	10	≥0.2, 1-5
Small	ReaxFF[d]	1563	25, 75	variable	40	5	Langevin(20)	10	≥0.2, 1-4
Small	ReaxFF[e]	1563	variable, 75	variable	40	5	CSVR(50)	10	≥0.2, 3-4
Large	Rigid[f]	15,000	variable, 500	280, 500	220	10	CSVR(100)	30	0.5, 15

[a] TIP3P, TIP3P-FB, SPC, SPC/E, OPC3, TIP4, TIP4P/2005, TIP4P-FB and OPC.
[b] TIP5P and TIP5P/2018.
[c] TIP3P/FS, SPC/Fw and mSPCFw.
[d] CHON-2017_weak and water-2017 targeting the 0.997 g cm^{-3} isochore.
[e] CHON-2017_weak and water-2017 targeting pressures above and below near-atmospheric pressure (see Sec. 8.3.2).
[f] TIP3P, SPC, SPC/E and TIP4P/2005.

where $A = L_x \times L_y$ is the cross-sectional area of the simulation box, δt is the timestep, and ΔU is the internal energy exchanged at each timestep, between each thermostatting region and its thermal reservoir.

The thermal conductivity λ was calculated from the NEMD simulations using Fourier's Law, $\boldsymbol{J}_q = -\lambda \nabla T$, where $\boldsymbol{J}_q$ is the heat flux and ∇T is the local temperature gradient. Local densities ρ and temperatures T were determined from a 5 Å bin taken along the z-axis of the simulation cell (the direction parallel to $\boldsymbol{J}_q$). Local temperature gradients were determined by fitting a straight line to the temperature profile within a range of ±8 Å around the selected state point. As demonstrated in Sec. 7.3.13, the temperature gradients $\nabla T < 12$ K nm^{-1} used in this work, are well within the linear regime.

8.2.2 Equilibrium simulations

Equilibrium MD simulations were performed in the NVT and NPT ensembles. Temperature was controlled by the Nosé-Hoover chain thermostat, with 3 chains, and a time constant of 0.5 ps. Additionally in the NPT simulations, pressure was controlled with a Nosé-Hoover chain barostat, also with 3 chains, and a time constant of 2 ps. Cubic simulation cells containing 2133 and 521 molecules were used for the traditional classical force fields and ReaxFF force fields, respectively. Each system was first equilibrated for at least 200 ps. Replicas were spawned from this equilibrated configuration, and run for an additional 100 ps in the NVT ensemble using CSVR thermostats (time constant $\tau = 0.5$ ps) with different random seeds to generate statistically independent trajectories. For the NPT simulations, an additional 100 ps of equilibration was performed with the Nosé-Hoover chain thermostat and barostat. Sampling consisted of N_{rep} replicas, each with a production length of t_{prod}. For the NPT (NVT) simulations: N_{rep} =8-20 and t_{prod} =5 ns (N_{rep} =13-15 and t_{prod} =3 ns) for the classical rigid force fields; N_{rep} =6-10 and t_{prod} =1 ns (N_{rep} =20-30 and t_{prod} =0.5 ns) for the classical flexible force fields; and N_{rep} =10-15 and t_{prod} =0.2-4 ns (N_{rep} =10 and t_{prod} =1-4 ns) for the ReaxFF force fields.

8.3 Results and discussion

All statistical uncertainties reported in this chapter, for quantities calculated in this thesis, correspond to the 95% confidence interval, unless specified otherwise.

8.3.1 Thermodynamic conditions and the equation of state

A wide range of thermodynamic states were investigated in this work. We consider: (1) near-standard thermodynamic conditions, T ∼300 K and ρ ≈1.00 g cm^{-3} or P ∼1 bar, for a survey of molecular force fields (Table 8.2); (2) temperatures in the range T =270-710 K along the 0.997 g cm^{-3} isochore using six different water models; and (3) T =190-500 K along different isobars for pressures $P < 1500$ bar, using five water models. Regarding (2) and (3), the equations of state (EOS) predicted by the selected force fields are shown in Fig. 8.2.

Each NEMD simulation generates a set of local (T, ρ) state points that corresponds to the pressure tensor component (P_{zz}) parallel to the direction of heat flux. In Fig. 8.2, we show that the NEMD simulations reproduce the EOS obtained from equilibrium-MD simulations: the densities/pressures agree to within their associated uncertainties. This indicates that the local equilibrium hypothesis is fulfilled in the NEMD simulations. Regarding the isobaric data (Fig. 8.2(a)), the NEMD P_{zz}/bar values are: 10 ± 1, 373 ± 1 and 1438 ± 1 for TIP4P/2005; 12 ± 1 for SPC/E; 0 ± 2 for SPC; and 22 ± 1 for TIP3P.

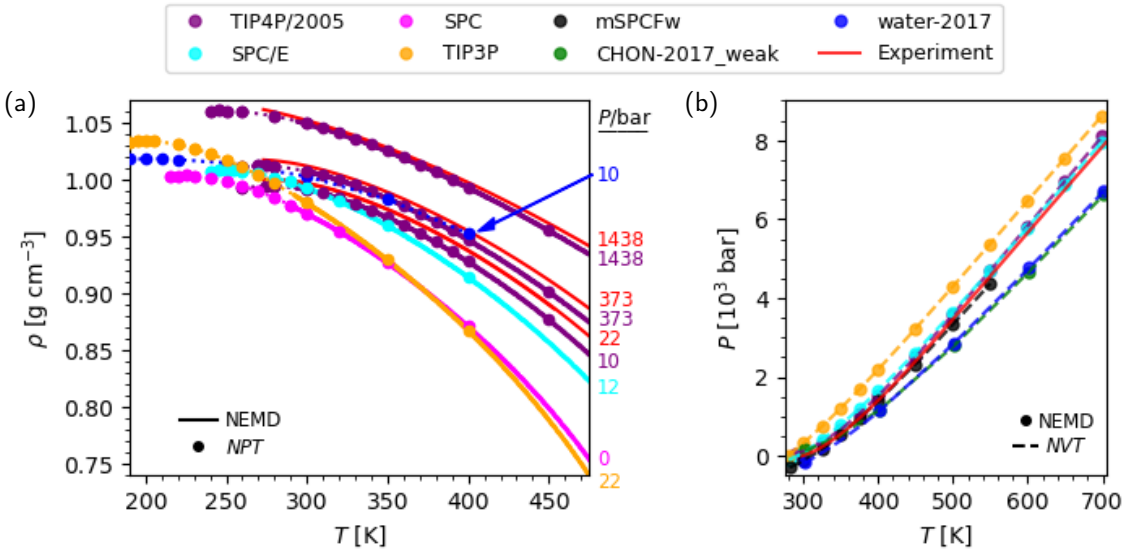


FIGURE 8.2: Equation of state of water, as predicted by selected force fields. (a) Density ρ as a function of temperature T from NEMD and equilibrium-NPT simulations. (b) Pressure P along the 0.997 g cm^{-3} isochore from NEMD and equilibrium-NVT simulations. Statistical uncertainties associated with the simulation data cannot be discerned on the scales of the plots. In (a), the experimental $\rho(T)$ lines for P/bar $= 10, 12$ cannot be discerned from the $P = 22$ bar data on the scale of the plot, except for their lower boiling points. Experimental data is from Ref. 3.

Out of all the force fields in Fig. 8.2(a), TIP4P/2005 best reproduces the experimental EOS. Using a LJ cutoff of 13 Å, it systematically underestimates the density, but only by $< 2\%$ for the simulated range of temperatures and pressures. Increasing the LJ cutoff or using tail corrections for the pressure is expected to bring the EOS into better agreement with experiment. For example, at (P, T) =(10 bar, 300 K), increasing the LJ cutoff to 19 Å increases the density from (0.9920 ± 0.0001) g cm^{-3} to (0.9952 ± 0.0006) g cm^{-3}, in better agreement with the experimental value[3] of (0.99696 ± 0.00001) g cm^{-3}. SPC/E and water-2017 reproduce the experimental EOS fairly well, while SPC and TIP3P greatly underestimate the densities at higher temperatures. All five force fields capture the density maximum (Table 8.3); TIP4P/2005 predicts a temperature of maximum density, T_{MD}, of (277 ± 3) K at 10 bar in agreement with the experimental value of 277 K, while the other force fields underestimate T_{MD} by ∼30-80 K. Our T_{MD} values are consistent with previous simulation studies of the rigid classical force fields (see Sec. 7.3.5).[28,29]

TIP4P/2005, SPC/E and mSPCFw accurately reproduce the pressure along the the 0.997 g cm^{-3} isochore, with maximal deviations ≤ 300 bar for the simulated temperature range. We note that due to the non-negligible probability of O-H bond dissociation, long simulations of mSPCFw are not possible at elevated temperatures; the highest simulated temperature was 550 K. As shown in Fig. 8.2(b), TIP3P systematically overestimates the pressure along the isochore, while water-2017 systematically underestimates it. CHON-2017_weak overestimates (underestimates) the pressure

for $T \gtrsim 350$ K ($T \lesssim 350$ K).

8.3.2 Thermal conductivity

Thermal conductivity at near-standard conditions

A survey of computational models. We show in Table 8.2 and Fig. 8.3 the thermal conductivity values of a wide range of models. It has recently come to light that the per-atom virial stress tensor-based instantaneous heat flux that has commonly been used in Green-Kubo (GK) and some NEMD calculations leads to inaccurate thermal conductivities (it is only rigorous for pairwise interactions, and constraint forces must be taken into account).[30–32] Thus, in our compilation of Table 8.2, we have excluded thermal conductivities calculated via this method. We additionally exclude studies[32–34] that do not include long-range electrostatic interactions, which can significantly affect the thermal conductivity.[35,36] The thermal conductivities in Refs. 35,37,38 were calculated from reverse non-equilibrium molecular dynamics (RNEMD) simulations that used the Müller-Plathe algorithm[39,40], whereby a heat flux is established by exchanging velocities between atoms/molecules located in different regions of the simulation cell. However, a weakly coupled global thermostat was applied to target a specific temperature, which alters the heat flux and temperature profile. In practice, the impact of this on the thermal conductivity was found to be relatively small for cyclohexane[41] ($\lesssim$0.02 W K^{-1} m^{-1} $\sim$10%) and a Lennard-Jones liquid[39] ($\lesssim$10%), but will nevertheless affect the result. Finally, we emphasize that Table 8.2 is an illustrative, not exhaustive, account of current state-of-the-art simulation results.

Our results add to the growing body of work demonstrating that traditional classical force fields typically overestimate λ by $\sim$10-50% at near-standard thermodynamic conditions. We perform simulations using a LJ cutoff of 19 Å$\approx 6\sigma_{\mathrm{OO}}$, which is long enough to reproduce the properties of the full potential, and therefore provides well-converged reference data for the force fields. The ReaxFF force fields and DFT functionals similarly overestimate λ by $\sim$30-40% and $\sim$20-50%, respectively. All these simulations did not explicitly account for nuclear quantum effects (NQEs), which owing to the low mass of the proton and the central role of hydrogen bonding can play an important role in determining the properties of water.[42] Indeed, the inclusion of NQEs lead to an estimated reduction in thermal conductivity of $\sim$10-30% in hexagonal (Ih) ice in the 150-200 K range,[43] and of $\sim$20-60% in liquid para-H_2.[44] For liquid water at near-standard, NQEs reduce both the isochoric and isobaric heat capacities by $\sim$30-40% (Sec. 7.3.9), which is related to the thermal conductivity via the thermal diffusivity (see Sec. 8.3.4). Our hypothesis is that NQEs, or lack thereof, are responsible for the universal overestimation of thermal conductivity by computational models that assume classical nuclear motion.

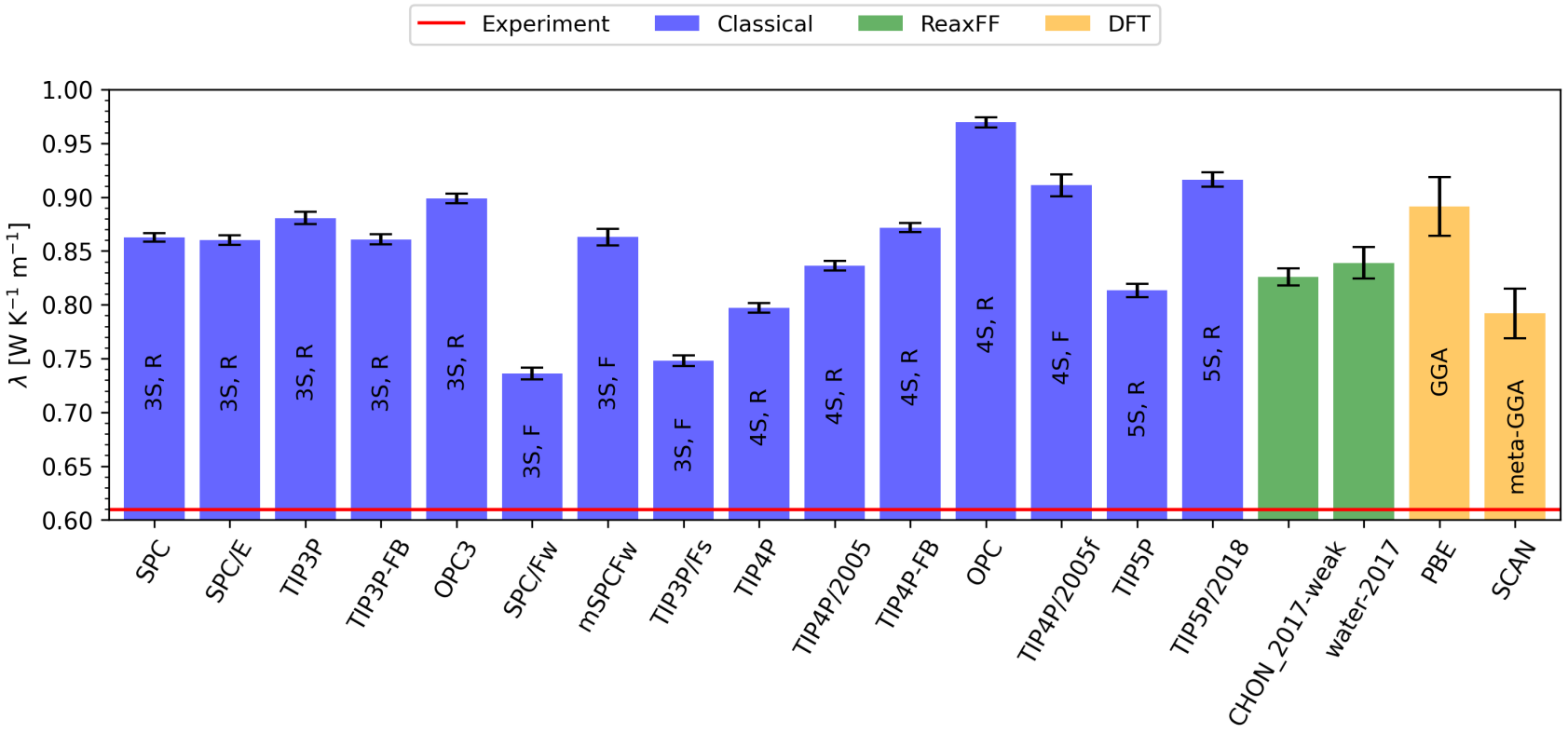


FIGURE 8.3: Thermal conductivity λ of water at close to 300 K and 1.00 g cm^{-3}, as predicted by selected computational models. Bars are colour coded and labelled according to the type of model; classical force fields are labelled NS-X, where N is the number of sites, and X=R,F denotes either rigid (R) or flexible (F). The classical force field values are from this work and correspond to a LJ cutoff of 19 Å, except for TIP4P/2005f from Ref. 45, which used a cutoff of 12 Å. The (machine-learned) DFT data is from, or estimated from, Ref. 46. The experimental value is from Ref. 47. See Table 8.2 for details and numerical data.

TABLE 8.2: Thermal conductivity λ at near-standard thermodynamic conditions as predicted by computational models. T, P and ρ are the temperature, pressure and density, respectively. Statistical uncertainties in the least significant figure are given in parentheses.

Force Field (LJ cutoff [Å])	Method	T [K]	P [bar]	ρ [g cm^{-3}]	λ [W K^{-1} m^{-1}]	Ref.
			Classical			
3-site, rigid						
SPC (19)	NEMD	300	470(1)	0.997	0.863(4)	This work
SPC (13)	NEMD	300	0(2)	0.9709(9)	0.836(7)	This work
SPC (10.4)	RNEMD	298	-	1.0	0.88(2)	Ref. 37
SPC (9)	RNEMD	300	-	1.0	0.802	Ref. 35
SPC (13)	NEMD	∼300	-	1.0	0.8108	Ref. 48
SPC/E (19)	NEMD	300	32(1)	0.997	0.860(4)	This work
SPC/E (13)	NEMD[a]	300	-	0.997	0.858(3)	This work
SPC/E (10.4)	RNEMD	298	-	1.0	0.930(16)	Ref. 37
SPC/E (9)	RNEMD	300	-	1.0	0.821	Ref. 35
SPC/E (13)	NEMD	∼300	-	1.0	0.8444	Ref. 48
SPC/E (13)	NEMD[a]	325	-	0.997	0.873(3)	This work
SPC/E (19)	NEMD	325	454(24)	1.0	0.87(4)	Ref. 49
TIP3P (19)	NEMD	300	270(1)	0.997	0.881(6)	This work
TIP3P (13)	NEMD[a]	300	-	0.997	0.878(4)	This work
TIP3P (13)	NEMD	300	22(1)	0.9801(9)	0.876(5)	This work
TIP3P (10.4)	RNEMD	298	-	1.0	0.880(19)	Ref. 37
TIP3P-FB (19)	NEMD	300	109(1)	0.997	0.861(5)	This work
OPC3 (19)	NEMD	300	91(1)	0.997	0.899(5)	This work
3-site, flexible						
SPC/Fw (19)	NEMD	300	−240(2)	0.997	0.736(6)	This work
SPC/Fw (9)	RNEMD	300	-	1.0	1.011	Ref. 35
SPC/Fd (9)	RNEMD	300	-	1.0	0.997	Ref. 35
mSPCFw (19)	NEMD	300	−178(2)	0.997	0.863(8)	This work
mSPCFw (13)	NEMD[a]	300	-	0.997	0.865(5)	This work
TIP3P/Fs (19)	NEMD	300	−642(3)	0.997	0.748(5)	This work
TIP3P/Fs (9)	RNEMD	300	-	1.0	1.063	Ref. 35
4-site, rigid						
TIP4P (19)	NEMD	300	126(1)	0.997	0.797(4)	This work
TIP4P (10.4)	RNEMD	298	-	1.0	0.820(15)	Ref. 37
TIP4P/2005 (19)	NEMD	300	61(1)	0.998	0.836(5)	This work
TIP4P/2005 (13)	NEMD[a]	300	-	0.997	0.837(3)	This work
TIP4P/2005 (13)	NEMD	300	10(1)	0.9917(8)	0.84(1)	This work
TIP4P/2005 (10.4)	RNEMD	298	-	1.0	0.910(14)	Ref. 37
TIP4P/2005 (13)	NEMD	∼300	-	1.0	0.8100	Ref. 48
TIP4P/2005 (13)	NEMD[a]	324	-	0.997	0.858(4)	This work
TIP4P/2005 (19)	NEMD	324	393(23)	1.0	0.85(3)	Ref. 49
TIP4P-FB (19)	NEMD	300	62(1)	0.998	0.872(4)	This work
OPC (19)	NEMD	300	63(1)	0.997	0.969(5)	This work
4-site, flexible						
TIP4P/2005f (12)	NEMD	300.5(3)	−4(21)	0.9971(5)	0.911(10)	Ref. 45
TIP4P/2005f	SAEMD	300	-	1.0	0.95(2)	Ref. 50
5-site, rigid						
TIP5P (19)	NEMD	300	312(7)	0.999	0.813(6)	This work
TIP5P (10.4)	RNEMD	298	-	1.0	0.680(7)	Ref. 37
TIP5P/2018 (19)	NEMD	300	63(4)	0.998	0.916(7)	This work
			ReaxFF			
water-2017	NEMD[b(i)]	300	1	1.0032(2)[b(ii)]	0.84(1)	This work
water-2017	NEMD	300	-	0.998	0.84(2)	Sec. 7.3.13
CHON-2017_weak	NEMD	300	-	0.998	0.826(8)	Sec. 7.3.13
			DFT			
PBE[c]	ER[d]	385	-	1.11	0.74(12)	Ref. 51
PBE	RNEMD	∼353	-	∼0.972	0.790	Ref. 38
PBE-ML[e]	GK	305	-	1.00	0.89(3)	Ref. 46
SCAN-ML[e,f]	GK	300	-	1.00	0.79(2)	Refs. 46
Experiment		300	1	0.99656(1)	0.609(4)	Ref. 3,47

[a] Interpolated from the isochore data, see Sec. 8.3.2. |[b] (i) Interpolated from isothermal data, see Sec. 8.3.2; (ii) ρ is from Sec. 7.3.5. |[c] Heavy water. |[d] Einstein relation. |[e] Machine-learned potentials. |[f] Linearly interpolated to 300 K from the two nearest $\lambda(T)$ data points in Ref. 46.

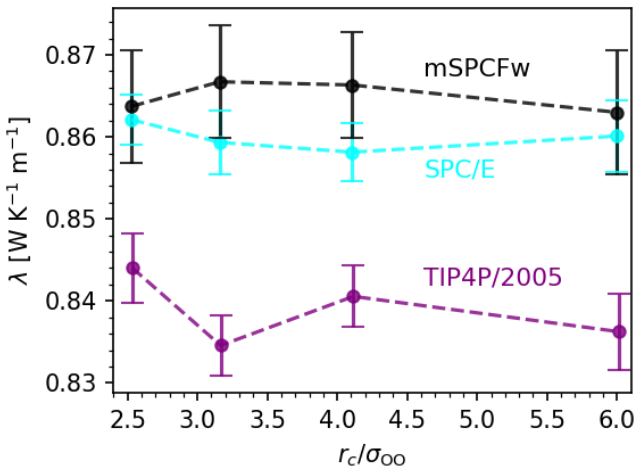


FIGURE 8.4: The effect of the Lennard-Jones cutoff r_c on the thermal conductivity λ of selected classical force fields for water. All values correspont to 300 K and (0.997±0.001) g cm^{-3}. σ_{OO} is the σ ("size") parameter of the oxygen-oxygen Lennard-Jones potential of the force field.

The effect of long-range dispersion. We show in Fig. 8.4, that for three classical force fields (TIP4P/2005, SPC/E and mSPCFw), increasing the LJ cutoff past 10 Å ($\approx 3.2\sigma_{OO}$) has only a minor impact on the thermal conductivity at 300 K and 1.00 g cm^{-3} (all values agree to within their statistical uncertainties). Comparing the thermal conductivities of LJ and WCA fluids, Ishii *et. al.* concluded that the attractive part of the LJ potential does not play a significant "direct" role in the thermal conduction of simple fluids, and that its "indirect" impact on λ is to fix the density of the system at a given thermodynamic state point.[52] Our data supports this conclusion for water, although only a single (ρ, T) state point has been tested.

The effect of molecular flexibility. It was previously concluded that molecular flexibility increases the thermal conductivity of water,[35] with classical flexible force fields typically predicting thermal conductivities ∼0.2 W K^{-1} m^{-1} higher than their rigid counterparts (see the data from Ref. 35 in Table 8.2). We reexamine this conclusion in light of the new simulation data presented in this work. At 300 K and 0.997 g cm^{-3}, λ for SPC/Fw is ∼ 15% lower than SPC and SPC/E, while mSPCFw predicts λ within ∼1% of the two rigid models. TIP3P/Fs also predicts a value ∼15% lower than TIP3P. In contrast, TIP4P/2005f has a value[45,50] ∼10% higher than TIP4P/2005. Clearly, flexible force fields can have thermal conductivities higher, lower or approximately equal to their rigid counterparts. We show in Appendix E.2 that despite the flexible models having very similar intermolecular potentials to their rigid counterparts, they have fairly different liquid structures, as evident from their radial distribution functions (RDFs) (see Fig. E.7). Thus, the addition of molecular flexibility must also be interpreted in terms of its structural perturbation of the liquid, which impacts the thermal conductivity.

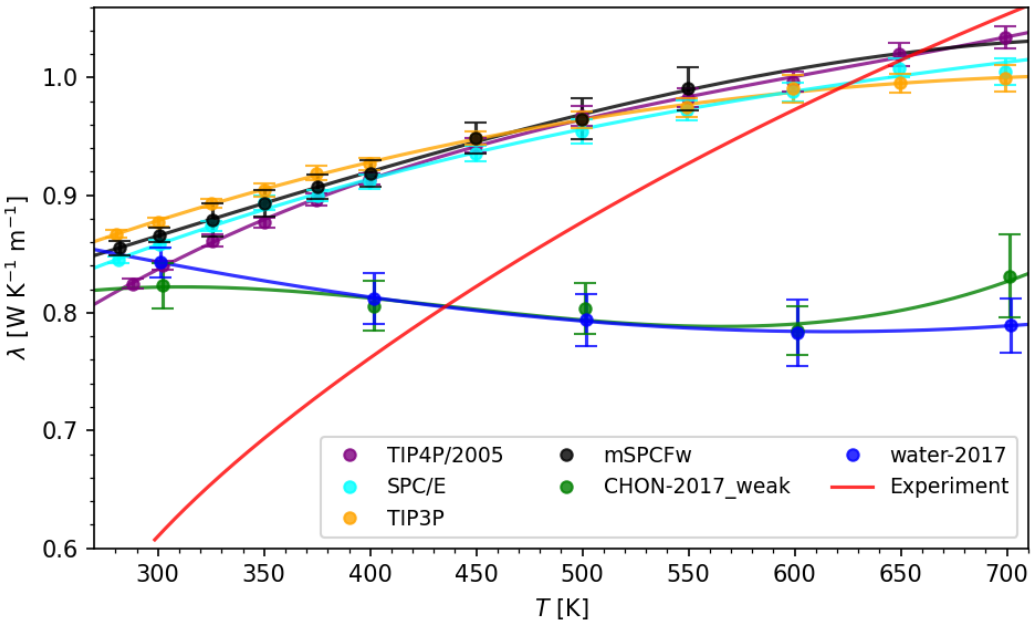


FIGURE 8.5: Thermal conductivity λ of water as a function of temperature T along the 0.997 g cm^{-3} isochore, as predicted by selected force fields. For the simulation data, solid lines show fits to cubic functions. Experimental values are from Ref. 47.

In classical water models, the bond stretching and bending degrees of freedom are populated according to equipartition theorem, and can transport energy. Physically however, vibrational energies of water near 300 K are much greater than $k_\mathrm{B}T$ and are more accurately described by quantum harmonic oscillators in the ground state, and should not significantly contribute to heat conduction.[35,41,53] As evident from our simulations results, these intramolecular degrees of freedom can indirectly impact the thermal conductivity by changing the potential energy surface, and consequently the structure and dynamics of the liquid.

Thermal conductivity along the 0.997 g cm^{-3} isochore

The NEMD thermal conductivity values along the 0.997 g cm^{-3} isochore are shown in Fig. 8.5, alongside the experimental values. For each force field, the data was fit to $\lambda(T) = aT^3+bT^2+cT+d$; the fitted functions overlap every simulation data point when accounting for their associated uncertainty, and we therefore deem cubic functions sufficient for accurately describing the temperature dependence of λ. The interpolated λ values are expected to be more accurate than the individual simulation data points, and have smaller uncertainties; we therefore report these in Table 8.2.

The traditional classical force fields correctly predict that λ monotonically increases with T, although they underestimate $d\lambda/dT$ by ∼50-90%. The ReaxFF models fail to qualitatively reproduce the temperature dependence of λ, predicting that λ is approximately constant with T. We show

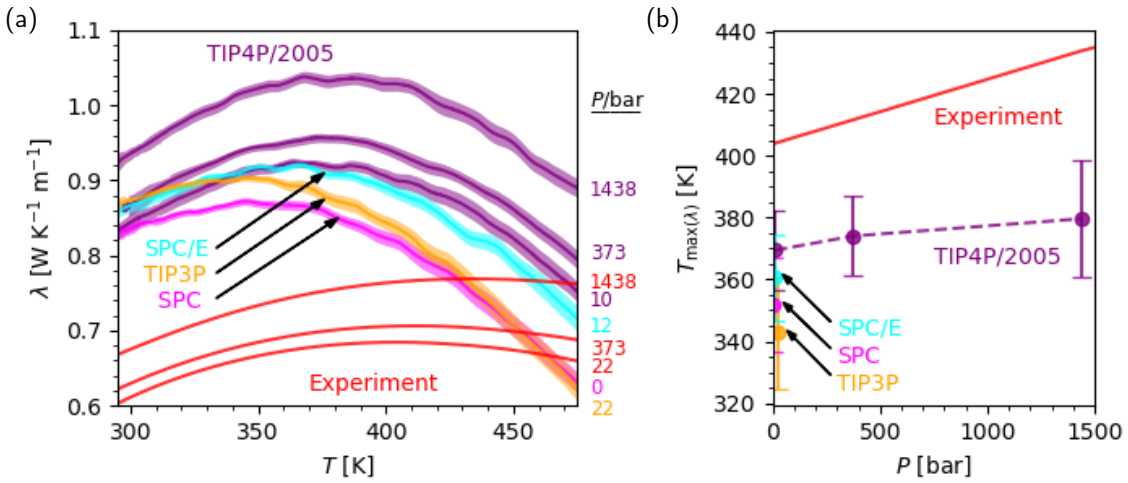


FIGURE 8.6: (a) Thermal conductivity λ of water as a function of temperature T along different isobars, as predicted by selected force fields. (b) The temperature of the thermal conductivity maximum, $T_{\max(\lambda)}$, as a function of pressure P. In (a), the experimental $\lambda(T)$ lines for $P/\text{bar} = 10, 12$ cannot be discerned from the $P = 22$ bar data on the scale of the plot, except for their lower boiling points. Experimental values are from Ref. 47.

in Sec. E.2 that the ReaxFF models have structure and dynamics benchmarks (radial distribution functions, vibrational power spectra, average number of hydrogen bonds and rotational diffusion coefficients[a]) with temperature dependencies consistent with the traditional classical force fields. We have therefore identified models of water that accurately describe hydrogen bonding along the isochore (at least using the metrics in Sec. E.2), but nevertheless fail to reproduce $\lambda(T)$.

Thermal conductivity at constant pressure

We show in Fig. 8.6(a) the thermal conductivity of TIP4P/2005, SPC/E, SPC and TIP3P along different isobars, alongside the experimental values. These force fields systematically overestimate λ for the simulated pressures. TIP4P/2005 correctly predicts that λ increases with increasing pressure. At $T \sim 460$ K, SPC and TIP3P coincide with the experimental value, then decrease further, underestimating it at higher temperatures (although SPC cannot be compared to experiment at 0 bar, when water is a vapour).

Crucially, we show that all four force fields reproduce the maximum in thermal conductivity as a function of temperature. We estimate the temperature at which the maximum occurs, $T_{\max(\lambda)}$, by self-consistently fitting a cubic function to the $\lambda(T)$ data within ± 50 K of the maximum. Our $T_{\max(\lambda)}$ values are shown in Fig. 8.6(a) and given in Table 8.3. The classical force fields underestimate $T_{\max(\lambda)}$ by ~40-60 K at ~ 10 bar. Of the three models, TIP4P/2005 most accurately predicts the position of the maximum, with $T_{\max(\lambda)} \sim 370$-$380$ K for $P < 1500$ bar. While the

[a]Our choice of rotational diffusion coefficients was motivated by Ref. 54, which found rotational intermolecular energy transfer to be the dominant contribution to heat conduction in water.

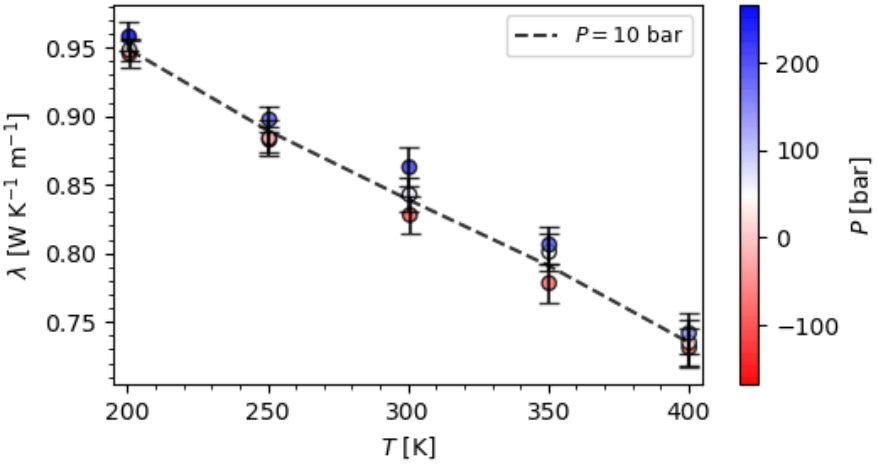


FIGURE 8.7: Thermal conductivity λ of the water-2017 force field as a function of temperature T. The data is colour coded according to the pressures P. The dashed line shows the interpolated $\lambda(T)$ data corresponding to 10 bar.

$T_{\max(\lambda)}$ values overlap given their statistical uncertainties, we observe the systematic trend that TIP4P/2005 reproduces the increase of $T_{\max(\lambda)}$ with pressure.

Thermal conductivity maxima have been inferred for TIP4P/2005 and SPC/E in previous NEMD simulation studies,[49] but quantitative estimates of $T_{\max(\lambda)}$ were not reported. Studies using the GK method have explicitly shown thermal conductivity maxima at near-atmospheric pressures (exact pressure conditions were not specified) for TIP4P/2005 ($T_{\max(\lambda)} \sim 400$ K), SPC/E ($T_{\max(\lambda)} \sim 400$ K) and TIP4P ($T_{\max(\lambda)} \sim 350$ K).[55,56] However, these studies report λ values as low as 0.2 W K^{-1} m^{-1} at 240-250 K in the supercooled liquid state, which is inconsistent with the 0.8-0.9 W K^{-1} m^{-1} from other[5,6] GK predictions using the same models. Thus, to the best of our knowledge, we report the first reliable quantitative predictions of $T_{\max(\lambda)}$ using molecular force fields.

Next, we consider the water-2017 force field. Owing to the increased computational cost of ReaxFF models compared to traditional classical force fields, it is not feasible to calculate $\lambda(T)$ across a large ($\gtrsim$100 K) temperature range in a single simulation. Instead, for each temperature we target different pressures using smaller simulations. The $\lambda(P;T)$ data can then be interpolated to estimate $\lambda(T)$ at a given P, and subsequently $\lambda(T)$ along an isobar. We show all the $\lambda(T,P)$ data in Fig. 8.7. The water-2017 force field predicts the monotonic decrease of λ with increasing temperature at constant pressure for $-70 \leq P/\text{bar} \leq 140$. Analogous to the isochore thermal conductivity, we have identified a water model that accurately describes hydrogen bonding, but nevertheless fails to reproduce the thermal conductivity maximum at constant pressure.

TABLE 8.3: The temperature T_{ex} at which extrema in thermophysical properties occur as a function of temperature at constant pressure P, as predicted by selected force fields. The temperatures of the density maximum T_{MD}, isothermal compressibility minimum $T_{min(\beta_T)}$, isentropic compressibility minimum $T_{min(\beta_S)}$, isentropic speed of sound maximum $T_{max(c_S)}$, Bridgman thermal conductivity maximum $T_{max(\lambda_B)}$, and thermal conductivity maximum $T_{max(\lambda)}$.

Force Field	P [bar]	T_{MD} [K]	$T_{min(\beta_T)}$ [K]	$T_{min(\beta_S)}$ [K]	$T_{max(c_S)}$ [K]	$T_{max(\lambda_B)}$ [K]	$T_{max(\lambda)}$ [K]
TIP4P/2005	10	277(3)	309(11)	327(12)	332(15)	325(11)	369(13)
TIP4P/2005	373	272(4)	314(12)	333(12)	345(15)	330(12)	374(13)
TIP4P/2005	1438	250(8)	318(11)	345(16)	369(14)	340(17)	380(19)
SPC/E	12	248(4)	261(17)	272(15)	280(13)	269(15)	361(14)
SPC	0	224(6)	250(10)	260(11)	270(12)	258(13)	352(15)
TIP3P	22	199(4)	238(9)	247(10)	254(12)	245(11)	343(18)
water-2017	10	204(8)	None	None	None	None	None
Exp.[a]	10	277	320	337	347	334	404
Exp.[a]	373	-	322	341	353	338	412
Exp.[a]	1438	-	325	347	365	343	434

[a] Experimental data are from, or calculated from, Refs. 47 & 3.

8.3.3 Correlations with the speed of sound and compressibility

The empirical Bridgman equation [57] connects the thermal conductivity of a liquid with its isentropic speed of sound c_S. For polyatomic substances:[57,58]

$$\lambda_B = 2.8 k_B v^{-2/3} c_S \tag{8.2}$$

where k_B is the Boltzmann constant and $v = M/\rho$ is the molecular volume (M is the molecular mass). Using the thermodynamic relations $c_S^2 = (\rho\beta_S)^{-1}$ and $\beta_T/\beta_S = C_P/C_V = \gamma$, Eq. 8.2 can be written as

$$\lambda_B = 2.8 k_B \left(\frac{\rho}{M}\right)^{2/3} c_S = 2.8 k_B \left(\frac{\rho}{M^4 \beta_S^3}\right)^{1/6} = 2.8 k_B \left(\frac{\rho \gamma^3}{M^4 \beta_T^3}\right)^{1/6} \tag{8.3}$$

and therefore provides a direct connection with the density ρ, isentropic compressibility β_S, isothermal compressibility β_T and adiabatic index γ. C_P and C_V are the isobaric and isochoric heat capacities, respectively. These quantities were calculated from NPT simulations using the fluctuation relations, as described in Chapter 7. For NPT simulations along the isochore, the pressures were first calculated from NVT simulations, and in all cases the simulated density was within ± 0.0005 g cm^{-3} of 0.997 g cm^{-3}.

Correlations at constant density: the 0.997 g cm^{-3} isochore

The Bridgman thermal conductivities along the 0.997 g cm^{-3} isochore are shown in Fig. 8.8(a). For each force field, cubic functions were fit to the $\lambda_B(T)$ data; the fitted functions predict every data

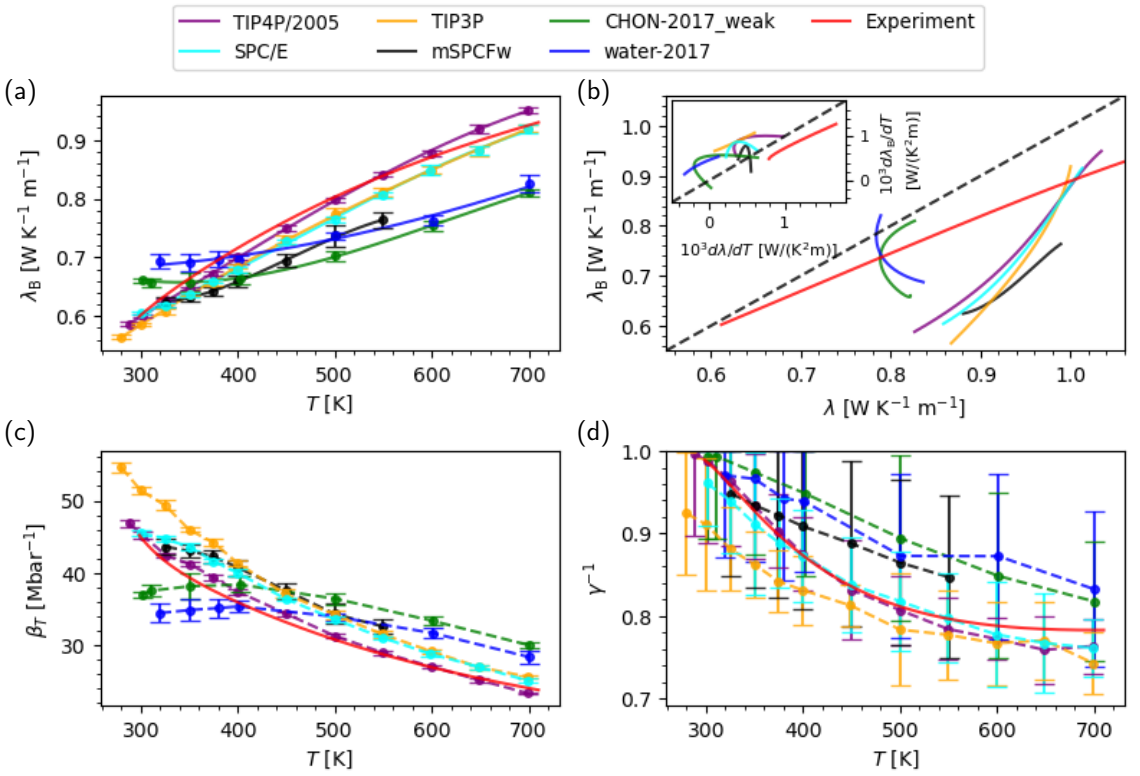


FIGURE 8.8: Bridgman thermal conductivity and related quantities along the 0.997 g cm^{-3} isochore, from experiment and as predicted by selected force fields. (a) Thermal conductivity predicted by the Bridgman equation, λ_B, as a function of temperature T. For the simulation data, solid lines show fits to cubic functions. (b) λ_B *vs.* the thermal conductivity λ; the inset shows $d\lambda_B/dT$ *vs.* $d\lambda/dT$. (c) Isothermal compressibility β_T *vs.* T. (d) γ^{-1} *vs.* T, where γ is the adiabatic index. Experimental data are from, or calculated from, Refs. 47 & 3.

point to within its associated uncertainty. Out of the six force fields, TIP4P/2005 best reproduces the experimental $\lambda_B(T)$ for $T \lesssim 630$ K. As shown in Fig. 8.8(b), the Bridgman equation reproduces the experimental thermal conductivity of water reasonably well, with greater deviations at higher temperatures; percentage errors range from of 1% at 300 K to 12% at 700 K. For the traditional classical force fields, λ_B underestimates λ for the entire simulated temperature range with greater deviations at lower temperatures, and maximal percentage errors of 25-35% at $T \sim 300$ K. The temperature dependence of λ is reflected in λ_B, and $d\lambda_B/dT$ is positively correlated with $d\lambda/dT$, as shown in the inset of Fig. 8.8(b). In particular, water-2017 and CHON-2017_weak feature weaker temperature dependencies compared to the classical force fields.

By definition, density is held constant along the isochore. Thus, the temperature dependence of λ_B is carried solely through β_S. For all six force fields (Fig. 8.8(d)), $\gamma^{-1} = \beta_S/\beta_T > 0.7$ for $280 \leq T/\text{K} \leq 710$. Furthermore, $\gamma^{-1} = 1.0$ (to 1 decimal place) at $T \sim 300$ K, except for TIP3P for which $\gamma^{-1} = 0.91 \pm 0.08$ at 300 K. Thus, $\lambda_B(T)$ is largely determined by $\beta_T(T)$, especially at lower temperatures. Comparing Figs. 8.8(a) and (c), it is evident that the temperature dependence

of λ_B is reflected by β_T. The weak temperature dependence of λ for the ReaxFF models can be correlated, through the Bridgman equation, to the weak temperature dependence of β_S and β_T.

Correlations at constant pressure

Next we consider the Bridgman thermal conductivity along different isobars, where density effects play a role in determining λ_B. We show in Fig. 8.9, λ_B, c_S, β_S and β_S for selected force fields. Compared to experiment, the rigid classical force fields underestimate λ_B and c_S, and accordingly overestimate β_S and β_T. In contrast, at 10 bar, water-2017 overestimates λ_B and c_S, and underestimates β_S and β_T. TIP4P/2005 correctly predicts that λ_B and c_S increase, and β_S and β_S decrease, with increasing pressure. Our results for the isothermal compressibility of the rigid classical force fields are consistent with previous studies.[28,59,60] TIP4P/2005 in particular has been investigated over an extensive range of temperatures ($190 \leq T/\mathrm{K} \leq 370$) and pressures (up to $P \sim 2000$ bar).[59,60]

All four empirical rigid classical force fields capture the extrema in the thermodynamic properties, while water-2017 does not: these are the maxima in $\lambda_B(T)$ and $c_S(T)$, and the minima in $\beta_S(T)$ and $\beta_T(T)$. Indeed, the ReaxFF model predicts a monotonic decrease (increase) of λ_B and c_S (β_S and β_S) with increasing temperature. To estimate the temperature T_{ex} at which the extrema occur (Table 8.3), a cubic function was fit to the simulation data for each thermodynamic property in a region close to its extremum. We show in Fig. 8.10 that the rigid classical force fields correctly predict $T_{\max(\lambda)} > T_{\max(c_S)} > T_{\min(\beta_S)} > T_{\max(\lambda_B)} > T_{\min(\beta_T)}$, and TIP4P/2005 reproduces the increase of T_{ex} with pressure for all four thermodynamic properties (as well as $T_{\max(\lambda)}$, see Sec. 8.3.2). However, many of the T_{ex} values overlap given their uncertainties; further sampling is required to validate these trends to a greater degree of statistical certainty.

λ_B, c_S, β_S and β_T are connected by thermodynamic relations. Since $\rho(T)$ and $\gamma(T)$ both increase monotonically in the temperature range that the extrema occur, Eqs. 8.2 & 8.3 imply that all four extrema share the same phenomenological origin (i.e., if one did not exist, then they all would not exist), and that the effect of $\rho(T)$ and $\gamma(T)$ is to shift T_{ex}. Thus, the Bridgman equation provides a possible thermodynamic explanation for the maximum in thermal conductivity. The final leap is to establish how representative λ_B is of λ. Clearly, Eq. 8.2 does not accurately predict the thermal conductivity for the range of temperatures and pressures investigated here, with percentage errors of ∼0-30% for the experimental data. However, it does reproduce the maximum, but with $T_{\max(\lambda)}$ shifted by 70-90 K, with greater shifts at higher pressures (i.e., $T_{\max(\lambda_B)}$ has a weaker pressure dependence than $T_{\max(\lambda)}$). We show in Fig. 8.10(b) that $T_{\max(\lambda)}$ is correlated with $T_{\max(\lambda_B)}$, and as implied by the Bridgman equation, with $T_{\max(c_S)}$, $T_{\min(\beta_S)}$ and $T_{\min(\beta_T)}$ as well. The key question is whether, and under what conditions, a maximum in λ_B implies that a maximum in λ exists. We have tested force fields of varying quality: all models that have a

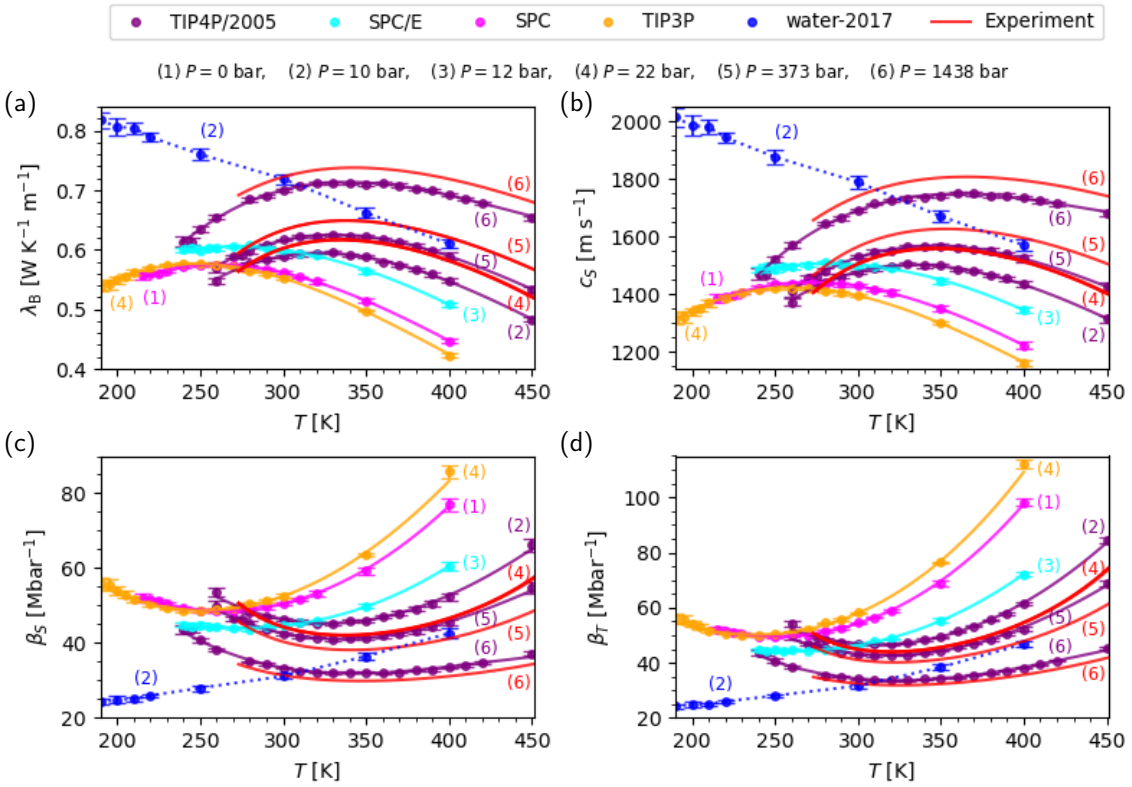


FIGURE 8.9: Thermodynamic properties of water as a function of temperature T along different isobars, as predicted by selected force fields and from experiment. The (a) Bridgman thermal conductivity λ_B, (b) isentropic seed of sound c_S, (c) isentropic compressibility β_S, and (d) isothermal compressibility β_T. For the simulation data, solid lines show fits to cubic functions to guide the eye. Experimental data for $P/\text{bar} = 10, 12$ cannot be discerned from the $P = 22$ bar data on the scale of the plots, except for their lower boiling points. Experimental data are from, or calculated from, Ref. 3.

maximum in λ_B also feature the maximum in λ, and the only force field (water-2017) that does not have a maximum in λ_B, similarly does not possess the maximum in λ.

The minimum in β_T has been studied extensively, and microscopic explanations have been proposed.[61–66] High energy x-ray diffraction experiments show a structural transition concomitant with the compressibility minimum: tetrahedral structures become more prominent at $T_{\min(\beta_T)}$ upon cooling (see Sec. 7.3.8 for a more detailed discussion).[61–63] These extended tetrahedral structures (the low-density liquid in the terminology of two-state models of water) take up more space than the more disordered arrangement (the high-density liquid).[64–66] Fluctuating tetrahedral structures therefore lead to an increased β_T.[64] An increased concentration of tetrahedral structures (increasing β_T) upon cooling competes with effect of increasing density (decreasing β_T), leading to a minimum. Thus, by connecting the λ maximum and β_T minimum, the Bridgman equation provides a possible microscopic explanation for the maximum in thermal conductivity.

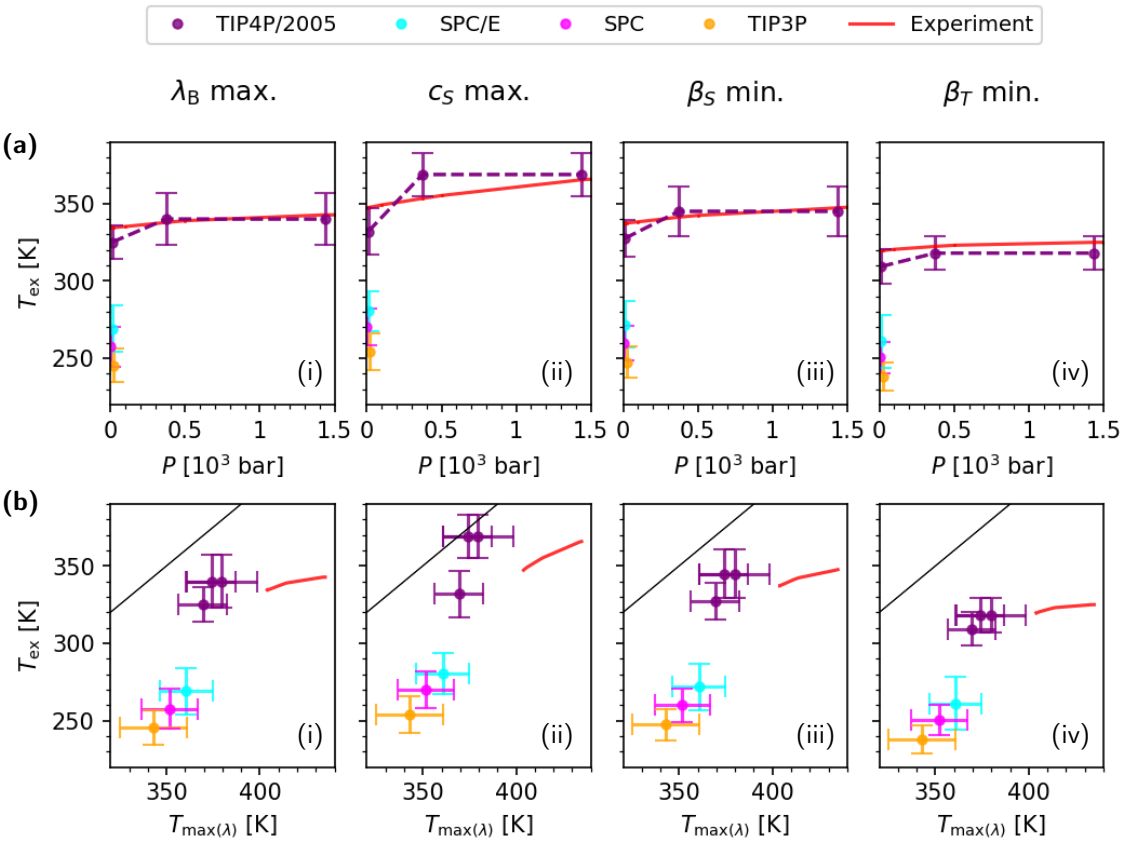


FIGURE 8.10: The temperature T_{ex} at which extrema (maxima or minima) in thermophysical properties occur as a function of temperature at constant pressure P, as predicted by selected force fields. (a) T_{ex} as a function of P. (b) Correlation plots of T_{ex} *vs.* $T_{max(\lambda)}$, where $T_{max(\lambda)}$ is the temperature of the thermal conductivity maximum. The: (i) Bridgman thermal conductivity λ_B; (ii) isentropic speed of sound c_S; (iii) isentropic compressibility β_S; and (iv) isothermal compressibility β_T. In (b), the black line shows $T_{ex} = T_{max(\lambda)}$ for reference. Experimental data are from, or calculated from, Refs. 47 & 3.

The lack of a compressibility minimum for water-2017 indicates that it is missing crucial aspects of the orientational correlations in liquid water, since these are linked to the tetrahedral order of the liquid. We show in Appendix. E.3 that TIP4P/2005 and water-2017 have qualitatively similar temperature dependencies at 10 bar for tetrahedral order parameters[67–72] widely used in the literature. Similarly, the RDFs of the two force fields have similar temperature dependencies along the isobar (Appendix E.2, Fig. E.8). Further work is required to identify the deficiency of the water-2017 force field that leads to the absence of the β_T minimum, and by extension, the lack of related extrema (the β_S minimum, and maxima in c_S, λ_B and λ).

8.3.4 Correlations with sound attenuation and longitudinal viscosity

The sound attenuation coefficient Γ is a measure of the energy loss during sound propagation through a medium. For a bulk single-component homogeneous fluid, hydrodynamics gives:[73]

$$\Gamma = \frac{(\gamma - 1)a_{\mathrm{TD}}}{2} + \frac{b}{2} \tag{8.4}$$

and for thermal conductivity,

$$\lambda = \frac{\rho C_P (2\Gamma - b)}{\gamma - 1} \tag{8.5}$$

where $a_{\mathrm{TD}} = \lambda/(\rho C_P)$ is the thermal diffusivity, and b is the kinematic longitudinal viscosity. In Eq. 8.4, the $(\gamma-1)a_{\mathrm{TD}}/2$ and $b/2$ terms correspond to energy losses due to thermal conduction and viscous effects (bulk and shear), respectively. The kinematic longitudinal viscosity was calculated from $b = \xi/\rho$ and $\xi = (4/3)\eta + \zeta$, where ξ, η and ζ are the longitudinal, shear and bulk viscosities, respectively. In turn, η and ζ were calculated using their Green-Kubo integral formulas (see Appendix. E.4).

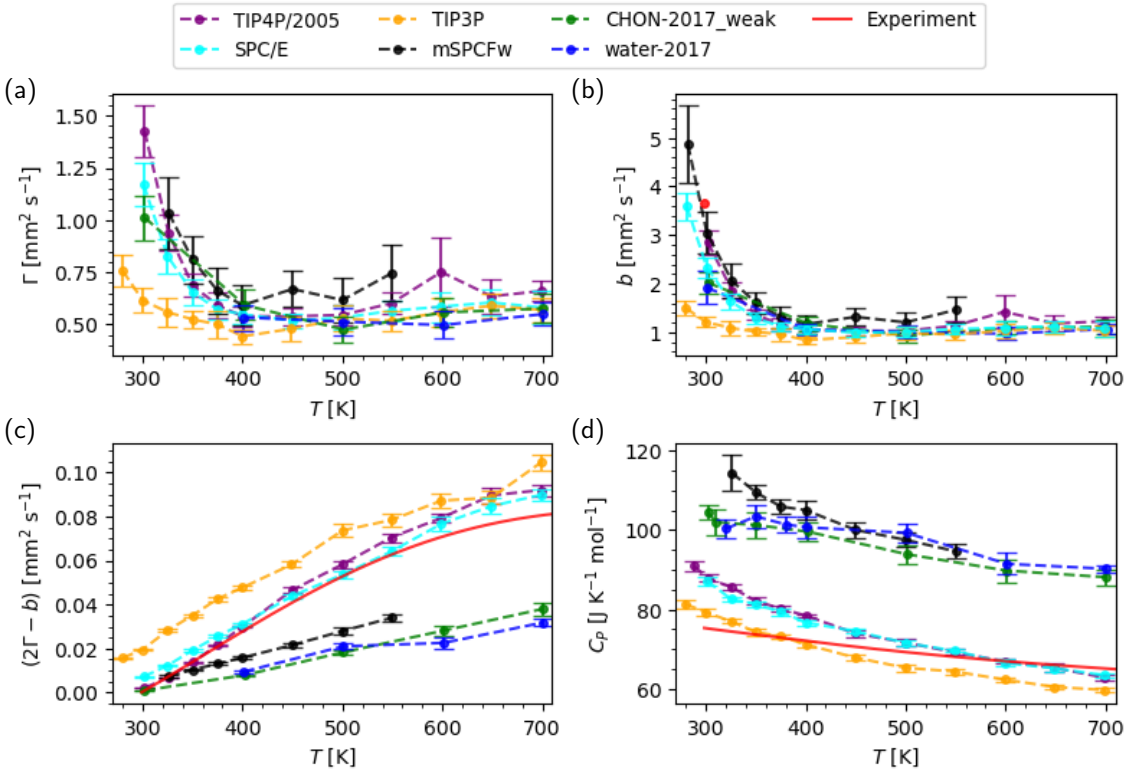


FIGURE 8.11: The (a) sound attenuation coefficient Γ, (b) kinematic longitudinal viscosity b, (c) $2\Gamma - b$, and (d) isobaric heat capacity C_P as a function of temperature T along the 0.997 g cm^{-3} isochore, as predicted by selected force fields. In (b), the experimental value[74] corresponds to 298.15 K and ambient pressure. Experimental data are from, or calculated from, Refs. 47, 3 & 74.

The variables entering Eqs. 8.4 & 8.5 are shown in Fig. 8.11 for temperatures along the 0.997 g cm^{-3} isochore. All six force fields predict that the $b/2$ term is the dominant contribution to Γ, amounting to 90-100% across the simulated temperature range, and 98-100% at 300 K. This is consistent with experimental measurements, which give $b/(2\Gamma) \approx 1.00$ at ambient pressure and temperatures close to 300 K.[74] Equivalently, the $2\Gamma - b = (\gamma - 1)a_{\mathrm{TD}}$ terms in Eqs. 8.5 & 8.5 are small, on the order of 10^{-2} mm^2 s^{-1}. As shown in Fig. 8.11(c), $2\Gamma - b$ features a weaker temperature dependence for the ReaxFF models, reflecting the trend in thermal conductivity. mSPCFw also has a weaker temperature dependence compared to the rigid force fields. With regards to C_P, the rigid models have smaller heat capacities because the intramolecular degrees of freedom are frozen out. As discussed in Sec. 7.3.9, C_P is expected to be overestimated due to the exclusion of nuclear quantum effects, which are less significant at higher temperatures. TIP3P systematically overestimates $2\Gamma - b$, but predicts lower C_P values compared to the other rigid force fields; these two discrepancies counteract each other, giving thermal conductivities consistent with TIP4P/2005 and SPC/E. TIP3P severely underestimates b, by $\sim 70\%$ at ~ 300 K. Clearly, $\lambda(T)$ cannot be interpreted in terms of just $2\Gamma - b$, as other variables enter into Eq. 8.5. However, for the ReaxFF models, the weak temperature dependencies of λ and $2\Gamma - b$ are correlated.

8.4 Conclusions

We have assessed the ability of a wide range of computational models to predict the thermal conductivity of water: (1) at near-standard conditions, $T \sim$300 K and $\rho \approx$1.00 g cm^{-3} or $P \sim$1 bar; (2) along the "standard liquid" 0.997 g cm^{-3} isochore; and (3) along different isobars for pressures $P < 1500$ bar.

Near-standard conditions. Our results add to the growing body of work demonstrating classical force fields, both "traditional" and ReaxFF, typically overestimate λ by ∼10-50%. The PBE and SCAN DFT functionals similarly overestimate λ by ∼20-50%.[38,46,51] Our hypothesis is that NQEs, or lack thereof, are responsible for the universal overestimation of thermal conductivity by computational models that assume classical nuclear motion. We showed that long-range dispersion does not significantly impact the thermal conductivity at a given temperature and density. This suggests that, as for simple liquids[52], it mainly affects λ by fixing the density of the system at a given thermodynamic state point. We also demonstrated that flexible models can have thermal conductivities higher, lower or approximately equal to their rigid counterparts. The addition of intramolecular degrees of freedom can significantly perturb the liquid structure, and hence indirectly impact the thermal conductivity.

The 0.997 g cm^{-3} isochore. Along the isochore, the traditional classical force fields correctly predict that λ increases with temperature, although underestimate $d\lambda/dT$ by ∼50-90%.

The ReaxFF models fail to qualitatively reproduce this temperature dependence, predicting that λ is approximately independent of temperature. This is despite having standard structure and dynamics benchmarks consistent with the state-of-the-art traditional classical force fields. We have therefore identified models that accurately describe hydrogen bonding along the isochore (at least using the metrics in Sec. E.2), but nevertheless fail to reproduce the thermal conductivity's temperature dependence. The weak temperature dependence of λ for the ReaxFF models can be correlated, through the empirical Bridgman equation and thermodynamic relations, to the weak temperature dependence of the isentropic and isothermal compressibilities, β_S and β_T, respectively. From hydrodynamics $\lambda \propto 2\Gamma - b$, where Γ and b are the sound attenuation coefficient and kinematic longitudinal viscosity, respectively. The weak temperature of λ for the ReaxFF models can also be rationalized by the weak temperature dependence of $2\Gamma - b$.

Constant pressure for $P < 1500$ bar. The classical force fields TIP4P/2005, SPC/E, SPC and TIP3P all capture the maximum in thermal conductivity, but underestimate $T_{\max(\lambda)}$ by ∼40-60 K at ∼10 bar. TIP4P/2005 also correctly predicts that $T_{\max(\lambda)}$ increases with pressure. It is remarkable that these relatively simple models reproduce the thermal conductivity maximum. While TIP4P/2005 is arguably the most successful general purpose water model for thermophysical properties (accordingly, it most accurately predicts $T_{\max(\lambda)}$), the others are less accurate:[17,28] TIP4P/2005, SPC/E and TIP3P have Vega-Abascal scores of 7.2, 5.1 and 2.7, respectively, out of 10.[28] In contrast, the water-2017 ReaxFF force field does not reproduce the thermal conductivity maximum. The Bridgman equation connects the thermal conductivity maximum with the nearby maximum in the speed of sound c_S, and thus to the minima in the compressibilities, β_S and β_T. We have shown that the position of these extrema are correlated with $T_{\max(\lambda)}$. Crucially, the only force field that does not capture the thermal conductivity maximum also fails to reproduce all these extrema. Thus, the Bridgman equation provides a possible thermodynamic explanation for the thermal conductivity maximum. The minimum in $\beta_T(T)$ at 319 K and 1 bar has been attributed to an increased concentration of extended tetrahedral hydrogen bonding structures.[64] Through β_T, the Bridgman equation therefore also provides a possible microscopic explanation for the maximum in thermal conductivity. However, water-2017 and TIP4P/2005 have qualitatively similar tetrahedral order parameter and RDF temperature dependencies at 10 bar (Appendix E). Further work is required to identify the deficiency of the water-2017 force field that leads to the absence of the β_T minimum, and by extension, possibly the thermal conductivity maximum as well.

Bibliography

[1] H. Fukuyama, T. Yoshimura, H. Yasuda and H. Ohta, *Int. J. Thermophys.*, 2006, **27**, 1760–1777.

[2] G. Chen, *J. Heat Transfer*, 2021, **144**, year.

[3] W. Wagner and A. Pruß, *J. Phys. Chem. Ref. Data*, 2002, **31**, 387–535.

[4] P. Kumar and H. E. Stanley, *J. Phys. Chem. B*, 2011, **115**, 14269–14273.

[5] F. Bresme, J. W. Biddle, J. V. Sengers and M. A. Anisimov, *J. Chem. Phys.*, 2014, **140**, 161104.

[6] N. J. English and J. S. Tse, *J. Phys. Chem. Lett.*, 2014, **5**, 3819–3824.

[7] W. L. Jorgensen, J. Chandrasekhar, J. D. Madura, R. W. Impey and M. L. Klein, *J. Chem. Phys.*, 1983, **79**, 926–935.

[8] L.-P. Wang, T. J. Martinez and V. S. Pande, *J. Phys. Chem. Lett.*, 2014, **5**, 1885–1891.

[9] H. J. C. Berendsen, J. P. M. Postma, W. F. van Gunsteren and J. Hermans, in *Interaction Models for Water in Relation to Protein Hydration*, ed. B. Pullman, Springer Netherlands, Dordrecht, 1981, pp. 331–342.

[10] H. J. C. Berendsen, J. R. Grigera and T. P. Straatsma, *J. Phys. Chem.*, 1987, **91**, 6269–6271.

[11] S. Izadi and A. V. Onufriev, *J. Chem. Phys.*, 2016, **145**, 074501.

[12] J. L. F. Abascal and C. Vega, *J. Chem. Phys.*, 2005, **123**, 234505.

[13] S. Izadi, R. Anandakrishnan and A. V. Onufriev, *J. Phys. Chem. Lett.*, 2014, **5**, 3863–3871.

[14] M. W. Mahoney and W. L. Jorgensen, *J. Chem. Phys.*, 2000, **112**, 8910–8922.

[15] Y. Khalak, B. Baumeier and M. Karttunen, *J. Chem. Phys.*, 2018, **149**, 224507.

[16] U. W. Schmitt and G. A. Voth, *J. Chem. Phys.*, 1999, **111**, 9361–9381.

[17] T. Wu, H. L. Tepper and G. A. Voth, *J. Chem. Phys.*, 2006, **124**, 024503.

[18] K. S. Smirnov, *Phys. Chem. Chem. Phys.*, 2017, **19**, 2950–2960.

[19] W. Zhang and A. C. T. van Duin, *J. Phys. Chem. B*, 2017, **121**, 6021–6032.

[20] W. Zhang and A. C. T. van Duin, *J. Phys. Chem. B*, 2018, **122**, 4083–4092.

[21] A. P. Thompson, H. M. Aktulga, R. Berger, D. S. Bolintineanu, W. M. Brown, P. S. Crozier, P. J. in 't Veld, A. Kohlmeyer, S. G. Moore, T. D. Nguyen, R. Shan, M. J. Stevens, J. Tranchida, C. Trott and S. J. Plimpton, *Comp. Phys. Comm.*, 2022, **271**, 108171.

[22] T. F. Miller, M. Eleftheriou, P. Pattnaik, A. Ndirango, D. Newns and G. J. Martyna, *J. Chem. Phys.*, 2002, **116**, 8649–8659.

[23] H. C. Andersen, *J. Comput. Phys.*, 1983, **52**, 24–34.

[24] J.-P. Ryckaert, G. Ciccotti and H. J. Berendsen, *J. Comput. Phys.*, 1977, **23**, 327–341.

[25] M. Allen and D. Tildesley, *Computer Simulation of Liquids*, Oxford: Clarendon Pr, 1987.

[26] E. Pollock and J. Glosli, *Comput. Phys. Commun.*, 1996, **95**, 93–110.

[27] H. M. Aktulga, J. C. Fogart, S. A. Pandit and A. Y. Grama, *Parallel Comput.*, 2012, **38**, 245–259.

[28] C. Vega and J. L. F. Abascal, *Phys. Chem. Chem. Phys.*, 2011, **13**, 19663–19688.

[29] W. L. Jorgensen and J. Tirado-Rives, *Proc. Natl. Acad. Sci. U. S. A.*, 2005, **102**, 6665–6670.

[30] P. Boone, H. Babaei and C. E. Wilmer, *J. Chem. Theory Comput.*, 2019, **15**, 5579–5587.

[31] D. Surblys, H. Matsubara, G. Kikugawa and T. Ohara, *Phys. Rev. E*, 2019, **99**, 051301.

[32] D. Surblys, H. Matsubara, G. Kikugawa and T. Ohara, *J. Appl. Phys.*, 2021, **130**, 215104.

[33] J. Muscatello, F. Römer, J. Sala and F. Bresme, *Phys. Chem. Chem. Phys.*, 2011, **13**, 19970–19978.

[34] S. Kuang and J. D. Gezelter, *J. Chem. Phys.*, 2010, **133**, 164101.

[35] T. W. Sirk, S. Moore and E. F. Brown, *J. Chem. Phys.*, 2013, **138**, 064505.

[36] J. Muscatello and F. Bresme, *J. Chem. Phys.*, 2011, **135**, 234111.

[37] Y. Mao and Y. Zhang, *Chem. Phys. Lett.*, 2012, **542**, 37–41.

[38] E. Tsuchida, *J. Phys. Soc. Jpn.*, 2018, **87**, 025001.

[39] F. Müller-Plathe, *J. Chem. Phys.*, 1997, **106**, 6082–6085.

[40] D. Bedrov and G. D. Smith, *J. Chem. Phys.*, 2000, **113**, 8080–8084.

[41] M. Zhang, E. Lussetti, L. E. S. de Souza and F. Müller-Plathe, *J. Phys. Chem. B*, 2005, **109**, 15060–15067.

[42] M. Ceriotti, W. Fang, P. G. Kusalik, R. H. McKenzie, A. Michaelides, M. A. Morales and T. E. Markland, *Chem. Rev.*, 2016, **116**, 7529–7550.

[43] R. Luo and K. Yu, *J. Chem. Phys.*, 2020, **153**, 194105.

[44] B. J. Sutherland, W. H. D. Moore and D. E. Manolopoulos, *J. Chem. Phys.*, 2021, **154**, 174104.

[45] A. Chapman and F. Bresme, *Phys. Chem. Chem. Phys.*, 2022, **24**, 14924–14936.

[46] D. Tisi, L. Zhang, R. Bertossa, H. Wang, R. Car and S. Baroni, *Phys. Rev. B*, 2021, **104**, 224202.

[47] M. L. Huber, R. A. Perkins, D. G. Friend, J. V. Sengers, M. J. Assael, I. N. Metaxa, K. Miyagawa, R. Hellmann and E. Vogel, *J. Phys. Chem. Ref. Data*, 2012, **41**, 033102.

[48] H. Dorrani and A. Mohebbi, *J. Engin. Thermophys.*, 2023, **32**, 138–161.

[49] F. Römer, A. Lervik and F. Bresme, *J. Chem. Phys.*, 2012, **137**, 074503.

[50] M. Puligheddu and G. Galli, *Phys. Rev. Mater.*, 2020, **4**, 053801.

[51] A. Marcolongo, P. Umari and S. Baroni, *Nat. Phys.*, 2016, **12**, 80–84.

[52] Y. Ishii, K. Sato, M. Salanne, P. A. Madden and N. Ohtori, *J. Chem. Phys.*, 2014, **140**, 114502.

[53] E. A. Algaer and F. Müller-Plathe, *Soft Materials*, 2012, **10**, 42–80.

[54] T. Ohara, *J. Chem. Phys.*, 1999, **111**, 6492–6500.

[55] S. H. Lee, *Mol. Phys.*, 2014, **112**, 2155–2159.

[56] S. H. Lee and J. Kim, *Mol. Phys.*, 2019, **117**, 1926–1933.

[57] P. W. Bridgman, *Proc. Natl. Acad. Sci. U.S.A.*, 1923, **9**, 341–345.

[58] J. O. Hirschfelder, C. F. Curtiss and B. R. Bird, *The Molecular Theory of Gases and Liquids*, Wiley, 1966.

[59] H. L. Pi, J. L. Aragones, C. Vega, E. G. Noya, J. L. F. Abascal, M. A. Gonzalez and C. McBride, *Mol. Phys.*, 2009, **107**, 365–374.

[60] M. A. González, C. Valeriani, F. Caupin and J. L. F. Abascal, *J. Chem. Phys.*, 2016, **145**, 054505.

[61] L. B. Skinner, C. J. Benmore, J. C. Neuefeind and J. B. Parise, *J. Chem. Phys.*, 2014, **141**, 214507.

[62] C. Huang, K. T. Wikfeldt, D. Nordlund, U. Bergmann, T. McQueen, J. Sellberg, L. G. M. Pettersson and A. Nilsson, *Phys. Chem. Chem. Phys.*, 2011, **13**, 19997–20007.

[63] D. Schlesinger, K. T. Wikfeldt, L. B. Skinner, C. J. Benmore, A. Nilsson and L. G. M. Pettersson, *J. Chem. Phys.*, 2016, **145**, 084503.

[64] A. Nilsson and L. G. M. Pettersson, *Nat. Commun.*, 2015, **6**, 8998.

[65] J. Russo and H. Tanaka, *Nat. Commun.*, 2014, **5**, 3556.

[66] M. Vedamuthu, S. Singh and G. W. Robinson, *J. Phys. Chem.*, 1995, **99**, 9263–9267.

[67] E. Duboué-Dijon and D. Laage, *J. Phys. Chem. B*, 2015, **119**, 8406–8418.

[68] P.-L. Chau and A. J. Hardwick, *Mol. Phys.*, 1998, **93**, 511–518.

[69] J. R. Errington and P. G. Debenedetti, *Nature*, 2001, **409**, 318–321.

[70] G. Ruocco, M. Sampoli and R. Vallauri, *J. Chem. Phys.*, 1992, **96**, 6167–6176.

[71] P. J. Steinhardt, D. R. Nelson and M. Ronchetti, *Phys. Rev. B*, 1983, **28**, 784–805.

[72] W. Mickel, S. C. Kapfer, G. E. Schröder-Turk and K. Mecke, *J. Chem. Phys.*, 2013, **138**, 044501.

[73] J.-P. Hansen and I. R. McDonald, *Theory of Simple Liquids with Applications to Soft Matter*, Academic Press, 4th edn., 2013.

[74] M. J. Holmes, N. G. Parker and M. J. W. Povey, *J. Phys.: Conf. Ser.*, 2011, **269**, 012011.

Chapter 9

Conclusions and future work

In this thesis, computer simulations and analytical theoretical models were used to investigate non-isothermal transport phenomena and coupling effects in a diverse range of fluids. Namely, the thermal diffusion and thermal conductivity of molecular mixtures, colloids, and polar fluids.

Soret coefficient minima in molecular mixtures

Rationalizing the phenomenology observed in experiments in terms of molecular properties and microscopic behaviour is a challenging problem. Minima/maxima in the Soret coefficient S_T are case in point: their physical origin remain largely unknown. In Chapter 3, we identified a liquid Lennard-Jones mixture that features a minimum in S_T as a function of composition (mole fraction x_1), demonstrating that S_T minima can occur in even the simplest mixtures. This S_T minimum arises due to a coincident minimum in the thermodynamic factor Γ, and is therefore connected to the non-ideality of the mixture. The microscopic origin of the S_T and Γ minima can be traced back primarily to the composition dependence of the excess coordination number $n_{12}^{\mathrm{ex},\infty}$, which represents the net depletion of species 2 around 1 relative to the ideal gas state. Theoretical models that do not account for the non-ideality of the mixture fail to reproduce the S_T minimum.

Mass dipole contribution to the isotopic Soret effect in molecular mixtures

In Chapter 4, we shifted our focus to the (pseudo-)isotopic Soret effect. We uncovered the mass dipole contribution in molecular mixtures, showing that mixtures of components that differ only by the first moment of their mass distributions can have non-zero Soret coefficients. For the isotopic mixtures of linear rigid molecules investigated in this work, the dependence of S_T on the mass dipole arises mainly through the thermal diffusion coefficient D_T. In turn, D_T is correlated with the dependence of the molecular librational modes on the mass dipole. We examined the interplay of the mass dipole and the moment of inertia in defining the isotopic Soret effect, and demonstrated that the mass dipole contribution can give rise to new phenomenology, including a reversal in sign. We proposed empirical equations that include the mass dipole contribution. Future

work should assess the magnitude of the mass dipole contribution in real molecular mixtures in order to determine how it affects their phenomenology.

Thermophoresis and thermal orientation of anisotropic colloids

Chapter 5 explored the coupling between the thermal orientation and thermophoresis of rod-like colloids. Using both theory and simulation, we rationalized how the Soret coefficient of these colloids can depend significantly their internal mass distribution, again introducing the mass dipole as a key property. Our theoretical derivation is based on the dependency of the colloid's friction coefficient on its average orientation. The thermal orientation (TO) effect reduces $S_T = D_T/D$ by increasing the diffusion coefficient D. Our results suggest that D_T features only a weak orientation dependence for suspensions characterized by Knudsen numbers $\mathrm{Kn} < 1$.

The TO effect also gives rise to new phenomenology. S_T can feature a maximum as a function of its total mass. Thus, for two colloids that differ only in their mass and mass distribution, it is possible for the lighter colloid to have a greater Soret coefficient. Another key message is that, through the TO effect, S_T can depend on the temperature gradient ∇T. Thus, understanding the coupling between TO and thermophoresis opens new avenues to manipulate anisotropic colloids. Our theory directly links S_T and the average orientation $\langle \cos\theta \rangle$ (accessible through optical techniques[1]), providing an attractive route for the experimental verification of our findings.

Thermal polarization of acetonitrile

Chapter 6 investigated the thermal polarization (TP) of acetonitrile at conditions ranging from near standard (NS) to supercritical (SC). The effect can be significant at NS conditions, with thermal polarization coefficients $S_{\mathrm{TP}} \sim -0.6$ mV K^{-1}. With the large temperature gradients 10^6-10^8 K m^{-1} now experimentally achievable, this corresponds to measurable electrostatic fields, 10^2-10^5 V m^{-1}. Similar coefficients $S_{\mathrm{TP}} \sim 10^{-1}$ mV K^{-1} are obtained at both NS and SC conditions. At NS conditions, dipolar contributions dominate S_{TP}, and its large magnitude results from large static relative permittivities and low temperatures. In contrast, higher order terms become the largest contributors to S_{TP} in the SC fluid, and its large magnitude is connected to the enhanced rotational diffusion, and the stronger cross-coupling between the heat and polarization fluxes. Unlike for water,[2] S_{TP} does not feature a reversal in sign in acetonitrile.

The impact of coupling effects on thermal conductivity

It is well established that thermal diffusion reduces the mixture's thermal conductivity, λ. The S_T minimum observed in Chapter 3 leads to a corresponding maximum decrease in thermal conductivity due to heat-mass coupling effects, amounting to $|\delta\lambda'| < 0.3\%$ when using the phenomenological

coefficients that account for the heat transported due to diffusion. This is consistent with the order of magnitude expected for liquid mixtures.[3]

Using acetonitrile as an exemplar, we quantified, for the first time, how thermal polarization impacts the thermal conductivity of polar fluids (Chapter 6). The coupling of heat and polarization fluxes leads to a reduction in thermal conductivity of $|\delta\lambda|$ ∼2-5%, for conditions from NS to SC. This is of fundamental significance, demonstrating that coupling effects must be included to obtain correct thermal conductivities. Our estimation of $\delta\lambda$ relied on an approximation to the phemenological coefficient L_{pp} within the Debye model. Deriving and implementing Green-Kubo relations (and the corresponding Einstein relations) for L_{pp} and L_{pq} are important next steps for the accurate calculation of $\delta\lambda$. To date, the effect of TP on thermal conductivity has been neglected in all "equilibrium" Green-Kubo calculations of thermal conductivity in polar fluids.

The anomalous thermal conductivity of water

In Chapter 7, we presented comprehensive benchmarks of the thermophysical properties of water for two state-of-the-art ReaxFF force fields, water-2017 and CHON-2017_weak. Based on our results, we recommend potential avenues of improvement for these models. While these models predict thermal conductivities consistent with "traditional" (empirical, all-atom, non-polarizable and non-reactive) classical force fields at ∼300 K and 1.00 g cm^{-3}, they fail to reproduce the temperature dependence along the 0.997 g cm^{-3} isochore. This motivated a more extensive investigation of the thermal conductivity.

In Chapter 8, we assessed the ability of molecular force fields to reproduce the thermal conductivity of water at near-standard thermodynamic conditions (T ∼300 K and ρ ≈1.00 g cm^{-3} or $P \sim 1$ bar). Our results add to the growing body of work demonstrating that computational models, including traditional classical force fields,[4–19] ReaxFF models and DFT functionals,[20–22] typically overestimate the thermal conductivity of water by ∼10-50% at near-standard conditions. All these simulations did not explicitly account for nuclear quantum effects (NQEs). Our hypothesis is that NQEs, or lack thereof, are responsible for the universal overestimation of thermal conductivity by computational models that assume classical nuclear motion. Future work should be directed towards understanding the impact of NQEs on the thermal conductivity of water.

We then examined the thermal conductivity along the "standard liquid" 0.997 g cm^{-3} isochore, and at constant pressure for $P < 1500$ bar. Through the Bridgman equation[23], and taking advantage of the (in)ability of different models to accurately predict the thermal conductivity, we correlated the thermal conductivity's temperature dependence with that of the speed of sound c_S, isentropic compressibility β_S and isothermal compressibility β_T. We connected the thermal conductivity maximum at constant pressure with the nearby c_S maximum and subsequently the β_S and β_T minima, providing a possible thermodynamic explanation for the maximum in thermal

conductivity. The minimum in $\beta_T(T)$ at 319 K and 1 bar has been attributed to an increased concentration of extended tetrahedral hydrogen bonding structures.[24] Thus, through β_T, our results provide a possible microscopic explanation for the maximum in thermal conductivity as well.

Final reflections

Understanding the non-isothermal transport properties of dense fluids in terms of microscopic behaviour is a challenging problem. For thermal diffusion in molecular mixtures, new physical insight can be found in even simple binary mixtures, as evidenced by the Soret coefficient minimum in a Lennard-Jones mixture. One key message of this thesis is that the coupling of shape and mass anisotropy can impact the Soret coefficient: the mass dipole contribution in molecular mixtures, and through thermal orientation in colloids. In polar fluids, these microscopic degrees of freedom give rise to thermal polarization, which reduces the thermal conductivity. The microscopic origin of water's anomalous thermal conductivity remains an open question. We hope that future work building on the results on this thesis will shed some light on heat conduction in this anomalous liquid.

Bibliography

[1] P. V. Ruijgrok, N. R. Verhart, P. Zijlstra, A. L. Tchebotareva and M. Orrit, *Phys. Rev. Lett.*, 2011, **107**, 037401.

[2] I. Iriarte-Carretero, M. A. Gonzalez, J. Armstrong, F. Fernandez-Alonso and F. Bresme, *Phys. Chem. Chem. Phys.*, 2016, **18**, 19894–19901.

[3] S. R. de Groot and P. Mazur, *Non-Equilibrium Thermodynamics*, Dover, 1984.

[4] T. Ohara, *J. Chem. Phys.*, 1999, **111**, 6492–6500.

[5] D. Bedrov and G. D. Smith, *J. Chem. Phys.*, 2000, **113**, 8080–8084.

[6] F. Bresme, *J. Chem. Phys.*, 2001, **115**, 7564–7574.

[7] M. Zhang, E. Lussetti, L. E. S. de Souza and F. Müller-Plathe, *J. Phys. Chem. B*, 2005, **109**, 15060–15067.

[8] T. Terao and F. Müller-Plathe, *J. Chem. Phys.*, 2005, **122**, 081103.

[9] W. Evans, J. Fish and P. Keblinski, *J. Chem. Phys.*, 2007, **126**, 154504.

[10] E. J. Rosenbaum, N. J. English, J. K. Johnson, D. W. Shaw and R. P. Warzinski, *J. Phys. Chem. B*, 2007, **111**, 13194–13205.

[11] H. Jiang, E. M. Myshakin, K. D. Jordan and R. P. Warzinski, *J. Phys. Chem. B*, 2008, **112**, 10207–10216.

[12] S. Kuang and J. D. Gezelter, *J. Chem. Phys.*, 2010, **133**, 164101.

[13] J. Muscatello and F. Bresme, *J. Chem. Phys.*, 2011, **135**, 234111.

[14] J. Muscatello, F. Römer, J. Sala and F. Bresme, *Phys. Chem. Chem. Phys.*, 2011, **13**, 19970–19978.

[15] F. Römer, A. Lervik and F. Bresme, *J. Chem. Phys.*, 2012, **137**, 074503.

[16] Y. Mao and Y. Zhang, *Chem. Phys. Lett.*, 2012, **542**, 37–41.

[17] T. W. Sirk, S. Moore and E. F. Brown, *J. Chem. Phys.*, 2013, **138**, 064505.

[18] S. H. Lee, *Mol. Phys.*, 2014, **112**, 2155–2159.

[19] S. H. Lee and J. Kim, *Mol. Phys.*, 2019, **117**, 1926–1933.

[20] A. Marcolongo, P. Umari and S. Baroni, *Nat. Phys.*, 2016, **12**, 80–84.

[21] E. Tsuchida, *J. Phys. Soc. Jpn.*, 2018, **87**, 025001.

[22] D. Tisi, L. Zhang, R. Bertossa, H. Wang, R. Car and S. Baroni, *Phys. Rev. B*, 2021, **104**, 224202.

[23] P. W. Bridgman, *Proc. Natl. Acad. Sci. U.S.A.*, 1923, **9**, 341–345.

[24] A. Nilsson and L. G. M. Pettersson, *Nat. Commun.*, 2015, **6**, 8998.

Appendix A

Theoretical background

A.1 Global and local balance equations

Consider a macroscopic system consisting of a continuous medium of volume V and bounded by a surface Σ.[1] Each extensive thermodynamic quantity (conserved or not) $A(t)$ can be written as:

$$A(t) = \int_V \rho(\boldsymbol{r}, t) a(\boldsymbol{r}, t)\, d\boldsymbol{r} \tag{A.1}$$

where $\rho(\boldsymbol{r}, t)$ is the mass density, and $a(\boldsymbol{r}, t)$ is the density per unit mass of $A(t)$. If $A(t)$ is a scalar quantity (e.g. mass, energy and entropy, but not momentum, which is a vector), the *global balance equation* is given by:

$$\frac{dA(t)}{dt} = \frac{d^e A(t)}{dt} + \frac{d^i A(t)}{dt} = -\int_\Sigma \boldsymbol{J}_A \cdot \boldsymbol{n}\, d\Sigma + \int_V \sigma_A\, d\boldsymbol{r} \tag{A.2}$$

where $(d^e A/dt)$ is rate of exchange of A with the external environment, and $(d^i A/dt)$ is the rate of internal production. By convention, $\delta A > 0$ if it is supplied to the system. $(d^e A/dt)$ is written in terms of the *flux density* $\boldsymbol{J}_A$ (the amount of A crossing the surface per unit area per unit time) and the unit vector $\boldsymbol{n}$ normal to the surface. σ_A is the rate of production of A (per unit volume per unit time) inside the system, often referred to as the *source density* or *sink density*. Using Green's theorem, Eq. A.2 can be rewritten as:

$$\frac{dA(t)}{dt} = -\int_V (\nabla \cdot \boldsymbol{J}_A)\, d\boldsymbol{r} + \int_V \sigma_A\, d\boldsymbol{r} \tag{A.3}$$

which is valid for any volume V. Thus, comparing Eq. A.3 with Eq. A.1, one obtains the *local balance equation*:

$$\frac{\partial(\rho a)}{\partial t} + \nabla \cdot \boldsymbol{J}_A = \sigma_A \tag{A.4}$$

If A is an extensive conserved quantity X_i, for which $\sigma_{X_i} = 0$, Eq. A.4 takes the form of a *continuity equation*,

$$\frac{\partial(\rho x_i)}{\partial t} + \nabla \cdot \boldsymbol{J}_i = 0 \tag{A.5}$$

where $\boldsymbol{J}_i$ denotes the flux density of X_i.

A.2 Curie's principle for an isotropic medium

Consider an isotropic medium subject to fluxes j (scalar), $\boldsymbol{J}$ (vector) and $\boldsymbol{T}$ (second-order symmetric tensor) with affinities $\boldsymbol{f}$ (vector) and $\boldsymbol{\mathcal{F}}$ (second-order tensor):[2]

$$j = j(\boldsymbol{f}, \boldsymbol{\mathcal{F}}), \quad \boldsymbol{J} = \boldsymbol{J}(\boldsymbol{f}, \boldsymbol{\mathcal{F}}), \quad \boldsymbol{T} = \boldsymbol{T}(\boldsymbol{\mathcal{F}}) \tag{A.6}$$

Isotropy imposes that under orthogonal transformation $\boldsymbol{Q}$

$$j(\boldsymbol{Q} \cdot \boldsymbol{f}; \boldsymbol{Q} \cdot \boldsymbol{\mathcal{F}} \cdot \boldsymbol{Q}^{\mathrm{T}}) = j(\boldsymbol{f}, \boldsymbol{\mathcal{F}}) \tag{A.7}$$

$$\boldsymbol{J}(\boldsymbol{Q} \cdot \boldsymbol{f}; \boldsymbol{Q} \cdot \boldsymbol{\mathcal{F}} \cdot \boldsymbol{Q}^{\mathrm{T}}) = \boldsymbol{Q} \cdot \boldsymbol{J}(\boldsymbol{f}, \boldsymbol{\mathcal{F}}) \tag{A.8}$$

$$\boldsymbol{T}(\boldsymbol{Q} \cdot \boldsymbol{\mathcal{F}} \cdot \boldsymbol{Q}^{\mathrm{T}}) = \boldsymbol{Q} \cdot \boldsymbol{T}(\boldsymbol{\mathcal{F}}) \cdot \boldsymbol{Q}^{\mathrm{T}} \tag{A.9}$$

and according to the representation theorems of isotropic tensors, the fluxes are isotropic if and only if

$$j(\boldsymbol{f}, \boldsymbol{\mathcal{F}}) = j[I_{\mathcal{F}}, II_{\mathcal{F}}, III_{\mathcal{F}}, \boldsymbol{f} \cdot \boldsymbol{f}, \boldsymbol{f} \cdot (\boldsymbol{\mathcal{F}} \cdot \boldsymbol{f}), \boldsymbol{f} \cdot (\boldsymbol{\mathcal{F}} \cdot \boldsymbol{\mathcal{F}} \cdot \boldsymbol{f})] \tag{A.10}$$

$$\boldsymbol{J}(\boldsymbol{f}, \boldsymbol{\mathcal{F}}) = (A_1 \boldsymbol{I} + A_2 \boldsymbol{\mathcal{F}} + A_3 \boldsymbol{\mathcal{F}} \cdot \boldsymbol{\mathcal{F}}) \cdot \boldsymbol{f} \tag{A.11}$$

$$\boldsymbol{T}(\boldsymbol{\mathcal{F}}) = B_1 \boldsymbol{I} + B_2 \boldsymbol{\mathcal{F}} + B_3 \boldsymbol{\mathcal{F}} \cdot \boldsymbol{\mathcal{F}} \tag{A.12}$$

where j and coefficients A_i are isotropic scalar functions of $\boldsymbol{f}$ and $\boldsymbol{\mathcal{F}}$, and B_i are isotropic scalars of $\boldsymbol{\mathcal{F}}$; $I_{\mathcal{F}}$, $II_{\mathcal{F}}$ and $III_{\mathcal{F}}$ are the principle invariants of $\boldsymbol{\mathcal{F}}$:

$$I_{\mathcal{F}} = \mathrm{Tr}(\boldsymbol{\mathcal{F}}), \quad II_{\mathcal{F}} = \frac{1}{2}[I_{\mathcal{F}}^2 - \mathrm{Tr}(\boldsymbol{\mathcal{F}} \cdot \boldsymbol{\mathcal{F}})], \quad III_{\mathcal{F}} = \det \boldsymbol{\mathcal{F}} \tag{A.13}$$

Assuming linear response, Eqs. A.10-A.12 simplify to

$$j = l \,\mathrm{Tr}\, \boldsymbol{\mathcal{F}}\,, \quad \boldsymbol{J} = A_1 \boldsymbol{f}\,, \quad \boldsymbol{T} = B_1 (\mathrm{Tr}\, \boldsymbol{\mathcal{F}}) \boldsymbol{I} + B_2 \boldsymbol{\mathcal{F}} \tag{A.14}$$

where l, A_1, B_1 and B_2 are now scalars independent of the affinities $\boldsymbol{f}$ and $\boldsymbol{\mathcal{F}}$. Thus in the linear regime, as shown in Eq. A.14, spatial symmetry only allows the coupling of fluxes and affinities of

the same tensorial order. In this case, it is evident that Curie's principle arises simply from the application of the representation theorems of isotropic tensors.

A.3 Minimum entropy production theorem

Consider a non-equilibrium process occurring in volume V at rest with time-independent constraints at its surface.[2,3] It is assumed that the state variables X_i obey the conservation laws

$$\rho \frac{\partial X_i}{\partial t} = -\nabla \cdot \boldsymbol{J}_i \quad (i = 1, 2, ..., n). \tag{A.15}$$

From Eq. 2.18 (where linear response has been assumed), the total entropy production P_S inside the system is given by

$$P_S = \int \sum_{i,k} L_{ik} \mathcal{F}_i \mathcal{F}_k \, \mathrm{d}V = \int \sum_{i,k} L_{ik} \nabla F_i \cdot \nabla F_k \, \mathrm{d}V \tag{A.16}$$

where we have taken advantage of the fact that the affinities $\mathcal{F}_i$ are usually gradients of intensive variables F_i, i.e. $\mathcal{F}_i = \nabla F_i$. Taking the time derivative of Eq. A.16, and assuming L_{ik} are symmetric (Onsager's reciprocal relations) and constant, one obtains

$$\frac{\mathrm{d}P_S}{\mathrm{d}t} = 2 \int \sum_{i,k} L_{ik} \nabla F_i \cdot \nabla \left(\frac{\partial F_k}{\partial t} \right) \mathrm{d}V \tag{A.17}$$

Recalling that the boundary conditions are time-independent, integration by parts gives

$$\begin{aligned} \frac{\mathrm{d}P_S}{\mathrm{d}t} &= -2 \int \sum_{k} \frac{\partial F_k}{\partial t} \nabla \cdot \left(\sum_{i} L_{ik} \nabla F_i \right) \mathrm{d}V \\ &= -2 \int \sum_{k} \frac{\partial F_k}{\partial t} \nabla \cdot \boldsymbol{J}_k \, \mathrm{d}V \\ &= 2 \int \rho \sum_{k} \frac{\partial F_k}{\partial t} \frac{\partial X_k}{\partial t} \, \mathrm{d}V \end{aligned} \tag{A.18}$$

where the linear flux-affinity relations (Eq. 2.17) and Eq. A.15 have been used. In the stationary state

$$\frac{\partial X_k}{\partial t} = 0 \quad \Rightarrow \quad \frac{\mathrm{d}P_S}{\mathrm{d}t} = 0 \tag{A.19}$$

In the transient regime

$$\frac{\mathrm{d}P_S}{\mathrm{d}t} = \int \sum_{i,k} \frac{\partial X_i}{\partial F_k} \frac{\partial F_i}{\partial t} \frac{\partial F_k}{\partial t} \, \mathrm{d}V \leq 0 \tag{A.20}$$

since $\partial X_i/\partial F_k \leq 0$ from the equilibrium stability criteria (noting that X_i characterize the stationary state and are thus well-defined). $\partial X_i/\partial F_k$ are negatives of thermodynamic response functions: e.g. negative heat capacities ($-C$) or the negative isothermal compressibility coefficient ($-\beta_T$). Thus from Eqs. A.19 and A.20, the total entropy production P_S decreases with time in the transient regime, until it reaches a minimum at the stationary state.

Bibliography

[1] N. Pottier, *Nonequilibrium Statistical Physics: Linear Irreversible Processes*, Oxford University Press, 2010.

[2] G. Lebon, D. Jou and J. Casas-Vázquez, *Understanding Non-equilibrium Thermodynamics: Foundations, Applications, Frontiers*, Springer, Berlin, Heidelberg, 2008.

[3] S. R. de Groot and P. Mazur, *Non-Equilibrium Thermodynamics*, Dover, 1984.

Appendix B

Methods and supporting information for Chapter 3

B.1 Soret coefficient and thermal conductivity from NEMD

B.1.1 Simulation details

The Soret coefficient S_T and thermal conductivity λ were calculated from boundary-driven non-equilibrium molecular dynamics simulations (NEMD) in the stationary state. An elongated (tetragonal) simulation cell of dimensions $(L_x, L_y, L_z) = (20, 20, 30)\sigma$ was used, with 3D periodic boundary conditions. Two thermostatting regions, hot and cold, were located in the centre and edges of the simulation, respectively (see Fig. B.1). The thermostatting regions had a width $\Delta z = 3\sigma$ and extended over the entire (x, y) plane, such that the temperature gradients were generated along the z-direction. For the thermostatting procedure, a simple velocity rescaling algorithm was used to maintain the hot and cold thermostatting regions at temperatures T_h and T_c, respectively. The velocities of all particles in each region were rescaled, every timestep, by a factor $\alpha = \sqrt{K_t/K_c}$ where K_t and K_c are the target and current kinetic energies of the region. This velocity rescaling procedure does not conserve linear momentum, so the system's centre-of-mass velocity was subtracted from each particle at every time step in order to ensure linear momentum conservation. A timestep of $\delta t = 0.002\ \tau$ was used.

For each system, the average density, mole fraction and thermostat temperatures were chosen to give $\langle P_{zz} \rangle$ within $\pm 0.001\ \epsilon\sigma^{-3}$ of the target pressure $P = 0.46\ \epsilon\sigma^{-3}$, where P_{zz} is the pressure tensor component parallel to the heat flux vector. Relatively small (by simulation standards) temperature differences $\Delta T = T_h - T_c \approx 0.04\ \epsilon k_B^{-1}$ and resulting gradients $\nabla T \approx 2.9 \times 10^{-3}\ \epsilon k_B^{-1}\sigma^{-1}$ were used to accurately target the thermodynamic state. For each system, 10 statistically independent replicas were generated, each consisting of an initial $2 \times 10^4 \tau$ to establish the stationary state, followed by $2 \times 10^6 \tau$ for data collection.

In the stationary state, this set-up results in two equal but opposite temperature gradients, and therefore in equal and opposite heat fluxes, such that the system is completely periodic. The heat flux across the system, $\boldsymbol{J}_q = (0, 0, \pm J_q)$, can be obtained from the continuity equation

$$J_q = \frac{|\langle \Delta U \rangle|}{2\delta t A} \tag{B.1}$$

where $A = L_x \times L_y$ is the cross-sectional area of the simulation cell, δt is the timestep, and ΔU is the internal energy exchanged at each timestep. The employed simple rescaling thermostat only changes the kinetic energy such that $\Delta U = \Delta K$. The factor of 2 in the denominator accounts for the two heat fluxes (equal magnitude and opposite direction) generated in this setup. The thermal conductivity λ was then calculated using Fourier's Law:

$$\boldsymbol{J}_q = -\lambda \nabla T \tag{B.2}$$

where ∇T is the *local* temperature gradient. The Soret coefficient S_T was calculated using Eq. 3.1 in Chapter 3, again employing local values of the gradients ∇T and ∇x_1. Local densities ρ, mol fractions x_1 and temperatures T were determined from a 1σ bin close to the centre of each *NVE* compartment. The position of the bin was chosen such that $T = 0.62\ \epsilon k_{\mathrm{B}}^{-1}$. The local values of ∇T and ∇w_1 were determined by fitting straight lines to the temperature and mole fraction profiles within a range of $\pm 2.5\sigma$ around the selected state point.

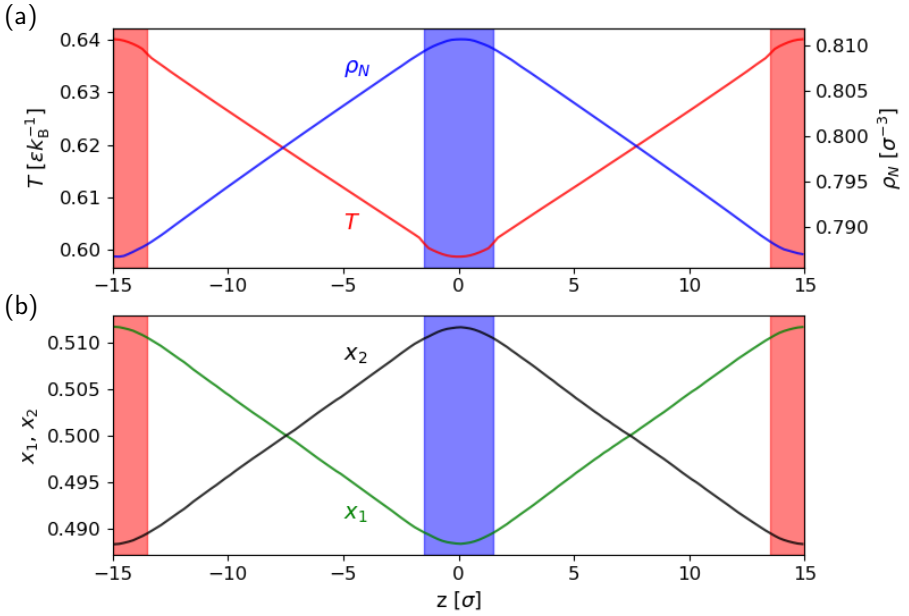


FIGURE B.1: Representative (a) temperature T and number density ρ_N profiles, and (b) mole fraction, x_1 and x_2, profiles for the NEMD simulations. The blue (cold) and red (hot) indicate the location of the thermostatting regions in the simulation cell.

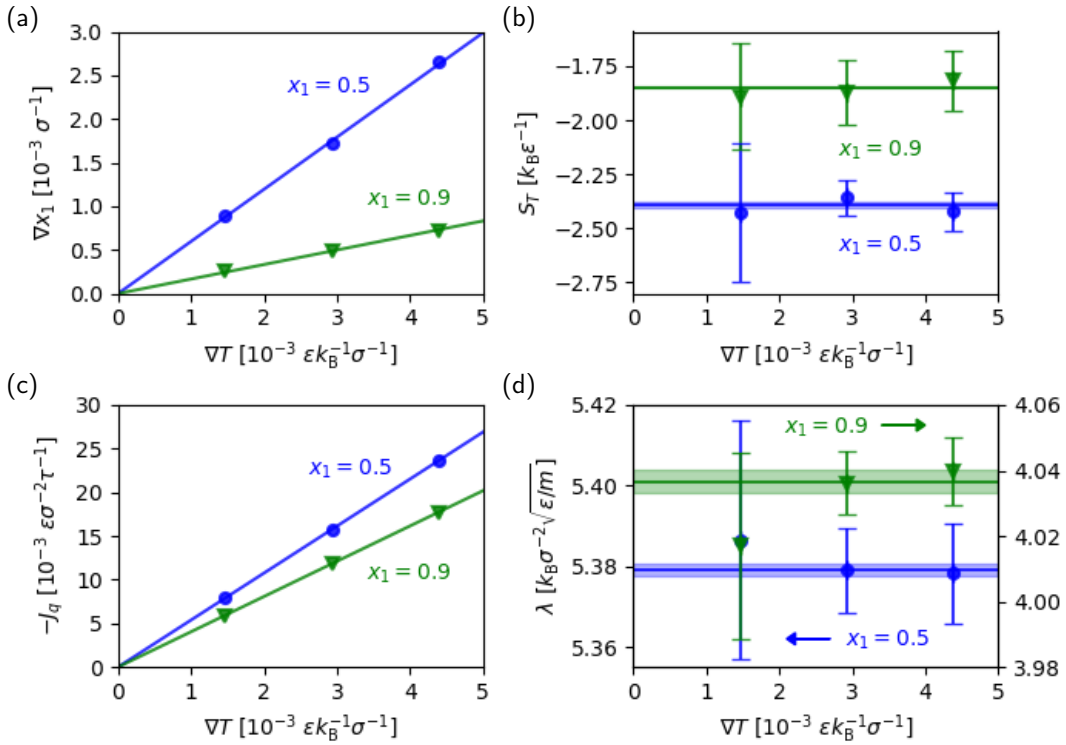


FIGURE B.2: Linear response of the Soret coefficient S_T and thermal conductivity λ: (a) mole fraction gradient ∇x_1, (b) S_T, (c) heat flux J_q and (d) λ as a function of temperature gradient ∇T. The solid lines show fits to $\nabla x_1 = -x_1 x_2 S_T \nabla T$ in (a) and (b), and to Fourier's law $-J_q = \lambda \nabla T$ in (c) and (d). In (a) and (c), statistical uncertainties are smaller than the size of the symbols. In (b) and (d) the shaded areas show the uncertainty associated with the fits.

B.1.2 Linear response

We demonstrate in Fig. B.2 that the magnitude of temperature gradients used in this work are within the linear regime. For these additional simulations, production runs of length $1.5 \times 10^6 \tau$ and $10^6 \tau$ were used for the $\nabla T \approx 1.5 \times 10^{-3}\ \epsilon k_B^{-1} \sigma^{-1}$ and $\nabla T \approx 4.4 \times 10^{-3}\ \epsilon k_B^{-1} \sigma^{-1}$ systems, respectively. The values for S_T and λ for $x_1 = 0.5, 0.9$ were calculated by fitting to their linear response (Fig. B.2).

B.1.3 Finite-size effects

We show in Fig. B.3 that the lateral simulation cell length $L_\perp = L_x = L_y$ has a significant effect on S_T. $|S_T|$ systematically decreases with $L_\perp$, by ∼0-10% (∼3-6%) when increasing $L_\perp$ from 10σ to 20σ (20σ to 40σ). These finite-size effects are greater for more non-ideal compositions. Nevertheless, fitting cubic functions to the $L_\perp/\sigma = 10, 20, 40$ data gives $x_1^{\min(S_T)} = 0.5 \pm 0.1$, and further increasing $L_\perp$ is not expected to significantly shift the position of the minimum. Finite-size

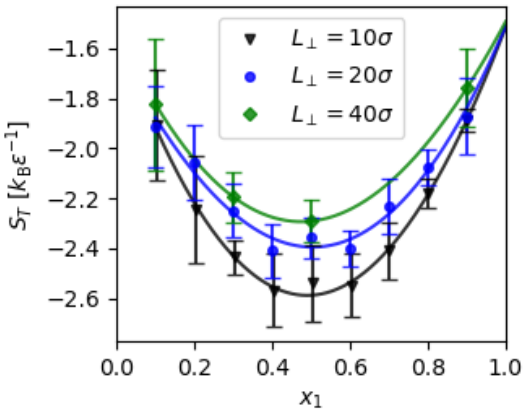


FIGURE B.3: Finite-size effects on the Soret coefficient S_T calculated from NEMD simulations. $L_\perp = L_x = L_y$ is the length of the simulation cell in the direction perpendicular to the heat flux. Solid lines show cubic functions fit to $S_T(x_1)$ where x_1 is the mole fraction of species 1.

effects in S_T are expected from those observed in self-diffusion coefficients (Sec. B.7 below) and D_{12}.[1,2] The impact of finite-size effects on D_T is less well known.

We do not observe appreciable finite-size effects for the thermal conductivity. This is consistent with the mechanism of thermal transport in molecular liquids (and liquid mixtures), which is dominated by collisions between nearest neighbors, setting a characteristic length scale for heat transport at $\sim 1\sigma$.

The additional simulations for $L_\perp = 10\sigma$ and $L_\perp = 40\sigma$ had production lengths of $4 \times 10^6\tau$ and $3 \times 10^5\tau$, respectively.

B.2 Equilibrium molecular dynamics simulations

Equilibrium molecular dynamics (EMD) simulations of the mixture were performed in the *NPT*, *NVT* and *NVE* ensembles, targeting various thermodynamic states. Unless stated otherwise (i.e. for the finite-size analyses) a cubic simulation cell containing 5000 particles was used. A timestep of 0.002τ was used for the *NPT* and *NVT* simulations. For the *NPT* and *NVT* simulations, temperature was controlled by the Nosé-Hoover chain thermostat, with 3 chains, and a time constant of 1 τ. Additionally in the *NPT* simulations, pressure was controlled using a Nosé-Hoover chain barostat, also with 3 chains, and a time constant of 4 τ. For the *NPT* simulations, a single replica was performed for each (x_1, P, T) state point, consisting of at least 2×10^4 τ of equilibration, followed by a 1-2$\times 10^5$ τ production run. For the *NVT* simulations, sampling consisted of 20-200 replicas for each (x_1, ρ, T) state point depending on the system size, which varied from N = 1000-120, 000 particles; each replica was equilibrated for 2×10^3 τ followed by 10^4 τ of production. The

exceptions to this were the large $N = 0.5\text{-}5 \times 10^6$ systems simulated for the KBIs (Sec. B.10 below), which had both equilibration and production times of $10^3\tau$.

Simulations in the *NVE* ensemble targeted different compositions along the ($P = 0.46\ \epsilon\sigma^{-3}$, $T = 0.62\ \epsilon k_\mathrm{B}^{-1}$) isobar-isotherm. For each state point, replicas were first spawned from *NVT* simulations and monitored for an initial $2 \times 10^3\ \tau$. If the average temperature was within $\pm 0.0005\ \epsilon k_\mathrm{B}^{-1}$ of $T = 0.62\ \epsilon k_\mathrm{B}^{-1}$, the replica was continued for a further $2 \times 10^4\ \tau$ of production. Replicas were also subsequently started from these successful *NVE* trajectories. A total of 50-100 statistically independent replicas were performed for each state point, all of which had an average temperature $\langle T \rangle_{NVE}$ within $\pm 0.0005\ \epsilon k_\mathrm{B}^{-1}$ of the target temperature. A smaller timestep of $\delta t = 0.001\ \tau$ was used to improve energy conservation (reduce temperature drift) and therefore increase the sampling times available in the small $\pm 0.0005\ \epsilon k_\mathrm{B}^{-1}$ temperature window, and also to reduce the discretization error for the numerical integration of correlation functions (see Sec. B.5 & B.7 below).

B.3 Radial distribution functions

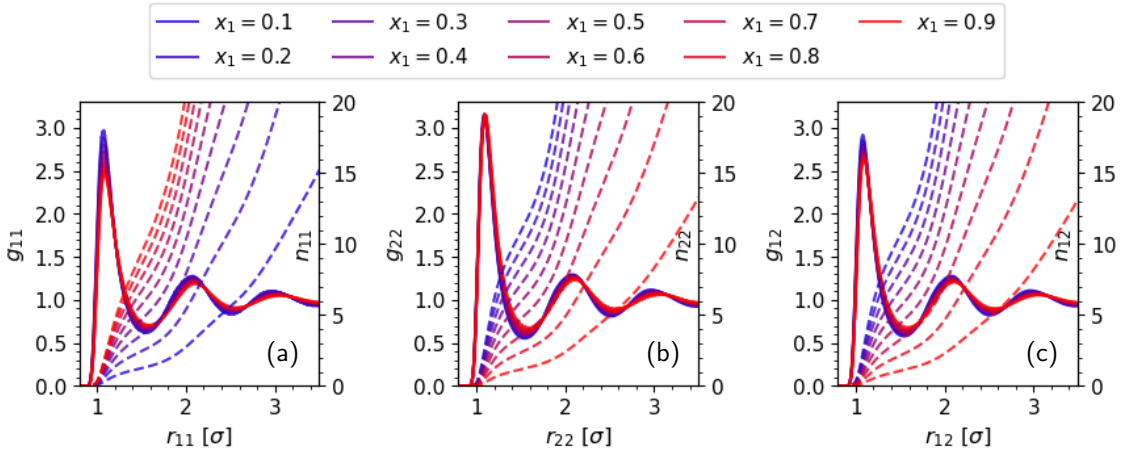


FIGURE B.4: Radial distribution functions g_{ij} and coordination number n_{ij} of the Lennard-Jones mixtures: (a) g_{11} and n_{11}; (b) g_{22} and n_{22}; (c) g_{12} and n_{12}. r_{ij} is the radial distance between species i and j. Solid lines show g_{ij} (left axis) and the dashed lines show n_{ij} (right axis).

B.4 Partial molar properties

Partial molar properties z_i were calculated using the equations $z_1 = Z + (1 - x_1)(\partial Z/\partial x_1)_{PTN_2}$ and $z_2 = Z - x_1(\partial Z/\partial x_1)_{PTN_2}$, where Z is the corresponding extensive property. $Z(x_1)$ were calculated from MD simulations in the NPT ensemble. At each selected x_1, two additional simulations were performed at $x_1 \pm 0.01$, and $(\partial Z/\partial x_1)_{PTN_2}$ was then calculated by fitting a straight line through these three points.

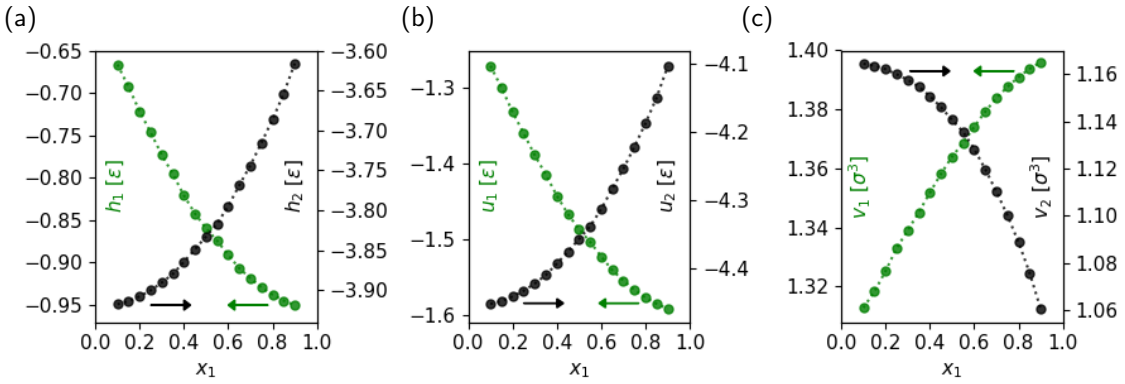


FIGURE B.5: Partial molar properties z_i of component $i = 1, 2$ as a function of mole fraction x_1: (a) partial molar enthalpy h_i; (b) partial molar internal energy u_i; and (c) partial molar volume v_i. Statistical uncertainties are smaller or comparable to the size of the symbols.

B.5 The phenomenological coefficients

The phenomenological coefficients $L_{\alpha\beta}$ were calculated using the Green-Kubo integral formula

$$L_{\alpha\beta} = \frac{V}{3k_\mathrm{B}} \lim_{t' \to \infty} \int_0^{t'} \langle \boldsymbol{J}_\alpha(t) \cdot \boldsymbol{J}_\beta(0) \rangle dt \tag{B.3}$$

where V is the volume of the simulation cell, and the factor of 3 in the denominator averages the contributions from each spatial dimension. In order to calculate L_{qq}, L_{1q}, L_{q1} and L_{11}, the expressions for the heat flux $\boldsymbol{J}_q$ and mass flux $\boldsymbol{J}_1$ in terms of microscopic quantities are required. These are:

$$\boldsymbol{J}_1 = \frac{1}{V} \sum_{i=1}^{N_1} m_i \boldsymbol{v}_i \tag{B.4}$$

where the sum runs over all N_1 particles of species 1, and in the case of two-body interactions the Irving-Kirkwood formula for heat flux is

$$\boldsymbol{J}_q = \frac{1}{V} \left(\sum_{i=1}^{N} U_i \boldsymbol{v}_i - \sum_{i=1}^{N} \boldsymbol{S}_i \boldsymbol{v}_i \right) = \frac{1}{V} \left(\sum_{i=1}^{N} (\mathcal{V}_i + K_i) \boldsymbol{v}_i - \frac{1}{2} \sum_{i=1}^{N} \sum_{j \neq i}^{N} (\boldsymbol{v}_i \cdot \boldsymbol{F}_{ij}) \boldsymbol{r}_{ij} \right) \tag{B.5}$$

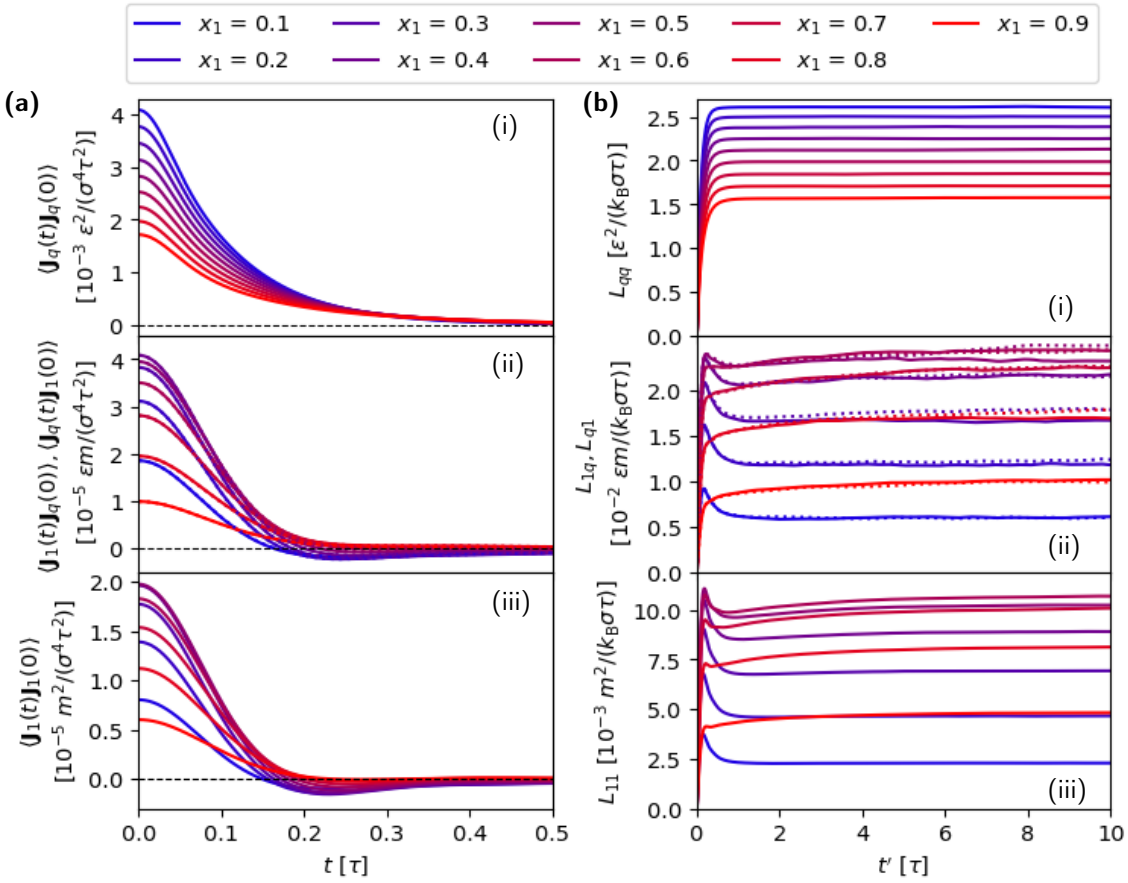


FIGURE B.6: (a) Correlation functions $\langle \boldsymbol{J}_\alpha(t) \cdot \boldsymbol{J}_\beta(0)\rangle$ as a function of time lag t. (b) Convergence of the phenomenological coefficients $L_{\alpha\beta}(t')$ with the correlation time t' used as the upper limit of the integral in Eq. B.3. In (a)(ii) and (b)(ii): solid lines show $\langle \boldsymbol{J}_1(t) \cdot \boldsymbol{J}_q(0)\rangle$ and L_{1q}; dotted lines show $\langle \boldsymbol{J}_q(t) \cdot \boldsymbol{J}_1(0)\rangle$ and L_{q1}

where U_i is the per-particle internal energy which can be split into potential $\mathcal{V}_i = (1/2)\sum_{j\neq i} u_{ij}(r_{ij})$ and kinetic energy $K_i = (1/2)m_i\boldsymbol{v}_i^2$ contributions; $\boldsymbol{S}_i$ is the per-particle stress tensor; $\boldsymbol{F}_{ij}$ is the force exerted on particle i by particle j; and $\boldsymbol{r}_{ij} = \boldsymbol{r}_j - \boldsymbol{r}_i$ where $\boldsymbol{r}_i$ is the position vector of particle i.

The unprimed coefficients were calculated from simulations in the NVE ensemble. A correlation time of $t' = 10\tau$ was used for the upper limit of Eq. B.3. Selecting this integration limit is a compromise between sampling efficiency and minimizing the resulting truncation error. We show in Fig. B.6 that 10 τ is sufficiently long to achieve a well-converged integral, while the exhaustive extent of our sampling is reflected in the associated uncertainty.

The primed coefficients $L'_{\alpha\beta}$ were then obtained from $L_{\alpha\beta}$ using the formulas

$$L'_{qq} = L_{qq} - (L_{1q} + L_{q1})(h_{s,1} - h_{s,2}) + L_{11}(h_{s,1} - h_{s,2})^2 \tag{B.6}$$

$$L'_{1q} = L_{1q} - L_{11}(h_{s,1} - h_{s,2}) \tag{B.7}$$

$$L'_{q1} = L_{q1} - L_{11}(h_{s,1} - h_{s,2}) \tag{B.8}$$

$$L'_{11} = L_{11} \tag{B.9}$$

where $h_{s,i}$ is the specific molar enthalpy of component $i = 1, 2$. These formulas can be derived by comparing expressions for entropy production in LNET, or trivially from the Green-Kubo integral formula (Eq. B.3) noting that $\boldsymbol{J}'_q = \boldsymbol{J}_q - (h_{s,1} - h_{s,2})\boldsymbol{J}_1$.[3,4] The difference between $\boldsymbol{J}'_q$ and $\boldsymbol{J}_q$ corresponds to the heat transported due to diffusion.

We show in Fig. B.7 the values of coefficients $L_{\alpha\beta}$ and $L'_{\alpha\beta}$. Consistent with Onsager's reciprocal relations, $L'_{1q} = L'_{q1}$ and $L_{1q} = L_{q1}$ to within their associated uncertainties. We therefore average over both reciprocal coefficients to give a single value each for $L'_{1q} = L'_{q1}$ and $L_{1q} = L_{q1}$.

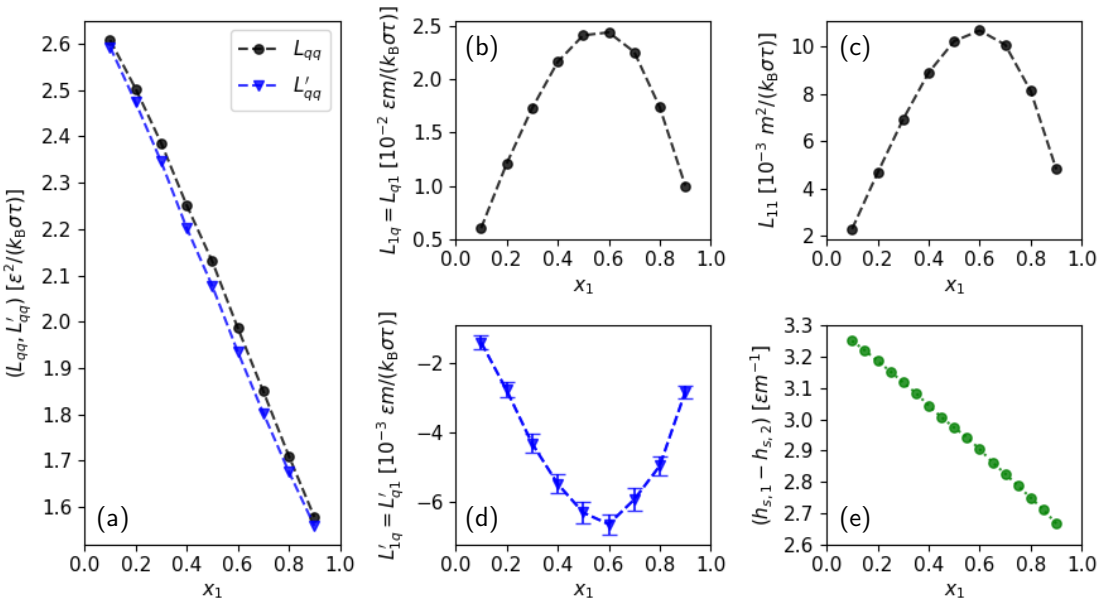


FIGURE B.7: The phenomenological coefficients as a function of the mole fraction x_1: (a) L_{qq} and L'_{qq}; (b) $L_{1q} = L_{q1}$; (c) L_{11}; and (d) $L'_{1q} = L'_{q1}$. (e) The difference in specific partial enthalpies $h_{s,1} - h_{s,2}$, where $h_{s,i}$ is the specific partial enthalpy of component i. Where error bars are not shown, the statistical uncertainty is smaller than the size of the symbol.

B.6 Chemical potentials

The chemical potential of species i was calculated in terms of its ideal (id) and excess (ex) contributions, $\mu_i = \mu_i^{\mathrm{id}} + \mu_i^{\mathrm{ex}}$. The ideal gas contribution μ_i^{id} is given by the formula

$$\mu_i^{\mathrm{id}} = k_B T \ln\left(\rho_{N,i}\Lambda_i^3\right) \tag{B.10}$$

where $\rho_{N,i} = x_i\rho_N$ and Λ_i are the number density and thermal de Broglie wavelength of species i, respectively. The densities were obtained from MD simulations in the NPT ensemble. By convention we set $\Lambda_2 = h/\sqrt{2\pi m_2 k_B T} = 1 \Rightarrow \ln\left(\Lambda_2^3\right) = 0$ (note that $\Lambda_1 = \Lambda_2$ since $m_1 = m_2$) for $T = 0.62\ \epsilon k_B^{-1}$, and in doing so fix the energy scale by assigning a value to Planck's constant h in Lennard-Jones units. This amounts to a constant shift in μ_i and does not affect $(\partial\mu_i/\partial x_1)_{P,T}$.

The excess chemical potential μ_i^{ex} was calculated from MD simulations at constant T and P using a free energy perturbation (FEP) method. A single particle was inserted into the simulation cell via $(n-1)$ small "steps" along a reversible alchemical thermodynamic path, analogous to slowly "growing" the particle. The Gibbs free energy change for this particle insertion, $\Delta_N^{N+1}G^{\mathrm{ex}}$, is given by

$$\mu_i^{\mathrm{ex}} \approx \Delta_N^{N+1}G^{\mathrm{ex}} = -k_B T \sum_{i=0}^{n-1} \ln \frac{\langle V \exp\left\{(-\Delta_{\zeta_i}^{\zeta_{i+1}}\mathcal{V}/k_B T)\right\}\rangle_{\zeta_i}}{\langle V\rangle_{\zeta_i}} \tag{B.11}$$

where V is the volume of the simulation cell, $\Delta_{\zeta_i}^{\zeta_{i+1}}\mathcal{V}(\zeta,\boldsymbol{r}) = \mathcal{V}_{\zeta_{i+1}}(\zeta,\boldsymbol{r}) - \mathcal{V}_{\zeta_i}(\zeta,\boldsymbol{r})$ and ζ is a coupling parameter that connects the reference (N) and perturbed $(N+1)$ systems according to $\mathcal{V}(\zeta,\boldsymbol{r}) = \zeta\mathcal{V}_{N+1}(\boldsymbol{r}) + (1-\zeta)\mathcal{V}_N(\boldsymbol{r})$, with ζ taking values from 0 to 1. In order to avoid singularities when $\zeta \to 0$, the FEP simulations were performed using a soft-core version[5] of the Lennard-Jones potential (LJSC)

$$\mathcal{V}_{ij}^{\mathrm{LJSC}}(r;\zeta,n,\alpha) = \zeta^n 4\epsilon_{ij}\left\{\frac{1}{\left[\alpha(1-\zeta)^2 + (r/\sigma_{ij})^6\right]^2} - \frac{1}{\alpha(1-\zeta)^2 + (r/\sigma_{ij})^6}\right\} \tag{B.12}$$

truncated and shifted at a cutoff radius of $r_c = 2.5\sigma$ such that $\mathcal{V}_{ij}^{\mathrm{LJSCTS}}(r) = (\mathcal{V}_{ij}^{\mathrm{LJSC}}(r) - \mathcal{V}_{ij}^{\mathrm{LJSC}}(r_c))\theta(r_c - r)$ with θ being the Heaviside step function. Values of $n = 1$ and scaling constant $\alpha = 0.5$ were used. For $\zeta = 1$, Eq. B.12 reduces to the standard Lennard-Jones potential, and in the limit $\zeta \to 0$ no work is required to change from $\alpha = 0$ to $0 < \alpha < \infty$ (i.e. the two potentials have equivalent initial states). Therefore, the soft-core version gives the same free energy difference as the standard LJ (or LJTS) potential.[5]

Each FEP simulation used a cubic simulation cell containing 5000 particles, and additionally the single particle being inserted. The systems were equilibrated for 20τ in the NVT ensemble, then for $2 \times 10^3\tau$ in the NPT ensemble. The particle insertion was then performed in steps of

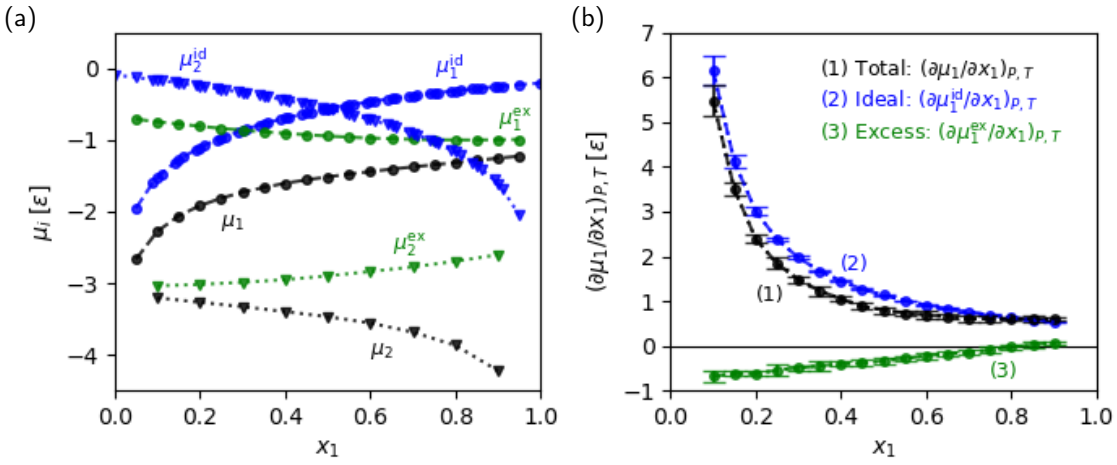


FIGURE B.8: The chemical potential and its derivative as a function of mole fraction x_i. (a) Total μ_i, ideal μ_i^{id} and excess μ_i^{ex} chemical potentials μ_i of species $i = 1, 2$. (b) $(\partial\mu_1/\partial x_1)_{P,T}$ and its ideal and excess contributions. In (a), statistical uncertainties are smaller than the size of the symbols.

0.01ζ over a $10^4\tau$ production run. A timestep of 0.002τ was used. Temperature (pressure) was controlled using the Nosé-Hoover chain thermostat (barostat), with 3 chains, and a time constant of 1τ (5τ). Sampling consisted of 1700-2000 replicas for μ_1^{ex}, and 500-600 replicas for μ_2^{ex}.

The chemical potentials and the derivative $(\partial\mu_1/\partial x_1)_{P,T} = (\partial\mu_1^{\mathrm{id}}/\partial x_1)_{P,T} + (\partial\mu_1^{\mathrm{ex}}/\partial x_1)_{P,T}$ are shown in Fig. B.8. $(\partial\mu_1^{\mathrm{id}}/\partial x_1)_{P,T}$ and $(\partial\mu_1^{\mathrm{ex}}/\partial x_1)_{P,T}$ were evaluated at x_1 by fitting a straight line through the three points within $x_1 \pm 0.01$ and $x_1 \pm 0.05$, respectively.

B.7 Self-diffusion coefficients and shear viscosity

The self-diffusion coefficients D_i of species $i = 1, 2$ were calculated from the average mean square displacement (MSD) using the Einstein relation

$$D_i = \frac{1}{2d} \lim_{t\to\infty} \frac{\langle |\boldsymbol{r}_i(t) - \boldsymbol{r}_i(0)|^2 \rangle}{t} \tag{B.13}$$

where $\boldsymbol{r}_i$ is the position vector of a particle of species i, t is the elapsed time from an arbitrary starting time, and $d = 3$ is the number of spatial dimensions. D_i was therefore calculated by fitting to the equation $\langle |\boldsymbol{r}_i(t) - \boldsymbol{r}_i(0)|^2 \rangle = 6tD_i$, excluding the first 10 τ of data to ensure only the diffusive regime was sampled (as opposed to the ballistic regime). In order to account for finite-size effects, the "infinite-size" diffusion coefficient $D_{i,0}$ was calculated by extrapolation to $L^{-1} = 0$, where L is the length of the cubic simulation cell. This finite-size analysis is shown in Fig. B.9, and follows from the equation derived by Yeh and Hummer[6] using a simple hydrodynamic model of a particle

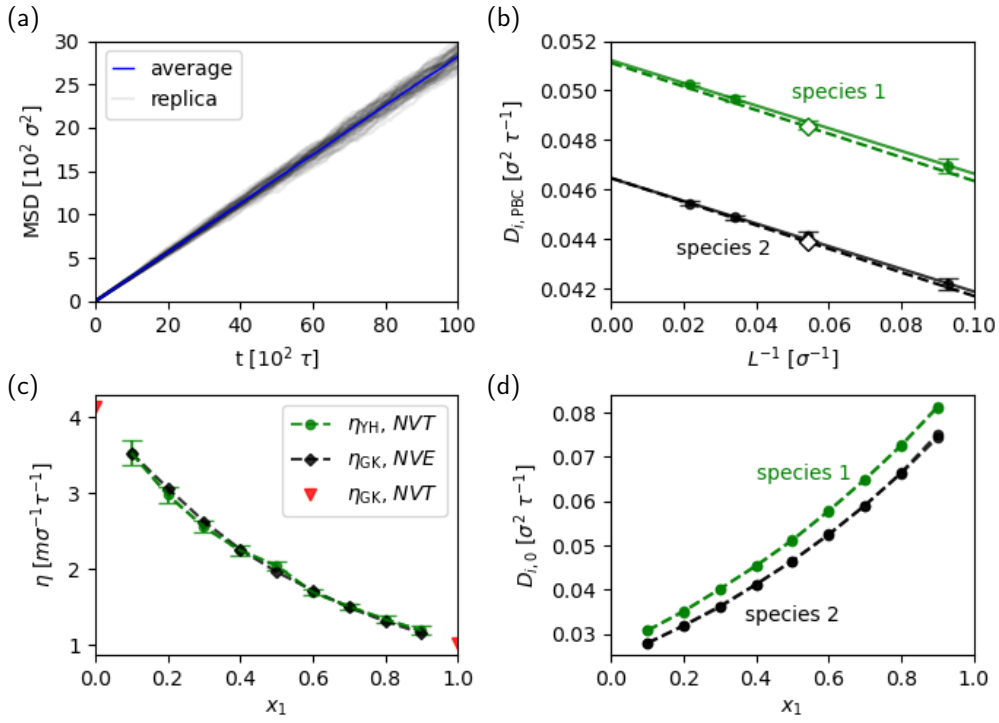


FIGURE B.9: Self-diffusion coefficients and shear viscosities of the Lennard-Jones mixtures. (a) Mean-square displacement (MSD) *vs.* time t for the $x_1 = 0.5$ and $N = 1000$ system. (b) Finite-size analysis for the $x_1 = 0.5$ mixture: $D_{i,\mathrm{PBC}}$ is the finite-size diffusion coefficient of species i and L is the length of the cubic simulation cell. Symbols: circles (○) and diamonds (◇) show the data from *NVT* and *NVE* MD simulations, respectively. Solid lines show a linear fit to the *NVT* data; dashed lines show a straight line through the single *NVE* data point with the gradient determined from η_{GK}. (c) The viscosities η as a function of mole fraction x_1, as determined from the different methods (see main text). (d) "Infinite-size" diffusion coefficients $D_{i,0}$ of species i as a function of x_1. $D_{i,0}$ from the two methods, *NVT* simulations with direct extrapolation (η_{YH}) and *NVE* simulations with η_{GK}, cannot be distinguished on the scale of the plot. Where error bars are not explicitly shown, the statistical uncertainty is smaller than the size of the symbol.

surrounded by a solvent of viscosity η_{YH} in a periodically replicated simulation cell,

$$D_{i,\mathrm{PBC}} = -\frac{\xi k_{\mathrm{B}} T}{6\pi\eta_{\mathrm{YH}}} L^{-1} + D_{i,0} \tag{B.14}$$

where $D_{i,\mathrm{PBC}}$ are the finite-size diffusion coefficients calculated from our MD simulations, and ξ is a dimensionless constant equal to 2.837297 for a cubic simulation cell with 3D periodic boundary conditions.[6] The same expression was obtained earlier[7] by Dünweg and Kremer using a closely related derivation. For each state point, the $i = 1$ and $i = 2$ data sets were simultaneously fit to Eq. B.14, giving a single viscosity η_{YH} for the mixture.

The shear viscosity η was additionally calculated using the Green-Kubo integral formula

$$\eta_{\mathrm{GK}} = \frac{V}{k_{\mathrm{B}} T} \lim_{t'\to\infty} \int_0^{t'} \langle P_{\alpha\beta}(t) P_{\alpha\beta}(0)\rangle dt \tag{B.15}$$

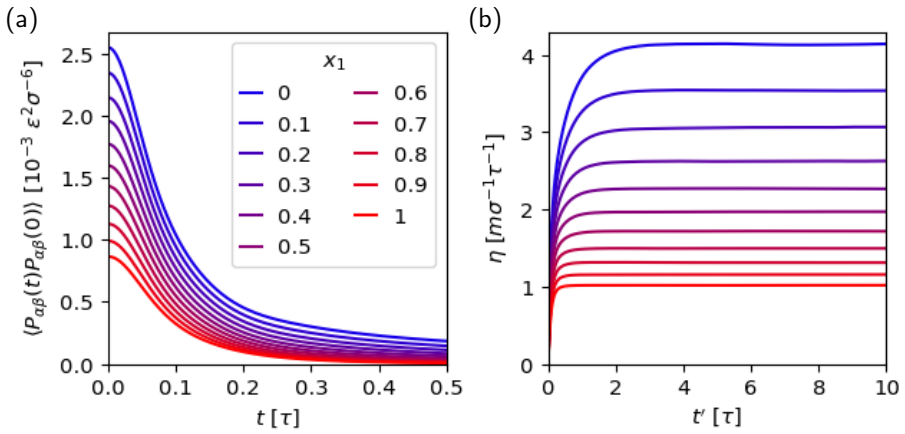


FIGURE B.10: (a) Autocorrelation functions $\langle P_{\alpha\beta}(t)P_{\alpha\beta}(0)\rangle$ as a function of time lag t. (b) Convergence of shear viscosity $\eta(t')$ with the correlation time t' used as the upper limit of the integral in Eq. B.15.

where $\alpha \neq \beta$ such that $P_{\alpha\beta}$ are the off-diagonal elements of the pressure tensor. Results were averaged over $(\alpha, \beta) = (x, y)$, (x, z) and (y, z). A correlation time of $t' = 10\tau$ was used for the upper limit of the integral, which is sufficient to obtain well-converged integrals (see Fig. B.10).

In order to accurately target a specific thermodynamic states when calculating $D_{i,\mathrm{PBC}}$, the NVT ensemble was sampled using a temperature-control algorithm that alters dynamics compared to the Newtonian dynamics of the NVE ensemble. It is therefore necessary to check whether the employed global Nosé–Hoover (three chains) thermostat affects the computed self-diffusion coefficients. We show in Fig. B.9(b&c) that it does not: all diffusion coefficients and viscosities calculated from NVT and NVE simulations, and using the different methods (eqs. B.14&B.15) agree to within their associated uncertainties. This is consistent with previous work that shows that "global" velocity scaling thermostats, including the Nosé–Hoover-chain thermostat, do not significantly alter diffusion coefficients or viscosity.[8]

B.8 Activation energies for diffusion and viscous flow

As shown in Fig. B.11, the activation energies for self-diffusion $\Delta G_i^{\ddagger}$ were calculated from $D_i = D_i^0 \exp\left\{(-\Delta G_i^{\ddagger}/k_{\mathrm{B}}T)\right\}$ by fitting a straight line to $\ln D_i = \ln D_i^0 - \Delta G_i^{\ddagger}/(k_B T)$, where D_i^0 is a constant and the self-diffusion coefficients D_i have been corrected for finite-size effects (see Sec. B.7).

A relevant question for the Shukla-Firoozabadi model is how to best estimate the parameters τ_i. Different methods have been proposed, with varying levels of approximations.[9–13] The most crude but still a widely adopted[14,15] approach is to set $\tau_1 = \tau_2 = 4.0$ or 3.5, stemming from the observation[9] that $\Delta U_{\mathrm{vap}}/\Delta U_{\eta}^{\ddagger} = 3$-4 for many non-associating liquids under normal boiling point

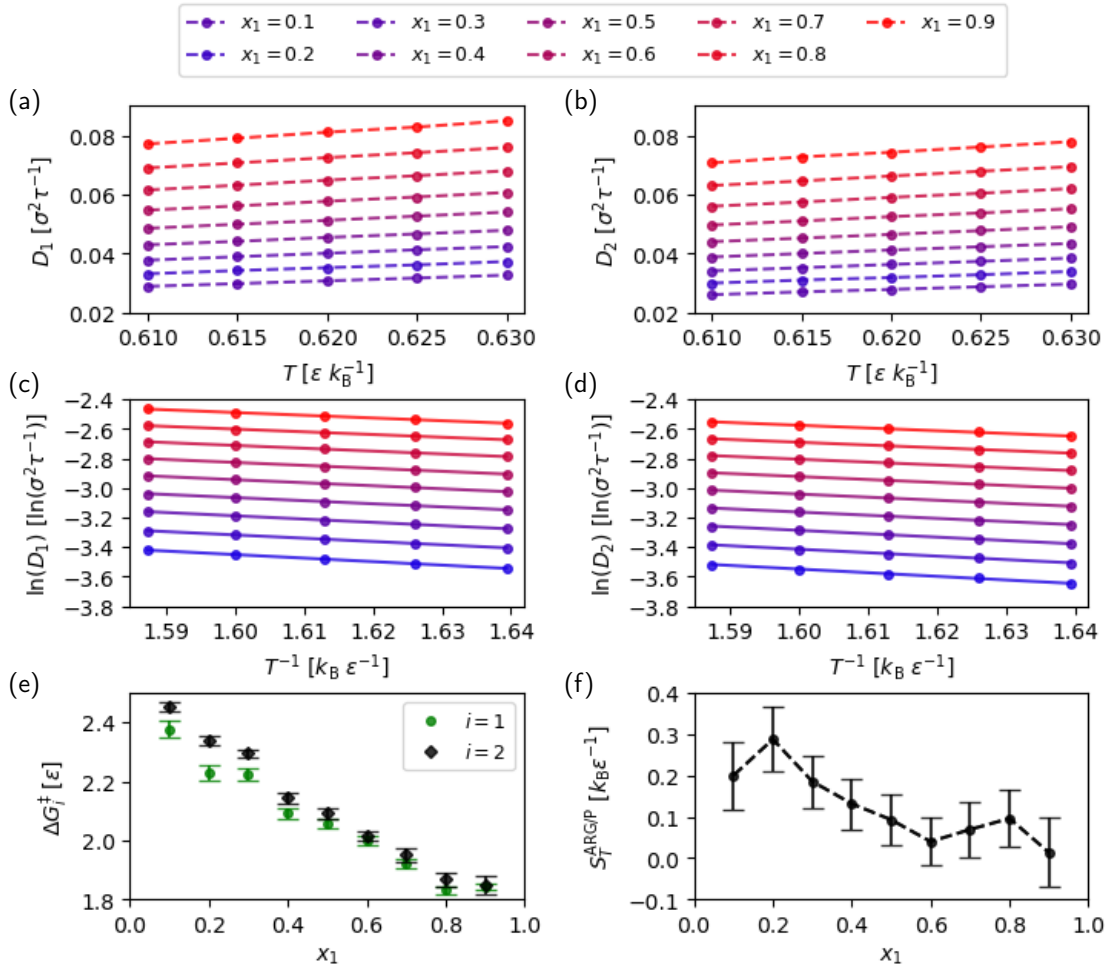


FIGURE B.11: The Soret coefficient predicted by the Artola-Rousseau-Galliéro and Prigogine models, $S_T^{\mathrm{ARG/P}}$, and related quantities. The self-diffusion coefficients D_i as a function of temperature T for species (a) $i = 1$ and (b) $i = 2$. $\ln D_i$ *vs.* T^{-1} for species (c) $i = 1$ and (d) $i = 2$; the solid lines show linear fits to $\ln D_i = \ln D_i^0 - \Delta G_i^{\ddagger}/(k_B T)$. (e) The activation energies $\Delta G_i^{\ddagger}$ and (e) $S_T^{\mathrm{ARG/P}}$ as a function of mole fraction x_1. Where error bars have not been shown, uncertainties are smaller than the size of the symbols.

conditions, where ΔU_{vap} is the energy of vaporization (ΔU_{vap} is an approximation to ΔU_c). While permissible for some mixtures, this approach is unsuitable for others and has been criticised.[10,12,13] In this work, we use the method originally proposed[9], but not employed, by Shukla and Firoozabadi with the caveat that they used the approximation $\Delta U_{\mathrm{vap}} \approx \Delta U_c$. As shown in Fig. B.12, we calculate τ_i of the pure components from $\eta_i = A \exp\left\{(\Delta U_{\eta,i}^{\ddagger}/k_{\mathrm{B}}T)\right\} = A \exp\{(\Delta U_{c,i}/\tau_i k_{\mathrm{B}}T)\}$ by fitting a straight line to $\ln \eta_i = \ln A + U_c/(\tau_i k_B T)$, where η_i is the shear viscosity, to give $(\tau_1, \tau_2) = (3.3 \pm 0.1, 3.8 \pm 0.1)$, and use these τ_i for the entire composition range. This approach does not account for the composition dependence of τ_i.

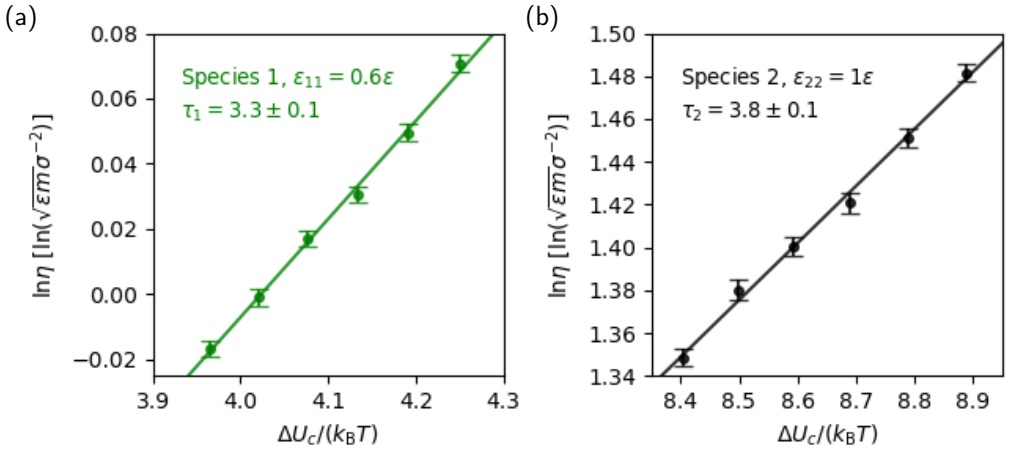


FIGURE B.12: $\ln(\eta_i)$ *vs.* $\Delta U_c/(k_BT)$, where η_i and ΔU_c are the shear viscosity and cohesive energy of a pure liquid of species $i = 1, 2$. (a) Species 1 and (b) species 2. The solid lines show linear fits to $\ln \eta_i = \ln A + U_c/(\tau_i k_B T)$. The data points correspond to $P = 0.46\epsilon\sigma^{-3}$ and $T/(\epsilon k_B^{-1}) = 0.605$, 0.61, 0.615, 0.62, 0.625 and 0.63.

B.9 Kirkwood-Buff integrals from grand canonical Monte Carlo simulations

KBIs were calculated from grand canonical Monte Carlo simulations. For each simulation, the temperature of the ideal gas reservoir was set to $T = 0.62\ \epsilon k_B^{-1}$, and the input chemical potentials μ_1 and μ_2 were determined from the free-energy perturbation simulations described in Sec. B.6. In all cases, a cubic simulation cell with length $L = 20\sigma$ was used. Each MC step, 100 trial displacement and 100 trial exchanges (insertions or deletions with equal probability) were attempted. For the displacement moves, a maximum translation distance of 1.0σ was allowed. Trial moves were accepted/rejected using the standard Metropolis criterion. Each replica was first equilibrated in an NVT MD simulation at the target x_1 and ρ_N for 200 τ, followed by 10^5 MC steps, and finally a production run of 10^7 MC steps. Sampling consisted of 400-500 statistically independent replicas for each state point.

The Kirkwood-Buff integrals G_{ij} were calculated from the particle number fluctuations according to

$$G_{ij} = V\frac{\langle N_i N_j\rangle - \langle N_i\rangle\langle N_j\rangle}{\langle N_i\rangle\langle N_j\rangle} - V\frac{\delta_{ij}}{\langle N_j\rangle} \tag{B.16}$$

where N_i is the number of particles of species i and V is the volume of the simulation cell. The average pressures are within $\pm 0.008\epsilon\sigma^{-3}$ of $P = 0.46\ \epsilon\sigma^{-3}$, corresponding to differences in number density on the order of $\delta\rho_N \sim 10^{-4}\sigma^{-3}$ relative to those calculated from NPT MD simulations (see Fig. 3.1(a)). Differences in G_{ij} and subsequently Γ due to the slightly different thermodynamic states being sampled are expected to be insignificant compared to their statistical uncertainties.

B.10 Kirkwood-Buff integrals from molecular dynamics (NVT) simulations

For an infinitely large and open three-dimensional system, the KBI for mixture components i and j is defined as

$$G_{ij} = 4\pi \int_0^\infty [g_{ij}^{\mu VT}(r) - 1] r^2 dr \tag{B.17}$$

where r is the radial distance between particles i and j. The infinite-size KBIs were calculated from a finite-size analysis of finite-volume KBIs

$$G_{ij}^V = \int_V [g_{ij}^{\mu VT}(r) - 1] w(r) dr \tag{B.18}$$

defined for finite and open subvolumes embedded in a reservoir.[16] For spherical symmetry $w(r) = 4\pi r^2(1 - 3x/2 + x^3/2)$ valid for $x < 1$, where $x = r/(2R)$ and R is the radius of the subvolume. $g_{ij}^{\mu VT}$ is the pair correlation function *in the thermodynamic limit*. It has been shown that G_{ij}^V scales linearly with R^{-1} and that the infinite-size G_{ij} can be obtained by extrapolating the linear regime to $R^{-1} = 0$.[16–18]

We calculate the RDFs from simulations of $N = 10^5$ to $N = 5 \times 10^6$ particles in the NVT ensemble. Because fluctuations transform between ensembles, $g_{ij}^{\mu VT}$ cannot be formally replaced with g_{ij}^{NVT}. However, for a sufficiently large system, the correlation lengths of particle density fluctuations are small compared to the linear dimension of the simulation cell, and local correlations are expected to be well reproduced. In addition to a large system size, we apply the tail correction[18] of Ganguly and van der Vegt to ensure the correct asymptotic limit ($\lim_{r\to\infty} g_{ij} = 1$) of the RDF.

$$g_{ij}^{GV}(r) = g_{ij}(r) \left(\frac{N_j h(r)}{N_j h(r) - n_{ij}^{ex}(r) - \delta_{ij}} \right) \tag{B.19}$$

$$h(r) = 1 - \frac{4\pi r^3}{3V} \tag{B.20}$$

where N_j is the total number of particles j in the simulation cell of volume V. However, we note that in our simulations, this correction does not have an appreciable effect on the linear regime and subsequently the extrapolated G_{ij} (see Fig. B.13). Other corrections[19,20] to the RDFs for calculating KBIs have been proposed; the correction of Ganguly and van der Vegt was found to be the most accurate for a WCA system, relative to a larger reference system ($L = 80\sigma$).[17]

We show in Fig. B.14 a finite-size analysis of the infinite-size KBIs. The final values for G_{ij} in Chapter 3 were taken from the largest system size, and the associated uncertainties were estimated from the convergence with system size.

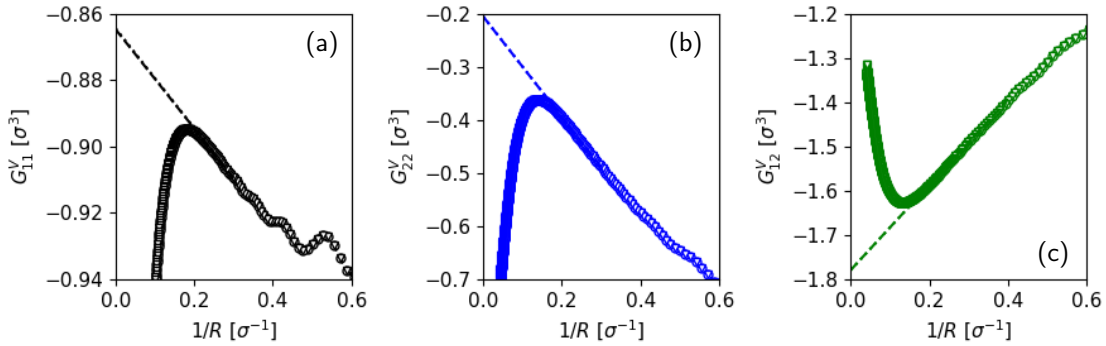


FIGURE B.13: Extrapolation of the finite-volume Kirkwood-Buff integrals G_{ij}^V to $R^{-1} = 0$, where R is the radius of the subvolume: (a) G_{11}^V, (b) G_{22}^V and (c) G_{12}^V. The data shown corresponds to mole fraction $x_1 = 0.5$ and a system size of $N = 5 \times 10^6$ particles. Symbols: circles $(\cdots\circ\cdots)$ and downward triangles $(\cdots\triangledown\cdots)$ denote the use of pair correlation function g_{ij} (uncorrected) and the corrected g_{ij}^{GV}, respectively, although these cannot be easily distinguished on the scale of the plots.

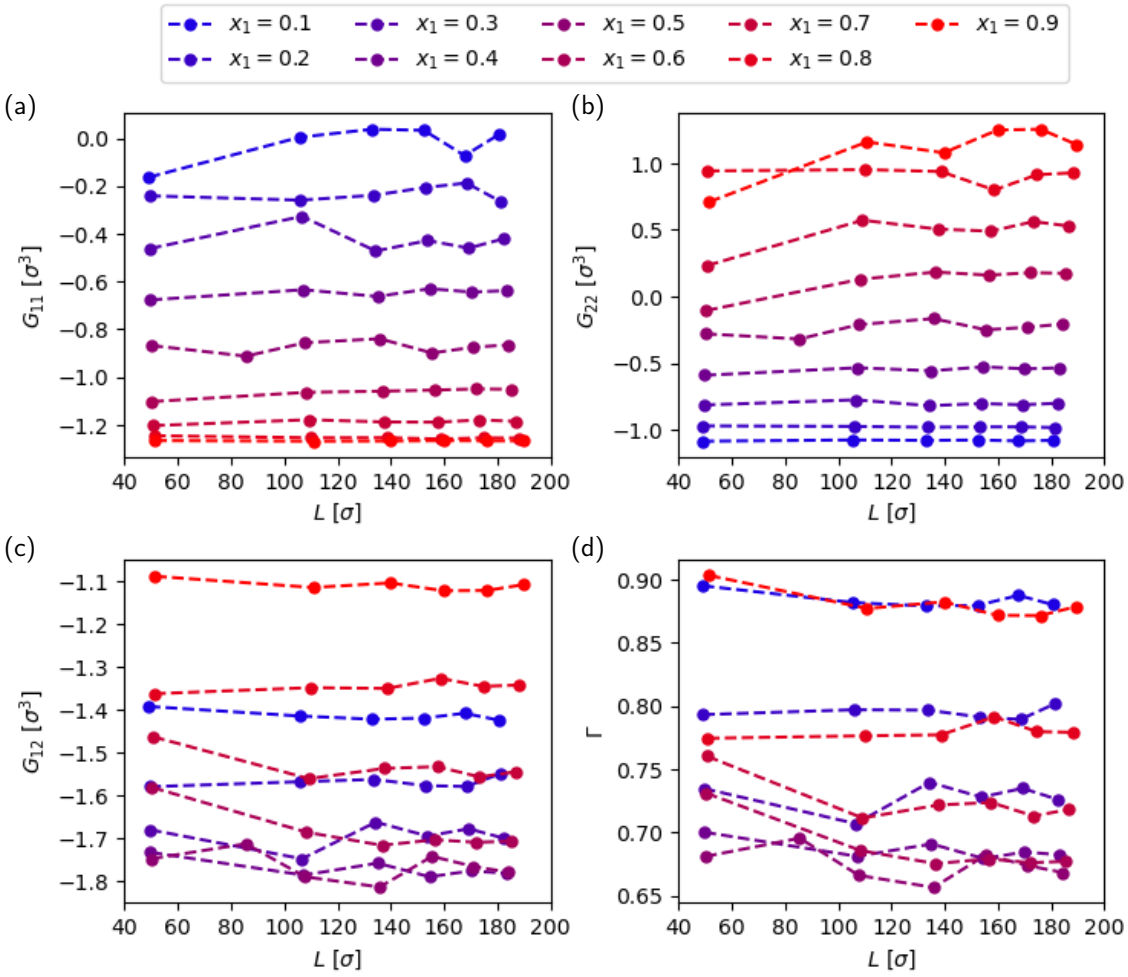


FIGURE B.14: Finite-size analysis of the infinite-size Kirkwood-Buff integrals G_{ij} as a function of simulation cell length L, for different mole fractions x_1. (a) G_{11}, (b) G_{22}, (c) G_{12}, and (d) thermodynamic factor Γ.

B.11 Melting points of the pure components

The melting temperatures T_m of the pure components $i = 1, 2$ were determined using the direct coexistence method in the NP_zT ensemble. This involves preparing a solid-liquid interface at a given (T, P) state point and observing whether the system completely melts, freezes, or remains in coexistence. In MD simulations, cooling a homogeneous liquid below its melting point usually results in a metastable supercooled liquid; freezing is not observed unless prohibitively long simulations are performed. Likewise, heating a solid slightly above its melting point results in a superheated solid. The presence of the interface lowers the kinetic barrier for melting/freezing.

First, the densities of the solid and liquid phases were determined from NPT simulations. Initial configurations were prepared by joining two half-boxes, one of the FCC-solid the other of the liquid, each containing $N = 5324$ particles and equilibrated in the NVT ensemble. The combined $N = 10648$ system was then equilibrated for 20τ, ensuring that the solid phase did not melt by restraining each solid particle to its equilibrium position $\boldsymbol{r}_0$ with a harmonic potential, $\mathcal{V}(\boldsymbol{r}) = k(\boldsymbol{r}-\boldsymbol{r_0})^2/2$ of force constant $k = 10\,\epsilon\sigma^{-2}$. A $4\times10^4\tau$ production run in the NP_zT ensemble was then performed, applying a barostat only to the direction parallel to the surface normal (the z-direction). A Nosé-Hoover chain barostat was used, with 3 chains, and a time constant of 4 τ. Likewise, a Nosé-Hoover chain thermostat was used, also with 3 chains, and a time constant of 1 τ. Sampling consisted of an initial 10 statistically independent replicas, followed by an additional 40 replicas if the initial set did not all either melt or freeze. In all cases, a homogeneous phase was observed by the end of the production run.

The simulations were performed in the NP_zT ensemble, and as such the simulation cell dimensions (L_x and L_y) were chosen to be consistent with the density of the solid at the (T, P) state point. Otherwise, the solid phase would possess internal stress,[21,22] corresponding to a higher free energy, and resulting in the overestimation of the coexistence pressure and/or underestimation of the melting temperature.

Each replica was determined to have either frozen or melted using the Q_6 ($l = 6$) bond-orientational order parameter. The Steinhardt order parameters Q_l were introduced to characterize local orientational order in atomic structures,[23] and are given by

$$Q_l = \sqrt{\frac{4\pi}{2l+1}\sum_{m=-l}^{+l}\bar{Y}_{lm}\bar{Y}_{lm}^*} \tag{B.21}$$

$$\bar{Y}_{lm} = \frac{1}{N_n}\sum_{j=1}^{N_n} Y_{lm}(\theta(\boldsymbol{r}_{ij}), \phi(\boldsymbol{r}_{ij})) \tag{B.22}$$

for each particle i, where $Y_{lm}(\theta, \phi)$ are the spherical harmonics, θ and ϕ are the polar angles of

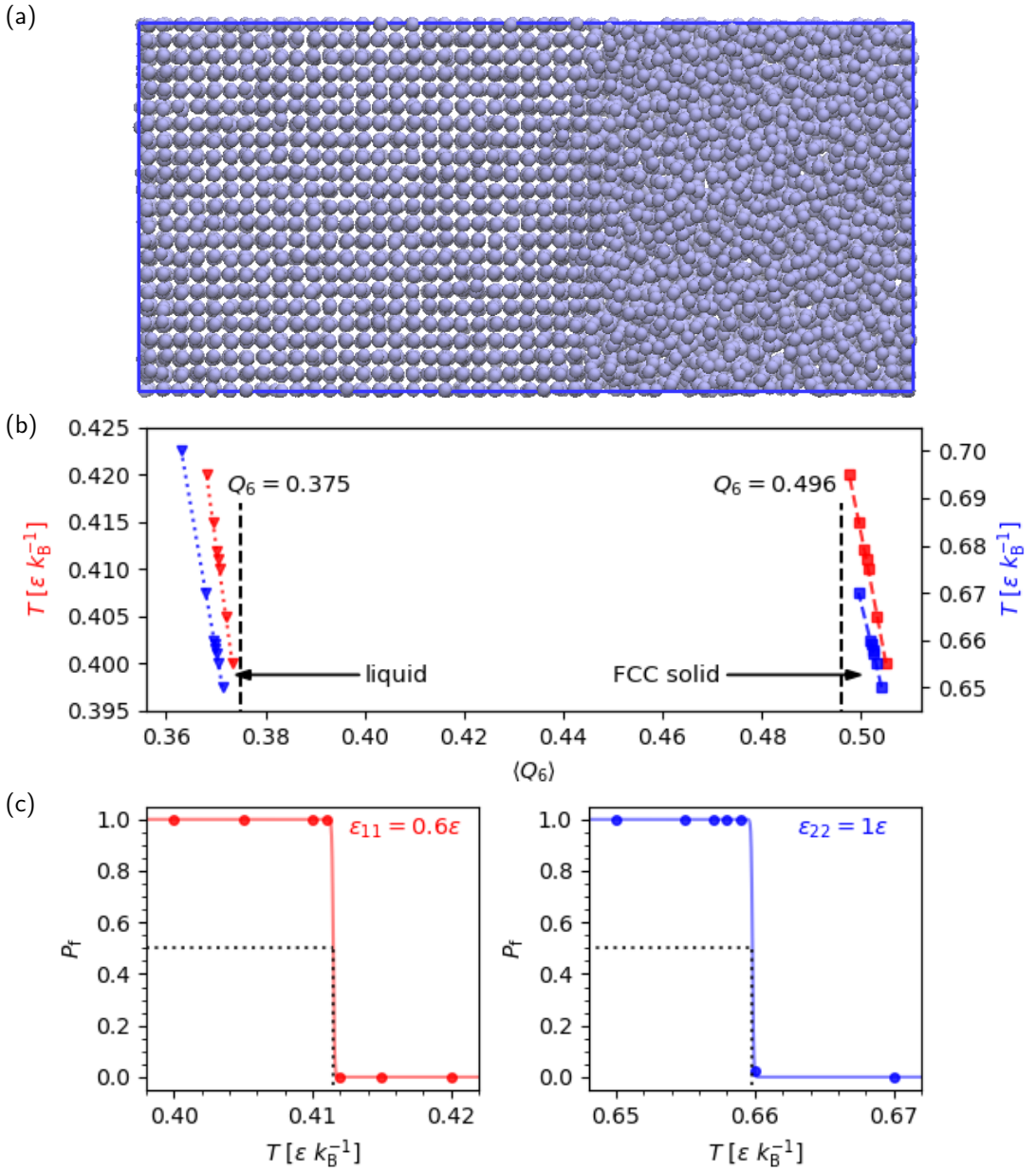


FIGURE B.15: Melting points of the pure components determined using the direct coexistence method. (a) Snapshot of the simulation cell in the process of melting/freezing. (b) Lennard-Jones liquids and FCC solids at temperatures T characterized by their average Q_6 order parameter. Species 1 (species 2) is shown in red (blue) and on the left (right) axis. (c) Probability of freezing P_f as a function of temperature T for species 1 (left) and 2 (right). Solid lines show the fitted sigmoid-like functions (Eq. B.23).

"bond" vector $\boldsymbol{r}_{ij}$ between i and neighbour j, and N_n is the number of nearest neighbours to particle i. Q_l is therefore a rotationally invariant non-negative amplitude. Q_l adopt well-defined values for high-symmetry structures; for a perfect FCC crystal ($Fm\bar{3}m$) and $N_n = 12$, $Q_6 = 0.575$.[24] We show in Fig. B.15 that the Q_6 order parameter can be used to distinguish between the FCC

solid and liquid phases. The replica was determined to have frozen if $\langle Q_6 \rangle > 0.496$, or melted if $\langle Q_6 \rangle < 0.375$. The average $\langle Q_6 \rangle$ was taken over the last 10 τ of the trajectory.

In the thermodynamic limit, a solid melts at $T > T_m$, and a liquid freezes for $T < T_m$. However, a finite-size system may stochastically melt or freeze with probabilities P_m and $P_f = 1 - P_m$ respectively. For each component, T_m was determined by fitting $P_f(T)$ to the sigmoid-like function (Fig. B.15):

$$P_f(T) = \frac{1}{2} - \frac{1}{2} \tanh\left[(T - T_m)/d\right] \tag{B.23}$$

where d controls the sharpness of the probability profile, with $\delta_{10-90} = 2.178d$ being the width of the interval where P_f goes from 0.1 to 0.9. The melting (coexistence) temperature is defined by $P_m(T_m) = P_f(T_m) = 0.5$. The melting temperatures are shown in Table B.1 alongside other coexistence properties (coexistence densities and enthalpies were determined by interpolating data from the NPT simulations).

TABLE B.1: Solid-liquid coexistence properties of the pure LJ components at $P = 0.46\ \epsilon\sigma^{-3}$: the melting temperature T_m; coexistence number densities of the FCC solid and liquid phases, $\rho_{N,s}$ and $\rho_{N,l}$, respectively; and the enthalpy of fusion ΔH_{fus}

Species	T_m $[\epsilon k_{\text{B}}^{-1}]$	$\rho_{N,s}$ $[\sigma^{-3}]$	$\rho_{N,l}$ $[\sigma^{-3}]$	ΔH_{fus} $[\epsilon]$
1	0.4115(5)	0.9550(2)	0.8500(3)	0.523(3)
2	0.6598(3)	0.9509(1)	0.8419(2)	0.927(3)

Bibliography

[1] S. H. Jamali, L. Wolff, T. M. Becker, A. Bardow, T. J. H. Vlugt and O. A. Moultos, *J. Chem. Theory Comput.*, 2018, **14**, 2667–2677.

[2] A. T. Celebi, S. H. Jamali, A. Bardow, T. J. H. Vlugt and O. A. Moultos, *Mol. Simul.*, 2021, **47**, 831–845.

[3] N. A. T. Miller, P. J. Daivis, I. K. Snook and B. D. Todd, *J. Chem. Phys.*, 2013, **139**, 144504.

[4] J. Armstrong and F. Bresme, *Phys. Chem. Chem. Phys.*, 2014, **16**, 12307–12316.

[5] T. C. Beutler, A. E. Mark, R. C. van Schaik, P. R. Gerber and W. F. van Gunsteren, *Chem. Phys. Lett.*, 1994, **222**, 529–539.

[6] I.-C. Yeh and G. Hummer, *J. Phys. Chem. B*, 2004, **108**, 15873–15879.

[7] B. Dünweg and K. Kremer, *J. Chem. Phys.*, 1993, **99**, 6983–6997.

[8] J. E. Basconi and M. R. Shirts, *J. Chem. Theory Comput.*, 2013, **9**, 2887–2899.

[9] K. Shukla and A. Firoozabadi, *Ind. Eng. Chem. Res.*, 1998, **37**, 3331–3342.

[10] M. Eslamian and M. Z. Saghir, *J. Non-Equilib. Thermodyn.*, 2009, **34**, 97–131.

[11] M. Eslamian and M. Z. Saghir, *Phys. Rev. E*, 2009, **80**, 011201.

[12] Y. Yan, P. Blanco, M. Z. Saghir and M. M. Bou-Ali, *J. Chem. Phys.*, 2008, **129**, 194507.

[13] S. Pan, M. Z. Saghir, M. Kawaji, C. G. Jiang and Y. Yan, *J. Chem. Phys.*, 2007, **126**, 014502.

[14] P.-A. Artola and B. Rousseau, *Phys. Rev. Lett.*, 2007, **98**, 125901.

[15] H. Hoang and G. Galliero, *Eur. Phys. J. E*, 2022, **45**, 42.

[16] P. Krüger, S. K. Schnell, D. Bedeaux, S. Kjelstrup, T. J. H. Vlugt and J.-M. Simon, *J. Phys. Chem. Lett.*, 2013, **4**, 235–238.

[17] N. Dawass, P. Krüger, S. K. Schnell, D. Bedeaux, S. Kjelstrup, J. M. Simon and T. J. H. Vlugt, *Mol. Simul.*, 2018, **44**, 599–612.

[18] P. Ganguly and N. F. A. van der Vegt, *J. Chem. Theory Comput.*, 2013, **9**, 1347–1355.

[19] J. J. Salacuse, A. R. Denton and P. A. Egelstaff, *Phys. Rev. E*, 1996, **53**, 2382–2389.

[20] R. Cortes-Huerto, K. Kremer and R. Potestio, *J. Chem. Phys.*, 2016, **145**, 141103.

[21] J. R. Espinosa, E. Sanz, C. Valeriani and C. Vega, *J. Chem. Phys.*, 2013, **139**, 144502.

[22] D. Frenkel, *Eur. Phys. J. Plus*, 2013, **128**, 1–21.

[23] P. J. Steinhardt, D. R. Nelson and M. Ronchetti, *Phys. Rev. B*, 1983, **28**, 784–805.

[24] W. Mickel, S. C. Kapfer, G. E. Schröder-Turk and K. Mecke, *J. Chem. Phys.*, 2013, **138**, 044501.

Appendix C

Supporting information for Chapter 4

C.1 Soret coefficient: verification of the linear regime

In order to generate different temperature gradients ∇T, additional NEMD simulations with $(T_c, T_h)/(\epsilon k_B^{-1}) = (2.7, 3.3)$ and $(2.3, 3.7)$ were performed for three mixtures. For the $(I_1 = I_2, d_1, d_2) = (80m\sigma^2, 2.7\sigma, 0)$ mixture a simulation with $(T_c, T_h)/(\epsilon k_B^{-1}) = (2.0, 4.0)$ was also performed. We demonstrate in Fig. C.1 that the thermal diffusion response changes linearly with the magnitude of temperature gradient. Thus, the simulated systems are in the linear regime.

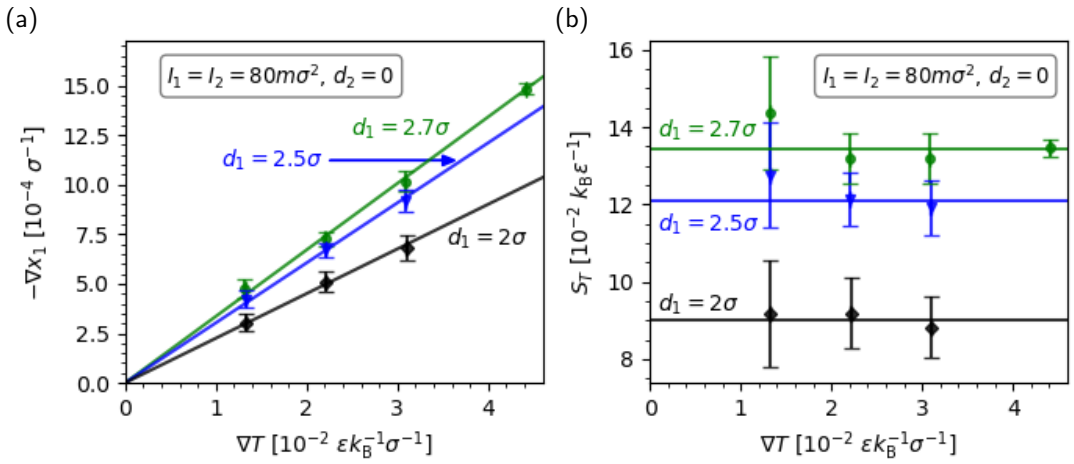


FIGURE C.1: Verification of the linear regime for thermal diffusion: the (a) mole fraction gradient ∇x_1 and (b) S_T as a function of temperature gradient ∇T. The solid lines show fits to $\nabla x_1 = -x_1 x_2 S_T \nabla T$.

C.2 Soret coefficient: finite-size effects

In order to gauge the finite-size effects associated with our S_T data, two additional NEMD simulations with $L_\perp/\sigma = 25, 100$ were performed for the $(I_1 = I_2, d_1, d_2) = (80m\sigma^2, 2.7\sigma, 0)$ mixture, where $L_\perp = L_x = L_y$ is the length of the simulation cell in the direction parallel to the heat flux. The simulations (10 replicas each) for $L_\perp = 25\sigma$ and $L_\perp = 100\sigma$ had production lengths of $26 \times 10^5\ \tau$ and $1.6 \times 10^5\ \tau$, respectively.

We show in Fig. C.2 that finite-size effects serve to decrease S_T. We fit the $S_T(L_\perp^{-1})$ data to a straight line; extrapolating to $L_\perp^{-1} \to 0$ gives $S_T = (12.6 \pm 0.4) \times 10^{-2}\ k_B\epsilon^{-1}$, which is a $\sim 4\%$ decrease relative to $S_T(L_\perp = 50\sigma)$.

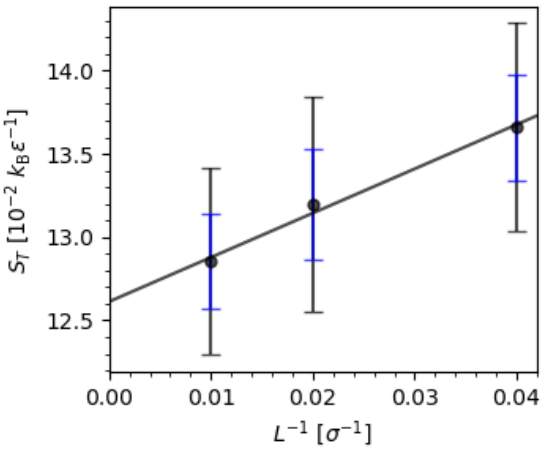


FIGURE C.2: Finite-size effects on the Soret coefficient S_T of the $(I_1 = I_2, d_1, d_2) = (80m\sigma^2, 2.7\sigma, 0)$ mixture calculated from NEMD simulations. $L_\perp = L_x = L_y$ is the length of the simulation cell in the direction parallel to the heat flux. Black and blue error bars show the 95% confidence interval and the standard error of the mean, respectively.

C.3 Convergence of Green-Kubo integral formulas

The Green-Kubo integral formula for the phenomenological coefficient L_{11} is given by Eq. 4.10. The shear viscosity η was calculated using the formula

$$\eta_{GK} = \frac{V}{k_B T} \lim_{t' \to \infty} \int_0^{t'} \langle P_{\alpha\beta}(t) P_{\alpha\beta}(0) \rangle dt \tag{C.1}$$

where $\alpha \neq \beta$ such that $P_{\alpha\beta}$ are the off-diagonal elements of the pressure tensor. Results were averaged over $(\alpha, \beta) = (x, y)$, (x, z) and (y, z). A correlation time of $t_c = 500\tau$ was used for the upper limit of the integrals for both L_{11} and η, which is sufficient to obtain well-converged integrals, as shown in Figs. C.3 & C.4. For all the mixtures considered, by $t' = 400\tau = 0.8t_c$, L_{11} and η converged within 5% and 3%, respectively, of their final values.

Rotational diffusion coefficients in the laboratory frame of reference were calculated using formula

$$D_r = \frac{1}{3} \lim_{t' \to \infty} \int_0^{t'} \langle \boldsymbol{\omega}_j(t) \cdot \boldsymbol{\omega}_j(0) \rangle dt \tag{C.2}$$

where $\boldsymbol{\omega}_j$ is the angular velocity of the j^{th} molecule and the factor of 1/3 averages the contributions from each spatial dimension. A correlation time of $t_c = 200\tau$ was used for the upper limit of the integral, which is sufficient to obtain well-converged integrals, as shown in Fig C.5. For all the components and mixtures considered, D_r converged to within 1% and 0.6% of its final value by $t' = 50\tau = 0.25t_c$ and $t' = 160\tau = 0.8t_c$, respectively.

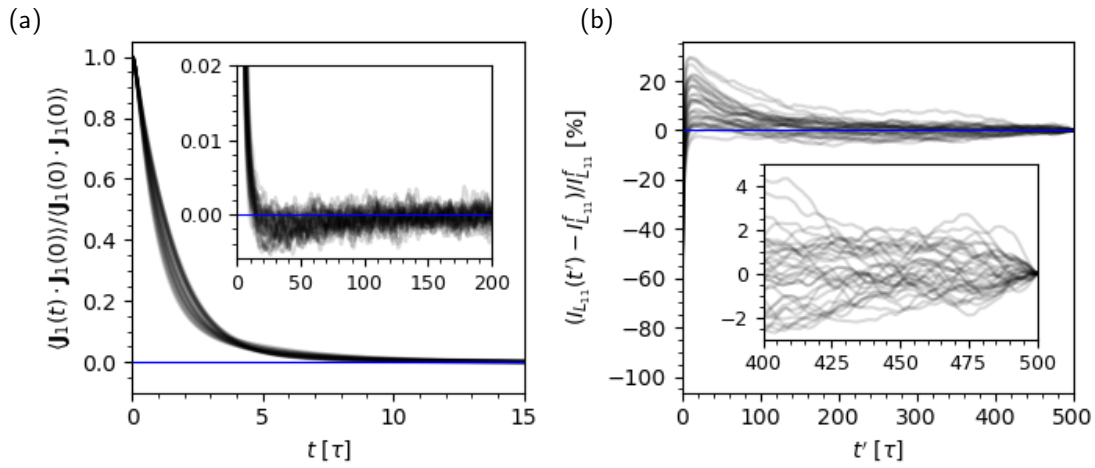


FIGURE C.3: (a) Normalized autocorrelation functions $\langle \boldsymbol{J}_1(t) \cdot \boldsymbol{J}_1(0) \rangle / \langle \boldsymbol{J}_1(0) \cdot \boldsymbol{J}_1(0) \rangle$ as a function of time lag t. (b) Convergence of the integral $I_{L_{11}} = \int_0^{t'} \langle \boldsymbol{J}_1(t) \cdot \boldsymbol{J}_1(0) \rangle dt$ with the correlation time t' used as the upper limit of the integral; $(I_{L_{11}}(t') - I^f_{L_{11}})/I^f_{L_{11}}$ is the relative deviation of $I_{L_{11}}(t')$ from the final value $I^f_{L_{11}} = I_{L_{11}}(t' = 500\tau)$ used to calculate the phenomenological coefficient L_{11}. Data is shown for all the mixtures that L_{11} was calculated for.

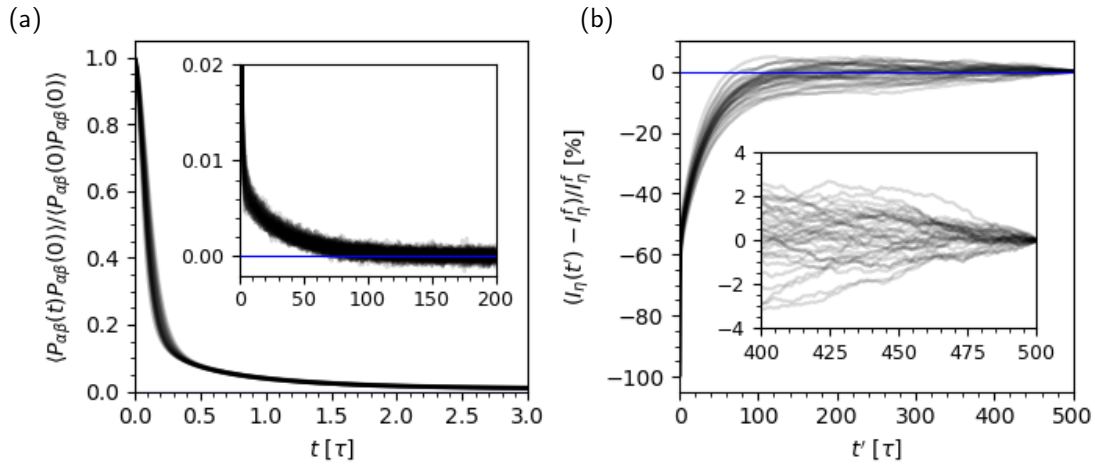


FIGURE C.4: (a) Normalized autocorrelation functions $\langle P_{\alpha\beta}(t)P_{\alpha\beta}(0)\rangle/\langle P_{\alpha\beta}(0)P_{\alpha\beta}(0)\rangle$ as a function of time lag t. (b) Convergence of the integral $I_\eta = \int_0^{t'} \langle P_{\alpha\beta}(t)P_{\alpha\beta}(0)\rangle dt$ with the correlation time t' used as the upper limit of the integral; $(I_\eta(t') - I_\eta^f)/I_\eta^f$ is the relative deviation of $I_\eta(t')$ from the final value $I_\eta^f = I_\eta(t' = 500\tau)$ used to calculate the viscosity. Data is shown for all the mixtures that the shear viscosity was calculated for.

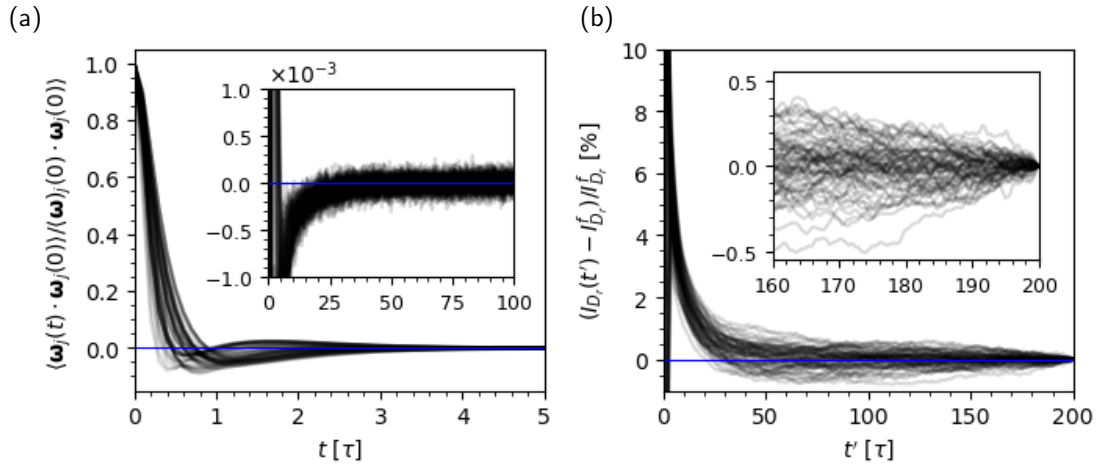


FIGURE C.5: (a) Normalized autocorrelation functions $\langle \boldsymbol{\omega}_j(t)\cdot\boldsymbol{\omega}_j(0)\rangle/\langle \boldsymbol{\omega}_j(0)\cdot\boldsymbol{\omega}_j(0)\rangle$ as a function of time lag t. (b) Convergence of the integral $I_{D_r} = \int_0^{t'} \langle \boldsymbol{\omega}_j(t)\cdot\boldsymbol{\omega}_j(0)\rangle dt$ with the correlation time t' used as the upper limit of the integral; $(I_{D_r}(t') - I_{D_r}^f)/I_{D_r}^f$ is the relative deviation of $I_{D_r}(t')$ from the final value $I_\eta^f = I_{D_r}(t' = 200\tau)$ used to calculate the rotational diffusion coefficient D_r. Data is shown for all the components and mixtures that D_r was calculated for.

C.4 Diffusion coefficients: finite-size effects

The self-diffusion coefficients D_i of species $i = 1, 2$ were calculated from the average mean square displacement (MSD) using the Einstein relation

$$D_i = \frac{1}{2d} \lim_{t\to\infty} \frac{\langle |\boldsymbol{r}_i(t) - \boldsymbol{r}_i(0)|^2 \rangle}{t} \tag{C.3}$$

where $\boldsymbol{r}_i$ is the position vector of a particle of species i, t is the elapsed time from an arbitrary starting time, and $d = 3$ is the number of spatial dimensions. D_i was therefore calculated by fitting to the equation $\langle |\boldsymbol{r}_i(t) - \boldsymbol{r}_i(0)|^2 \rangle = 6tD_i$, excluding the first 200τ of data to ensure only the diffusive regime was sampled (as opposed to the ballistic regime).

In order to assess the impact of finite-size effects, the "infinite-size" diffusion coefficients $D_{i,0}$ were calculated using the equation of Yeh and Hummer[1], which was derived using a simple hydrodynamic model of a particle surrounded by a solvent of viscosity η in a periodically replicated simulation cell:

$$D_{i,0} = D_{i,\mathrm{PBC}} + \frac{\xi k_\mathrm{B} T}{6\pi\eta L} = D_{i,\mathrm{PBC}} + \Delta_\mathrm{YH} \tag{C.4}$$

where $D_{i,\mathrm{PBC}}$ are the finite-size diffusion coefficients calculated from our MD simulations, and ξ is a dimensionless constant equal to 2.837297 for a cubic simulation cell of length L with 3D periodic boundary conditions.[1] The same expression was obtained earlier[2] by Dünweg and Kremer using a closely related derivation. It has recently been shown that this finite-size correction can also be applied to the Fickian mutual diffusion coefficient D_{12}.[3]

The impact of finite-size effects on diffusion coefficients is shown in Fig. C.6. The finite-size correction amounts to an increase in D_{12}, D_1 and D_2 of $< 4\%$. As shown in Fig. C.6, the finite-size correction does not affect the observed qualitative trends.

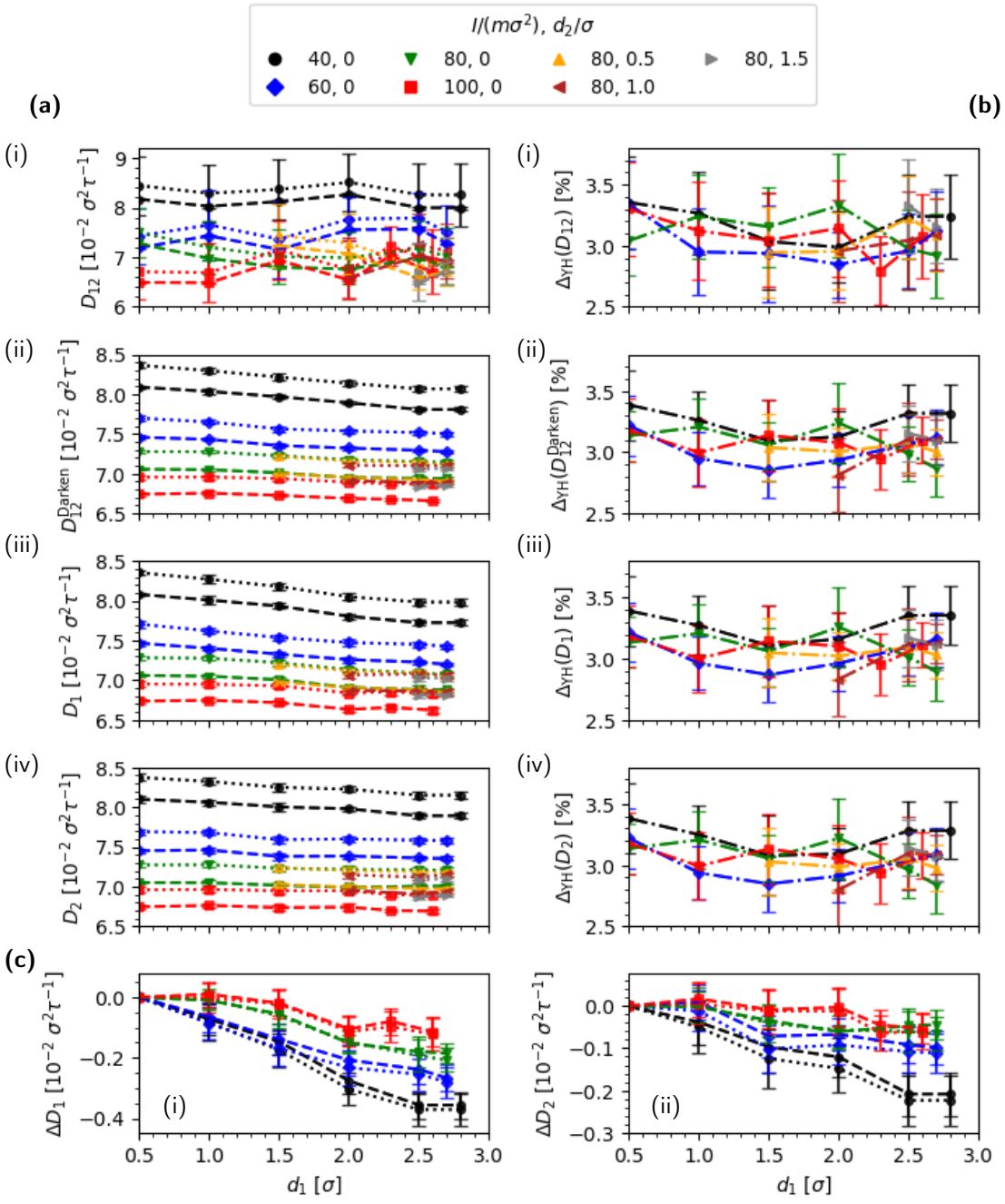


FIGURE C.6: The impact of finite-size effects on diffusion coefficients. The (a) corrected and uncorrected diffusion coefficients D_X and (b) finite-size correction $\Delta_{\mathrm{YH}}(D_X)$ as a percentage of the uncorrected D_X for: (i) the Fickian mutual diffusion coefficient D_{12}; the Darken approximation D_{12}^{Darken}; and the self-diffusion coefficients (iii) D_1 and (iv) D_2. (c) The corrected and uncorrected change in self-diffusion coefficient, $\Delta D_i = D_i - D_i(d_1 = 0.5\sigma)$: (i) $i = 1$ and (ii) $i = 2$. All data are shown as a function of mass dipole, d_1, of species 1. In (a) and (c), the corrected and uncorrected D_X are denoted by dotted (...) and dashed (---) lines, respectively.

C.5 Isotropic-nematic coexistence

Coexistence conditions were estimated directly from our simulations. Along each isobar, the coexistence temperature was estimated as $T_{IN} = (T_{N,\max} + T_{I,\min})/2$, where $T_{N,\max}$ ($T_{I,\min}$) and is the highest (lowest) temperature at which a nematic (isotropic) phase was observed. Analogously, an upper (lower) bound on the nematic (isotropic) coexistence density is given by the density corresponding to $T_{N,\max}$ ($T_{I,\min}$). We emphasize that for each included (P, T) state point, the replicas from the upward and downward branches agreed to within their associated uncertainties, indicating that hysteresis effects are not significant.

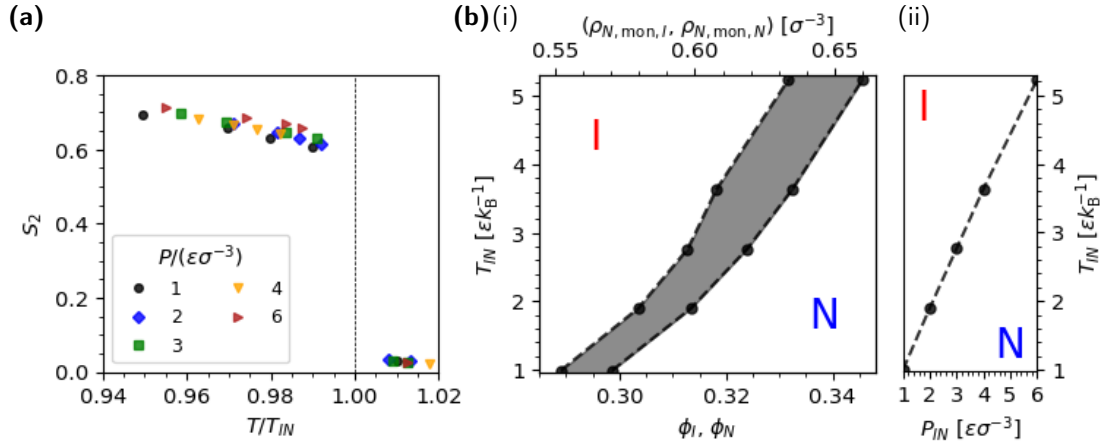


FIGURE C.7: Isotropic-nematic coexistence. (a) Uniaxial orientational order parameter S_2 as a function of T/T_{IN}, close to the coexistence temperature T_{IN}, where T is the temperature. (b) Phase diagrams: (i) T_{IN} *vs.* coexistence volume fractions ϕ_X and monomer number densities $\rho_{N,\mathrm{mon},X}$, where $X = I$ (isotropic) and N (nematic); (ii) T_{IN} *vs.* coexistence pressure P_{IN}. Uncertainties are smaller or comparable to the size of the symbols, except for T/T_{IN} in (a) where the error bars have been omitted for clarity.

TABLE C.1: Isotropic-nematic coexistence properties: coexistence pressure P_{IN} and temperature T_{IN}; coexistence volume fraction (monomer number density) of the isotropic and nematic phases, ϕ_I and ϕ_N ($\rho_{N,\mathrm{mon},I}$ and $\rho_{N,\mathrm{mon},N}$), respectively.

P_{IN} $[\epsilon\sigma^{-3}]$	T_{IN} $[\epsilon k_B^{-1}]$ [a]	ϕ_I [b]	ϕ_N [c]	$\rho_{N,\mathrm{mon},I}$ $[\sigma^{-3}]$ [b]	$\rho_{N,\mathrm{mon},N}$ $[\sigma^{-3}]$ [c]
1	0.99(1)	0.2890	0.2986	0.5519	0.5703
2	1.89(1)	0.3035	0.3134	0.5796	0.5985
3	2.76(2)	0.3128	0.3239	0.5974	0.6187
4	3.63(7)	0.3182	0.3324	0.6077	0.6349
6	5.23(6)	0.3317	0.3456	0.6334	0.6600

[a] Statistical uncertainties in the least significant figure are given in parentheses and correspond to $\delta T_{IN} = (T_{N,\max} - T_{I,\min})/2$.
[b] Lower bound.
[c] Upper bound.

C.6 Thermal diffusion coefficient: fitting empirical equations

As discussed in the main text, the thermal diffusion coefficients of the $I = I_A = I_B$ mixtures were modelled using the empirical equation $D_T = a(d_1 - d_2)^k$. The parameters a and k were determined by fitting to the equation $\ln D_T = k \ln(d_1 - d_2) + \ln a$. These fits are shown in Fig. C.8.

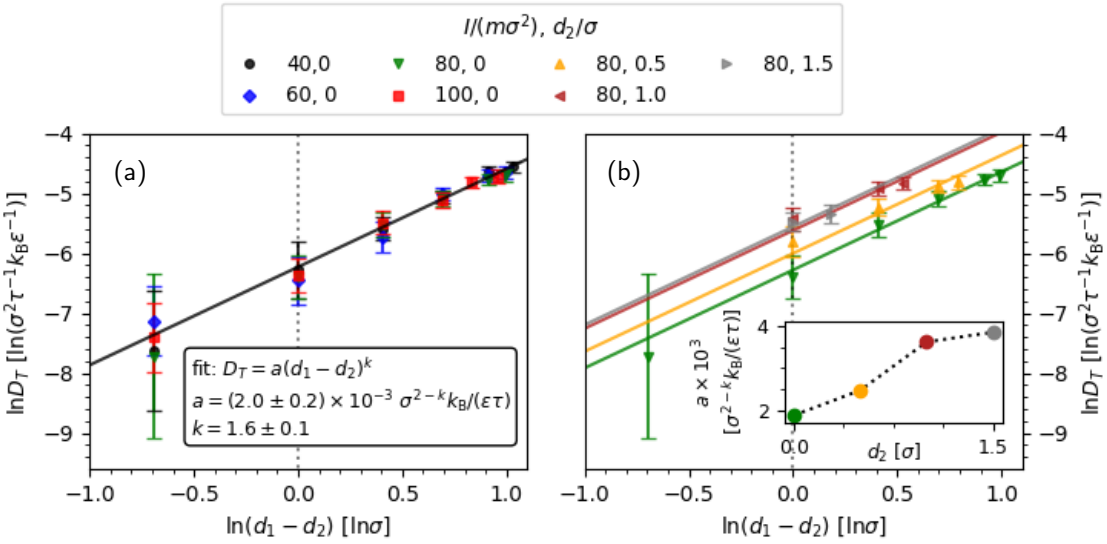


FIGURE C.8: Fitting the empirical equations for the thermal diffusion coefficient: $\ln D_T$ *vs.* $\ln(d_1 - d_2)$ for (a) the $(I = I_1 = I_2, d_1, d_2 = 0)$ and (b) $(I = I_1 = I_2, d_1, d_2 \neq 0)$ mixtures. In (b), the constraint $k = k_{d_2=0}$, as determined from (a), was applied.

Bibliography

[1] I.-C. Yeh and G. Hummer, *J. Phys. Chem. B*, 2004, **108**, 15873–15879.

[2] B. Dünweg and K. Kremer, *J. Chem. Phys.*, 1993, **99**, 6983–6997.

[3] S. H. Jamali, L. Wolff, T. M. Becker, A. Bardow, T. J. H. Vlugt and O. A. Moultos, *J. Chem. Theory Comput.*, 2018, **14**, 2667–2677.

Appendix D

Additional numerical data for Chapter 6

TABLE D.1: Thermodynamic states simulated using non-equilibrium molecular dynamics. ρ_{box}, T_{box}, P_{zz}, represent the average density, temperature and pressure parallel to the direction of the heat flux, respectively. T_h and T_c are the temperatures of the hot and cold thermostats, λ is the thermal conductivity, S_{TP} is the thermal polarization coefficient, and E and E_P are the total electrostatic field and the dipolar contribution to the total field, respectively. All local properties (columns 8-12) were computed at the thermodynamics conditions specified by density ρ and temperature T. Statistical uncertainties (standard error of the mean) in the least significant figure are given in parenthesis.

ρ_{box}	T_c	T_h	T_{box}	P_{zz}	ρ	T	∇T	λ	S_{TP}	E	E_P
[g cm^{-3}]	[K]	[K]	[K]	[bar]	[g cm^{-3}]	[K]	[K nm^{-1}]	[W/(K m)]	[mV K^{-1}]	[mV nm^{-1}]	[mV nm^{-1}]
0.770	255	355	302	43(8)	0.770	303	4.9(1)	0.239(7)	-0.56(6)	-2.7(3)	-2.5(3)
0.770	350	450	397	1205(6)	0.770	397	5.3(1)	0.229(5)	-0.41(6)	-2.2(3)	-1.8(3)
0.770	450	550	498	2400(20)	0.770	498	5.4(1)	0.236(5)	-0.34(6)	-1.8(3)	-1.6(4)
0.770	550	650	599	3470(10)	0.770	598	5.2(2)	0.246(9)	-0.32(7)	-1.6(3)	-1.2(4)
0.770	650	750	698	4506(3)	0.770	697	5.5(2)	0.234(9)	-0.21(6)	-1.1(3)	-0.8(3)
0.350	650	750	699	353(4)	0.333	700	4.9(2)	0.072(3)	-0.07(3)	-0.3(1)	-0.1(2)
0.500	650	750	698	740(6)	0.495	700	5.4(2)	0.109(4)	-0.16(3)	-0.8(2)	-0.7(2)
0.650	650	750	704	2037(4)	0.650	700	5.3(1)	0.179(4)	-0.18(2)	-0.9(1)	-0.5(1)
0.249	600	700	637	104(1)	0.249	607	0.99(8)	0.26(2)	-0.3(1)	-0.3(1)	0.2(1)
0.249	605	705	644	109(2)	0.249	613	1.18(6)	0.21(1)	-0.19(8)	-0.22(9)	0.32(9)
0.249	620	720	660	124(2)	0.249	627	1.74(9)	0.144(8)	-0.12(7)	-0.2(1)	0.3(1)
0.249	630	730	671	133(1)	0.249	638	2.07(9)	0.121(5)	-0.15(5)	-0.3(1)	0.1(1)
0.249	640	740	681	142(2)	0.249	648	2.40(9)	0.106(4)	-0.09(4)	-0.20(9)	0.2(1)
0.249	650	750	692	151(2)	0.249	658	2.7(1)	0.097(6)	-0.10(5)	-0.3(1)	0.1(1)
0.249	660	760	703	159(2)	0.249	667	3.0(1)	0.088(4)	-0.10(5)	-0.3(1)	0.0(1)

Appendix E

Supporting information for Chapter 8

For the (non-ReaxFF) classical force fields, a cutoff of 13 Å was used for the oxygen-oxygen Lennard-Jones (LJ) potential unless specified otherwise.

E.1 Response functions: SHAKE vs. RATTLE

SHAKE[1] and RATTLE[2] are holonomic constraint algorithms that enforce fixed geometries (e.g., bond distances and angles). SHAKE was invented for time integration algorithms where only the particle positions are explicitly updated, such as the Verlet algorithm. If particle velocities are also integrated explicitly, as with the velocity Verlet algorithm, then a second set of constraining forces is required to eliminate velocity components along the bonds – this is done in RATTLE. LAMMPS uses the velocity Verlet algorithm, making RATTLE the more appropriate choice. RATTLE, as implemented in LAMMPS, should be called after all other changes to the velocity and forces, but before changes to the simulation cell dimensions.[3,4] This leads to conflicting requirements for the *NPT* simulations in Chapter 8. Here, we assess how accurately SHAKE and RATTLE calculate the response functions for the water simulations in Chapter 8.

All results in this section correspond to the SPC/E force field, using the simulation parameters given in Sec. 8.2. Simulations containing 2133 water molecules were performed in the *NPT* ensemble (Sec. 8.2.2). Here we report the results from two sets of simulations that use different holonomic constraints, SHAKE and RATTLE, but are otherwise identical. RATTLE was called after the time integration algorithms. In both cases a tolerance of 10^{-8} was used. All simulations were carried out using LAMMPS[5] (v. 7Aug2019).

The thermal expansion coefficient α_P, isothermal compressibility β_T and isobaric heat capacity C_P are defined as:

$$\alpha_P = -\frac{1}{V}\left(\frac{\partial V}{\partial T}\right)_P, \quad \beta_T = -\frac{1}{V}\left(\frac{\partial V}{\partial P}\right)_T, \quad C_P = \left(\frac{\partial H}{\partial T}\right)_P \tag{E.1}$$

where T is the temperature, P is the pressure, V is the volume, H is the enthalpy, and k_B is the Boltzmann constant. These response functions are given by the fluctuation relations:

$$\alpha_P = \frac{\langle \delta V \delta H \rangle_{NPT}}{k_\mathrm{B} T^2 V}, \quad \beta_T = \frac{\langle \delta V^2 \rangle_{NPT}}{V k_\mathrm{B} T}, \quad C_P = \frac{\langle \delta H^2 \rangle_{NPT}}{k_\mathrm{B} T^2} \tag{E.2}$$

where $\delta \mathcal{A} = \mathcal{A} - \langle \mathcal{A} \rangle_\mathrm{ens}$ and $\langle \mathcal{A} \rangle_\mathrm{ens}$ is the ensemble average of variable $\mathcal{A}$.

We show in Fig. E.2(b),(d)&(f) the response functions calculated using SHAKE and RATTLE via Eqs. E.2: α_P and C_P agree to within their associated uncertainty, but the β_T values predicted by RATTLE are significantly lower than for SHAKE. This implies that the volume (i.e. density) fluctuations are different, as shown explicitly in Fig. E.1. The equation of state (EOS) (ρ and H) predicted by SHAKE and RATTLE are consistent (Fig. E.2(a),(c)&(e)); all values agree to within their uncertainties. The response functions were additionally calculated from the EOS using Eqs. E.1. For $T = 300$ K and $P = 1$ bar, C_P and α_P were calculated by fitting a straight lines through the $H(T)$ and $V(T)$ data, respectively. For $T = 300$ K and $P = 1000$ bar, β_T was calculated by fitting a straight line through the $V(P)$ data. β_T from the EOS is consistent with the SHAKE value using Eq. E.2, indicating the RATTLE results are incorrect. Thus, RATTLE as implemented in LAMMPS (v. 7Aug2019) does not reproduce the correct density fluctuations in the NPT ensemble for our simulation set-up.

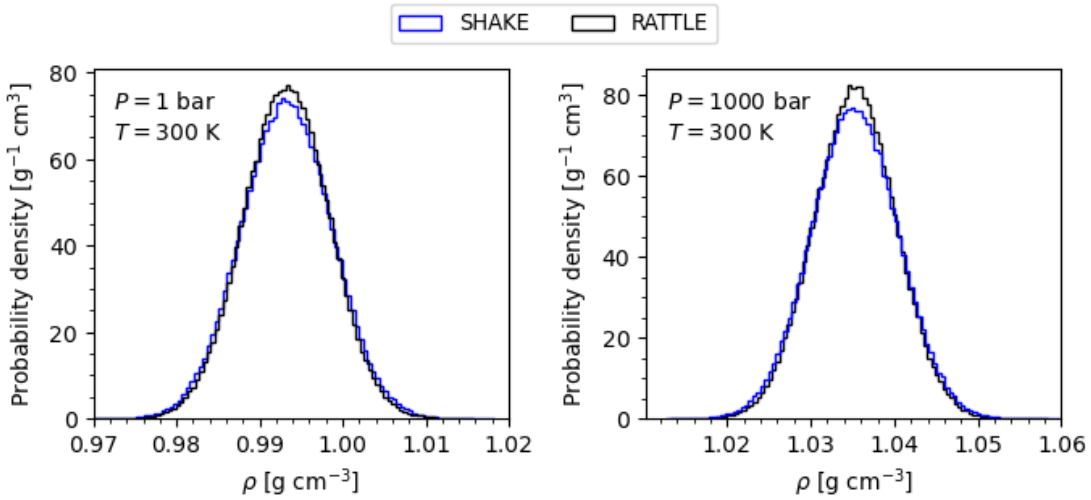


FIGURE E.1: Probability density functions of the density ρ of SPC/E using SHAKE and RATTLE.

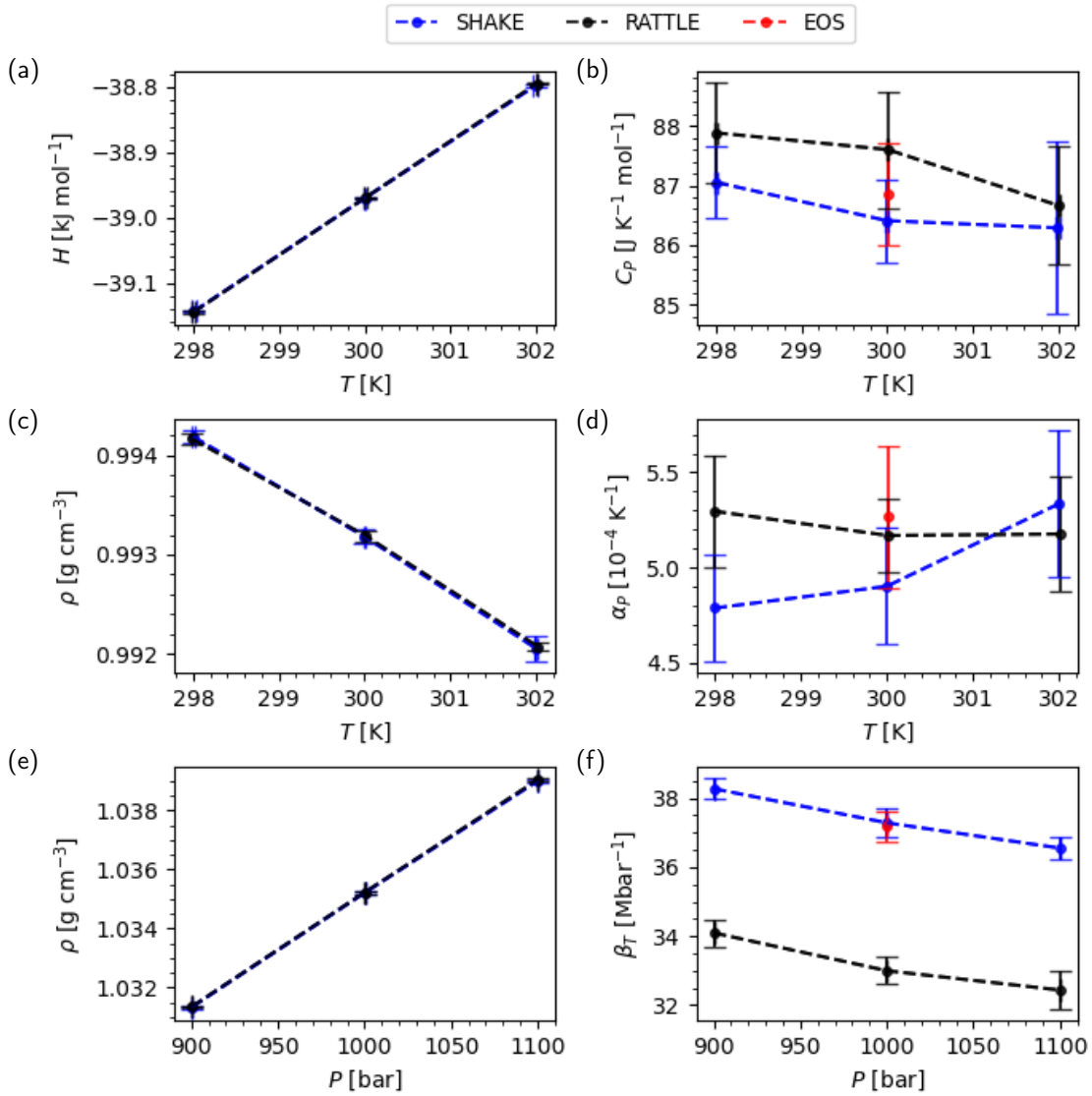


FIGURE E.2: Thermodynamic properties and response functions of SPC/E predicted using SHAKE and RATTLE. The (a) enthalpy H, (b) isobaric heat capacity C_P, (c)&(e) density ρ, (d) thermal expansion coefficient α_P and (e) isothermal compressibility β_T. T is the temperature and P is the pressure. (a)-(d) correspond to $P = 1$ bar; (e)&(f) correspond to $T = 300$ K. In (b),(d)&(f), the SHAKE and RATTLE labels correspond to the fluctuation relations Eqs. E.2; the equation of state (EOS) results correspond to Eqs. E.1.

E.2 Structure and dynamics benchmarks

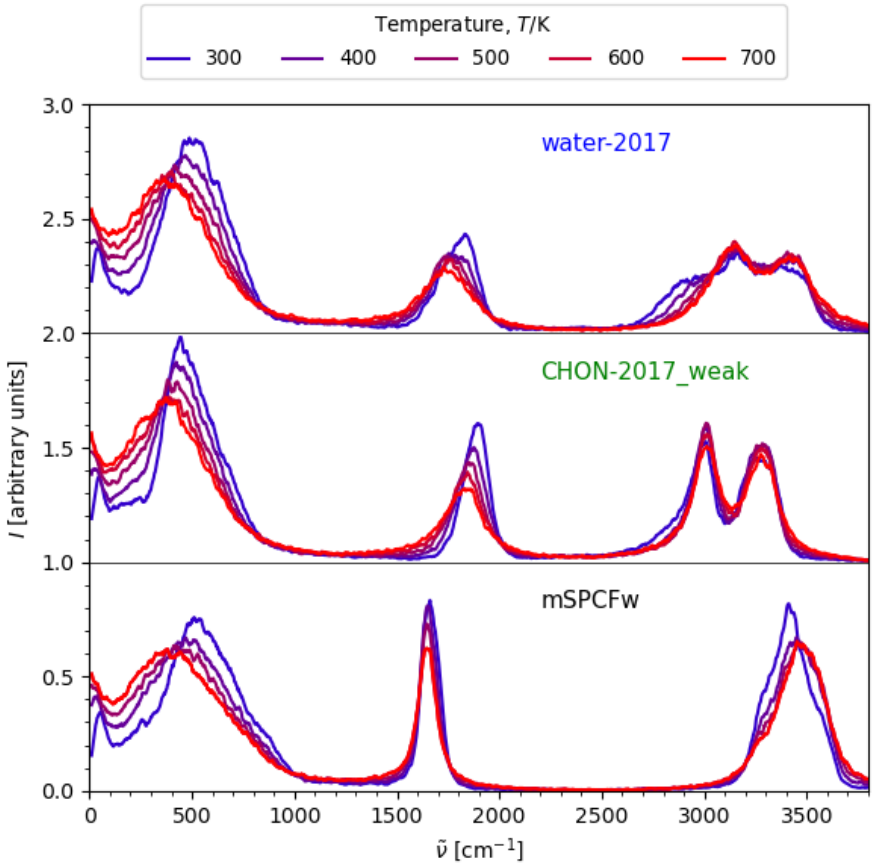


FIGURE E.3: Vibrational power spectrum of liquid water at temperatures T and 0.997 g cm^{-3}, as predicted by the mSPCFw, CHON-2017_weak and water-2017 force fields. I is the intensity at wavenumber $\tilde{\nu}$. Power spectra share the same normalization condition $\int_0^\infty I(\tilde{\nu})d\tilde{\nu} = C$, where C is a constant. For clarity the intensity for CHON-2017_weak and water-2017 have been shifted by 1 and 2, respectively.

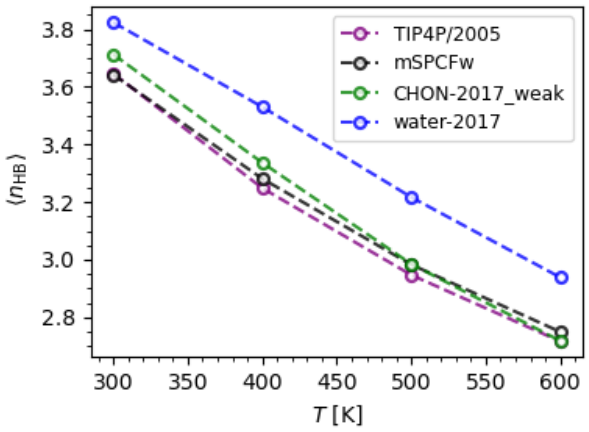


FIGURE E.4: The average number of hydrogen bonds $\langle n_{\mathrm{HB}} \rangle$ as a function of temperature T for selected force fields. The data corresponds to 0.997 g cm^{-3}. Hydrogen bonds were defined by the standard geometric criteria: an O-O distance of $r_{\mathrm{HB}} \leq 3.5$ Å and an H-O$\cdots$O angle of $\theta_{\mathrm{HB}} \leq 30°$.

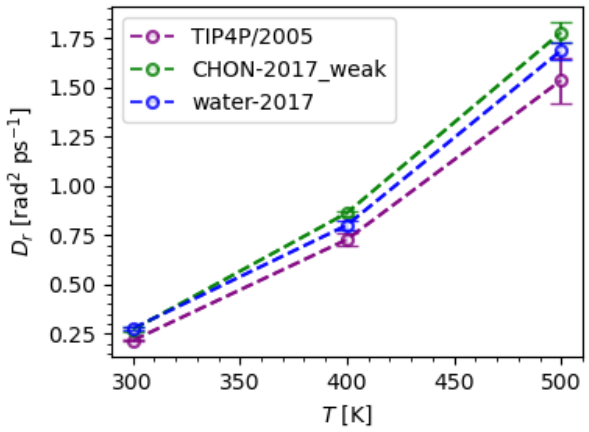


FIGURE E.5: The rotational diffusion coefficient D_r as a function of temperature T for selected force fields. The data corresponds to 0.997 g cm^{-3}.

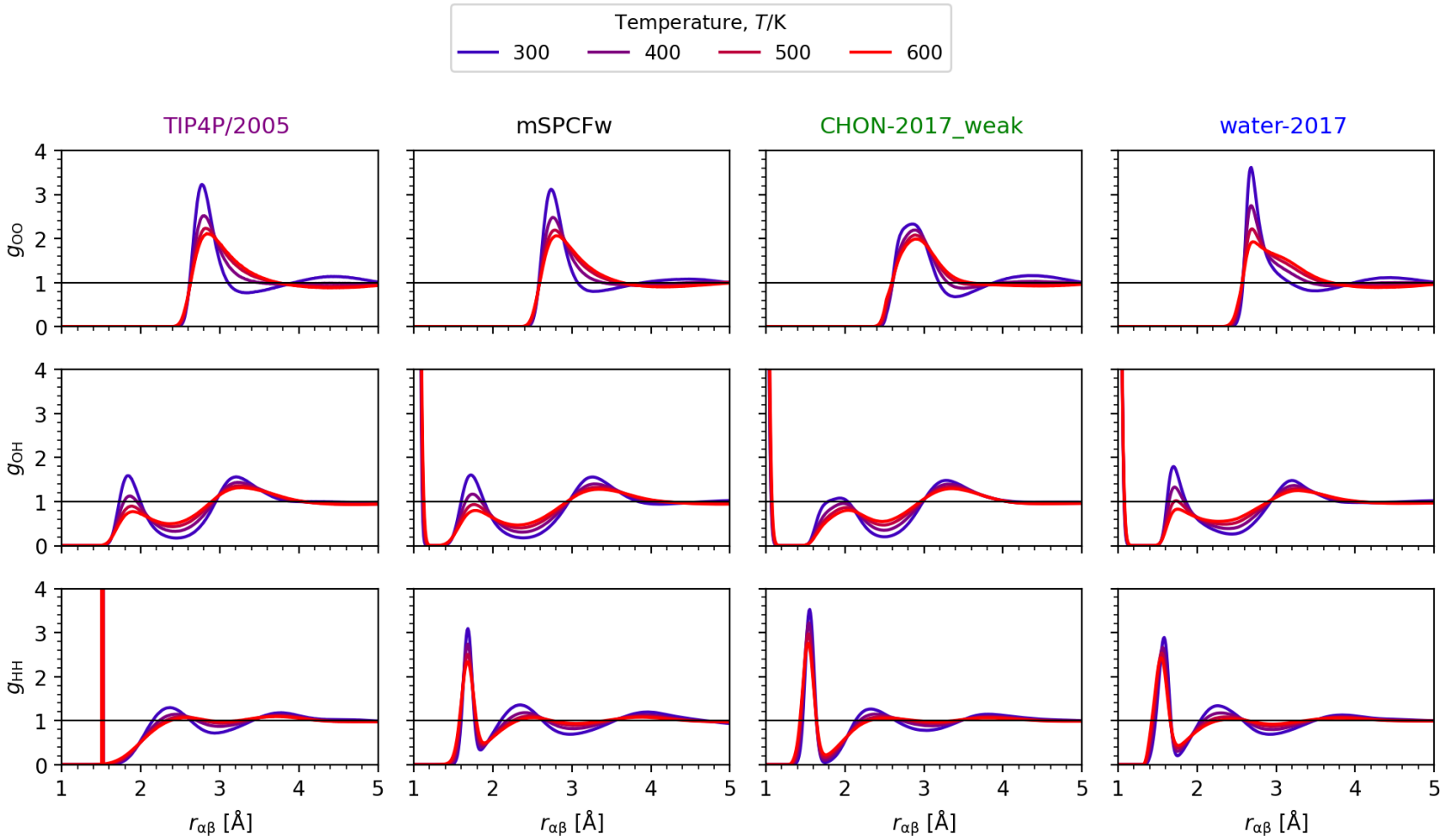


FIGURE E.6: Radial distribution functions (RDFs) of liquid water at temperature T and 0.997 g cm^{-3} as predicted by selected force fields. (top) Oxygen-oxygen RDFs g_{OO}. (middle) Oxygen-hydrogen RDFs g_{OH} (bottom) Hydrogen-hydrogen RDFs g_{HH}. $r_{\alpha\beta}$ is the radial distance between species α and β.

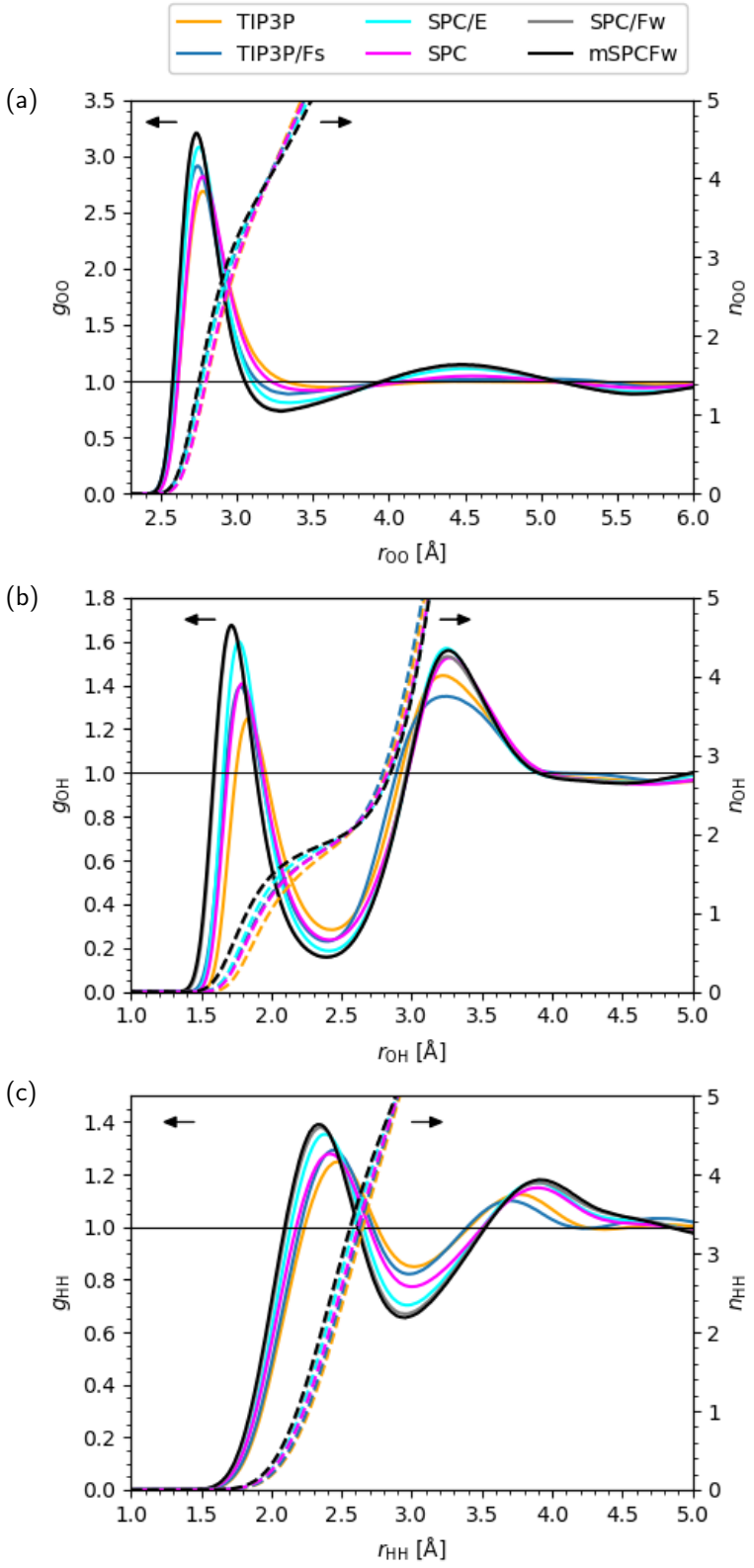


FIGURE E.7: Radial distribution functions (RDFs) of water at 300 K and 0.997 g cm^{-3} as predicted by selected flexible and rigid force fields. (a) Oxygen-oxygen RDFs g_{OO} and coordination numbers n_{OO}. (b) Oxygen-hydrogen RDFs g_{OH} and coordination numbers n_{OH}. (c) Hydrogen-hydrogen RDFs g_{HH} and coordination numbers n_{HH}. $r_{\alpha\beta}$ is the radial distance between species α and β. Data corresponds to a Lennard-Jones cutoff of 19 Å.

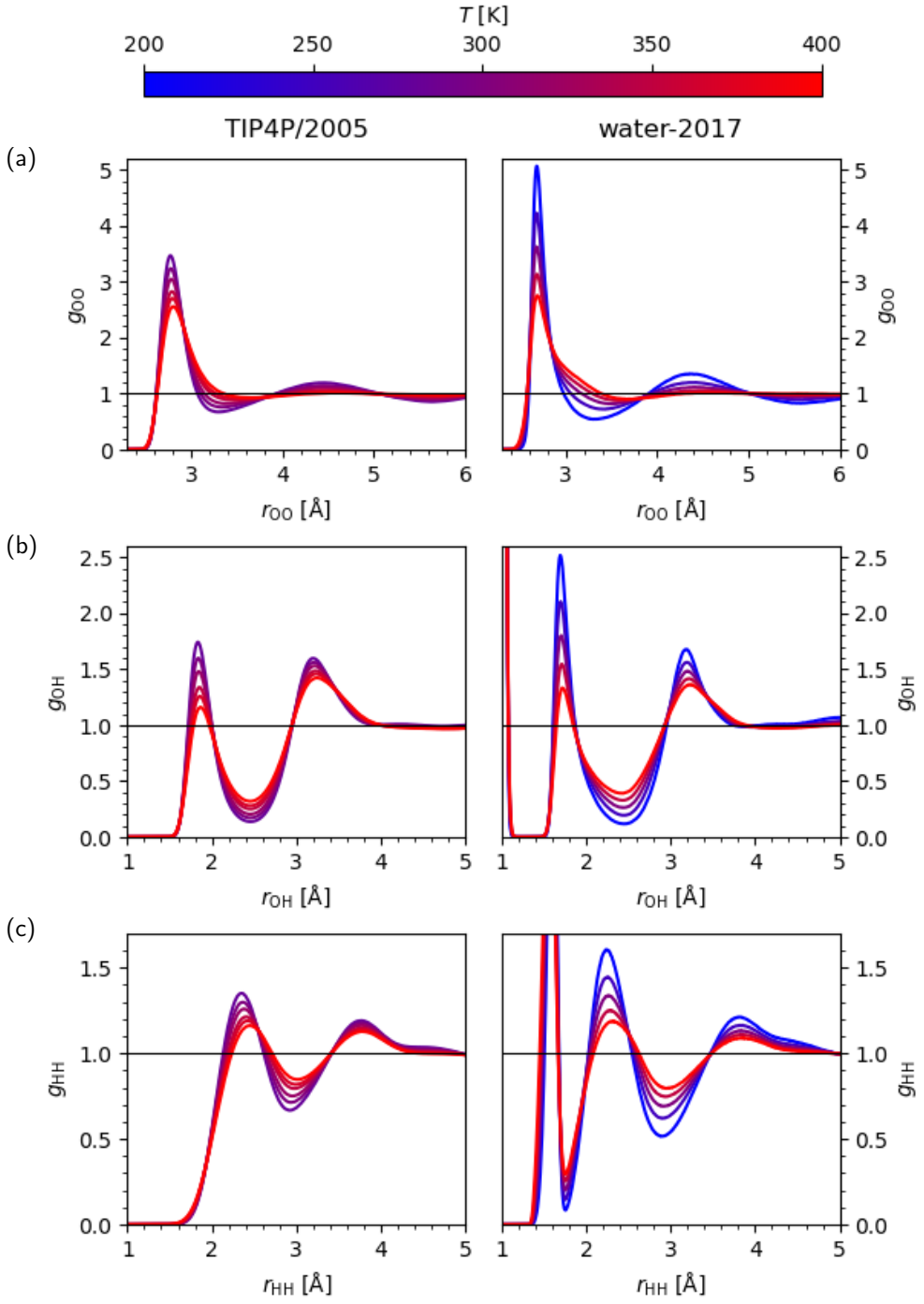


FIGURE E.8: Radial distribution functions (RDFs) of water at temperatures T and $P = 10$ bar, as predicted by the TIP4P/2005 and water-2017 force fields. (a) Oxygen-oxygen RDFs g_{OO}. (b) Oxygen-hydrogen RDFs g_{OH}. (c) Hydrogen-hydrogen RDFs g_{HH}. $r_{\alpha\beta}$ is the radial distance between species α and β. The data is colour coded according to the temperature T.

E.3 Order parameters for water

Orientational tetrahedral order parameter, q. This is probably the most widely used tetrahedral order parameter for water.[6] It probes the angular order between a water molecule and its four nearest neighbours, and is defined[7,8] as

$$q = 1 - \frac{3}{8}\sum_{j=1}^{3}\sum_{k=j+1}^{4}\left(\cos\psi_{jk} + \frac{1}{3}\right)^2 \tag{E.3}$$

where ψ_{jk} is the angle formed by the lines joining the oxygen atom of the central molecule and its nearest neighbour O atoms j and k. The average $\langle q \rangle$ ranges from 0 for an ideal gas, to 1 for a regular tetrahedron. By construction it is only sensitive to angular order, and not radial order.

Translational tetrahedral order parameter, S_k. This order parameter measures the variance of the radial distances between the O atom of the central water molecule and the O atoms of its four nearest neighbours. It is defined[6,7] as

$$S_k = 1 - \frac{1}{3}\sum_{k=1}^{4}\frac{(r_k - \bar{r})^2}{4\bar{r}^2} \tag{E.4}$$

where r_k is the distance from the central O atom to its k^{th} nearest O atom. S_k increases with local tetrahedral order, reaching a maximum of $S_k = 1$ for a perfect tetrahedron.

Asphericity of the Voronoi cell, η_{AVC}. The shape of a Voronoi polyhedron is characterized by its asphericity parameter, which is independent of the polyhedron's size. It is defined[6,9] as

$$\eta_{\mathrm{AVC}} = \frac{A^3}{36\pi V^2} \tag{E.5}$$

where A and V are the area and volume of the Voronoi polyhedron, respectively. η_{AVC} takes values of 1 for a perfect sphere, 3.31 for a regular tetrahedron, and 2.25 for ice I_h.[6,9]

Steinhardt order parameters, Q_l. These order parameters characterize local orientational order. The Steinhardt order parameters are defined[10] as

$$Q_l = \sqrt{\frac{4\pi}{2l+1}\sum_{m=-l}^{+l}\bar{Y}_{lm}\bar{Y}_{lm}^*} \tag{E.6}$$

$$\bar{Y}_{lm} = \frac{1}{N_n}\sum_{j=1}^{N_n}Y_{lm}(\theta(\boldsymbol{r}_{ij}), \phi(\boldsymbol{r}_{ij})) \tag{E.7}$$

for each particle i, where $Y_{lm}(\theta, \phi)$ are the spherical harmonics, θ and ϕ are the polar angles of "bond" vector $\boldsymbol{r}_{ij}$ between i and neighbour j, and N_n is the number of nearest neighbours to particle i. Q_l is therefore a rotationally invariant non-negative amplitude. Q_l adopt well-defined

values for high-symmetry structures; when $N_n = 12$ a perfect HCP crystal ($P6_3/mmc$), which is the structure of ice Ih, corresponds to: $Q_4 = 0.097$, $Q_5 = 0.252$ and $Q_6 = 0.484$.[11]

Order parameters for TIP4P/2005 and water-2017.

We show in Fig. E.9 the average order parameters for the TIP4P/2005 and water-2017 force fields at various temperatures along the 10 bar isobar. In Fig. E.10, we show the distributions of the order parameters.

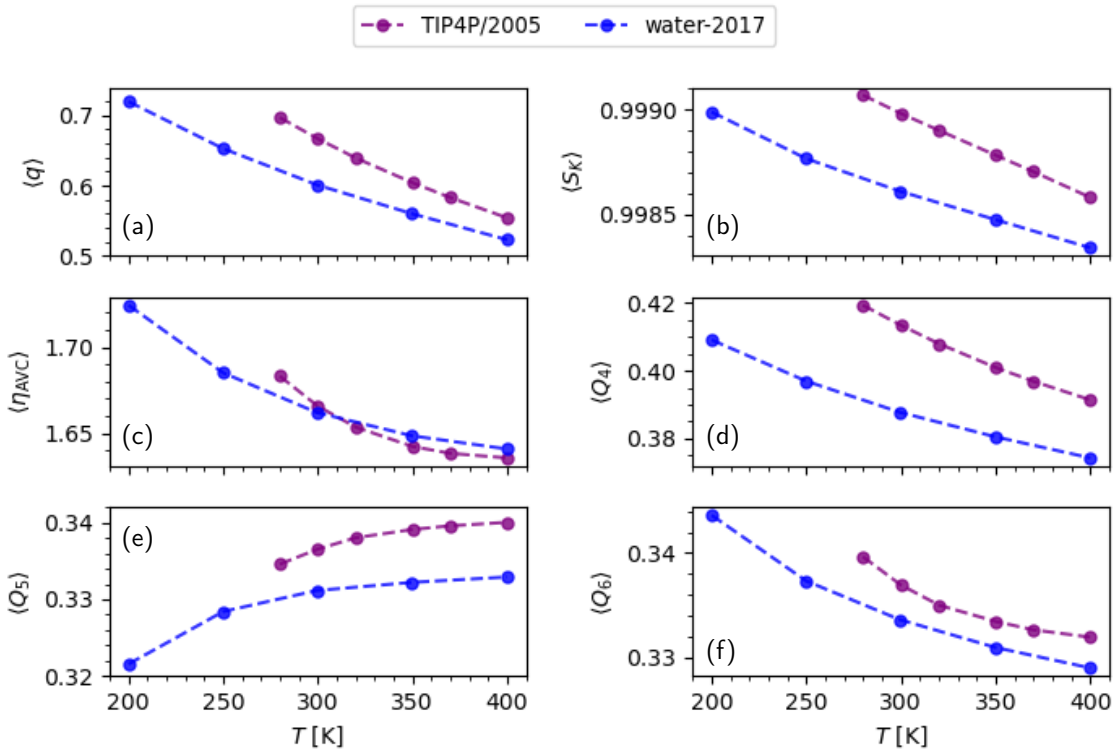


FIGURE E.9: Average order parameters of water as a function of temperature T along the 10 bar isobar, as predicted by the TIP4P/2005 and water-2017 force fields: (a) Orientational tetrahedral order parameter, q; (b) translational tetrahedral order parameter, S_k; (c) asphericity of the Voronoi cell, η_{AVC}; the Steinhardt order parameters, (d) Q_4, (e) Q_5 and (f) Q_6. Statistical uncertainties are smaller than the size of the symbols.

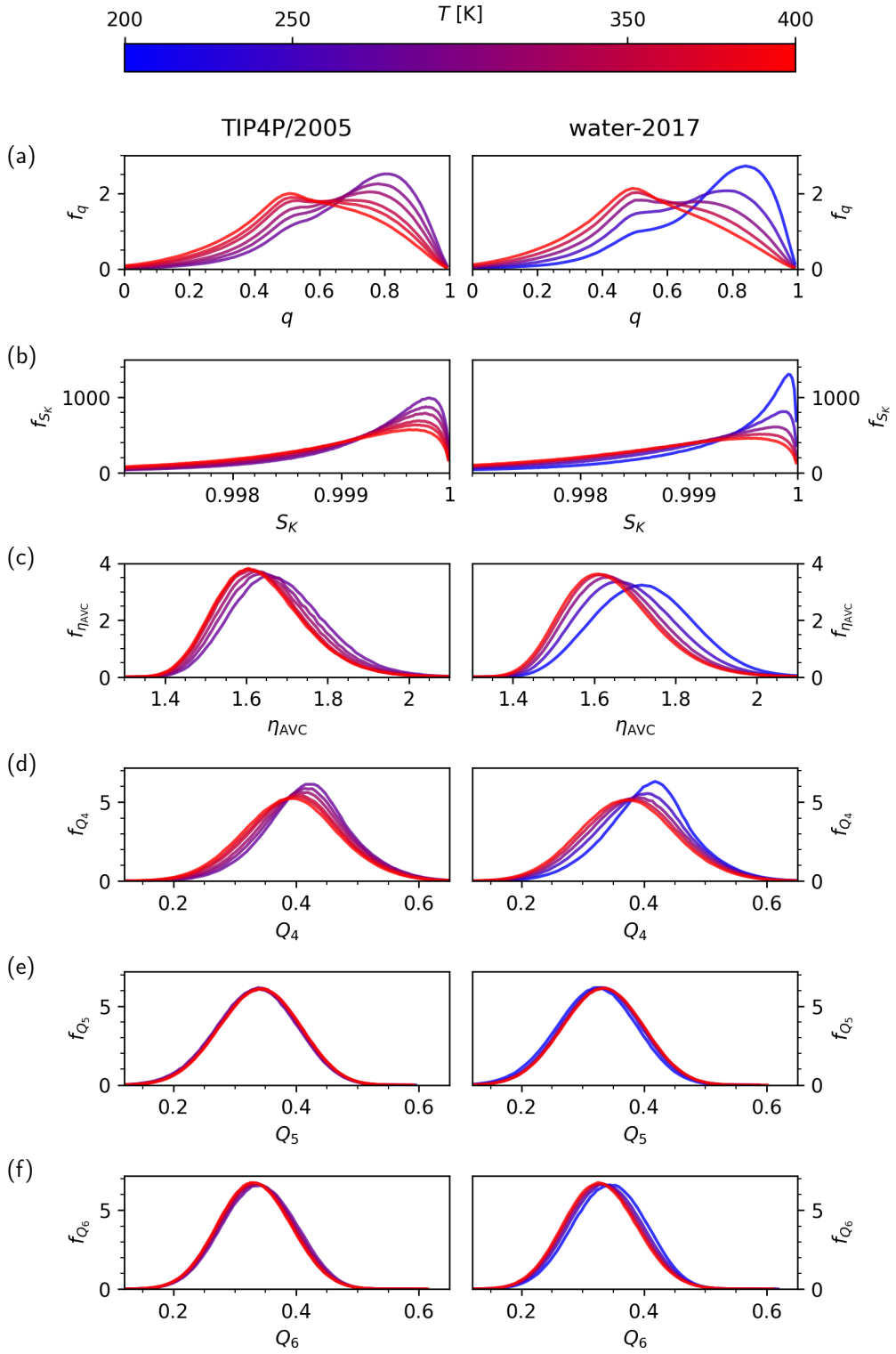


FIGURE E.10: Order parameter probability density functions f_X (where X is the variable) of water at temperatures T and pressure $P = 10$ bar, as predicted by the TIP4P/2005 and water-2017 force fields: (a) Orientational tetrahedral order parameter, q; (b) translational tetrahedral order parameter, S_k; (c) asphericity of the Voronoi cell, η_{AVC}; the Steinhardt order parameters, (d) Q_4, (e) Q_5 and (f) Q_6. The data is colour coded according to the temperature T.

E.4 Shear, bulk and longitudinal viscosity

The shear viscosity η and bulk viscosity ζ were calculated using the Green-Kubo integral formulas:

$$\eta_{\mathrm{GK}} = \frac{V}{k_{\mathrm{B}}T} \lim_{t'\to\infty} \int_0^{t'} \langle P_{\alpha\beta}(t) P_{\alpha\beta}(0)\rangle dt \tag{E.8}$$

$$\zeta_{\mathrm{GK}} = \frac{V}{k_{\mathrm{B}}T} \lim_{t'\to\infty} \int_0^{t'} \langle \delta P(t) \delta P(0)\rangle dt \tag{E.9}$$

where V is the volume of the simulation cell, T is the temperature, k_{B} is the Boltzmann constant and t is the time. $\alpha \neq \beta$ such that $P_{\alpha\alpha}$ and $P_{\alpha\beta}$ are the diagonal and off-diagonal elements of the pressure tensor, respectively. The pressure fluctuations $\delta P(t)$ are defined as $\delta P(t) = P(t) - \langle P\rangle_{\mathrm{ens}}$ where $P(t) = (P_{xx}(t) + P_{yy}(t) + P_{zz}(t))/3$ is the instantaneous pressure at time t and $\langle P\rangle_{\mathrm{ens}}$ is the ensemble average. For η_{GK}, results were averaged over $(\alpha, \beta) = (x, y)$, (x, z) and (y, z). Correlation times of t_c =15-30 ps and t_c =20-50 ps were used for the upper limits of the integrals in Eq. E.8 and Eq. E.8, respectively, depending on the temperature. The longitudinal viscosity ξ was then calculated from $\xi = (4/3)\eta + \zeta$.

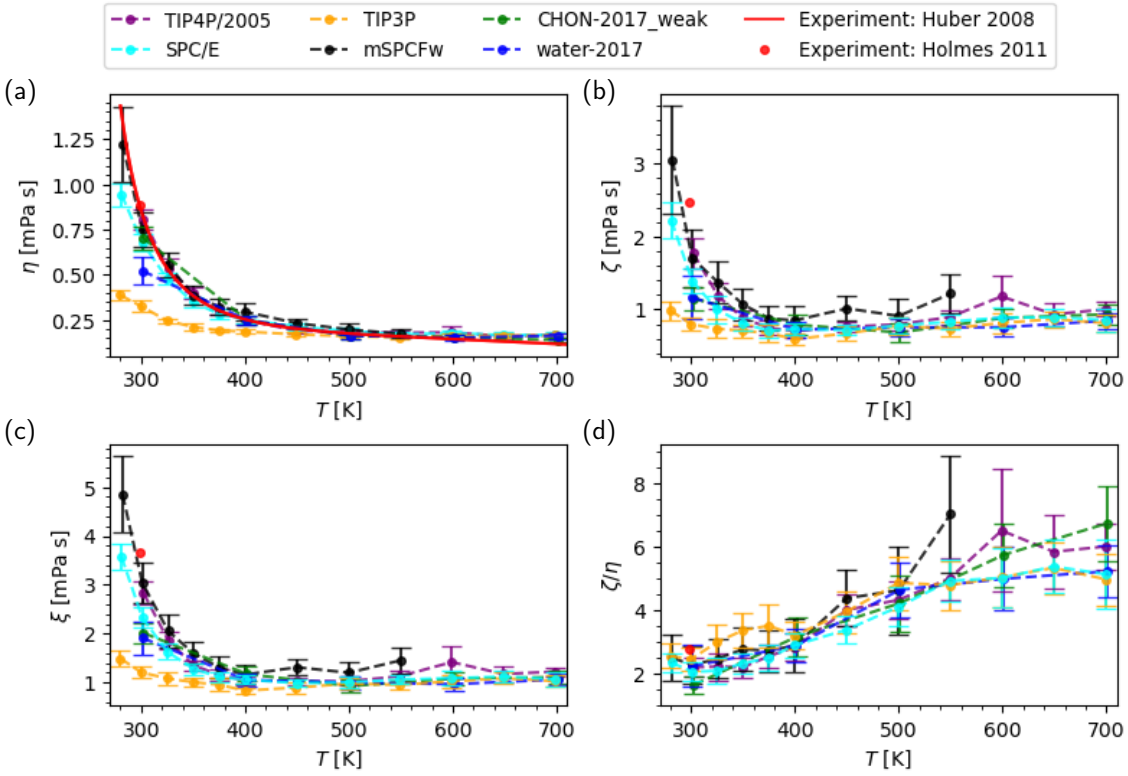


FIGURE E.11: Viscosity of water as a function of temperature T along the 0.997 g cm^{-3} isochore, as predicted by selected force fields. The (a) shear viscosity η, (b) bulk viscosity ζ, (c) longitudinal viscosity ξ and (d) the ratio ζ/η. The experimental data of Holmes *et. al.*[12] corresponds to 298.15 K and ambient pressure. In (a), the experimental data of Huber *et. al.*[13] corresponds to 0.997 g cm^{-3}.

Bibliography

[1] J.-P. Ryckaert, G. Ciccotti and H. J. Berendsen, *J. Comput. Phys.*, 1977, **23**, 327–341.

[2] H. C. Andersen, *J. Comput. Phys.*, 1983, **52**, 24–34.

[3] LAMMPS Development Team, *LAMMPS source code (v. 7Aug19)*, https://www.lammps.org/.

[4] LAMMPS Development Team, *LAMMPS Documentation (accessed: 1st July 2022)*, https://docs.lammps.org/fix_shake.html.

[5] A. P. Thompson, H. M. Aktulga, R. Berger, D. S. Bolintineanu, W. M. Brown, P. S. Crozier, P. J. in 't Veld, A. Kohlmeyer, S. G. Moore, T. D. Nguyen, R. Shan, M. J. Stevens, J. Tranchida, C. Trott and S. J. Plimpton, *Comp. Phys. Comm.*, 2022, **271**, 108171.

[6] E. Duboué-Dijon and D. Laage, *J. Phys. Chem. B*, 2015, **119**, 8406–8418.

[7] P.-L. Chau and A. J. Hardwick, *Mol. Phys.*, 1998, **93**, 511–518.

[8] J. R. Errington and P. G. Debenedetti, *Nature*, 2001, **409**, 318–321.

[9] G. Ruocco, M. Sampoli and R. Vallauri, *J. Chem. Phys.*, 1992, **96**, 6167–6176.

[10] P. J. Steinhardt, D. R. Nelson and M. Ronchetti, *Phys. Rev. B*, 1983, **28**, 784–805.

[11] W. Mickel, S. C. Kapfer, G. E. Schröder-Turk and K. Mecke, *J. Chem. Phys.*, 2013, **138**, 044501.

[12] M. J. Holmes, N. G. Parker and M. J. W. Povey, *J. Phys.: Conf. Ser.*, 2011, **269**, 012011.

[13] M. L. Huber, R. A. Perkins, A. Laesecke, D. G. Friend, J. V. Sengers, M. J. Assael, I. N. Metaxa, E. Vogel, R. Mareš and K. Miyagawa, *J. Phys. Chem. Ref. Data*, 2000, **38**, 101–125.